

The Risk Assessment Study of Potential Forest Fire in Idukki Wildlife Sanctuary using RS and GIS Techniques

Ajin R.S.¹, Ana-Maria Loghin², Mathew K. Jacob³, Vinod P.G.¹ and Krishnamurthy R.R.⁴

¹Geomatics Division, GeoVin Solutions Pvt. Ltd., Thiruvananthapuram, Kerala, India

²Faculty of Hydrotechnical Engineering, Geodesy and Environmental Engineering, Gheorghe Asachi Technical University of Iasi, Romania

³Department of Geology, Sree Narayana College, Sivagiri, Kerala, India

⁴Department of Applied Geology and Centre for Environmental Sciences, University of Madras, Chennai, India

Publication Date: 9 February 2016

Article Link: <http://scientific.cloud-journals.com/index.php/IJAESE/article/view/Sci-325>



Copyright © 2016 Ajin R.S., Ana-Maria Loghin, Mathew K. Jacob, Vinod. P.G. and Krishnamurthy R.R. This is an open access article distributed under the **Creative Commons Attribution License**, which permits unrestricted use, distribution, and reproduction in any medium, provided the original work is properly cited.

Abstract In recent years, forest fires have become a major disaster in many countries of the world because of their impact on biodiversity, landscape, health, environment, ecology and economy. Forest fires are one of the major natural hazards occurring in the forests of the Western Ghats, a biodiversity hotspot in India. The present study aims to demarcate the risk zones of potential forest fire in Idukki Wildlife Sanctuary using integrated Remote Sensing (RS) and Geographic Information System (GIS) techniques. Every year, during March-May months, the forests in this area are affected by severe fires. In order to generate the fire risk zone map of the study area, a thematic study was carried out on each of the influencing factors *viz.* land cover type, slope, distance from settlement, distance from road, and elevation. A Fire Risk Index method was used to prepare the risk zone map. The area of the final map was grouped into five different categories of risk zones, *viz.* very low, low, moderate, high, and very high. Finally the risk zone map was validated with the fire incidence data for the last 10 years. Results of this study show that the most important factors which contribute to fire ignition are the human induced factors, also known as the anthropogenic factors. The resulting map of forest fire risk zone can be of great benefit for understanding the fire problem and will offer a more effective database for the preparation and control of forest fires.

Keywords *Fire Risk Index; Natural Hazards; Biodiversity; Western Ghats*

1. Introduction

Forest fires are one of the major natural hazards, becoming a serious threat to the environment. Forest fires are considered to be a potential hazard with physical, biological, ecological, and environmental consequences (Somashekar et al., 2009). It typically occurs during periods of increased temperature and drought (Tatli and Türkeş, 2014). The major causative factor inducing forest fires is the climate change, along with the anthropogenic activities. The causes of forest fire are varying throughout the world. There are two different types of forest fires, depending on the causative factors. Thus, in some parts, there are naturally occurring fires, which are climate induced, in most

cases by lightning, and secondly, in other zones, there are human induced fires. Forest fires can cause extensive damage to the biodiversity, ecosystem, landscape, and endangers human and animal life. It can also cause atmospheric pollution. During forest fires, significant amount of gaseous and particulate matter pollutants will get emitted into the atmosphere (Lazaridis et al., 2008). On the other hand, forest fires can also have some positive impacts. In many ecosystems, forest fires help the natural regeneration process by stimulating the germination of certain species, clearing space for the invasion and growth of others, and releasing a periodic flush of nutrients into the soil (Dawson et al., 2001). The effects of fire on forests vary, depending upon weather, topography, and fuel type (Podur and Martell, 2009). Fires occur in forest areas from all over the world. This phenomenon also occurs in the Indian forests, and is a major cause of degradation. It is estimated that the proportion of forest areas prone to fires annually ranges from 33% in some states to over 90% in others (Roy, 2003). Forest fires are frequent in Kerala, in the forests of the Western Ghats, a biodiversity hotspot in southwest India. The study area is represented by the Idukki Wildlife Sanctuary, which is a part of the Western Ghats. This area was affected by fires especially during the months from March to May. The risk of forest fire will be severe in ecologically sensitive area like the Western Ghats, which can adversely affect the wildlife, micro climate, and forest regeneration.

RS and GIS are effective techniques, which can be used in forest fire risk zonation. Many researchers delineated forest fire risk zones using RS and GIS techniques (Ajin et al., 2015; Singh, 2014; Thakur and Singh, 2014; Veeraanarayanaa and Ravikumar, 2014; Rajabi et al., 2013; Singh and Ajay, 2013; Assaker et al., 2012; Chavan et al., 2012; Ghobadi et al., 2012; Mahdavi et al., 2012; Sowmya and Somashekar, 2010; Dong et al., 2005; Chuvieco et al., 1999; Chuvieco and Salas, 1996). Ajin et al. (2014a) delineated forest fire risk zones of Peppara Wildlife Sanctuary in Thiruvananthapuram district using RS and GIS techniques. The factors selected for the study are land use/land cover, distance from settlement, distance from road, slope, and elevation. Gangapriya and Indulekha (2013) demarcated forest fire risk areas in Thiruvananthapuram Reserve Forest using GIS techniques. The factors selected are vegetation type, proximity to human settlements, distance from roads, and slope. Somashekar et al. (2009) mapped burnt areas in Bandipur National Park using LISS III data, and RS and GIS techniques. The factors such as vegetation type, historical data, slope, and road are used. Eskandari et al. (2013) demarcated fire risk areas of Northern forests in Iran using GIS techniques and Dong model. The factors such as vegetation type, vegetation density, slope, aspect, elevation, and distance from road, distance from settlement, and distance from farmland are used for the study.

The objective of this study is to delineate the forest fire risk zones of Idukki Wildlife Sanctuary in Kerala using RS and GIS techniques. In order to generate the fire risk zone map of the study area, five important influencing factors such as land cover type, slope, distance from settlement, distance from road, and elevation are selected. A Fire Risk Index (FRI) method is used for the delineation of the identified risk zones.

2. Materials and Methods

2.1. Study Area

The present study area, the Idukki Wildlife Sanctuary is located in the Thodupuzha and Udumbanchola taluks of Idukki district. The sanctuary spans approximately an area of 105.364 sq. km, bounded within 76°52'00" and 77°7'00"E longitudes and 9°43'00" and 9°51'00"N latitudes. This is one of the most nature rich areas in Kerala, with steep mountains and undulating hills and valleys. The major rivers flowing through the area are Periyar and Cheruthoniar. The importance of this area is increased by the world famous Idukki arch dam; built on the Periyar River, with a length of 365.85 m. Located at an altitude of 167.68 m, it is one of the highest arch dams in Asia, and the third tallest (168.91 m) arch dam in the world. This dam was constructed along with two other dams, viz. Cheruthoni and Kulamavu. Together these three dams form the Idukki reservoir of 33 sq. km. In the

sanctuary, the temperature varies from 13°C to 29°C; the warmest period is March-April. The annual average rainfall in this area is about 3800 mm. The forest types include West Coast tropical evergreen forests, semi-evergreen forests, moist deciduous forests, hill shoals, and grasslands. The major tree species are *Dipterocarpus indicus*, *Palaquium ellipticum*, *Calophyllum polyanthum*, *Vernonia arborea*, *Mesua ferrea*, *Hopea parviflora*, *Persea macrantha*, *Artocarpus hirsutus*, *Lagerstroemia microcarpa*, *Cinnamomum zeylanicum*, *Tectona grandis*, *Dalbergia latifolia*, *Terminalia paniculata*, *Terminalia bellirica*, *Grewia tiliaefolia*, *Pterocarpus marsupium*, etc. The common animals found are Elephant, Sambar deer, Barking deer, Mouse deer, Bonnet macaque, Nilgiri langur, Malabar giant squirrel, Wild dog, Wild boar, Porcupine, Jackal, etc; and also various species of snakes including Cobra, Viper, Krait and numerous non-poisonous ones are found. Birds include Grey junglefowl, Malabar grey hornbill, several species of Woodpeckers, Bulbuls, Flycatchers, etc. The study area map is shown in Figure 1.

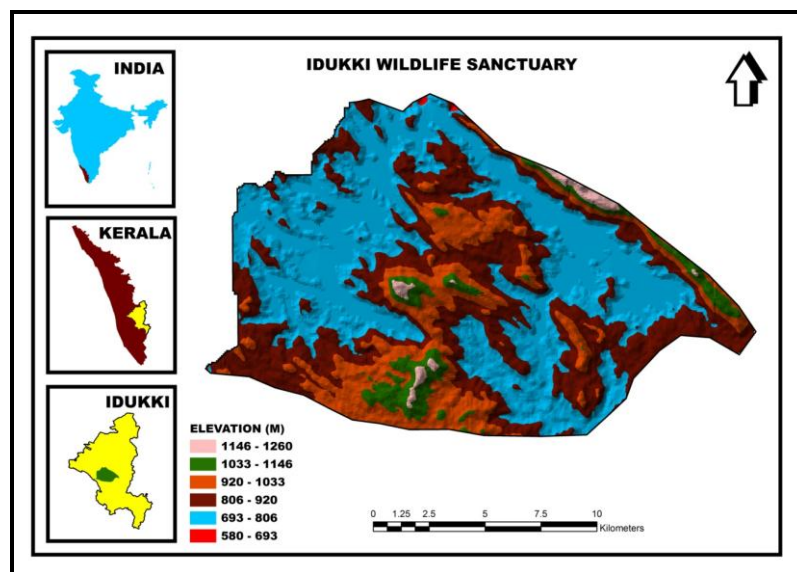


Figure 1: Location Map of the Study Area

2.2. Methodology

The flowchart of methodology used for the present study is shown in Figure 2. The study area was delineated from the Survey of India (SOI) topographic maps (58 C/13, 58 C/14, 58 G/1, and 58 G/2) of 1:50,000 scale. The thematic maps required for this study were prepared using ArcGIS 9.3 and ERDAS Imagine 9.2 software. The land cover type map was prepared from the IRS-P6 LISS-III image of 23.5 m resolution. The ERDAS Imagine software was used for the supervised classification of satellite image. The road networks and human settlements were digitized from the toposheets and Google Earth data/map, and the distance from road and distance from settlement maps were prepared from the digitized data using ArcGIS spatial analyst tools. The contour data was derived from the Cartosat 1 DEM of 30 m resolution. ArcGIS spatial analyst and 3D analyst tools were used to prepare the slope and elevation maps from the 10 m interval contour data. In order to demarcate the forest fire risk zones in the study area, a FRI method was used. The thematic map layers of the selected factors were reclassified using Equal Interval method. Different ranks were assigned to each class of the thematic layers, and also, different weights were assigned to each thematic layer, according to their sensitivity to fire or their fire-inducing capability. The index (Table 1) was derived from the weight and rank, being equal to the multiplication of weight with the corresponding rank (Index = Weight X Rank). In order to prepare the forest fire risk zone map, the index map layers were overlaid using ArcGIS tools. Field survey was conducted to collect the fire incidence points as well as

to check the accuracy of land cover type map. Finally the risk zone map was validated with the forest fire incidence points collected from the Forest Survey of India (FSI) and during the field survey and primary data collection.

Table 1: Rank, Weight, and Index Assigned for Different Factors

Sl. No.	Factor	Class	Rank	Weight	Index
1	Land cover type	Water body	1	10	10
		Built up area	2		20
		Wasteland	3		30
		Evergreen forest	4		40
		Forest plantation	5		50
		Grassland	6		60
		Deciduous forest	7		70
2	Slope (degree)	0 – 9.91	1	3	3
		9.91 – 19.82	2		6
		19.82 – 29.74	3		9
		29.74 – 39.65	4		12
		39.65 – 49.57	5		15
3	Distance from settlement (m)	0 – 895	5	2	10
		895 – 1791	4		8
		1791 – 2686	3		6
		2686 – 3582	2		4
		3582 – 4478	1		2
4	Distance from road (m)	0 – 922	5	2	10
		922 – 1845	4		8
		1845 – 2767	3		6
		2767 – 3690	2		4
		3690 – 4613	1		2
5	Elevation (m)	580 - 715	1	1	1
		715 – 850	2		2
		850 – 985	3		3
		985 – 1120	4		4
		1120 – 1255	5		5

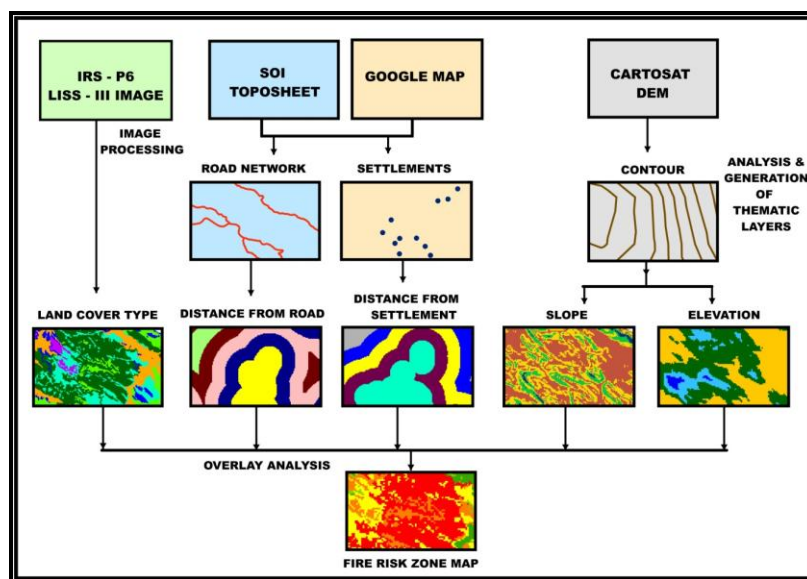


Figure 2: Flowchart for Delineating the Forest Fire Risk Zones

3. Results and Discussion

3.1. Land Cover Type

Land cover is represented by the physical material at the surface of the earth, which includes grass, trees, bare ground or water. The vegetative cover has the most significant influence on fire behaviour. For example, the areas with dry and dense vegetation are more susceptible to fire than those which are moist and sparse. The land cover types found in this sanctuary area are deciduous forest, grassland, forest plantation, evergreen forest, wasteland, built up area, and water body. In this sanctuary, the areas which are more susceptible to wild fire are deciduous forest and grassland. The deciduous forests are found mainly in the central part of the study area, and most of the grasslands are found in the northwestern parts. The map representing the land cover types of the Idukki Wildlife Sanctuary is shown in Figure 3.

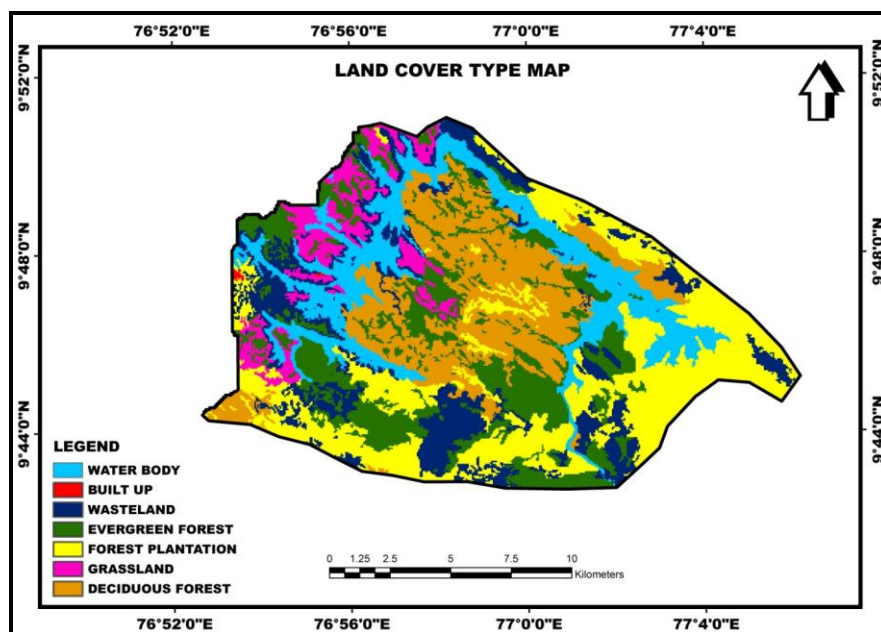


Figure 3: Land Cover Type Map

3.2. Slope

Slope represents the degree of inclination of the land surface, the measure of steepness, has great influence on fire behaviour. This is a natural factor which affects the rate of fire spread and also has significant influence on fire intensity. Fire moves most quickly up slope and least quickly down slope (Rothermel and Richard, 1972). The rate of fire spread is higher in the areas with steeper slopes, because the fire flames are angled closer to the ground surface and the effects of the wind supplies the process of heat convection (Zhong et al., 2003). Generally, currents of wind move upslope, and this phenomenon pushes the heat flames to newer areas and also to newer fuels. Thus, the rate of fire spread increases with slope steepness. The steeper the terrain, the faster is the fire spreading. The areas with steeper slopes, found in the central and northeastern parts of the sanctuary are more susceptible to forest fire. In this study, the slope of the area is grouped into five classes, viz. $0 - 9.91^\circ$, $9.91 - 19.82^\circ$, $19.82 - 29.74^\circ$, $29.74 - 39.65^\circ$, and $39.65 - 49.57^\circ$. The slope map is shown in Figure 4.

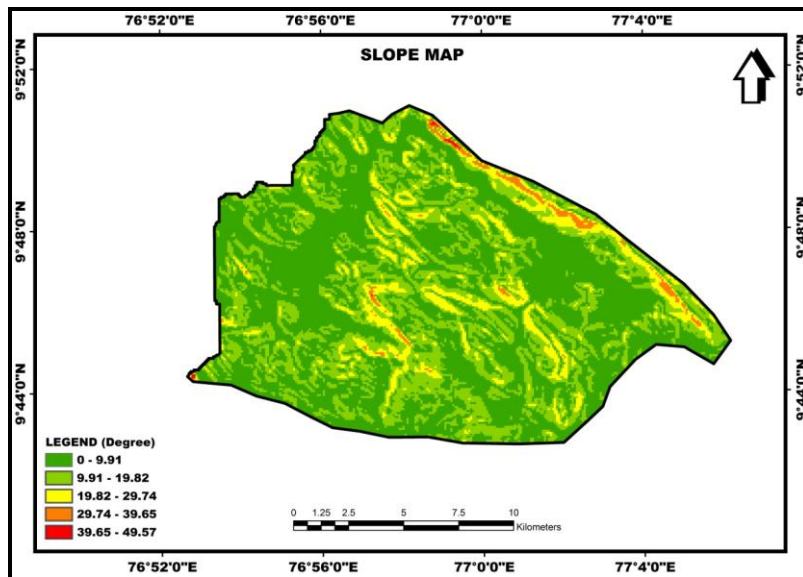


Figure 4: Slope Map

3.3. Distance from Settlement

Forest peripheral human settlements and tribal settlements within the forest, both in fact are very potential threats to forest. The tourists travelling through the area or the tribal population living there can cause fire intentionally or unintentionally. In the first case, they often set fire with some intentions like: clearing forest paths, hiding illicit felling of trees, encroachment upon forest land. They also set fires as a part of tribal customs/rituals, for the collection of Non Timber Forest Products (NTFP) like honey, etc. Secondly, they set the fire unintentionally; for example, carelessly throwing lighted cigarette butts, improper setting of campfires, leaving behind lighted fire woods recklessly, etc. Therefore the areas closer to human settlements are more prone to forest fires. Depending on the distance from settlements, the study area of Idukki Wildlife Sanctuary has been grouped into five classes' viz. 0 – 895 m, 895 – 1791 m, 1791 – 2686 m, 2686 – 3582 m, and 3582 – 4478 m. The map showing the distribution of all these classes is represented in Figure 5.

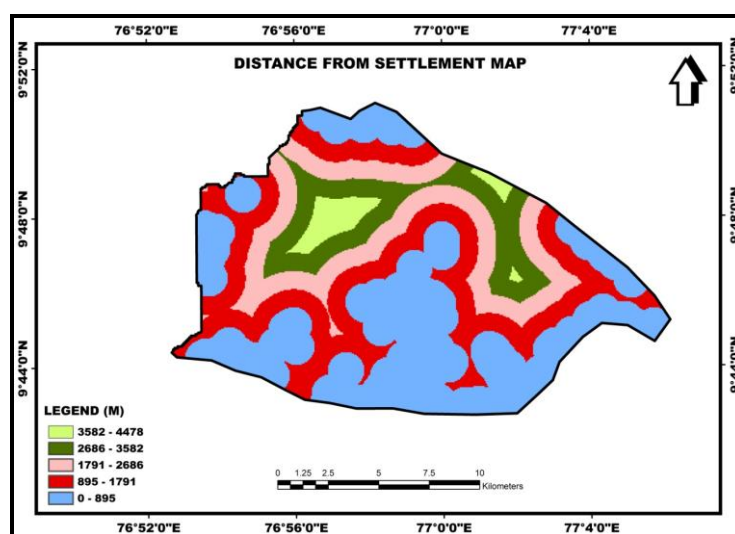


Figure 5: Distance from Settlement Map

3.4. Distance from Road

Wildlife sanctuary, bird sanctuary, and National parks are attracting lots of tourists every year. The study area, Idukki Wildlife Sanctuary is also a famous tourism destination, having a rich biodiversity that attracts lots of people every year. Also, the world famous Idukki arch dam is located within this sanctuary. To promote ecotourism, some of the traditional forest foot paths have been broadened for vehicular access to take tourists well into the forests. Ecotourism attractions in the forest can be a waterfall or any other geomorphological features. The movement of tourists through these roads can cause accidental forest fires, due to carelessly thrown burning cigarette butts or match sticks, way side food making by lighting stoves, burning tar for road making, etc. Therefore the forest areas closer to the roads are more prone to fires. Depending on the distance from roads, the study area has been grouped into five different classes viz., 0 – 922 m, 922 – 1845 m, 1845 – 2767 m, 2767 – 3690 m, and 3690 – 4613 m. The distance from road map is shown in Figure 6.

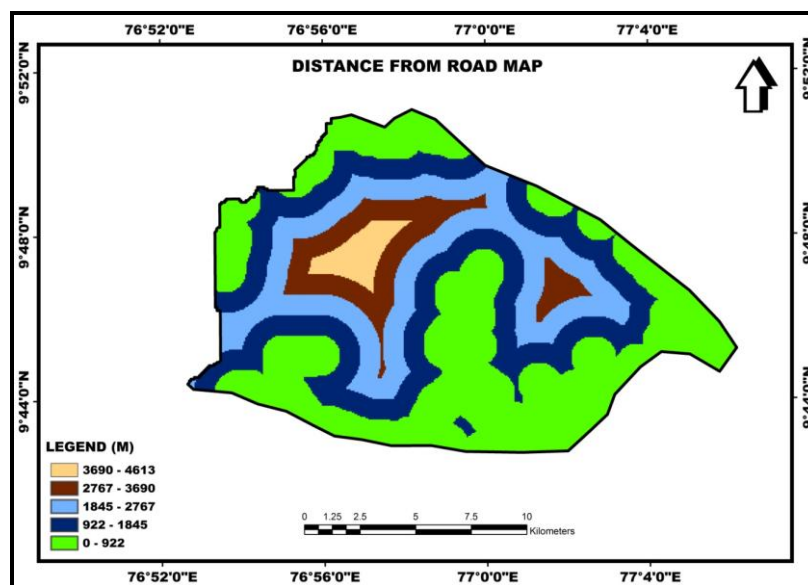


Figure 6: Distance from Road Map

3.5. Elevation

Another important factor which influences fire spreading is represented by the topographical factor of elevation. The elevation of the area influences fuel moisture and air humidity (Singh and Ajay, 2013). The humidity and temperature have higher influence on fire at higher altitude areas than lower ones (Thompson et al., 2000). Even though, the higher elevation areas of this sanctuary are more prone to forest fires. The regions with a higher elevation are more exposed to the prevailing winds, than the lower ones. During day time, the warm air rises and it will cause uphill draughts. In areas of higher elevation, the number of lightning strikes is usually more and hence a higher risk of lightning induced forest fire. These areas are found in the south, central, and northeastern parts of the sanctuary. The elevation of the study area, Idukki Wildlife Sanctuary is grouped into five different classes viz. 580 – 715 m, 715 – 850 m, 850 – 985 m, 985 – 1120 m, and 1120 – 1255 m. The elevation map is shown in Figure 7.

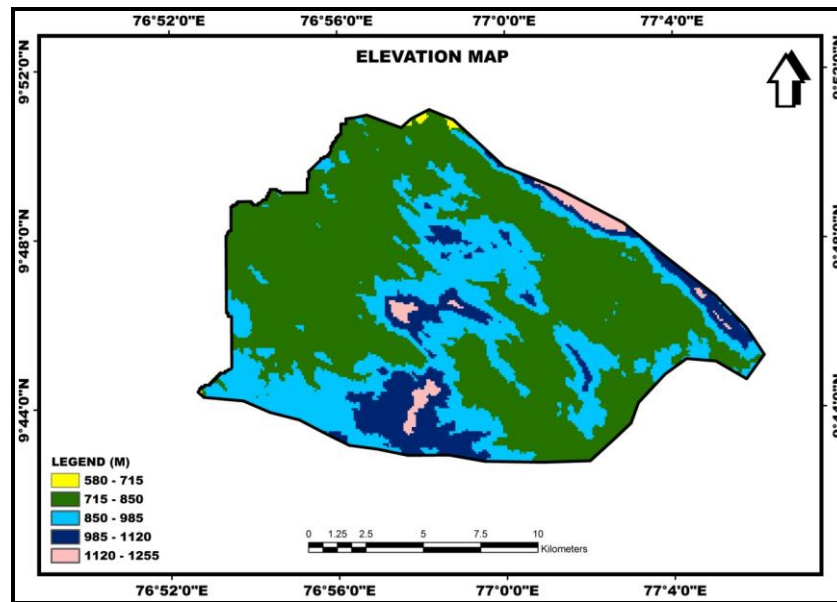


Figure 7: Elevation Map

3.6. Fire Risk Zones

The final forest fire risk zone map of the study area is generated by taking into account five influencing factors such as land cover type, slope, distance from settlement, distance from road, and elevation. During the process, there were assigned different weights to all these factors, according to their sensitivity to fire or their fire-inducing capability. The forest fire risk zone map is prepared by overlaying the index map layers using GIS tools. The study area is divided into five risk zones ranging from 'very low' to 'very high'. The risk zone map is validated with the fire incidence points for the last 10 years (2004 – 2014) collected from the FSI and during the field survey. In this study area of the Idukki Wildlife Sanctuary, a total of 35 forest fires have been recorded. Results show that out of the 35 fires, 29 (82.85%) forest fires occurred in the high and very high risk zones, 4 (11.42%) occurred in the moderate risk zone, and 2 (5.71%) occurred in the low and very low risk zones. The forest fire risk zone map is shown in Figure 8. Most of the forest fires occurred near the roads and settlements, which points out an anthropogenic origin (intentionally or unintentionally caused by humans). The result of this study is compared with the work done by Ajin et al. (2014b). They demarcated forest fire risk zones of Idukki Wildlife Sanctuary using Natural Breaks (Jenks) reclassification method. The result of that study reveals that 80% of the past forest fires occurred in the high and very high risk zones. Thus it is clear that the Equal Interval method will give more accurate result for the present methodology in this study area.

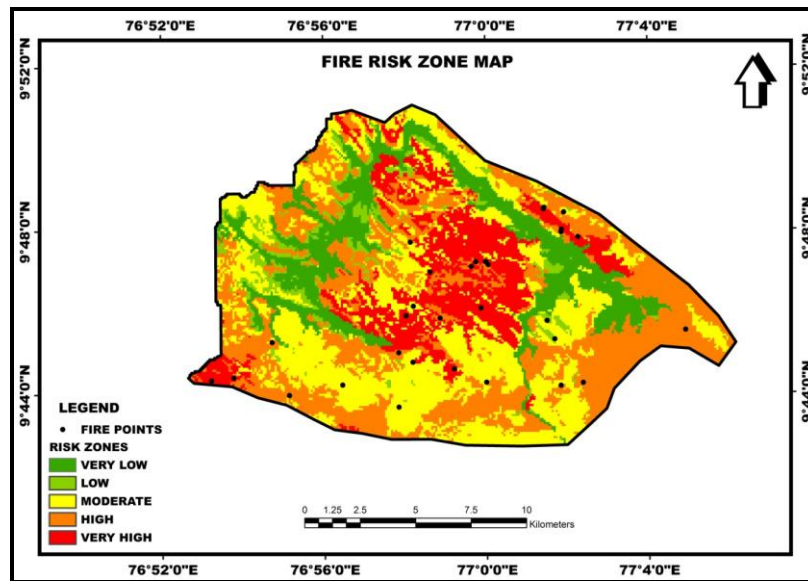


Figure 8: Fire Risk Zone Map

4. Conclusion

A method integrating RS and GIS techniques is used in this study. RS and GIS are effective techniques and which offer a great help in the monitoring and mapping of forest fire risk zones. A GIS is an optimal technique in forest fire research, because of the relation between fire occurrence and the spatial characteristics of the influencing factors. These factors have different influences and therefore, in the modelling process for the forest fire risk zonation of the study area, they were assigned different weights, according to their influence and capacity in inducing and spreading fire. The area of the sanctuary is grouped into five different risk zones, ranging from “very low” to “very high”. Results show that most of the fire incidence points fall spatially in the vicinity of roads and settlements. This fact points out that the forest fires have an anthropogenic origin, which means that they are induced by humans intentionally or unintentionally. The carelessly throwing lighted cigarette butts, fires set by the villagers for scaring away wild animals, unextinguished campfires set by the tourists, sparks of fire due to cooking food near the roads, and fire released during the heating of coal tar for road surfacing are some of the possible reasons for the occurrence of unintentional forest fires in this study area. On the other hand, the use of fire by the timber smugglers to hide the stumps of illicit felling, small fires set by the villagers to clear off forest path covered by tree branches and leaves, and the fires set for the collection of NTFP, etc are the causes of intentional forest fires in the sanctuary. This study confirms that 82.85% of the fire incidence points fall spatially over the high and very high risk zones. The present methodology gives good results, being suitable for forest fire risk zone mapping. The methodology presented in this paper is an excellent tool for the analysis, management, study and assessment of forest fires, in order to reduce their frequency and to avoid damage. With the help of fire risk zone maps, the forest fire managers can easily identify the risk zones and can take proper actions to minimize the impacts of fires for a better forest fire management.

References

- Ajin, R.S., Ciobotaru, A., Vinod, P.G., and Jacob, M.K. *Forest and Wildland Fire Risk Assessment Using Geospatial Techniques: A Case Study of Nemmara Forest Division, Kerala, India*. Journal of Wetlands Biodiversity. 2015. 5; 29-37.
- Ajin, R.S., Jacob, M.K., Menon, A.R.R., and Vinod, P.G., 2014a: *Forest Fire Risk Analysis using Geo-Information Technology: A Study of Peppara Wildlife Sanctuary, Thiruvananthapuram, Kerala, India*. Proceedings, 2nd Disaster Risk and Vulnerability Conference, Thiruvananthapuram, India, 160-165.
- Ajin, R.S., Vinod, P.G., and Menon, A.R.R., 2014b: *Forest Fire Risk Analysis using GIS and RS Techniques: An Approach in Idukki Wildlife Sanctuary, Kerala, India*. Proceedings, 24th Swadeshi Science Congress, Tirur, India. 406-413.
- Assaker, A., Darwish, T., Faour, G., and Noun, M. *Use of Remote Sensing and GIS to assess the Anthropogenic Impact on Forest fires in Nahr Ibrahim Watershed, Lebanon*. Lebanese Science Journal. 2012. 13 (1) 15-28.
- Chavan, M.E., Das, K.K., and Suryawanshi, R.S. *Forest Fire Risk Zonation using Remote Sensing and GIS in Huynial watershed, Tehri Garhwal District, UA*. International Journal of Basic and Applied Research. 2012. 2; 6-12.
- Chuvieco, E., and Salas, J. *Mapping the Spatial Distribution of Forest Fire Danger Using GIS*. International Journal of Geographical Information Systems. 1996. 10 (3) 333-345.
- Chuvieco, E., Salas, J., Carvacho, L., and Rodríguez-Silva, F., 1999: *Integrated Fire Risk Mapping. Remote Sensing of Large Wildland Fires in the European Mediterranean Basin*. Springer. 61-100.
- Dawson, T.P., Butt, N., and Miller, F. *The Ecology of Forest Fires*. ASEAN Biodiversity. 2001. 1 (3) 18-21.
- Dong, X., Li-min, D., Guo-fan, S., Lei, T., and Hui, W. *Forest Fire Risk Zone Mapping from Satellite Images and GIS for Baihe Forestry Bureau, Jilin, China*. Journal of Forestry Research. 2005. 16 (3) 169-174.
- Eskandari, S., Ghadikolaei, J.O., Jalilvand, H., and Saradjian, M.R. *Detection of Fire High-Risk Areas in Northern Forests of Iran Using Dong Model*. World Applied Sciences Journal. 2013. 27 (6) 770-773.
- Gangapriya, P., and Indulekha, K.P. *Development of GIS Based Disaster Risk Information System for Decision Making*. International Journal of Innovative Research in Science, Engineering and Technology. 2013. 2 (sp. issue 1) 140-148.
- Ghobadi, G.J., Gholizadeh, B., and Dashliburun, O.M. *Forest Fire Risk Zone Mapping From Geographic Information System in Northern Forests of Iran (Case study, Golestan province)*. International Journal of Agriculture and Crop Sciences. 2012. 4 (12) 818-824.
- Lazaridis, M., Latos, M., Aleksandropoulou, V., Hov, Ø., Papayannis, A., and Tørseth, K. *Contribution of Forest Fire Emissions to Atmospheric Pollution in Greece*. Air Quality, Atmosphere and Health. 2008. 1; 143-158.

- Mahdavi, A., Shamsi, S.R.F., and Nazari, R. *Forests and Rangelands' Wildfire Risk Zoning Using GIS and AHP Techniques*. Caspian Journal of Environmental Sciences. 2012. 10 (1) 43-52.
- Podur, J.J., and Martell, D.L. *The Influence of Weather and Fuel Type on the Fuel Composition of the Area Burned by Forest Fires in Ontario, 1996–2006*. Ecological Applications. 2009. 19; 1246-1252.
- Rajabi, M., Alesheikh, A., Chehregan, A., and Gazmeh, H. *An Innovative Method for Forest Fire Risk Zoning Map Using Fuzzy Inference System and GIS*. International Journal of Scientific & Technology Research. 2013. 2 (12) 57-64.
- Rothermel, P., and Richard, C., 1972: A Mathematical Model for Predicting Fire Spread in Wild Land Fires. USDA Forest Service Research Paper INT – 115. Ogden, Utah, USA.
- Roy, P.S., 2003: *Forest Fire and Degradation Assessment using Satellite Remote Sensing and Geographic Information System*. Satellite Remote Sensing and GIS Applications in Agricultural Meteorology. World Meteorological Organization, Switzerland. 361-400.
- Singh, D. *Historical Fire Frequency based Forest Fire Risk Zonation Relating Role of Topographical and Forest Biophysical Factors with Geospatial Technology in Raipur and Chilla Range*. SSARSC International Journal of Geo Science and Geo Informatics. 2014. 1 (1) 1-9.
- Singh, R.P., and Ajay, K. *Fire Risk Assessment in Chitrakoot Area, Satna MP, India*. Research Journal of Agriculture and Forestry Sciences. 2013. 1 (5) 1-4.
- Somashekar, R.K., Ravikumar, P., Mohan Kumar, C.N., Prakash, K.L., and Nagaraja, B.C. *Burnt Area Mapping of Bandipur National Park, India using IRS 1C/1D LISS III data*. Journal of the Indian Society of Remote Sensing. 2009. 37 (1) 37-50.
- Sowmya, S.V., and Somashekar, R.K. *Application of Remote Sensing and Geographical Information System in Mapping Forest Fire Risk Zone at Bhadra Wildlife Sanctuary, India*. Journal of Environmental Biology. 2010. 31 (6) 969-974.
- Tatli, H., and Türkeş, M. *Climatological Evaluation of Haines Forest Fire Weather Index over the Mediterranean Basin*. Meteorological Applications. 2014. 21 (3) 545-552.
- Thakur, A.K., and Singh, D. *Forest Fire Risk Zonation Using Geospatial Techniques and Analytic Hierarchy Process in Dehradun District, Uttarakhand, India*. Universal Journal of Environmental Research and Technology. 2014. 4 (2) 82-89.
- Thompson, W.A., Vertinsky, I., and Schreier, H. *Using Forest Fire Hazard Modelling in Multiple use Forest Management Planning*. Forest Ecology and Management. 2000. 134; 163-176.
- Veeraanarayanaa, B., and Ravikumar, S.K. *Assessing Fire Risk in Forest Ranges of Guntur District, Andhra Pradesh: Using Integrated Remote Sensing and GIS*. International Journal of Science and Research. 2014. 3 (6) 1328-1332.
- Zhong, M., Fan, W., and Liu, T. *Statistical analysis on current status of China forest fire safety*. Fire Safety Journal. 2003. 38; 257-269.

Evaluation of Clearness and Diffuse Index at a Semi-Arid Station (Anantapur) using Estimated Global and Diffuse Solar Radiation

Rama Gopal K.¹, Pavan Kumari S.¹, Balakrishnaiah G.¹, Raja Obul Reddy K.¹, Md. Arafath S.¹, Siva Kumar Reddy N.¹, Chakradhar Rao T.¹, Lokeswara Reddy T.¹, and Reddy R.R.^{1,2}

¹Aerosol & Atmospheric Research Laboratory, Department of Physics, Sri Krishnadevaraya University, Anantapur, Andhra Pradesh, India

²Srinivasa Ramanujan Institute of Technology, B.K. Samudram Mandal, Anantapur, Andhra Pradesh, India

Publication Date: 12 April 2016

Article Link: <http://scientific.cloud-journals.com/index.php/IJAESE/article/view/Sci-388>



Copyright © 2016 Rama Gopal K., Pavan Kumari S., Balakrishnaiah G., Raja Obul Reddy K., Md. Arafath S., Siva Kumar Reddy N., Chakradhar Rao T., Lokeswara Reddy T., and Reddy R.R. This is an open access article distributed under the **Creative Commons Attribution License**, which permits unrestricted use, distribution, and reproduction in any medium, provided the original work is properly cited.

Abstract In the present study, collocated and simultaneous measurements on meteorological parameters and solar radiation on horizontal surface were obtained from different meteorological sensors and pyranometer sensor over a semi-arid station, Anantapur (14.62° N, 77.65° E and 331 m asl) during January–December 2013. The temperature is usually lower at midnight, decreasing in the early hours of the morning around 08:00 LT (Local Time) (24.71 ± 2.7 °C), and then increasing rapidly until just after midday at 15:00 LT (31.88 ± 3.2 °C). It decreases to 26.70 ± 2.9 °C during the night around 23:00 LT. The relative humidity ranges from 30–76%, 20–65%, 46–80% and 48–90% during winter, summer, monsoon, and post-monsoon seasons respectively. The diurnal variation of soil moisture exhibits slight variations at different depths over the region. The diurnal and monthly variations of solar radiation as well as clearness index (k_t), diffusion index (k_d) were studied in the present study. In diurnal variation, it shows a steady rise in solar radiation received at the surface after 7:30 LT and attains a maximum solar radiation between 12:00 – 13:00 LT. The amount of solar radiation also varies depending on the time of day and the season. The annual mean of daily global, extraterrestrial and diffuse radiation at Anantapur is found to be 202.43 ± 40.45 , 408.15 ± 61.63 and 49.33 ± 11.26 W/m². The high global and diffuse solar radiations were observed during March-May (257.67 ± 34.18 W/m², 65.07 ± 11.20 W/m²) whereas low global and diffuse solar radiations during monsoon months (137.66 ± 12.41 , 33.47 ± 7.44 W/m²). In the case of extraterrestrial solar radiation was high in the month of December (472.92 ± 0.67 W/m²) and low in the month of June (312.87 ± 2.58 W/m²).

Keywords *Global Solar Radiation; Diffuse Solar Radiation; Extra Terrestrial Solar Radiation; Clearness Index; Diffuse Index*

1. Introduction

The air temperature variation brings about a change in water evaporation and air saturation and leading to the change in air humidity. Furthermore, the air temperature differences between different

locations will also cause air pressure differences, which in turn would produce air movement, thereby wind. This variation in humidity and wind speed leads to direction affect on rainfall. Thus, all weather variations on the Earth are more or less affected by each other. Two components of global solar radiation come to the earth surface are from the sun i.e. one is direct solar radiation and the other originates from dispersing of direct solar radiation in the atmosphere i.e. diffuse solar radiation. The radiation that reflects from surroundings (so-called albedo) is of importance for some angle to the horizontal surface. This radiation is mainly diffuse and comes to the receiving surface under different angles. Solar radiation is received at the earth's surface under different atmospheric conditions, which clearly affect the amount and quality of radiation obtained at the ground. Turbidity, transparency, air mass, atmospheric water vapor contents layers and distribution of cloud cover have been suggested as the atmospheric conditions that exert influence solar radiation at the earth's surface through the process of absorption, scattering and reflection of the incoming solar radiation. Clearness index (k_t) is expressed as the ratio of the monthly mean daily global solar radiation on the horizontal surface to the monthly mean daily extraterrestrial horizontal radiation. Clearness index indicates the availability of global solar radiation at a particular location. The diffuse fraction of solar radiation (the ratio of the diffuse solar radiation to the global solar radiation) is particularly required in assessing the climatologically potential of a locality for solar energy utilization and in estimating the expected values of the output of concentrating solar collectors [1].

In this paper, the diurnal and monthly average total of extraterrestrial radiation, global solar radiation, diffuse solar radiation, clearness index (k_t) and diffuse index (k_d) in Anantapur are analyzed. In addition, a frequency distribution of clearness index and diffuse index of global solar radiation are also presented and discussed.

2. Instrumentation and Site Description

Mini Boundary Layer Mast (MBLM) has been established across the country with broad objective to characterize and analyse the region wise specific surface layer structures in terms of surface roughness, the bulk coefficients for surface fluxes, similarity coefficients and the scaling laws for surface transports, etc., for varying stability conditions. The Mini Boundary Layer Mast is a 15 m high, guyed, uniform triangular lattice structure designed to withstand wind speed of 60 m/s. The system uses advanced high resolution sensors to measure the ambient temperature, relative humidity and wind vector. The booms on MBLM are fitted at 4 m, 8 m and 15 m heights above the ground. The system uses advanced high resolution sensors to measure ambient temperature, relative humidity and wind vector at three different levels at 4.0 m, 8.0 m and 15 m. In addition to this it will measure rainfall, net incoming solar radiation in long wave and short wave range, atmospheric pressure, soil temperature at seven levels and soil moisture at six levels. All the data are collected at one second resolution and averaged for every four minutes. The data are stored in a local data logger as well and can be downloaded using a USB drive. The system shall be useful to study the boundary layer process at fine scale. The details of experiment facility and the instrumentation were discussed by [2].

2.1. Description of Study Area

Anantapur district in Rayalaseema region of Andhra Pradesh is geographically situated in a semi-arid zone and occupied the second place to Rajasthan. Anantapur is a very dry semi-arid and rain shadow region. The region gets very little rain that from during South-West monsoon and North-East monsoon periods. The observation site (14.62°N, 77.65°E and 331 masl), Sri Krishnadevaraya University (SKU) is situated at about 12 km away from the southern edge of the Anantapur town (Figure 1). This region receives very little rainfall and the average annual rainfall was around to the 313.5mm. Within a 50 km radius, this region is surrounded by a number of cement plants, lime kilns, slab polishing and brick making units.

The study area is also at a relatively short distance from the national highways (NH 7 and NH 205) and the diesel vehicles and biomass burning to cause the air pollution. Based on different meteorological conditions prevailing over the observation site, the months of the year are classified into four seasons namely winter (December-February), summer (March-May), monsoon (June-August) and post-monsoon (September-November). The climate here is primarily hot and dry in the summer, hot and humid during the monsoon and post monsoon and dry in winter season.

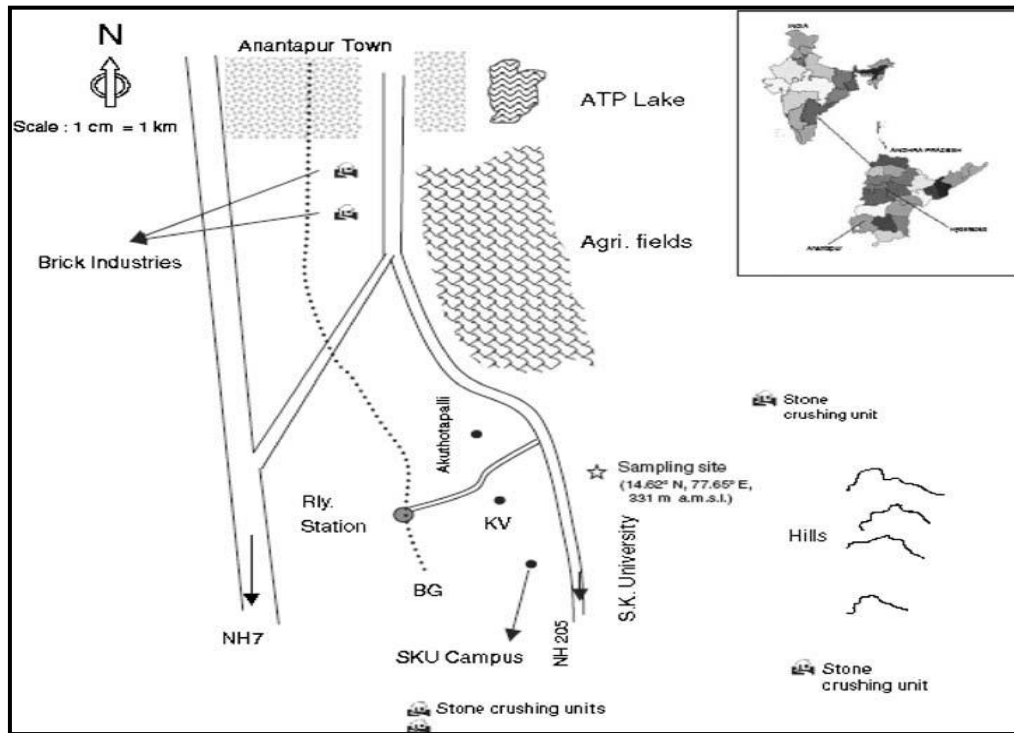


Figure 1: Location map of the Anantapur city in India

2.2. Extraterrestrial Radiation for Hourly or Shorter Periods (H_o)

For hourly or shorter periods the solar time angle at the beginning and end of the period should be considered when calculating H_o :

$$H_o = \frac{12(60)}{\pi} G_{sc} d_r [(\omega_2 - \omega_1) \sin(\varphi) \sin(\delta) + \cos(\varphi) \cos(\delta) (\sin(\omega_2) - \sin(\omega_1))] \quad (1)$$

Where

H_o extraterrestrial radiation in the hour (or shorter) period [$MJm^{-2}hour^{-1}$], G_{sc} solar constant = $0.0820 MJm^{-2}min^{-1}$, d_r inverse relative distance Earth-Sun, φ latitude (rad) δ solar declination (rad), ω_1 solar time angle at beginning of period (rad), ω_2 solar time angle at end of period (rad),

The solar time angles at the beginning and end of the period are given by:

$$\omega_1 = \omega - \frac{\pi t_1}{24} \quad (2)$$

$$\omega_2 = \omega + \frac{\pi t_1}{24} \quad (3)$$

Where

ω solar time angle at midpoint of hourly or shorter period (rad), t_1 length of the calculation period (hour): i.e., 1 for hourly period or 0.5 for a 30 minute period.

The solar time angle at midpoint of the period is:

$$\omega = \frac{\pi}{12} [(t + 0.06667(L_z - L_m) + S_c) - 12] \quad (4)$$

Where

't' standard clock time at the midpoint of the period (hour). For example for a period between 14:00 and 15:00 hours, $t = 14.5$, L_z longitude of the centre of the local time zone (degrees west of Greenwich).

For example, $L_z = 75, 90, 105$ and 120° for the Eastern, Central, Rocky Mountain and Pacific time zones (United States) and $L_z = 0^\circ$ for Greenwich, 330° for Cairo (Egypt) and 255° for Bangkok (Thailand), $L_z = 82.5^\circ$ for India. L_m longitude of the measurement site (degree west of Greenwich), S_c seasonal correction for solar time (hour).

The seasonal correction for solar time is:

$$S_c = 0.1645\sin(2b) - 0.1255\cos(b) - 0.025\sin(b) \quad (5)$$

$$b = \frac{2\pi(J - 81)}{364} \quad (6)$$

Where J is the number of the day in the year.

2.3. Diffuse Solar Radiation for Daily Periods

The total solar radiation consists of direct or beam radiation coming directly from the solar disc and the diffuse component scattered to the ground from the sky dome. The latter depends on the clarity of the sky and could be estimated from the correlation of (Collares-Pereira and Rabl, 1979) which gives the daily average diffuse radiation, H_{d1} as:

$$H_{d1} = H\{0.775 + 0.0060(\omega_s - 90) - [0.505 + 0.00455(\omega_s - 90)]\cos(115k_t - 103)\} \quad (7)$$

Where k_t is the clearness index for the day, defined as the ratio of the daily radiation (H) on a horizontal surface to the daily extraterrestrial radiation (H_o) on that surface, that is:

$$k_t = \frac{H}{H_o} \quad (8)$$

Its measure of the availability of the solar radiation or the transmissivity of the atmosphere.

The hourly values of the diffuse solar radiation can be estimated from the equation by (Liu and Jordan, 1960) which gives:

$$I_d = H_d \frac{24}{\pi} \frac{\cos(\omega) - \cos(\omega_s)}{\sin(\omega_s) - \frac{\pi\omega_s}{180} \cos(\omega_s)} \quad (9)$$

2.4. The Diffuse Index (k_d)

K_d is the diffuse index for the day, defined as the ratio of the daily diffuse radiation (H_d) on a horizontal surface to the daily global solar radiation (H) on that surface, that is:

$$k_d = \frac{H_d}{H} \quad (10)$$

This is the transmission characteristics of diffuse solar radiation and hence mirrors the effectiveness of the sky in transmitting diffuse solar radiation.

3. Results and Discussion

3.1. Diurnal Variation of Meteorological Parameters

Based on different meteorological conditions prevailing over the observation site, the months of the year are classified into four seasons namely winter (December-February), summer (March-May), monsoon (June-August) and post-monsoon (September-November). The diurnal and monthly variations of average temperature, relative humidity, and atmospheric pressure are shown in Figure 2 (a) - (d) and statistical data are presented in Table 1. Figure 2 (a) illustrates that the temperature is usually lower at midnight, decreasing in the early hours of the morning around 08:00 LT (Local Time) (24.71 ± 2.7 °C), and then increasing rapidly until just after midday at 15:00 LT (31.88 ± 3.2 °C). It decreases to 26.70 ± 2.9 °C during the night around 23:00 LT. The noontime values are mostly due to the high intensity of solar radiation reaching the earth's surface. Figure 2 (a) reveals that the relative humidity is usually high at midnight and in the early morning 7:00 LT (75%), drops rapidly, after the sun rises until it is lowest just after midday around 15:00 LT (40%). It increases again at midnight, rapidly in the late afternoon and early evening and levels off around midnight.

Monthly variation of temperature and relative humidity are shown in Figure 2 (c). From Figure 2 (c) it is found that the temperature increases with the decreasing of relative humidity and vice versa. The minimum temperature of 25.28 ± 3.7 °C was observed during the January 2013 and a maximum of 32.68 ± 3.6 °C during May 2013. The temperature recorded in the study area ranged between 31.95 °C – 19.37 °C, 38.24 °C – 24.21 °C, 32.25 °C – 23.82 °C and 30.09 °C – 21.19 °C during the winter, summer, monsoon, and post-monsoon respectively. The relative humidity ranges observed during winter, summer, monsoon, and post-monsoon are 30 – 76%, 20 – 65%, 46 – 80% and 48 – 90% respectively. The minimum relative humidity observed in summer was 23% and a maximum of 88% during post-monsoon seasons.

Atmospheric pressure is the total weight of the air above the unit area at the point where the pressure was measured. The semi diurnal variation of atmospheric pressure was shown in Figure 2 (b) and which indicates a significant semi diurnal variation with a morning peak around 07:00 – 09:00 LT with a pressure value of 968 hPa and a minimum of 963 hPa at 16:00 LT. As the air warms up the molecules in the air become more active and they rise up with more individual space, even though there is the same number of molecules. It leads to increase in the air pressure. When the temperature cools, the molecules slow down and they do not move and bump into each other, it causes a decrease in air pressure. The Figure 2 (d) illustrates the monthly variation of pressure and the

maximum pressure was observed during the winter months (970 hPa) due to stronger confinement by the nocturnal boundary layer, which would be very shallow in the winter months due to low night temperature and minimum pressure (962 hPa) was recorded in the monsoon months due to the high winds, which are originating from the Arabian Ocean. The variations of wind speed (WS) and wind direction (WD) for the study period are shown in Figure 3 (a). Apart from the wind speed, wind direction also plays a vital role in determining the type of aerosols present over the location as they help in bringing and identifying aerosols from different neighboring regions to the measurement site. The maximum wind speed has been found to be 4 ± 0.9 m/s in the monsoon months and minimum values are found to be 1.79 ± 0.6 m/s during the post-monsoon months. From Figure 3 (a) wind directions are variable for different months of a year, i.e., winds are confined to $240^\circ - 270^\circ$ (South-easterly) during the monsoon months, $90^\circ - 135^\circ$ (Northeasterly or South-easterly) during the winter seasons, $90^\circ - 270^\circ$ during the summer and the post-monsoon months over the study area. Surface wind vectors slowly change their direction towards southwesterly during summer and post-monsoon seasons.

Therefore, during these seasons, aerosols over the observation site will have a possible influence on the marine air masses coming from the Arabian Sea [3], [4], [5]. The average monthly variation of rainfall (RF) during the study period was shown in Figure 3 (b). The maximum average rainfall was observed in the month of September (171.4 mm) and minimum during the summer months (7.3 mm). The seasonal rainfall was recorded to be 206.8, 89.1, 8.2 and 7.3 mm in the post monsoon, monsoon, winter and summer seasons, respectively. This region receives very little rainfall and the average annual rainfall was around to the 313.5 mm.

Table 1: The Monthly Average Values of the Meteorological Parameters (mean \pm SD) for the Study Period at Anantapur

Month	Wind Speed (m/s)	Wind Direction (degree)	Temperature ($^\circ$ C)	Relative humidity (%)	Pressure (hPa)	Rainfall (mm)
Jan	2.06 \pm 1.03	125.92 \pm 37.30	25.283 \pm 3.71	51 \pm 16	970 \pm 1.47	0
Feb	2.63 \pm 1.08	124.70 \pm 21.00	26.91 \pm 3.43	49 \pm 14	969 \pm 1.56	8.2
Mar	2.53 \pm 1.17	132.32 \pm 29.96	29.84 \pm 3.66	36 \pm 11	968 \pm 1.57	0
Apr	2.05 \pm 0.49	205.86 \pm 30.34	32.74 \pm 3.82	36 \pm 13	964 \pm 1.72	2.5
May	2.84 \pm 0.38	242.24 \pm 20.32	32.68 \pm 3.64	45 \pm 13	961 \pm 1.25	4.8
Jun	3.25 \pm 0.88	256.33 \pm 8.26	28.26 \pm 2.53	62 \pm 10	962 \pm 1.12	9.9
Jul	3.28 \pm 0.99	254.64 \pm 6.71	27.00 \pm 2.15	67 \pm 08	963 \pm 1.31	29.4
Aug	2.96 \pm 0.87	262.18 \pm 10.98	26.92 \pm 2.30	67 \pm 09	964 \pm 1.39	49.8
Sep	1.77 \pm 0.58	243.40 \pm 10.30	26.38 \pm 2.32	76 \pm 10	965 \pm 1.35	171.4
Oct	1.71 \pm 0.68	226.53 \pm 24.34	26.46 \pm 2.01	73 \pm 09	969 \pm 1.56	32.6
Nov	1.89 \pm 0.87	119.72 \pm 25.63	25.15 \pm 2.66	67 \pm 13	968 \pm 1.32	2.8
Dec	2.17 \pm 0.97	125.24 \pm 32.14	23.54 \pm 3.14	57 \pm 13	969 \pm 1.40	2.1

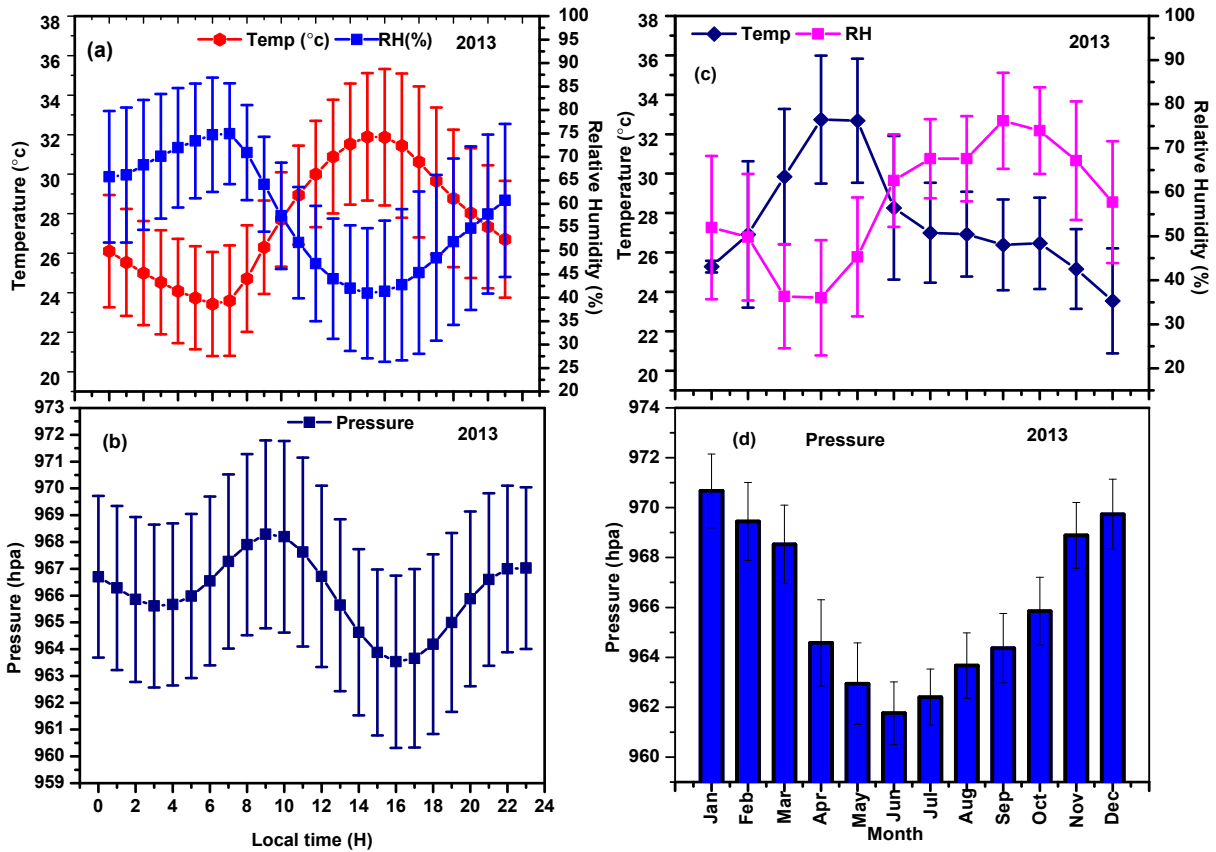


Figure 2: Diurnal variation of (a) temperature and relative humidity (RH) (b) pressure and monthly variation of (c) temperature and relative humidity (d) pressure for the period of January – December 2013

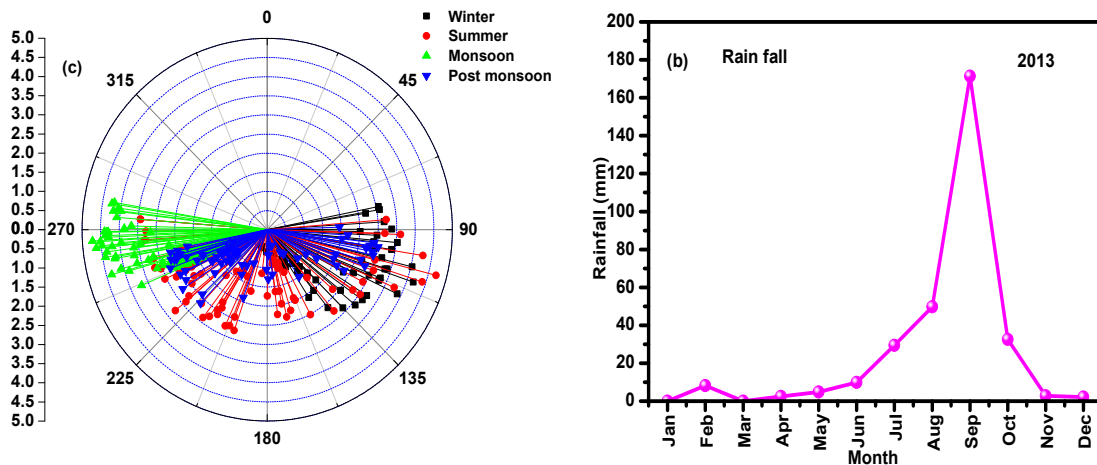


Figure 3: Diurnal and monthly variations of (a) wind speed (WS), wind direction (WD) and (b) rain fall for the entire study period

3.2. The Diurnal Variation of Soil Temperature and Soil Moisture for Different Depths

Soil temperature is widely used for the estimation of the soil conditions whether it is hot or cold and also it controls many chemical and biological processes within the soil. The diurnal variation of soil temperature at different depths (0cm, 5cm, 10cm, 40cm and 100cm) are shown in Figure 4 (a).

In the diurnal variation of soil temperature, the maximum value was observed during 15:00 LT due to the high temperature. After the noon time onwards the soil temperature decreased and reaches a minimum value at morning hours 06:00 LT and is due to the reduction of sun radiation and increase relative humidity and low atmospheric temperature. The similar diurnal variation of soil temperature at different depths was reported by [6]. Some interesting features will happen in the soil which involves the temperature flow of heat and how soils make heat up. In other words, the amount of heat the soil absorbs and makes to increase the soil temperature. In the first case, heat in the soil flows from places of high temperature to a low temperature so heat can move into the deeper layers of the soil profile.

Soil moisture is a key variable in controlling the exchange of water and heat energy between the land surface and the atmosphere through evaporation and plant transpiration [7]. The Figure 4 (b) shows the diurnal variation of soil moisture for different depths. The spatial structure of soil moisture and its evolution in time is both cause and consequence of vegetation [8]. The diurnal variation reaches its minimum around 8:00 LT and maximum around 16:00 LT. It is observed that soil water content varied greatly in the rainy season and less in the dry season. It is natural to suspect that this pattern might be greatly related to precipitation and evaporation. The diurnal variations at 40 and 100 cm depths do not have obvious changes in 3 contrasts to shallow layer. A similar variation in soil moisture is also reported by [9], [10].

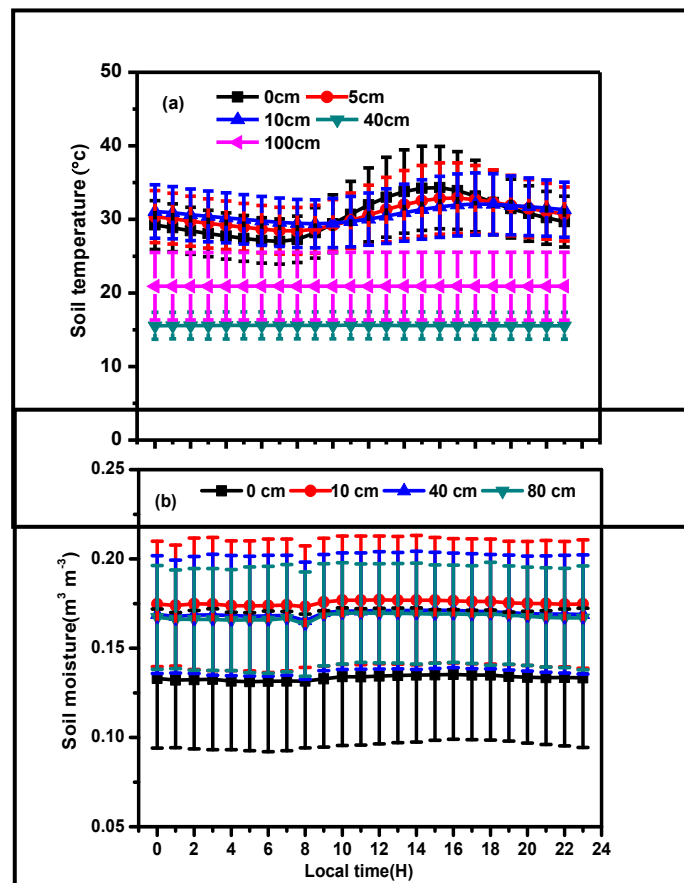


Figure 4: Diurnal Variation of (a) Soil Temperature and (b) Soil Moisture for Different

3.2.1. Diurnal and Monthly Variation of Short Wave and Long Wave Solar Radiation

The Figures 5 (a) (b) shows the diurnal and monthly variation of short wave and long wave solar radiation at Anantapur over a study period. Shortwave radiation (visible light) contains a lot of energy

and long wave radiation (infrared light) contains less energy than shortwave radiation. Solar energy enters into the atmosphere as shortwave radiation in the form of ultraviolet (UV) rays (the ones that give us sunburn) and visible light. The earth is much cooler, but still emits radiation. The radiation emitted from the earth as long wave radiation because it contains a smaller amount of energy. From the Figures 5 (a), (b) the incoming short wave solar radiation values observed were positive and outgoing long wave solar radiation values were negative. The incoming solar radiation varies from 0 W/m² (minimum) to about 723.56 W/m² (maximum). It showed maximum (723.56 W/m²) value at noon (12:00 LT) and minimum (16.52 W/m²) in the morning (06:00 – 07:00 LT) and evening (18:00 – 20:00 LT) (187.39 W/m²). Similarly, the outgoing long wave solar radiation showed the negative magnitude (-91 W/m²) at noon, indicating the high emissivity compared to morning and evening hours. The highest values of solar radiation at short and long wavelengths were recorded to be 312.87 ± 79.66 W/m² and -91.31 ± 20.9 W/m² in the month of March whereas lowest values were found to be 180.29 ± 44.3 W/m² and -34.14 ± 5.08 W/m² in the month of July respectively. In the winter time, sunshine duration was shorter than summer, but the radiation was higher than summer and in the case of rain season which was lower becomes the radiation is due to the rainy cloud.

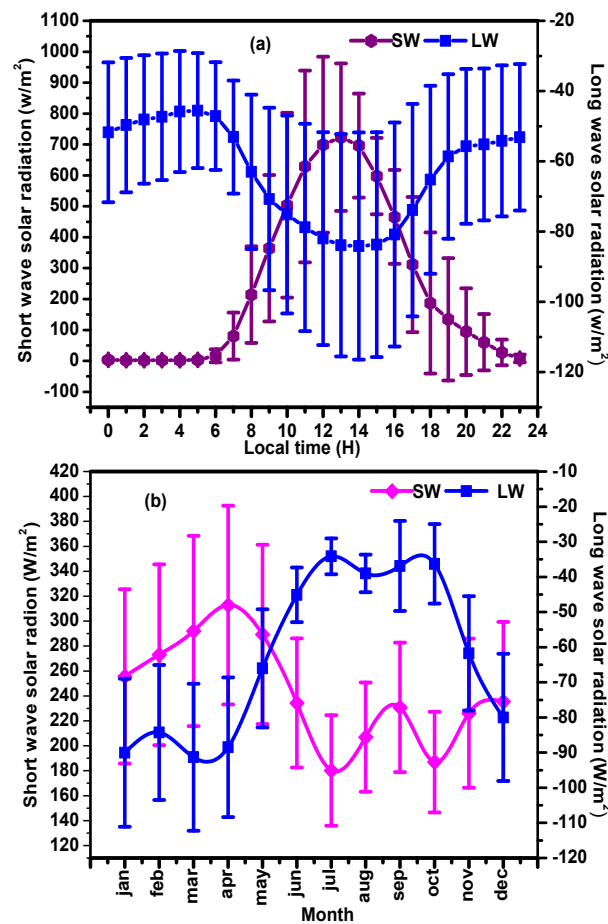


Figure 5: Diurnal Variation of (a) Short Wave and Long Wave Solar Radiation and (b) Monthly Variation Short Wave and Long Wave Solar Radiation

3.3. Diurnal Variation of Extraterrestrial (H_o), Global (H) and Diffuse Solar Radiation (H_d)

The Figures 6 (a), (b), (c) shows the diurnal variation of extraterrestrial (H_o), global (H) and diffuse solar radiation (H_d) at Anantapur during January – December 2013. In the diurnal variation, it shows a steady rise in solar radiation received at the surface after 7:30 LT and attains a maximum solar radiation between 12:00 – 13:00 LT. The amount of solar radiation also varies depending on the time

of day and the season. In general, more solar radiation is present during midday than during either the early morning or late afternoon. At mid-day, the sun is positioned high in the sky and the path of the sun's rays through the earth's atmosphere is shortened. Consequently, less solar radiation is scattered or absorbed, and more solar radiation reaches the earth's surface. [11], [12], [13] observed that the lower values (sunrise and sunset) of solar radiations are due to higher zenith angles, higher atmospheric optics mass and higher distance between the sun to earth, which make the occurrence of greater attenuation of direct radiation by the processes of scattering, absorption, and reflection.

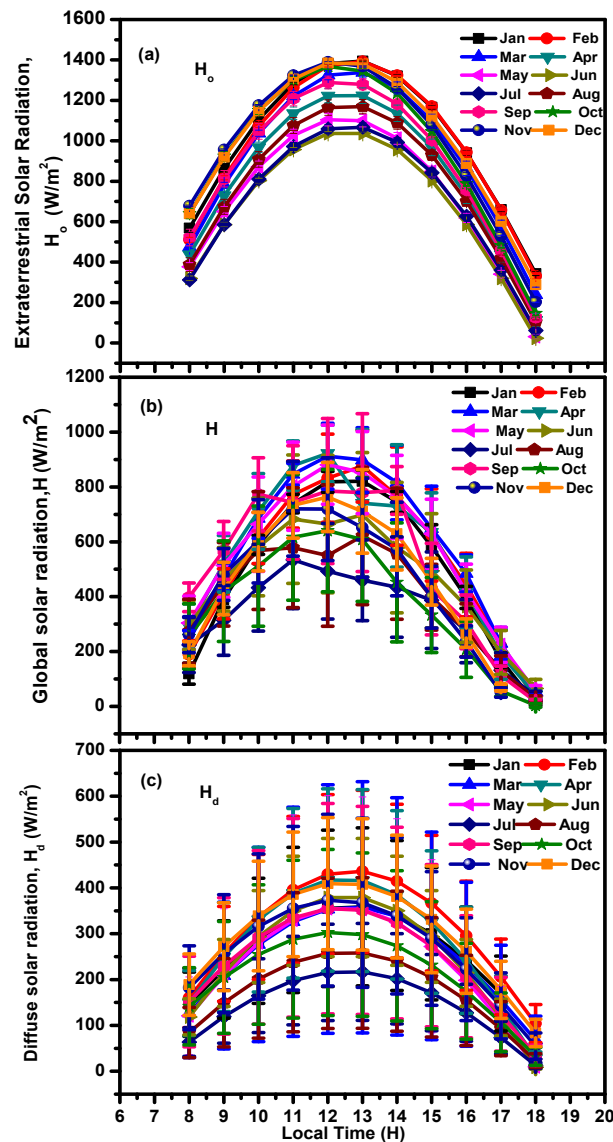


Figure 6: Diurnal variation of (a) extraterrestrial (b) global and (c) diffuse solar radiation for the entire study period for different months

In a monthly variation, the solar radiation varies from month to month due to the rotation of the earth as well as local weather conditions. The Figures 7 (a), (b), (c) shows the monthly average of the extraterrestrial solar radiation (H_o), daily global solar radiation (H) and diffuse solar radiation (H_d) on a horizontal surface. The annual mean of daily global, extraterrestrial and diffuse radiation at Anantapur is found to be 202.43 ± 40.45 , 408.15 ± 61.63 and 49.33 ± 11.26 W/m^2 .

The high global and diffuse solar radiations were observed during March-May (257.67 ± 34.18 W/m^2 , 65.07 ± 11.20 W/m^2) whereas low global and diffuse solar radiations are noticed during monsoon

months (137.66 ± 12.41 , $33.47 \pm 7.44 \text{ W/m}^2$). The high values of global and diffuse solar radiation during summer months are due to clear sky clouds and some aerosol particles that attenuate the incident of solar radiation to the earth's surface. The low values are mainly due to the presence of cloud, rainfall, suspension of water particles that lead to scattering, absorption and reflection of incoming solar radiation to the earth's surface [14]. Extraterrestrial solar radiation was high in the month of December ($472.92 \pm 0.67 \text{ W/m}^2$) and low in the month of June ($312.87 \pm 2.58 \text{ W/m}^2$).

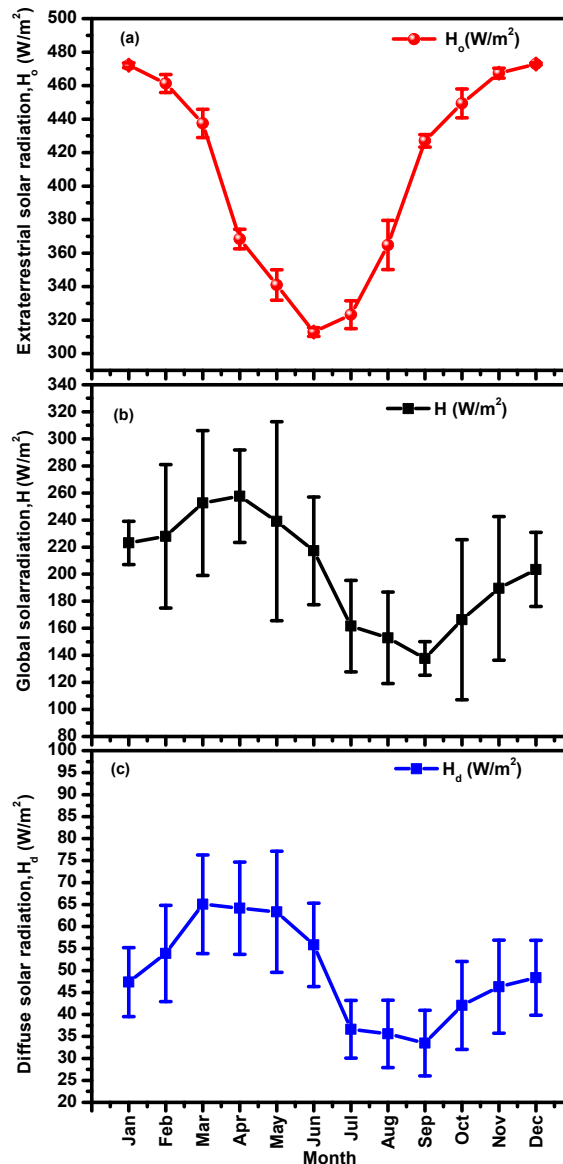


Figure 7: Monthly variation of (a) extraterrestrial (b) global and (c) diffuse solar radiation

3.4. Diurnal Variation of Clearness Index (K_t) and Diffuse Index (k_d)

Figures 8 (a), (b) represents the plots of the diurnal variations of monthly mean clearness index (k_t) and diffuse index (k_d) for the period of study. In general clearness index is widely used for the classification of sky conditions. From Figure 8 (a) it is clear that the clearness index was observed low during sunrise and sunset periods and high values at noon. The low values of k_t (0.30 ± 0.14) are mainly due to low global solar radiation and large values of k_t (0.89 ± 0.67) are due to high global solar radiation, which is dominated by the direct component of the radiation. In the case of diffuse

index (k_d), very low values were observed at noon and high values at sunrise and sunset periods. During sunrise and sunset, the solar radiation received at the surface mainly of the diffuse component. This is consistent with the dependence of diffuse solar radiation reaching the surface on solar elevation, atmospheric turbidity, air mass, atmospheric water vapor content and layers and its distribution of cloud cover [15]. During the noon timings, when the sun is over-headed or near over-headed it is noticed that high global radiation may be mainly due to the direct component of radiation.

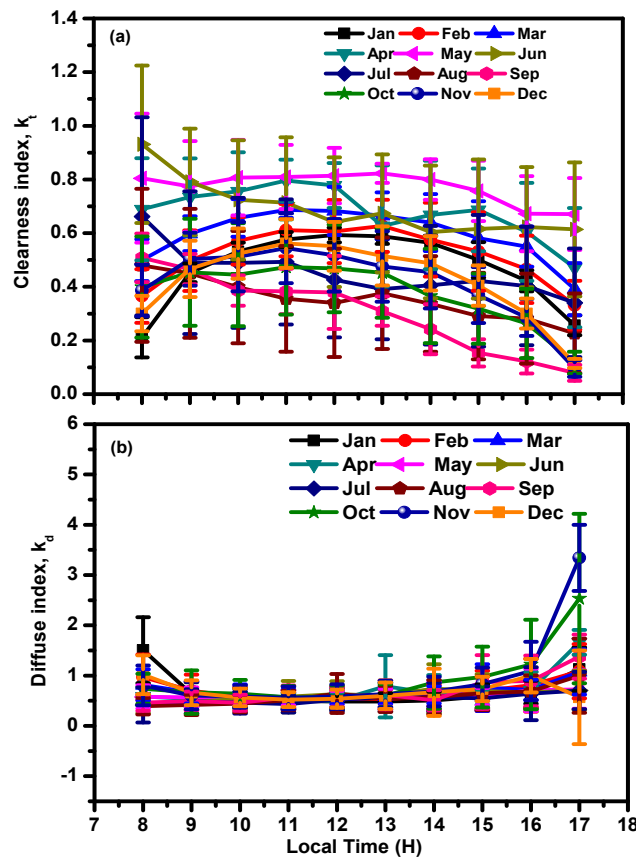


Figure 8: Diurnal variation of (a) clearness index and (b) diffuse index for different months

3.5. Monthly Variation of Clearness Index (k_t) and Diffuse Index (k_d)

The monthly variations of the clearness index (k_t) and diffuse index (k_d) for Anantapur throughout the year were shown in Figure 9. The clearness index, k_t is defined as the ratio of the global radiation at ground level on a horizontal surface and the extraterrestrial global solar irradiation [16]. The average values of clearness index and diffuse index were (0.50) and (0.24) respectively for the entire study period. It is observed that the clearness index is during June (0.69) to September (0.32) and then it increases to the maximum in May (0.71). The variation in clearness index is due to the level of humidity and the position of the sun relative to the observation site. The clearness of the sky is generally higher during the summer season. During the northeast monsoon, when both the clearness index and temperatures are low, the global solar radiation is likely to be low, and which is due to the low clearness index and also the solar radiation energy reduces dramatically [17]. The diffuse index maximum and minimum values are observed to be 0.26 (May) and 0.21 (January) respectively [18].

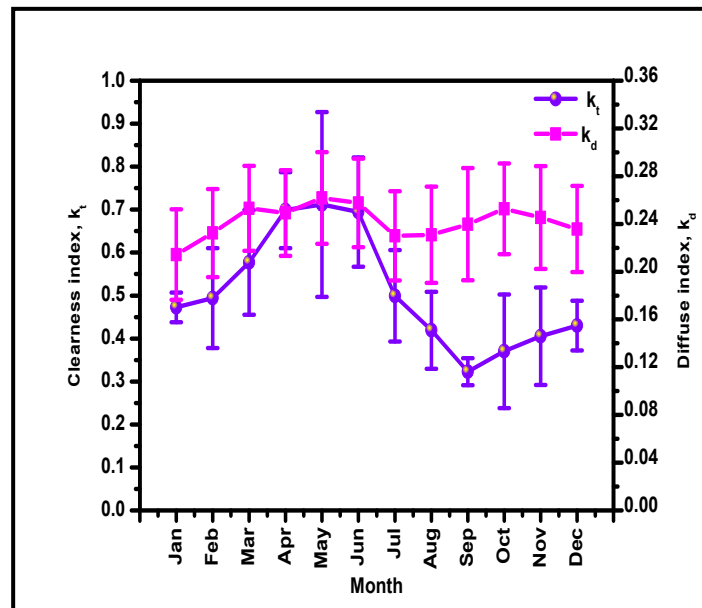


Figure 9: Monthly variation of clearness index and diffuse index for the entire study period

3.6. Relationship between Clearness Index (k_t), Diffuse Index (k_d) and Measured Global Solar Radiation (H)

Clearness index (k_t) is a measure of the degree of clearness of the sky and also a measure of solar radiation extinction in the atmosphere, which includes effects due to radiation interaction with other atmospheric constituents [19], [20]. The monthly average values of measured global solar radiation, clearness index and diffuse index are presented in Table 2. Figure 10 (a) shows the positive correlation between global solar radiation (H) and clearness index (k_t). Clearness index is increasing with increasing of global solar radiation and vice versa. It clearly indicates that the maximum values of H and k_t can be harvested in the summer season and minimum values during the monsoon season. In the case of diffuse index, it shows the negative correlation with global solar radiation. Diffuse index found to be low in the month of January (0.21) and high in the month of May (0.26).

Table 2: The Monthly Average Values of Measured Global Solar Radiation, Clearness Index (K_t) and Diffuse Index (k_d)

Month	Measured solar radiation (H) (W/m^2)	Extraterrestrial solar radiation (H_o) (W/m^2)	Diffuse solar radiation (H_d) (W/m^2)	Clearness index (k_t) H / H_o	Diffusion index (k_d) H_d / H
Jan	223.084	472.106	47.361	0.472	0.214
Feb	227.966	461.258	53.866	0.494	0.232
Mar	252.628	437.143	65.068	0.577	0.253
Apr	257.669	368.430	64.164	0.698	0.249
May	239.133	340.948	63.347	0.711	0.262
Jun	217.248	312.876	55.829	0.694	0.258
Jul	150.546	323.232	32.569	0.465	0.219
Aug	177.363	364.433	39.863	0.485	0.223
Sep	208.525	422.586	47.686	0.491	0.218
Oct	166.307	449.346	42.046	0.37	0.253
Nov	189.497	467.419	46.303	0.405	0.245
Dec	203.467	472.923	48.340	0.43	0.236

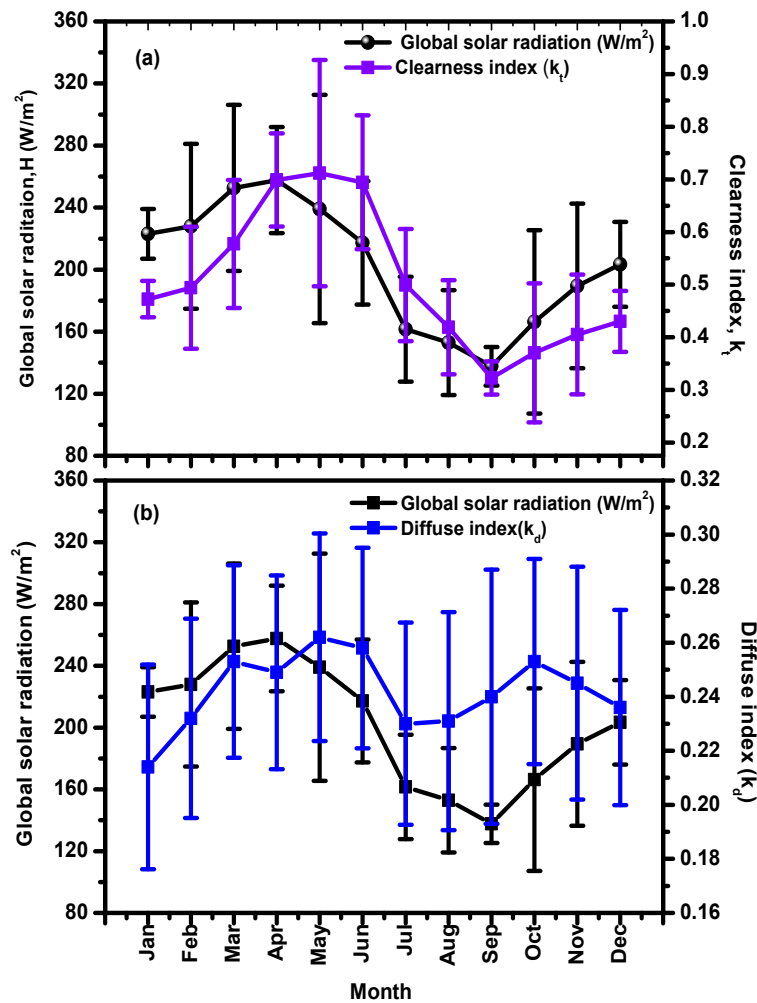


Figure 10: Relationship between (a) Clearness Index (k_t) and measured global solar radiation (H) and (b) diffuse index (k_d) and measured global solar radiation (H)

3.7. Variation of Global Solar Radiation with Temperature and Precipitation

The variances of global solar radiation with temperature and precipitation were shown in Figures 11 (a), (b). The maximum temperature was higher in the summer months (April and May) (32.74 ± 3.82 °C and 32.68 ± 3.64 °C) and low in the winter month (25.24 ± 3.43 °C). Higher values of global solar radiation energy recorded in summer months i.e., 386.59 ± 42.56 W/m² and lower ones during monsoon months 299.78 ± 53.35 W/m² observed in Anantapur. From the Figure 11 (a) it is noticed that in summer, the general trend is that global radiation is high where the temperature is high. In the case of variation of global solar radiation in precipitation, the higher value of precipitation was occurring in the month of September 171.4mm. The distance of the sun rays reached to the earth is smallest during summer, which should result in higher solar radiation. However, the presence of cloud and precipitation reduces the amount of solar radiation received at the ground level [21]. Variations of solar radiation reaching the Earth are thought to influence precipitation, but it is still hard to understand how the periodic variation of solar radiation influences the variation of the precipitation on land, and the extent of this influence on timescales of millennia to decades still remains unclear. It is significant that further investigations and detailed studies of the physical mechanism of solar radiation can probably improve the medium-term and long-term prediction of annual precipitation in the area.

Solar radiation prediction is being paid more attention and the prediction methods are being improved [22].

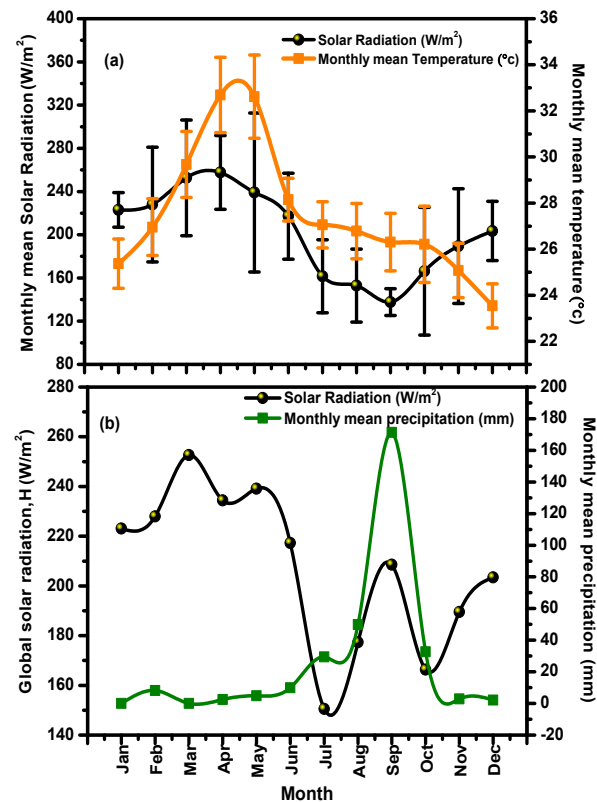


Figure 11: Variation of global solar radiation with (a) temperature and (b) precipitation

4. Conclusions

The measurements of meteorological parameters and solar radiation retrieved from MBLM (Mini Boundary Layer Mast) station and Net radiometer sensors during Jan – Dec 2013 was carried out in the present study. These parameters are useful in understanding the energy exchange between land and atmosphere and also helpful to examine the changes in aerosol physical properties and trace gases associated with the changes in prevailing meteorology. The main conclusions drawn from the present study are shown below.

- The minimum temperature of 25.28 ± 3.7 °C was observed during the January 2013 and a maximum of 32.68 ± 3.6 °C during May 2013. The variability in temperature ranges have been found to be 19 - 31, 24 - 38, 23 - 32 and 21 - 30 °C during winter, summer, monsoon and post monsoon respectively.
- The maximum relative humidity was found to be 76% in the month of September whereas low (36 %) in the month of April.
- The wind speed and directions were measured and the reasons for determining the type of aerosols present over the site and direction from which region they transported are analyzed.
- Diurnal variation of solar radiation shows a steady rise of radiation received at the surface after 7:30 LT and attains a maximum radiation between 12:00 – 13:00 LT.
- The annual means of extraterrestrial, global and diffuse solar radiation was about 408.15 ± 61.63 , 202.43 ± 40.45 and 49.33 ± 11.26 W/m² respectively.

- The maximum global and diffuse solar radiations were observed during March-May ($257.67 \pm 34.18 \text{ W/m}^2$, $65.07 \pm 11.20 \text{ W/m}^2$) whereas minimum global and diffuse solar radiations are noticed during monsoon months (137.66 ± 12.41 , $33.47 \pm 7.44 \text{ W/m}^2$).
- The maximum and minimum amount of extraterrestrial solar radiation of $472.92 \pm 0.67 \text{ W/m}^2$ and $312.87 \pm 2.58 \text{ W/m}^2$ were recorded in December and June respectively.
- The monthly variation of clearness index (k_t) revealed that the month of September has the least value of 0.37 and the month of May has the highest clearness index of 0.71 whereas the diffuse index found to be low in the month of January (0.21) and high in the month of May (0.26).

Acknowledgements

The authors are indebted to Indian Space Research Organization (ISRO), Bangalore for carrying out this work through its Geosphere Biosphere Programme (GBP) under Aerosol Radiative Forcing over India (ARFI) project. We would like to thank NASA's Goddard Earth Sciences Data and Information Services Center.

References

- [1] Iziomon, M.G., and Aro, T.O. *The Diffuse Fraction of Global Solar Irradiance at a Tropical Location*. Theoretical and Applied Climatology. 1998. 61; 77-84.
- [2] Rao, Kusuma G., Narendra Reddy, N., Ramakrishna, G., Satyanarayana, S., Bhuyan, P.K., Bhuyan, K., Kalita, G., Pathak, B., and Kundu, S.S. 2011: *Field Experiment during the Total Solar Eclipse on 22 July 2009 at Dibrugarh, Monogram*. ISRO Publication, Indian Space Research Organisation, Bangalore, India.
- [3] Balakrishnaiah, G., Raghavendra Kumar, K., Suresh Kumar Reddy, B., Swamulu, C., Rama Gopal, K., Reddy, R.R., Reddy, L.S.S., Nazeer Ahammed, Y., Narasimhulu, K., Krishna Moorthy, K., and Suresh Babu, S. *Anthropogenic Impact on the Temporal Variations of Black Carbon and Surface Aerosol Mass Concentrations at a Tropical Semi-Arid Station in Southeastern Region of India*. Journal of Asian Earth Science. 2011. 42; 1297-1308.
- [4] Kumar, K.R., Narasimhulu, K., Balakrishnaiah, G., Reddy, B.S.K., Gopal, K.R., Reddy, R.R., Satheesh, S.K., Moorthy, K.K. and Babu, S.S. *Characterization of Aerosol Black Carbon over a Tropical Semi-arid Region of Anantapur, India*. Atmospheric Research. 2011. 100; 12-27.
- [5] Ganguly, D., Jayaraman, A., and Gadhavi, H. *Physical and Optical Properties of Aerosols over an Urban Location in Western India: Seasonal Variabilities*. Journal of Geophysical Research. 2006. 111 (D24).
- [6] Tessy Chacko, P., and Renuka, G. *Temperature Mapping, Thermal Diffusivity and Subsoil Heat Flux at Kariavattom of Kerala*. Proceedings of the Indian Academy of Sciences – Earth and Planetary Sciences. 2002. 111; 79-85.
- [7] Song, Y.M., Guo, W., and Zhang, Y. *Numerical Study of Impacts of Soil Moisture on the Diurnal and Seasonal Cycles of Sensible/Latent Heat Fluxes Over Semi-Arid Region*. Advance in Atmospheric Science. 2009. 26 (2) 319-326.
- [8] Rodriguez-Iturbe, I., Porporato, A., Ridolfi, L., Isham, V., and Cox, D.R. *Probabilistic Modeling of Water Balance at a Point: The Role of Climate, Soil and Vegetation*. Proceedings of the Royal Society of London A. 2000. 455; 3789-3805.
- [9] Cheen, S.Q., Lu, S.H., Ao, Y.H., Zhang, Y., Li, S.S., and Shang, L.Y. *Characteristics of Temperature and Moisture of Jinta Oasis in summer under Different Soil Moisture and Weather Conditions*. Journal of Desert Research. 2007. 27 (4) 621-626. (In Chinese)

- [10] Guan, X.D., Huang, J.P., Guo, N., Bi, J.R., and Wang, G. *Variability of Soil Moisture and Its Relationship with Surface Albedo and Soil Thermal Parameters over the Loess Plateau*. *Advances in Atmospheric Science*. 2009. 26 (4) 692-700.
- [11] Al-Rawahi, N.Z., Zurigat, Y.H., and Al-Azri, N.A. *Prediction of Hourly Solar Radiation on Horizontal and Inclined Surfaces for Muscat/ Oman*. *Journal of Engineering Research*. 2011. 8; 19-31.
- [12] Teramoto, E.T., and Escobedo, J.F. *Analysis of the Annual Frequency of the Sky Conditions in Botucatu, São Paulo, Brazil*. *Revista Brasileira de Engenharia Agrícola e Ambiental*. 2012. 16 (9) 985-992.
- [13] Souza, A.P., Escobedo, J.F. *Estimates of Hourly Diffuse Radiation on Tilted Surfaces in Southeast of Brazil*. *Institute International Journal of Renewable Energy Research*. 2013. 3; 1.
- [14] Sanusi, Y.K., and Ojo, M.O. *Generation of Clearness Index Maps for Selected Cities in South Western, Nigeria Using Kriging Technique*. *International Journal of Humanities, Arts, Medicine and Sciences (IJHAMS)*. 2015. 3; 1-12.
- [15] Okogbue, E.C., Adedokun, J.A., and Holmgren, B. *Hourly and Daily Clearness Index and Diffuse Fraction at a Tropical Station, Ile-Ife, Nigeria*. *International Journal of Climatology*. 2009. 29; 1035-1047.
- [16] Ashok Kumar Rajput, Rajesh Kumar Tewari, and Atul Sharma. *Utility Base Estimated Solar Radiation at Destination Pune, Maharashtra, India*. *International Journal of Pure and Applied Sciences and Technology*. 2012. 13 (1) 19-26.
- [17] Abdul Majeed Muzathik, Wan Mohd Norsani Bin Wan Nik, Khalid Bin Samo, and Mohd Zamri Ibrahim. *Reference Solar Radiation Year and Some Climatology Aspects of East Coast of West Malaysian* *American Journal of Engineering and Applied Sciences*. 2010. 3 (2) 293-299.
- [18] Hassan A.N. Hejase, and Ali H. Assi, 2014: *Estimation of Global and Diffuse Horizontal Irradiance in Abu Dhabi, United Arab Emirates*. 13th World Renewable Energy Congress (WREC XIII), London, UK.
- [19] Falayi, E.O., Rabi, A.B., and Teliat, R.O. *Correlations to Estimate Monthly Mean of Daily Diffuse Solar Radiation in Some Selected Cities in Nigeria*. *Advances in Applied Science Research*. 2011. 2 (4) 480-490.
- [20] Ndilemeni, C.C., Momoh, M., and Akande, J.O. *Evaluation of Clearness Index of Sokoto Using Estimated Global Solar Radiation*. *IOSR Journal of Environmental Science, Toxicology and Food Technology (IOSR-JESTFT)*. 2013. 5; 51-54.
- [21] Poudyal, K.N., Bhattarai, B.K., Sapkota, B.K., Berit Kjeldstad, and Karki, N.R. *Estimation of Global Solar Radiation using Pyranometer and NILU-UV Irradiance Meter at Pokhara Valley in Nepal*. *Journal of the Institute of Engineering*. 2014. 9; 69-78.
- [22] Wang, B., and Ho, L. *Rainy Season of the Asian-Pacific Summer Monsoon*. *Journal of Climatology*. 2002. 15; 386-398.

Participatory Monitoring of Natural Resources in Shivamogga District of Karnataka, India: The Shinduvadi Experience

Indu K Murthy^{1,2,3} and Rakesh Tiwari¹

¹Centre for Sustainable Technologies, Indian Institute of Science, Bengaluru, Karnataka, India

²Department of Ecology and Environment, Pondicherry University, Puducherry, India

³Aranya Climate Change Services, Basaveshwarnagar, Bengaluru, Karnataka, India

Publication Date: 14 March 2016

Article Link: <http://scientific.cloud-journals.com/index.php/IJAESE/article/view/Sci-392>



Copyright © 2016 Indu K Murthy and Rakesh Tiwari. This is an open access article distributed under the **Creative Commons Attribution License**, which permits unrestricted use, distribution, and reproduction in any medium, provided the original work is properly cited.

Abstract With a growing human and livestock population, there is tremendous pressure on the natural resources and they are being continuously exploited. Gaining an understanding of the status of resources and the drivers of change would aid in better planning and management, particularly at the village level. Given the vast resources, multitude of issues and a dearth of funds, a centralized monitoring system is difficult to put in place. Therefore, promoting participatory natural resource management is the key to creating awareness and also generation of basic information on the status of natural resources and factors contributing to changes in those resources. This paper highlights one such case study of participatory research of natural resources involving scientists, undergraduate students and the community of Shinduvadi village in the Western Ghats region of Karnataka India. This endeavor was aimed at demonstrating the feasibility of monitoring village ecosystems by local institutions by adopting an indicator-based method and guidelines developed by the Centre for Sustainable Technologies, Indian Institute of Science, Bangalore. The Shinduvadi study has identified key environmental issues and also suggested management options for the same. In the process of this participatory monitoring exercise, students have not only gained understanding of the natural resources, the pressures on them, the inter-linkages but also gained as individuals as the experience helped integrate academic content with community service. The Shinduvadi experience is a milestone in participatory research in India and is an example for educational institutions across the country and elsewhere to take up pro-societal research initiatives.

Keywords *Natural Resources; Participatory Monitoring; Students; Monitoring*

1. Introduction

Natural resources are being continuously exploited and suffer degradation due to high human and livestock population density as well as poor management. This has adverse implications for stable food production, supply of fresh water, fish production, fodder, fuelwood, timber supply. The status of natural resources is critical in determining the environment, economy and livelihoods of rural communities. Planning, management and developmental activities happen at the village level and this

requires understanding of the status of resources and their inter-linkages. The first step in promoting participatory natural resource management is therefore creation of awareness and generation of basic information on the status of natural resources and factors contributing to changes in those resources. Participatory research is a dynamic process that involves individuals and institutions from a variety of backgrounds, with varying sets of values. It is sometimes referred to as community-based participatory research as it refers to a method that involves participants as full partners in the research process (Metzler et al., 2003). Maguire (1993) defines participatory research as a process of collective, community-based investigation, education, and action while the *Commission d'étude sur les universités au Québec* defines participatory research as research undertaken by scholars who, coupling theory with intervention, work with groups outside of their institution, analyze with them the problems faced by communities and help them perceive these problems more clearly and formulate strategies to take charge of the sectors that influence their collective life (Alery et al., 1990). These definitions encapsulate the key elements of participatory research. i.e., research through collaboration, education and action (Boutilier, 1997; Yeich, 1992).

In participatory research the research process is as important as the outcome (Cornwall, 1995). It is therefore a process of education, a continuous enhancement of knowledge, skills and resources for all partners with the thrust being on shared decision making, power, responsibility and benefits. The aim of participatory research is therefore not only data collection and analysis to solve problems and generate knowledge, but to increase research capacity, and empower participants in other aspects of their lives. Conducting participatory research is considered transformative for participants (Morford et al., 2003) and is deemed successful if all parties are satisfied with the utility of the process and the outcomes. This paper highlights one such case study of participatory research of natural resources involving scientists, undergraduate students and the community of Shinduvadi village.

2. Location and Methods

Shinduvadi is a small village in the Western Ghats region of Karnataka, India, which is one of the biodiversity hotspots of the world. It is spread over 503 ha and the village is part of Mandagadde panchayat of Thirthahalli taluk of Shivamogga district, about 4 km from river Tunga. The village is characterized by moist semi evergreen—dry deciduous forest type and is primarily an agricultural village. Paddy and areca are the major crops. Shinduvadi is surrounded by four villages: Haalaga to the north, Halasawala to the east, Hemmakki to the south and Ubbur to the west. Settlements are scattered but mostly confined to the central part of the village. Shinduvadi is 650 m above the sea level and is about 4 km from river Tunga. However, agriculture is primarily rainfed.

The Village Natural Resource Monitoring Cell at the Centre for Sustainable Technologies, Indian Institute of Science enlisted selected students of Sahyadri Science College, Shivamogga, in the exercise. Enlisting was based on a test conducted for the students to elucidate their awareness of natural resources and their interest. These students from varied streams put in their efforts and valuable time to understand the problems and issues related to natural resources and communities depending on them by interacting with the people of Shinduvadi.

The selected students were trained in basic monitoring techniques that included: i) collection of information from secondary records or any published studies, ii) land survey to demarcate and map different land-use systems and cropping pattern as well as estimate the area under different land use, iii) field measurements for estimating biomass in different vegetation components, including agro-forestry, fuelwood and water consumption patterns, dung production of cattle and for assessment of fish resource and diversity, iv) laboratory measurements wherein water samples – both drinking and irrigated collected from field sites were analyzed for quality and soil samples collected from different use systems were analysed for soil organic carbon, physical properties, pH and micronutrients

v) household survey to obtain information of individual households with regard to population, gender distribution, land holding, cropping pattern, livestock holding, energy and sanitation status and use of the various resources within the village ecosystem, including changes in cropping pattern, and drivers of change, and vi) Participatory Rural Appraisal techniques to obtain information on communities perception of environmental issues, livelihood issues, trends and status of resources over the years.

3. Results and Discussion

The natural resource monitoring exercise helped integrate academic content with community service, bringing in a sense of connectedness between classroom learning and personal lives of students as well as the lives of others within the larger community (Stanton, Giles and Cruz, 1999), particularly the village community. Howard (1998) defines service-learning as a reciprocal relationship between community service and academic learning that transforms both processes. He states, “Academic service learning is a pedagogical model that intentionally integrates academic learning and relevant community services” (Howard, 1998) and that there is an intentional effort made in service-learning to utilize community-based learning on behalf of academic learning, and utilize academic learning to inform the community service. It also integrates two kinds of learning, experiential and academic – both working together to strengthen each other.

In the Shinduvadi case, the students of Sahyadri Science College got an opportunity to learn basic research methodologies involved in natural resource monitoring at a budding stage and the interactions with the communities especially during surveys and participatory discussions natural resource monitoring exercise sensitized the students to issues and problems of the farming community and the underlying causes. This endeavor by students is a unique exercise wherein collaboration between a research institute and a college has produced an output which could be used for policy-making at the grassroots' level. The researchers from the Indian Institute of Science were confronted with a learning process that was very different from typical classroom setting as the students were not only learning the fundamentals of participatory research but also its application at the grassroots' level with all its nuances and particularities of context.

The students in the process of this exercise learned about themselves, the Shinduvadi community, and the process of participatory research. Working closely with the community and interacting with them, the students gained significant understanding of how local communities operate within their villages as well as specific issues facing resource use and management at the community level. Focus group discussions held with the community to understand trends in resource status and use over a period of time helped students to gain an understanding of the strengths and resiliency of the Shinduvadi community and their coping strategies in the face of resource degradation.

3.1. Students' Learnings

Students had the following to say during reflections, on site discussions and critique of work that was carried out.

Relationship Building

Many students expressed their satisfaction and happiness in learning the art of relationship building and conceded that they were guests in the community and they could build good rapport with the community because of this realization as evidenced in the warmth with which they were received by the local households during subsequent visits.

Team Work

Students expressed their pleasure in working together as a team and the advantages of being in a team. They recognized that being in a team complimented the strengths of different members and that they could achieve tasks assigned to them faster and in a more efficient manner.

Personal Understanding

For many of the students' participatory research helped them gain personal understanding of the ways local communities operate and that they follow no step-by-step methodological outlines in addressing issues. They also learnt that political and personal dynamics operate within villages and these factors influence the work they conducted. In the process, a few students in the group reconsidered their intent of '*doing research on communities*' and realized that success was in working '*with the communities*'.

Personality Development

An overall development of their personality including patience, discipline, and compassion for each other was reported by many students. A few students expressed that at the time of initiation of the study, they were reservations and as they progressed, their view about the entire exercise changed and that they were happy to be part of the research. A few students who were reserved and less communicative in the classroom were outgoing and forthcoming in their views and efforts when in field, reflecting a new side of their personality to their team members and the faculty.

Knowledge

All students expressed that they had learned more about scientific methods as well as the reality of doing research by getting involved in this study than a traditional training course or regular curriculum.

3.2. Validity in Participatory Research

Some researchers, conditioned by the traditional science paradigm (Susman, 1978), are concerned that the participatory research approach implies less rigorous methodology which could lead to less valid results. But our experience shows that participatory research enhances the validity of data as contextual factors are taken into consideration and the base for data collection is broad. Validation is ensured by the depth and variety of data collected – for instance information on trends in resource use is obtained through household surveys as well as focus group discussions and can be validated then and there. Reliability is measured by triangulation of data from more than one source and the rigor with which analysis and interpretation are undertaken (Goodwin and Goodwin, 1984).

4. Conclusion

Rhodes (1997) points to the significance of community service needing to be of mutual benefit between equals and that it is a hallmark of participatory research. Palmer (1993) stated that the most significant issue for education "...is whether we are educating students in ways that make them responsive to the claims of community upon their lives". Participatory research prompts students as well as researchers to engage in learning within the community and in reciprocal form benefits all involved.

In participatory research, learning takes place through mutual interaction and sharing between all partners involved and the collaboration is iterative and reflective as well as reciprocal in nature. Knowledge emerges through the process itself and is not imposed from external theory or expertise.

As Kolb (1984) said, if one interjects students into the participatory research collaboration, both the student and the community members are engaging in a process that involves direct, ongoing experience followed by reflection and conceptualization, that brings the participants into testing and acting on the developing ideas in the real world. Thus, participatory research brings together abstract concepts and research ideas with concrete experience, and through reflection and action, engages students in a cycle of learning and knowledge building.

Successful research should be of immediate use to the local community, through enhancing resources for community-based problem solving (Rolfe, 1996). The Shinduvadi experience is a clear example of this as the study has identified key environmental issues and also suggested management options for the same. The same has been published as a summary for policy for makers and circulated among local government bodies. As a result, there are discussions on carrying forward measures for addressing few of the issues identified, for example, the desilting of pond to improve water availability for irrigation. The Shinduvadi experience is definitely a milestone in participatory research in India and is an example for educational institutions across the country and elsewhere to take up pro-societal research initiatives.

References

- Alery, J. et al., 1990 (editors): *Community Care & Participatory Research*. Montreal: Nu-age Editions.
- Boutlier, M., Mason, R., and Rootman, I. *Community Action and Reflective Practice in Health Promotion Research*. Health Promotion International. 1997. 12; 69-78.
- Cornwall, A., and Jewkes, R. *What is Participatory Research?* Social Science and Medicine. 1995. 41 (12) 1667-76.
- Goodwin, L.D., and Goodwin, W.L. *Are Validity and Reliability "Relevant" in Qualitative Evaluation Research?* Evaluation and the Health Professions. 1984. 7 (4) 413-26.
- Howard, J.P.F. *Academic Service Learning: A Counternormative Pedagogy*. New Directions for Teaching and Learning, No. 73, Spring 1998. 21-29.
- Kolb, D.A., 1984: *Experiential Learning: Experience as a Source of the Learning and Development*. Englewood Cliffs, N.J.: Prentice-Hall.
- Maguire, P., 1993: *Challenges, Contradictions and Celebrations: Attempting Participatory Research as a Doctoral Student*. In: Park, P., Brydon-Miller, M., Hall, B., Jackson, T. (editors). *Voices of Change: Participatory Research in the United States and Canada*. Toronto: OISE Press; 157-76.
- Metzler, M.M., Higgins, D.L., Beeker, C.G., Freudenberg, N., Lantz, P.M., Senturia, K.D., Eisinger, A.A., Viruell-Fuentes, E.A., Gheisar, B., Palermo, A., and Softley, D. *Addressing Urban Health in Detroit, New York City, and Seattle through Community-Based Participatory Research Partnerships*. American Journal of Public Health. 2003. 93 (5) 803-811.
- Morford, S., Robinson, D., Mazzoni, F., Corbett, C., and Schaiberger, H. *Participatory Research in Rural Communities in Transition: A Case Study of the Malaspina-Ucluelet Research Alliance*. BC Journal of Ecosystems and Management. 2004. 5 (2) 39-43.
- Palmer, P.J., 1993: *To know as we are known: Education as a Spiritual Journey*. New York: Harper Collins.

Rhodes, R.A., 1997: *Community Service and Higher Learning: Explorations of the Caring Self*. New York: SUNY Press.

Rolfe, G. *Going to Extremes: Action Research, Grounded Practice and the Theory-Practice Gap in Nursing*. *Journal of Advanced Nursing*. 1996. 24; 1315-20.

Shiduvadi Village Ecosystem (2007): *State of Environment and Natural Resources*. Centre for Sustainable Technologies, Indian Institute of Science. <http://ces.iisc.ernet.in/ravi/vnrm/SoENR.html>

Stanton, T.K., Giles, D.E., and Cruz, N.I., 1999: *Service-Learning: A Movement's Pioneers reflect on its Origins, Practice, and Future*. San Francisco, CA: Jossey-Bass.

Susman, G.I., and Evered, R.D. *An Assessment of the Scientific Merits of Action Research*. *Administrative Science Quarterly*. 1978. 23; 582-603.

Yeich, S., and Levine, R. *Participatory Research's Contribution to a Conceptualization of Empowerment*. *Journal of applied Social Psychology*. 1992. 22 (24) 1894-1908.

Statistical Correlation between Land Surface Temperature (LST) and Vegetation Index (NDVI) using Multi-Temporal Landsat TM Data

Anbazhagan S. and Paramasivam C.R.

Centre for Geoinformatics & Planetary Studies, Dept. of Geology, Periyar University, Salem, Tamilnadu, India

Publication Date: 12 April 2016

Article Link: <http://scientific.cloud-journals.com/index.php/IJAESE/article/view/Sci-409>



Copyright © 2016 Anbazhagan S. and Paramasivam C.R. This is an open access article distributed under the **Creative Commons Attribution License**, which permits unrestricted use, distribution, and reproduction in any medium, provided the original work is properly cited.

Abstract Remote sensing TIR as a part of the electromagnetic spectrum is one of the best observations of Land surface temperature (LST). Our earth contains heterogeneous land feature and it is composed of a variety of materials. Now-a-days there are many remote sensing satellites that provide thermal data. In the present study, the Landsat TM data with multi temporal periods such as 1992, 2001 and 2010 were utilized to study LST in the mining area. The aim of the study is to prepare LST mapping for estimating land surface temperature from multi temporal Landsat TM thermal bands and compare with the associated phenomenal condition. The Landsat 5 TM data of 11-03-1992, 09-02-2010 and Landsat 7 data of 15-05-2001 were used and the land surface emissivity's for these particular periods were estimated. The Normalized Difference Vegetation Index (NDVI) was calculated in the same period. The image processing was adopted using the ENVI 4.7 software. The results of emissivity and vegetation index interpreted for each period indicated that when the emissivity increases vegetation index shows negative anomaly. The standardization of error coefficient was founded with the aid of statistical software SPSS, which strengthened the approach of the study. The statistical regression analysis of NDVI and LST were shown in Standardized regression coefficient (B) value as -0.209, -0.143 and -0.190 in the years of 1992, 2001 and 2010 respectively. Comparison of LST and its associated constraint will precisely indicate that these variables are mutually important. Remote sensing multi temporal satellite data when coupled with an image processing technique will support for estimate land surface temperature, normalized vegetation index and preferably utilized for an empirical data report from the Indian Meteorological Department (IMD) ground based observation data.

Keywords LST; NDVI; Remote Sensing; Image Processing; Regression

1. Introduction

LST defines the remote sensing, monitoring surface temperature of ground as pixel based derived observation. These clustering of pixels can be grouped as different class features. LST possesses soil surface temperature, canopy, and vegetation body. In this context, the spatial resolution of satellite remote sensing thermal data can be defined as the average temperature of surface existing features represented on pixel scale that demarcate the differences in emissivity of the land.

Estimation of land surface temperature (LST) is an indication of surface emissivity changes due to anthropogenic activities. Many researchers have estimated the temperature by using land observation stations and well equipped instruments which are expensive, in relationship with the remote sensing thermal band being utilized and it was found as easy and low cost effective tool to identify the surface emissivity. The TIR remote sensing data for land surface temperature estimation in Band 3 and Band 4 for Normalized Difference Vegetation Index studies were carried out by many researchers with various satellite data products as well as they adopted various statistical approaches to achieve their interpreted results (Valor & Caselles, 1996; Goetz, 1997; Sandholt et al., 2002; Kim et al., 2005). The temperatures of the region and vegetation condition were monitored through Landsat TM data for multitemporal periods. Land surface temperature emissivity in thick forest, usually low and NDVI remarks as positive, and the bare soil without vegetation surface temperature emissivity become high as represented in the negative indices (Anderson et al., 2008). The vegetation index may be varied based on terrain condition and types of trees cover. Surface emissivity can be measured by satellite data and the emissivity of temperature compared as a part of accuracy assessment (Srivastava, 2010). Satellite temperature estimation with strong correlation of IMD derived temperature data and vegetation indices were evaluated by NDVI observation. Land Surface Temperature is an important parameter to determine the energy exchange between the surfaces of the earth (Shah et al., 2013; Orhan et al., 2014) and the radiant temperature that will help to understand the change of the surface temperature. Identification of changes on LST over a period of time is one of the most important environmental parameters in the study domain. The radiant temperature can be calculated and interference for the terrain condition for future perspective (Balamurugan et al., 2009). NDVI can analyze the temporal changes over the study region to visualize the change in the concentration of temperature radiant with respect to time. The heat energy accounting from high to low by radiation, convection or conduction process and it is applied to surfaces emissivity studies (Gupta, 2005) for various applications. LST-NDVI estimated through satellite derived products and defines their relationship through conventional statistical approach. (Weng et al., 2004; Goetz, 1997). Finally, this review will support to study the relationship of land surface temperature and Normalized vegetation index. Meanwhile, the intend of parameters like meteorological earth observed temperature and annual rainfall is utilized from an IMD report for support parameters.

2. Study Area

The study area Salem magnesite mining zone lies in the southern part of India and it covers 190 sq. km area in between 78°06'16" E to 78°19'25" E longitude and 11°66'47" N to 11°78'76" N latitude and located in bottom of Shervroy hills (Figure 1), Salem magnesite mining landform located adjacent to dense forest (Kurumpampatti reserved forest), agriculture land, shrubs, rice crops and other plantation. Geologically, the study area bounded by ultramafic of Achaean age with a rich of magnesite ore as vein deposits and it appears white colour therefore termed as "Chalk hills". The climate in mining area is dry and moderate with temperature ranges from 23°C to 38°C. The average annual rainfall varies from 800mm to 1600mm. The climate during January and February are generally pleasant, the dry summer begins in March, with the year's highest temperatures reach during May. The weather continues more temperate in June and July, and in August become cloudy. The northeast monsoon contributes rainfall during September to December.

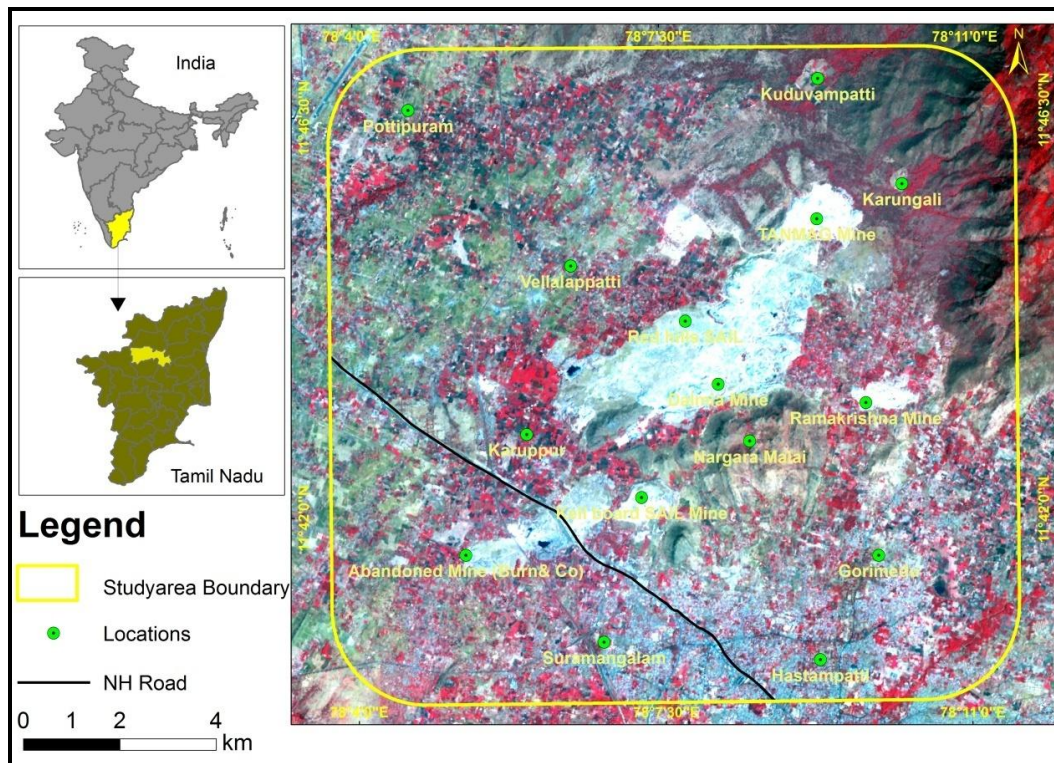


Figure 1: LANDSAT TM 5 Satellite Data 2010 Show the Magnesite Mining Region Located in Parts of Salem, India

3. Methodology

Landsat TM 5 and TM 7 satellite data were utilized for estimation of Land Surface Temperature (LST) and generate vegetation indices. The specifications of satellite data products are represented in Table 1. The ENVI 4.7 software image processing utilized to determine the LST & NDVI. The maximum and minimum values in study region were found in the generated map and the simple

Table 1: Satellite Data used in this Study

S. No.	Data Type	Resolution	Year of Product	Source
1	LANDSAT 5	30 m*	11-03-1992	USGS
2	LANDSAT 7	30 m*	15-05-2001	USGS
3	LANDSAT 5	30 m*	09-02-2010	USGS

*Spatial resolution in thermal infrared is 120 m, but it is resampled to 30 m pixels

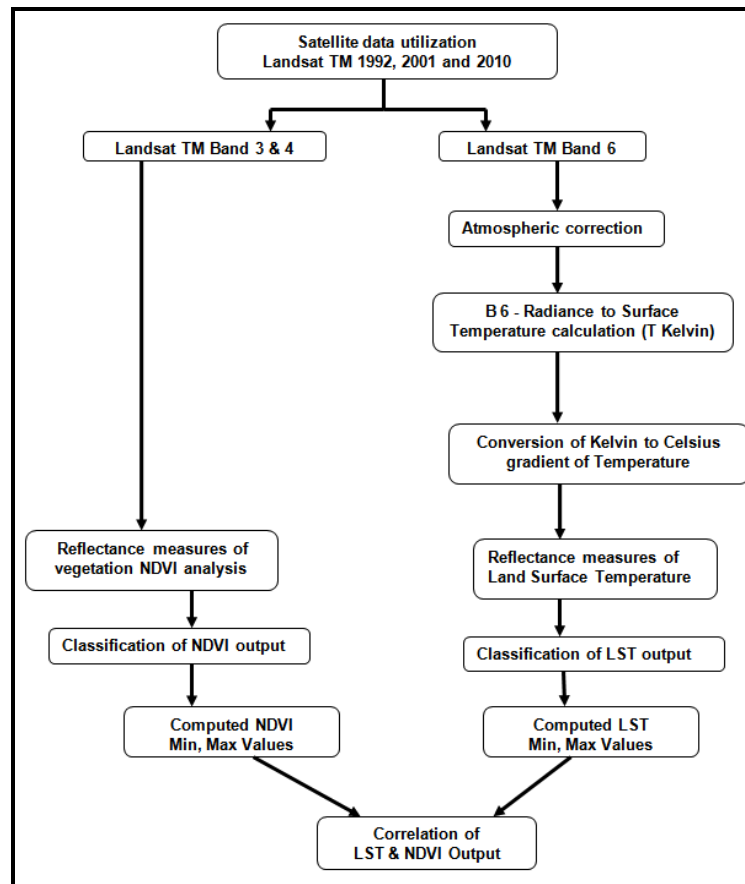


Figure 2: Methodology Adopted for Computation of LST and NDVI

correlation was applied to improve results. TM data Band 6 with (1.40-12.50 μm resampled with 30m spatial resolution) is utilized for LST output NDVI analysis carried out with the help of Band 3 (0.63-0.69 μm) with 30m spatial resolution) and Band 4 (0.76-0.90 μm with 30m spatial resolution) were utilized. The detailed image processing technique adopted in this study is shown in Figure 2. The linear regression model was used to estimate (SPSS package) the regression coefficient for dependent variable LST and in the same way independent variable NDVI value ranges.

3.1. Land Surface Temperature Estimation

Surface temperature is a general, non-specific term referring to the aggregate temperature of all objects, comprising the existing surface. LST maintains by the incoming solar and long wave irradiation, (Li et al., 2013) the outgoing terrestrial infrared radiation, the sensible and latent heat flux, and the ground flux. It is a good indicator of the energy balance at the earth's surface. The LST measurement in satellite data to digital format of DN values and the defined utilization methods for computing land surface temperature by various workers (Chander and Markham, 2003; Chander et al., 2009; Srivastava et al., 2010; Sheela et al., 2011) find out the surface temperature measurements through satellite derived data. Based on reviews and better understanding methods would be followed to execute for surface temperature measurements in Landsat TM TIR data in 1992, 2001 and 2010 respectively. The following steps are strengthening to estimate Land surface temperature with a mathematically derived formula to find the surface temperature of particular domain pixel.

Step 1: Radiometric correction requires converting remotely sensed digital numbers (DN) to spectral radiance values and data comparable. To perform the conversion of DN to spectral radiance by using the equation (1)

$$L_{\lambda} = L_{min} + (L_{max} - L_{min}) * DN / 255 \quad Eq. (1)$$

Where,

L_{λ} = Spectral radiance

L_{min} = 1.238 (Spectral radiance of DN value 1)

L_{max} = 15.600 (Spectral radiance of DN value 255)

DN = Digital Number

The above equation (1) converts DN values into spectral radiance (L_{λ})

Step 2: Conversion at sensor spectral radiance

In radiometric calibration, pixel values (Q) in the raw data and unprocessed image data were converted into absolute radiance value and the following equation (2) is performed for this conversion and satellite data scaled into 8 bits ($Q_{calmax}=255$) values.

$$L_{\lambda} = \left(\frac{L_{MAX_{\lambda}} - L_{MIN_{\lambda}}}{Q_{calmax} - Q_{calmin}} \right) (Q_{cal} - Q_{calmin}) + L_{MIN_{\lambda}} \quad Eq. (2)$$

Or

$$L_{\lambda} = G_{rescale} * Q_{cal} + B_{rescale}$$

Where,

$$G_{rescale} = \frac{L_{MAX_{\lambda}} - L_{MIN_{\lambda}}}{Q_{calmax} - Q_{calmin}}$$

$$B_{rescale} = L_{MIN_{\lambda}} - \left(\frac{L_{MAX_{\lambda}} - L_{MIN_{\lambda}}}{Q_{calmax} - Q_{calmin}} \right) Q_{calmin}$$

Where,

L_{λ} = Spectral radiance at the sensor's aperture [W/ (m² sr μm)]

Q_{cal} = Quantized calibrated pixel value [DN]

Q_{calmin} = Minimum quantized calibrated pixel value corresponding to $L_{MIN_{\lambda}}$ [DN]

Q_{calmax} = Maximum quantized calibrated pixel value corresponding to $L_{MAX_{\lambda}}$ [DN]

$L_{MIN_{\lambda}}$ = Spectral at-sensor radiance that is scaled to Q_{calmin} [W/ (m² sr μm)]

$L_{MAX_{\lambda}}$ = Spectral at-sensor radiance that is scaled to Q_{calmax} [W/ (m² sr μm)]

$G_{rescale}$ = Band-specific rescaling gain factor [(W/ (m² sr μm))/ DN]

$B_{rescale}$ = Band-specific rescaling bias factor [W/ (m² sr μm)]

Step 3: Conversion to TOA reflectance (L_{λ} -to- pp)

Landsat TM Top of Atmosphere Reflectance (TOA), data must be corrected and processed because of variation in solar zenith angles due to the time difference between data acquisitions. The TOA reflectance of the Earth is computed according to the equation (3)

$$\rho_{\lambda} = \frac{\pi \cdot L_{\lambda} \cdot d^2}{ESUN_{\lambda} \cdot \cos\theta_s} \quad Eq. (3)$$

Where,

ρ_{λ} = Planetary TOA reflectance [unitless]

π = Mathematical constant approximately equal to 3.14159 [unitless]

L_{λ} = Spectral radiance at the sensor's aperture [W/ (m² sr μ m)]

d = Earth-Sun distance [astronomical units]

$ESUN_{\lambda}$ = Mean exoatmospheric solar irradiance [W/ (m² μ m)]

θ_s = Solar zenith angle

Step 4: Radiance from sensor to effective at-sensor brightness temperature (L_{λ} to T)

The thermal band data (Band 6 on the TM and ETM+) need to be converted from at-sensor spectral radiance to effective at-sensor brightness temperature. At-sensor temperature uses the prelaunch calibration constants adapted from Table 2. The conversion formula for the at sensor's spectral radiance to at-sensor brightness temperature are in the equation (4)

$$T = \frac{K2}{\ln\left(\frac{K1}{L_{\lambda}} + 1\right)} \quad Eq. (4)$$

Where,

T = Effective at-sensor brightness temperature [K]

K2 = Calibration constant 2 [K]

K1 = Calibration constant 1 [W/ (m² sr μ m)]

L_{λ} = Spectral radiance at the sensor's aperture [W/ (m² sr μ m)]

ln = Natural logarithm

Table 2: Pre- Launch TM Thermal Band Calibration Constants

Constant	LANDSAT TM	LANDSAT ETM+
K1	607.76	666.09
K2	1260.56	1282.71

(Courtesy: NASA, LANDSAT Handbook, 2011)

Step 5: Conversion of temperature Kelvin (T_K) to Celsius ($^{\circ}C$)

The surface temperature output from satellite image is Kelvin (T_K) and the same temperature need to convert into Celsius ($^{\circ}C$), for that the temperature T in Kelvin (K) subtracted by 273.15 as illustrated in the equation (5)

$$T(^{\circ}C) = T_{(K)} - 273.15 \quad Eq. (5)$$

The above steps were adopted for converting Landsat calibrated DNs to absolute units of at-sensor spectral radiance, TOA reflectance, and at-sensor brightness temperature.

3.2. Derivation of Normalized Difference Vegetation Index

The Normalized Difference Vegetation Index (NDVI) shows that the indices derived from remote data under visible and near infrared bands of the electromagnetic spectrum. NDVI were adopted for various applications (Pettorelli et al., 2005; Holm et al., 1987; Anbazhagan et al., 2014). The NDVI

values directly related to land cover parameters like total count of biomass. In this context, the reflectance ratio calculated from the remotely sensed satellite data is used to derive the density of vegetation indices as expressed in the following equation (6)

$$NDVI = \left(\frac{NIR}{RED} \right) / (NIR + RED) \quad Eq.(6)$$

Where, NIR and RED are the DN value of Near-infrared and red band respectively.

Generally, healthy vegetation will absorb most of the visible light that falls on it, and reflects a major portion of the near-infrared region. Unhealthy or sparse vegetation reflects more visible light and less near-infrared region. Bare soils on the other hand reflect moderately in both the red and infrared portion of the electromagnetic spectrum (Lillsand et al., 2009) and the results will appear zero. The NDVI outputs were obtained from the Landsat TM images for the year of 1992, 2001 and 2010 and respectively shown in the Figures 6, 7 & 8.

4. Results and Discussion

The primary objective of the study is to find out land surface temperature as well as vegetation index and correlation the variables using multi temporal Landsat TM data. The LST and NDVI obtained for the year of 1992, 2001 and 2010. Figures 3, 4 & 5 have shown that the spatial distribution of estimated LST respectively, for the years 1992, 2001 and 2010. The maximum and minimum temperature and statistics of LST are shown in Table 3. The minimum is 23.61⁰C and maximum of 40.01⁰C with the mean average of 16.4⁰C. In Landsat TM 2001, the estimated value of LST represents a minimum of 22.28⁰C and maximum of 35.72⁰C and mean average of 13.44⁰C. Using Landsat TM 2010 data, LST was calculated and the minimum temperature was found to be 30.99⁰C and maximum of 33.58⁰C and so the mean average of 12.35⁰C. The maximum and minimum LST are graphically represented in Figure 9. An archive report obtained from the Indian Meteorological Department (IMD) as listed in Table 4. The satellite derived estimates LST and IMD ground station observed temperature is comparable and validated findings of estimated temperature. The IMD observations and satellite derived LST are nearly in agreement with respect to temperature values in the respective years. In the study region, high temperature is mostly plunge at middle and southwest portions. The middle portion covered by the magnesite mining act and there is no count of trees, meanwhile the other portions may exhibit high emissivity due to barren area and the rest of the area fall in medium temperature.

Figure 6, 7 & 8 shows the spatial distribution of NDVI indices derived from the Landsat image 1992, 2001 and 2010. NDVI of 1992, minimum of -0.23 and maximum of 0.65 values with mean value is 0.63. In 2001, NDVI value with minimum of -0.30 and maximum 0.48 with mean value 0.66 and NDVI values of 2010 signify as a minimum of -0.58 and maximum of 0.34 and mean value of 0.53. The statistics of NDVI are listed in Table 3 and the difference shown in Figure 10. It is observed that in all three years NDVI with negative values appeared in the central portions of the study area indicates that absence of vegetation or short vegetation cover like shrubs. This area located mainly in and around the magnesite mining region. The NDVI value corresponding high in the North-East portion indicating dense vegetation cover and tall plantations in the study region. A medium NDVI associated with seasonal crops and agricultural activities in the study region. In particular, NDVI of 2010 shows the lowest NDVI value in the south west portions which is due to increasing of urbanization in those regions. As such the combinations of LST and NDVI are the best tools to identify temperature of the region and NDVI support as a validation of study. The ground based IMD temperature results is also nearly identical to the estimated value. The middle portion has higher emissivity records because soil surfaces have an influence on the measured brightness temperature due to mining activities.

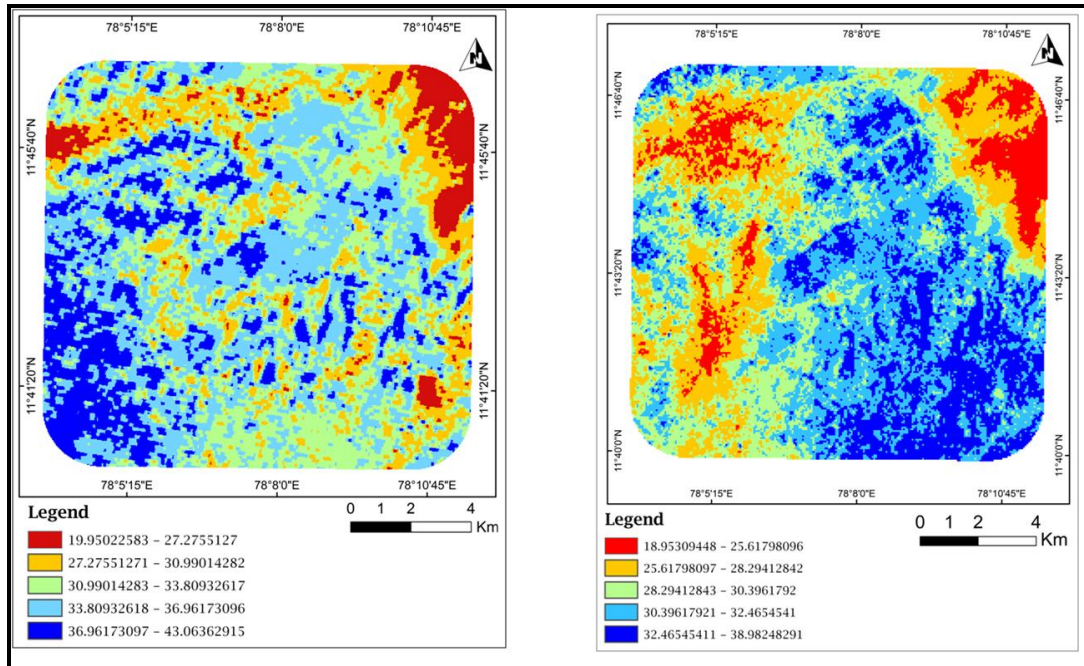


Figure 3: Land Surface Temperature (Celsius) Gradient Derived from LANDSAT TM 5 for 1992 data

Figure 4: Land Surface Temperature (Celsius) Gradient Derived from LANDSAT TM 7 for 2001 data

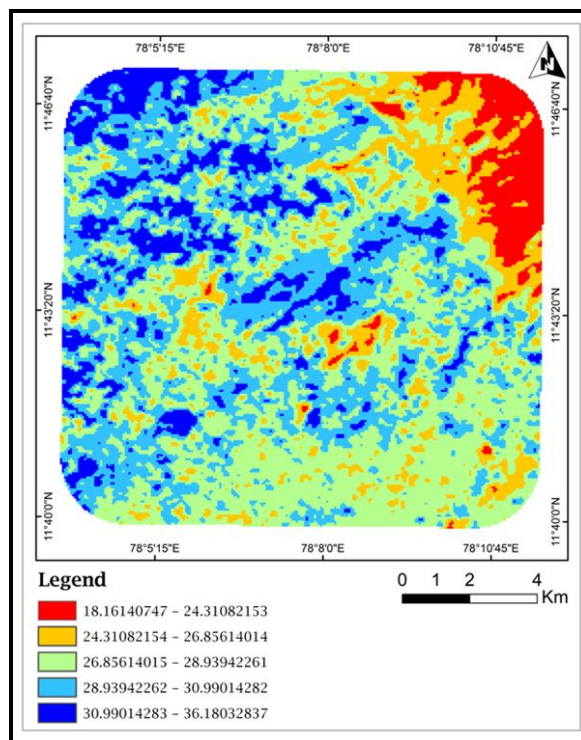


Figure 5: Land Surface Temperature (Celsius) Gradient Derived from LANDSAT TM 5 for 2010 data

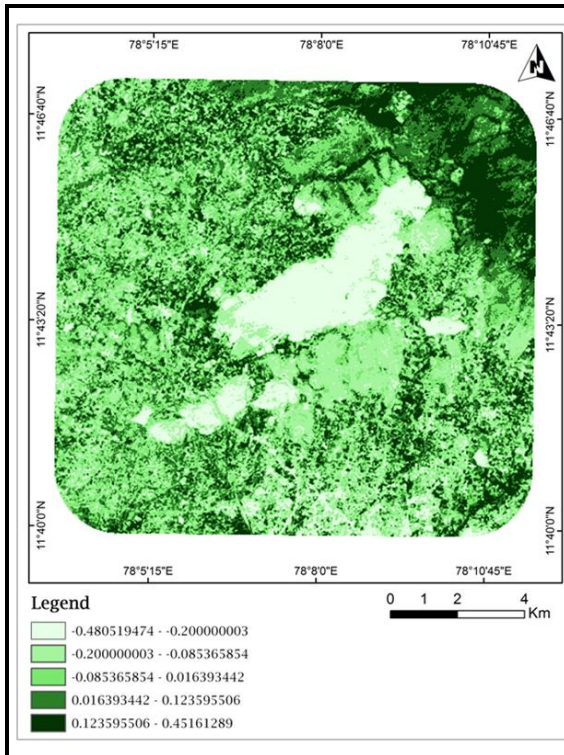


Figure 6: NDVI derived from LANDSAT TM 5 for the year 1992

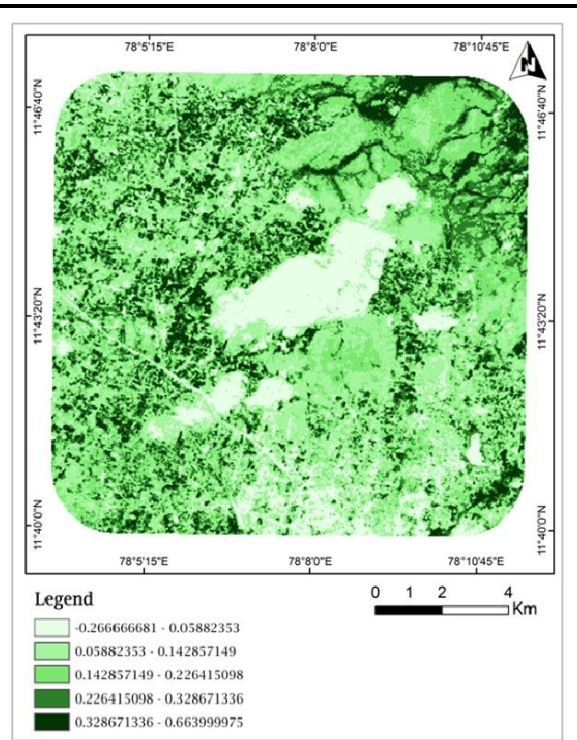


Figure 7: NDVI derived from LANDSAT TM 7 for the year 2001

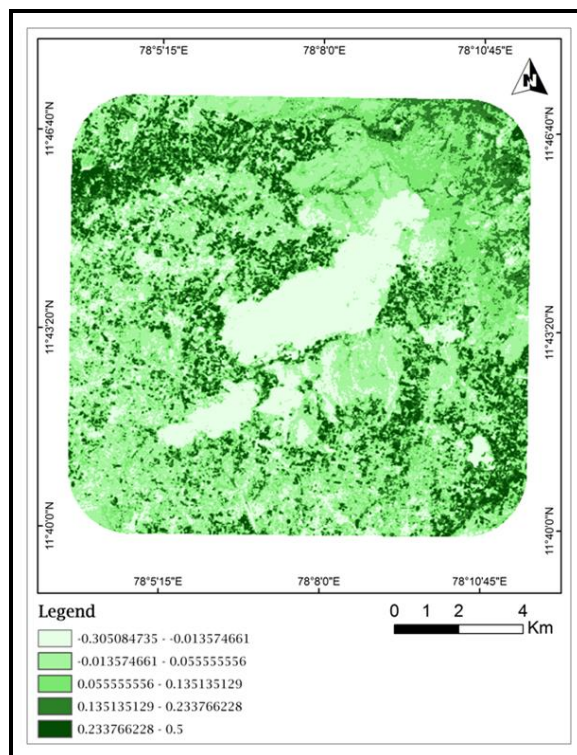


Figure 8: NDVI Derived from LANDSAT TM 5 for the year 2010

Table 3: Satellite Data Derived Estimates Land Surface Temperature, NDVI Index and Range calculations

Year	LST		NDVI		LST & NDVI Range	
	Minimum (° C)	Maximum (° C)	Minimum	Maximum	Temperature Range	NDVI Range
1992	23.61	40.01	-0.23	0.65	16.4	0.63
2001	22.28	35.72	-0.30	0.48	13.44	0.66
2010	30.99	33.58	-0.58	0.34	12.35	0.53

Table 4: IMD observations on Land Surface Temperature & Annual rainfall

Year	Minimum Temperature (° C)	Maximum Temperature (° C)	Average Annual Rainfall (in mm)
1992	22.5	33.7	162.7
2001	25.5	36.8	110.9
2010	20.2	33.7	0.00

(Courtesy: IMD, Meteorological Observatory Data)

Table 5: Interpreted Temperature Ranges from LST & NDVI Indices and Associated Pixel Count during 1992, 2001 & 2010

Years	LST		NDVI	
	Temperature (° C)	Pixel counts	Indices	Pixel counts
1992	20-27	2538	-0.48 - -0.20	11126
	27-31	7613	-0.20 - -0.09	21219
	31-34	18468	-0.09 - 0.01	15176
	34-37	22361	0.01 - 0.12	10287
	37-43	12244	0.12 - 0.45	5373
2001	19-26	4811	-0.26 - 0.05	6959
	26-28	12185	0.05 - 0.14	13896
	28-30	14905	0.14 - 0.23	16659
	30-32	19785	0.23 - 0.33	15761
	32-39	11423	0.33 - 0.66	9905
2010	18-24	3378	-0.30 - -0.01	8351
	24-27	7746	-0.01 - 0.05	19243
	27-29	25224	0.05 - 0.13	18187
	29-31	19595	0.13 - 0.23	11197
	31-36	7107	0.23 - 0.5	6215

Ultimately, it exhibits high emissivity cluster appearing in temperature value. The present study reveals that the maximum surface temperature observed in the middle portion of the mining area because of lower contributions of evaporation and transpiration in the absence or lesser vegetation cover. Soil surfaces have an influence on the measured brightness temperature. Perhaps some places of vegetation regions show high temperature due to short shrub coverage. The comparison of maximum and minimum values makes an impact on the statistics in the particular region. (Figure 11 and Table 3)

The standardized regression coefficient value obtained with the aid of the SPSS statistical package to find the B-Standardized regression coefficient parameters were observed in the regression analysis. The regression value indicates that NDVI B-values show negative (Table 6). Hence, it is to be concluded that in the study region, NDVI shows a negative result due to absence or limited vegetation cover. The vegetation indices not only based on temperature emissivity, but also depend on rainfall and circumstance of the season. The rainfall data obtained from IMD for the periods of 1992, 2001 and 2010 and the average annual rainfall distribution are 162.7 mm, 110.9 mm and zero respectively (Table 4).

Table 6: Statistical Regression Analysis between LST Vs NDVI

Dependent Variable	Independent Variable	B value
LST 1992	NDVI 1992	-0.209
LST 2001	NDVI 2001	-0.143
LST 2010	NDVI 2010	-0.190

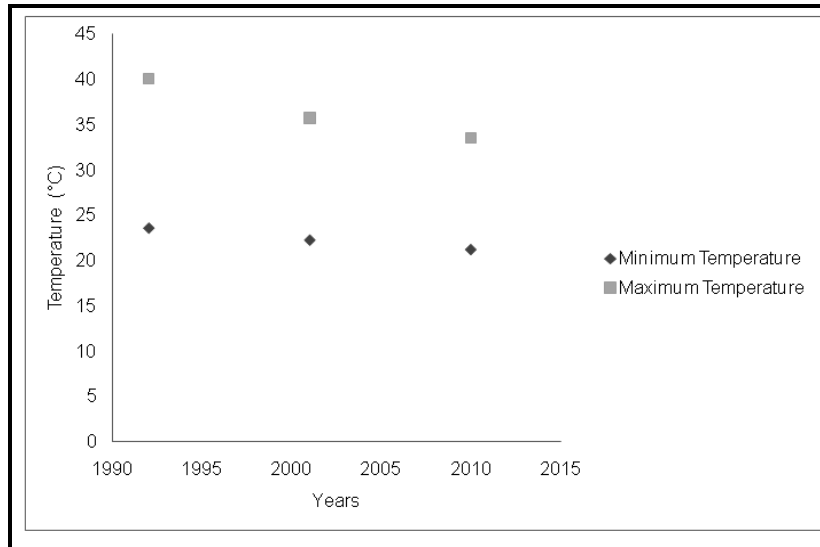


Figure 9: LST Minimum and Maximum during 1992, 2001 and 2010

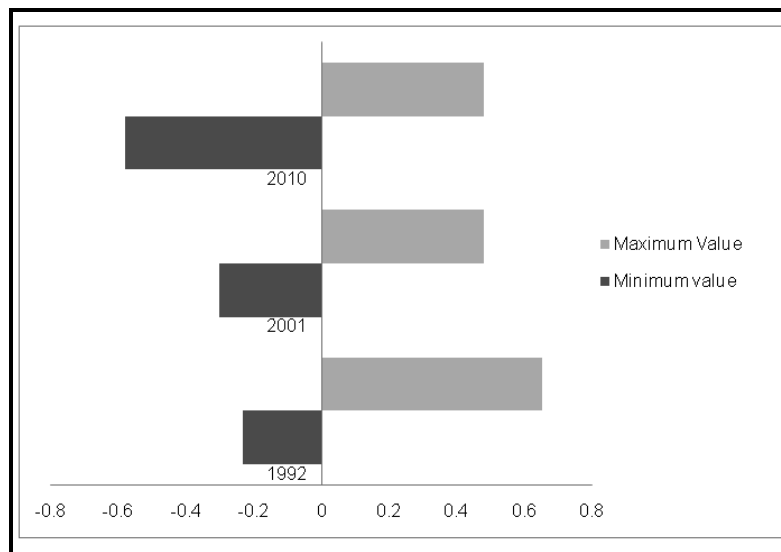


Figure 10: Minimum and Maximum NDVI during 1992, 2001 and 2010

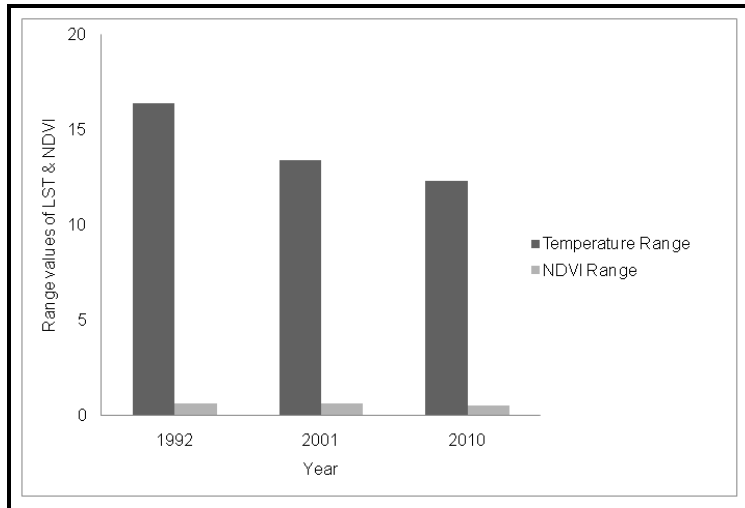


Figure 11: The range of LST Vs NDVI during the years of 1992, 2001 and 2010

This implies that in the year of 2010 there was no rainfall and it was a prime cause for negative vegetation indices. The number of pixels presence in each category of LST and NDVI was calculated. For better understanding the phenomenal changes were observed through histogram generation in each category with the respective years (Table 5). The histogram difference clearly indicates that increase of temperature with decreases of vegetation indices (Figure 12, 13). Meanwhile, in numerical statistical regression analysis, the results of standard regression coefficient (B) show that negative values of NDVI in the domain region with the correlation of the LST. The resultant image depicts the statistical approach used to find the LST and NDVI values of area in and around magnesite mining region.

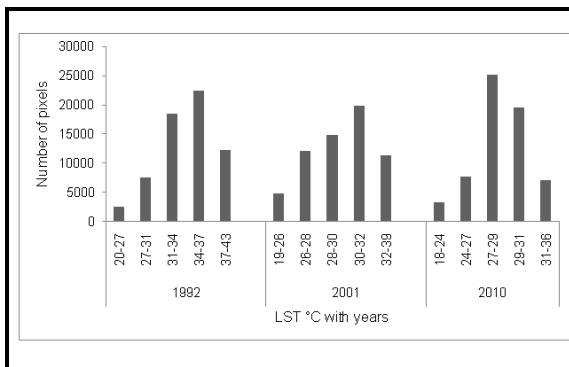


Figure 12: LST histogram distributions in the mining area during different time period

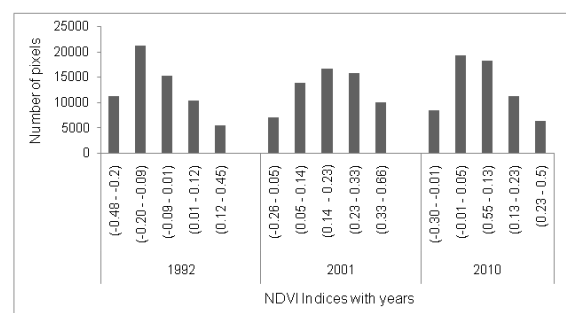


Figure 13: NDVI histogram distributions in the mining area during different time period

4.1. Statistical Regression Analysis

The statistical analysis was carried out by SPSS (version 22) to find out the regression analysis between LST & NDVI parameters. Logistic regression estimates numerical comparison of input variable derived from output results. In this method LST has considered as dependent variable and NDVI as independent variables to find out the regression coefficient. The standard regression coefficient (B) values are - 0.209, - 0.143 and - 0.190 respectively for the years of 1992, 2001 and 2010 as shown in Table 6.

5. Conclusion

The results have shown that satellite derived LST values and NDVI of vegetation cover have shown the surface condition of the region. The LST is comparable with NDVI provided valuable results for the study region. It's bringing out an idea of surface temperature for the entire region. In the absence of meteorological data, we can find out the surface temperature using satellite thermal data. Also the same could be employed to find the vegetation condition of the terrain because both are identical parameters. Thus, it informs, that the studies attempted will be merely an estimation of LST in correlation with NDVI parameters. The surface temperature is increased due to intrusion of mining, deforestation of vegetation, settlement and imbalanced climatic changes. Active mining region exhibit NDVI with negative values and at the same time, the reclaimed region in the presence of vegetation appears as positive values. The utilized satellite data fall in the dry season and the rainfall in those periods derived from IMD ground based observed data were shown as an asymmetrical pattern in the study region. Persistently, the measures of the region will support developmental implementations and optimistic approach for future environmental deeds.

Acknowledgement

The authors are grateful for USGS Global Landcover Facility (GLCF) for freely downloaded TM satellite data products and IMD for providing Meteorological data. The second author acknowledges the University Grants Commission (UGC) for granting BSR-SRF fellowship in this research work.

References

- Anbazhagan, S., Dasgupta, S. and Jothibas, A. *Monitoring of Drought using Remote Sensing Data in Uppar Odai, Sub-basin, Tamil Nadu, India*. International Journal of Earth Sciences and Engineering. 2014. 7 (03) 930-937.
- Anderson, M.C., Norman, J.M., Kustas, W.P., Houborg, R., Starks, P.J., and Agam, N. *A Thermal-Based Remote Sensing Technique for Routine Mapping of Land-Surface Carbon, Water and Energy Fluxes from Field to Regional Scales*. Remote Sensing of Environment, Elsevier. 2008. 112; 4227-4241.
- Balamurugan, G., Anbazhagan, S., Biswal, T.K., and Kushma, K.N., 2009: *Surface Temperature mapping using ETM TIR images in Parts of Precambrian Terrain, India*. Developments in Exploration Geology and Geoinformatics, Macmillan, New Delhi. 237-244.
- Chander, G., and Markham, B. *Revised Landsat-5 TM Radiometric Calibration Procedures and Post Calibration Dynamic Ranges*. IEEE Transactions on Geoscience and Remote Sensing. 2003. 41 (11) 2674-2677.
- Chander, G., Markham, B.L., and Helder, L.D. *Summary of Current Radiometric Calibration Coefficients for Landsat MSS, TM, ETM+, and EO-1 ALI Sensors*. Remote Sensing of Environment. 2009. 113; 893-903.
- Goetz, S.J. *Multi-Sensor Analysis of NDVI, Surface Temperature and Biophysical Variables at a Mixed Grassland Site*. International Journal of Remote Sensing. 1997. 18 (1) 71-94.
- Gupta, R.P., 2005: *Remote Sensing Geology*. Second Edition. Springer International Edition. 627.

Holm A.M., Burnside, D.G., and Mitchell, A.A. *The Development of a System for Monitoring Trend in Range Condition in the Arid Shrub Lands of Western Australia*. Australian Range Land Journal. 1987. 9 (1) 14-20.

IMD Cumulative Report, 2014: *India Meteorological Department, Meteorological Observatory Report on 1998-2014*.

Sandholt, I., Rasmussen, K., and Andersen, J. *A Simple Interpretation of the Surface Temperature and Vegetation Index Space for Assessment of Surface Moisture Status*. Remote Sensing of Environment. 2002. 79; 213-224.

Kim, H.M., Kim, B.K., and You, K.S. *A Statistic Correlation Analysis Algorithm between Land Surface Temperature and Vegetation Index*, International Journal of Information Processing Systems, 2005. 1 (1) 102-106.

Li, Z.L, Tang, B.H., Wu, H., Ren, H., Yan, G., Wan, Z., Trigo, I.F., and Sobrino, J.A. *Satellite-Derived Land Surface Temperature: Current Status and Perspectives*. Remote Sensing of Environment. 2013. 131; 14-37.

Lillsand, T.M., Kiefer, R.W., and Chipman, J.W., 2009: *Remote Sensing and Image Interpretation*. 5th edition. New York: John Wiley and Sons, Inc. 753.

NASA, 2011: *Landsat 7 Science Data Users Handbook*. Landsat Project Science Office at NASA Goddard Space Flight Centre, Greenbelt, 186 (<http://landsathandbook.gsfc.nasa.gov>)

Orhan, O., Ekercin, S., and Filiz Dadaser-Celik. *Use of Landsat Land Surface Temperature and Vegetation Indices for Monitoring Drought in the Salt Lake Basin Area, Turkey*. The Scientific World Journal. 2014. 1-11.

Pettorelli, N., Vik, J.O., Mysterud, A., Jean-Michel Gaillard, Compton J. Tucker and Nils Chr. Stenseth. *Using the Satellite-Derived NDVI to Assess Ecological Responses to Environmental Change*. Trends in Ecology and Evolution. 2005. 20 (9) 503-510.

Shah, D.B., Pandya, M.R., Trivedi, H.J., and Jani, A.R. *Estimating Minimum and Maximum Air Temperature Using MODIS Data Over Indo-Gangetic Plain*. Journal of Earth System Science Indian Academy of Sciences. 2013. 122 (6) 1593-1605.

Sheela A.M., Letha J., Sabu Joseph, Ramachandran K.K., and Sanalkumar S.P. *Trophic State Index of a Lake System Using IRS (P6-LISS III) Satellite Imagery*. Environ Monitor Assess. 2011. (177) 575-592.

Srivastava, P.K., Majumdar, T.J., and Bhattacharya, A.K. *Study of Land Surface Temperature and Spectral Emissivity using Multi-Sensor Satellite Data*. Journal of Earth System Science. 2010. 119 (1) 67-74.

Valor, E., and Caselles, V. *Mapping Land Surface Emissivity from NDVI: Application to European, African, and South American Areas*. Remote Sensing of Environment. 1996. 57; 167-184.

Weng, Q., Lu, D., and Schubring, J. *Estimation of Land Surface Temperature–Vegetation Abundance Relationship for Urban Heat Island Studies*. Remote Sensing of Environment. 2004. 89; 467-483.

Study of Groundwater Quality using GIS in Hirehalla Sub-basin of Koppal District, Karnataka, India

Sreenivasa A. and Ajay Kumar N. Asode

Department of Studies in Geology, Karnatak University, Dharwad, Karnataka, India

Publication Date: 12 April 2016

Article Link: <http://scientific.cloud-journals.com/index.php/IJAESE/article/view/Sci-419>



Copyright © 2016 Sreenivasa A. and Ajay Kumar N. Asode. This is an open access article distributed under the **Creative Commons Attribution License**, which permits unrestricted use, distribution, and reproduction in any medium, provided the original work is properly cited.

Abstract Water quality problems were reported in the groundwaters of Hirehalla Sub-basin, Koppal district, Karnataka, India. 21 representative samples were collected and subjected to hydrochemical investigations. Major cations- Ca, Mg, Na, K and anions- CO₃, HCO₃, Cl, SO₄ were analysed. Physical parameters such as pH, EC, TDS, H were also determined. Piper hill trilinear diagram were plotted to study the hydrochemical characters of groundwater and it was found the groundwater to be of class- NaCl and CaMgCl type. Fluoride ion concentration was found to be in the range 0.26 to 6.42 mg/lit. Based on EC values it was found that 61% of water samples fall in excellent category. Drinking use suitability was determined by comparing the analysis results of water samples with BIS and WHO standards and it was found that 65% of the water samples are safe and fit for drinking purposes. Parameters like SAR and Na% were calculated to evaluate the suitability of waters for irrigational purposes. USSL and Wilcox diagram were plotted to determine agriculture suitability. It was found that 90% of the water samples are fit for irrigation. Different spatial variation maps were generated in GIS environs. Thus GIS based approach was efficient tool in assessment of water quality of Hirehalla Sub-basin.

Keywords Hirehalla Sub-Basin; Hydrogeochemistry; Water Quality; Fluoride; SAR; GIS

1. Introduction

The quality of water is one of the major concern and problem of almost all nations of the world. Not all of the available water resources on the globe can be used directly for drinking, agriculture and industrial purposes. While of the available limited direct resources many have the problem of water quality some are due to natural processes (geogenic) and others due to anthropogenic activities. Thus making mankind to explore other source of water such as groundwater to fulfil and meet his demand for different purposes.

In this quest of finding water resources, suitable groundwater potential sites are being located and explored. Due to this over-exploitation the water table levels are slowly lingering deeper and deeper. And with the irregular trend of monsoons and no other source of recharge the groundwaters are depleting at faster rates.

The quality of water resources is governed by many factors such as climate, topography, soil characters, sub-surface litho-units, groundwater flow, anthropogenic activities (Rajesh et al., 2002; Lakshmanan et al., 2003; Srivastava, 2005; Das Brijraj and Kaur, 2007; Cloutier et al., 2008; Prasanna et al., 2010). The study area in particular being a typical hard rock terrain of Peninsular India consisting predominantly granites and gneiss here it is mainly controlled by factors such as weathering and its features and impact of anthropogenic activities.

Many researchers and scientists from different parts of the world have studied the water quality in different geologic regimes with both conventional methods and GIS approach (Sreedevi, 2002; Anbazhagan and Archana, 2003; Subbarao and John Devdas, 2003; Subbarao, 2006; Subramani et al., 2010).

Thus in the present study an attempt has been made to assess the water quality of Hirehalla Sub-basin with the help of GIS. Further suggest the respective authorities for proper planning, management and development of groundwater resources.

2. Study Area

The present study area Hirehalla Sub-basin of Koppal district, Karnataka, India is geographically located between $15^{\circ}23'$ to $15^{\circ}32'$ N latitude and $75^{\circ}45'$ to $76^{\circ}07'$ E longitude and is covered in Survey of India (SOI) toposheets numbered 48M/14, 48M/15 and 57A/03 and spread over an area of 389 km². It is a tributary of Tungabhadra River.

Physiographically major portion is covered by plains with shallow troughs and mounds at some places. The highest and lowest elevations are 625 and 552 meters respectively. The major rock types include granitic gneiss and schist. These rocks are highly weathered and the resulting fractures, joints act as conduit for storage of water. The waters are found to be in phreatic conditions. The study area experiences semi-arid type of climate which is characterized by hot summer where maximum temperature reaches upto 45°C in the month of April and May while coolest month is December and January where temperature drops upto 16°C (Figure 1).

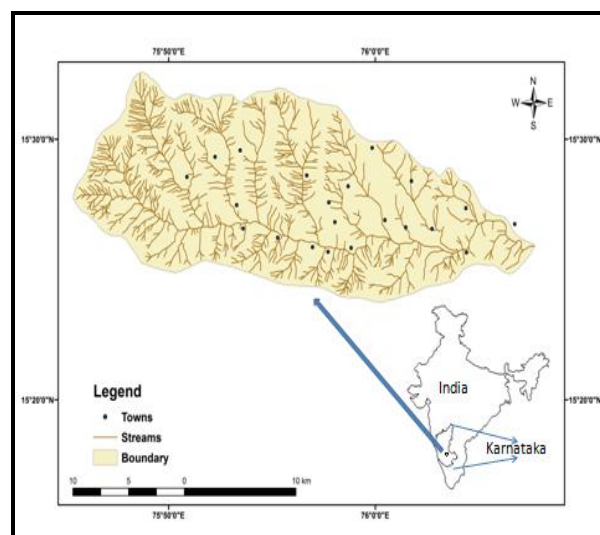


Figure 1: Location Map of Hirehalla Sub-basin

3. Materials and Methods

Water samples were collected in one litre polyethylene cans which were pre-rinsed and washed in the laboratory using proportionate distilled water and dil. HCl and later in the field it was washed using representative sample. Standard procedure of analysis was followed that of APHA (APHA, 1995). Table 1 depicts the list of parameters the samples were subjected for analysis and the methodology/instrument applied for same. Table 2 shows the results obtained after physico-chemical analyses. All the thematic and variation maps were generated in GIS environ using different tools of arcGIS v10 such as spatial analyst, interpolation.

Table 1: List of Physico-Chemical Parameters and Analytical Methods

Sl. No.	Parameters	Analytical Methods/Instruments
1	pH	Elico LI120
2	Electrical Conductivity (EC)	Elico CM180
3	Total Dissolved Solids (TDS)	EC*0.65 (Todd 1980)
4	Hardness (H)	Trimetric
5	Calcium (Ca)	Trimetric
6	Magnesium (Mg)	Calculation
7	Sodium (Na)	Atomic Absorption Spectrophotometer (AAS)
8	Potassium (K)	Atomic Absorption Spectrophotometer (AAS)
9	Carbonate (CO ₃)	Trimetric
10	Bicarbonate (HCO ₃)	Trimetric
11	Chloride (Cl)	Trimetric
12	Sulphate (SO ₄)	Colorimeter
13	Fluoride (F)	Ion Selective Method

Table 2: Physico-Chemical Analyses Results

Sl No	LOCATION	TDS	EC	H	pH	Ca	Mg	Na	K	CO ₃	HCO ₃	Cl	SO ₄	F
1	HIREHANCIHALLA	320	490.61	120	7.9	24.04	14.61	109.53	2.19	0	180	63.9	60	1.1
2	BINNALA	2860	443.41	1752	8.11	352.7	212.46	415.72	1.86	0	250	1356.1	710	0.69
3	CHIKENAKOPPA	3030	460.97	2128	7.58	432.86	255.34	494.96	1.77	0	225	2157.3	380	0.26
4	SHIDNEKOPPA	1920	297.67	1260	7.5	192.38	190.04	476.21	15	0	365	1262.6	700	0.43
5	SOMPUR	7840	124.8	3220	7.16	838.47	274.83	845	2.38	0	350	3494	380	0.35
6	MALEKOPPA	5370	102.32	2640	7.28	585.16	287.5	820	1.94	0	325	3061.2	380	0.36
7	MANNAPUR	2090	324.03	1060	7.49	157.11	162.75	656.7	7.87	0	375	1704.22	560	1.98
8	LINGAPUR	1620	251.16	680	7.61	128.25	87.71	421.15	7.51	0	280	681.6	550	2.29
9	LINGAPUR	1180	182.94	404	7.93	64.12	59.44	392.54	6.5	0	320	731.3	430	2.33
10	ITAGI	1100	170.54	720	7.64	128.25	97.45	179.57	7.88	0	300	546.7	450	0.44
11	MANDALGERI	1380	213.95	1260	7.55	264.52	146.18	226.18	9.25	0	205	1072.1	600	0.51
12	BETAPANAHALLI	5570	863.56	2440	7.6	689.37	175.42	746	9.01	0	355	2350	380	0.47
13	GORLEKOPPA	620	960.12	320	7.77	40.08	53.6	196.04	5.31	0	360	79.52	170	1.89
14	KUKNUR	1150	178.29	940	7.29	272.54	63.34	134.39	5.2	0	275	809.4	268	0.44
15	GAVARHALLA	600	930.02	300	7.83	64.12	64.11	155.92	2.36	0	265	191.7	70	0.59
16	CHENDURU	1390	215.5	960	7.32	173.14	128.64	301.37	5.15	0	460	898.86	275	1.08
17	VIRAPUR	970	150.38	212	7.83	48.09	22.41	383.66	2	0	525	156.2	312	6.42
18	MUDLAPUR	370	570.36	100	8.2	19.23	12.66	151.2	1.59	0	210	107.92	80	2.02
19	BENAKAL	2100	325.58	200	8.28	40.08	24.36	651.03	2.21	0	775	866.2	350	5.94
20	NITALLI	2350	364.34	1760	7.27	288.57	253.39	434.02	6.21	0	335	1830	600	1.15
21	MOSOBANAHCHINALA	1460	226.35	980	7.3	296.59	58.47	269.3	4.42	0	350	781	400	0.57

4. Results and Discussion

4.1. Water Quality

4.1.1. Electrical Conductivity (EC)

EC value in the study area range from 102 to 960 $\mu\text{S}/\text{cm}$. Water samples are classified based on Sarma et al. (1982) (Table 3) and accordingly it was found that approximately 62% of water samples fall in excellent category followed by 19% each falling in good and permissible category. Figure 2 shows the EC distribution in the study area.

Table 3: EC Classification based on Sarma et al.

Class	EC range in $\mu\text{S}/\text{cm}$	No. of Samples	Percentage
Excellent	0-333	13	61.90
Good	333-500	04	19.04
Permissible	500-1000	04	19.04
Brackish	1000-1500	-	-
Saline	1500-10,000	-	-

4.1.2. Total Dissolved Solids (TDS)

TDS can be defined as the different types of mineral present in water in the dissolved state. To ascertain the suitability of groundwater for any purpose, TDS is an important factor. Thus the waters of the study area were classified based on Freeze and Cherry (1979) (Table 4). It suggests that 76% of the water samples in the Hirehalla Sub-basin are brackish while 24% are fresh waters. Figure 3 shows the distribution of TDS in the study area.

Table 4: Classification of TDS based on Freeze and Cherry

TDS (mg/lit)	Nature of Water	No. of Samples	%
<1000	Fresh	05	23.80
1000-10000	Brackish	16	76.19
10000-100000	Saline	-	-
>100000	Brine	-	-

4.1.3. Hardness (H)

The classification of water samples of Hirehalla Sub-basin based on Sawyer and McCarthy (1967) (Table 5) shows that 85% of the water samples fall in water class hard while 9.52% fall in moderately hard and 4.76% fall in very hard class. Figure 4 shows the distribution of hardness in the study area.

Table 5: Classification of Waters Based on Hardness

Hardness (CaCO_3) in ppm	Water Class	No. of Samples	%
0-75	Soft	-	-
75-150	Moderately Hard	02	9.52
150-3000	Hard	18	85.71
>3000	Very Hard	01	4.76

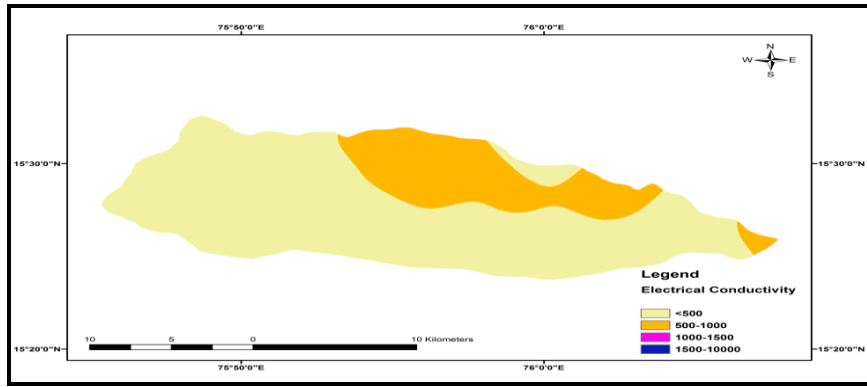


Figure 2: Spatial distribution of Electrical Conductivity (EC)

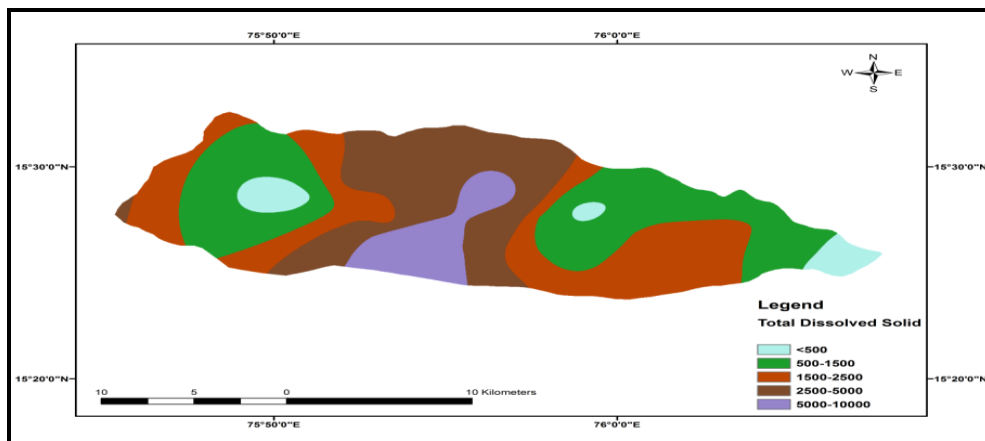


Figure 3: Spatial distribution of Total Dissolved Solids (TDS)

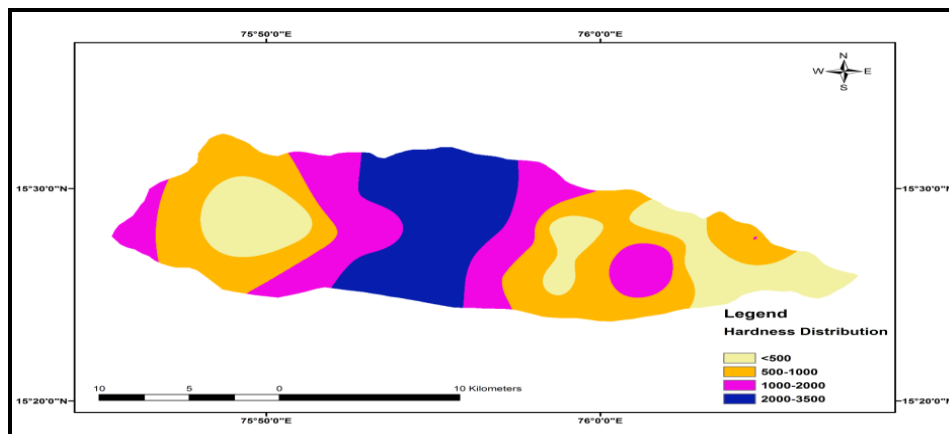


Figure 4: Spatial distribution of Hardness (H)

4.2. Hydrochemical Facies (Piper Hill Tri-linear Diagram)

The chemical processes and the evolution of the groundwater in the aquifer due to prolonged presence and flow may be assessed using the hydrochemical facies. This can be best illustrated and interpreted using Hill Piper plot wherein plot of cations mainly Ca, Mg, Na+K versus anions HCO₃, Cl, SO₄ is plotted. From the plot (Figure 5) it was found that the groundwaters of Hirehalla Sub-basin falls

in field 2 & 4 and are categorized as –NaCl and Mixed CaMgCl type. This indicates strong acid exceeding weak acid and alkali exceeding alkaline.

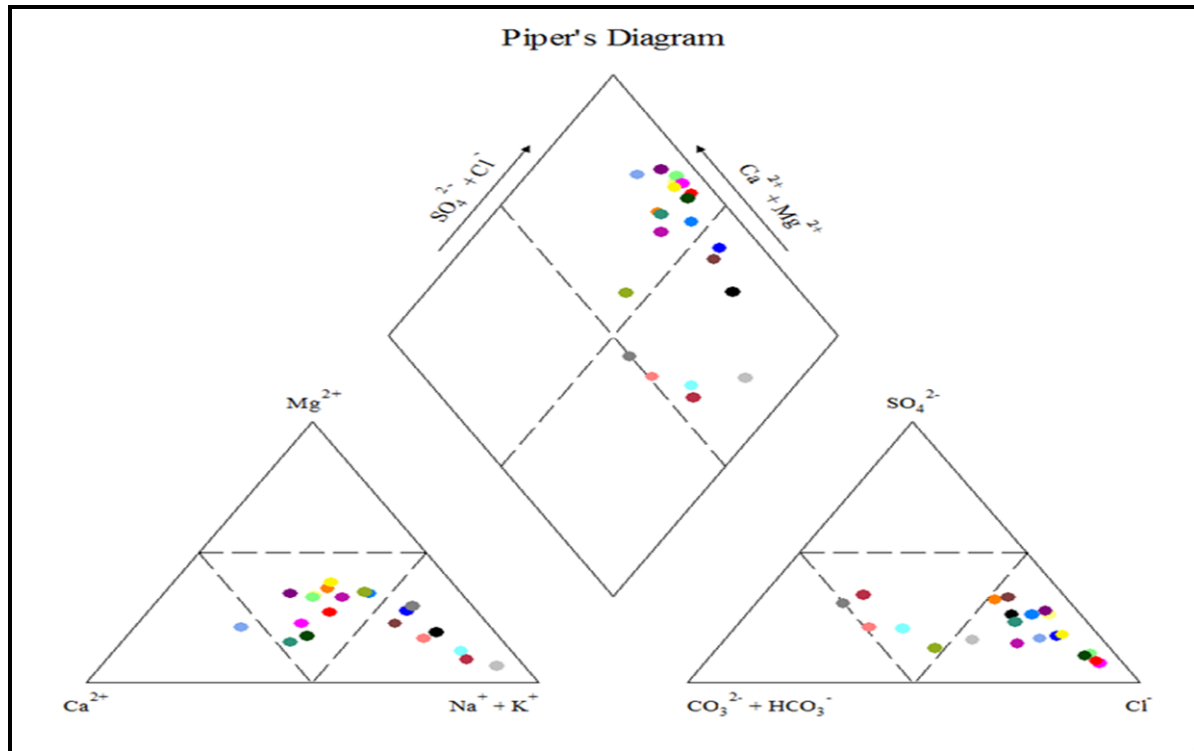


Figure 5: Piper's Diagram for the waters of Hirehalla Sub-basin

4.3. Drinking Quality

Physico-chemical analyses results of the Hirehalla Sub-basin were compared with Bureau of Indian Standards (BIS, 2003) and World Health Organisation (WHO, 2005) to decipher the quality of water for drinking purpose (Table 7). The comparison study revealed that on an average 65% of the water samples for all parameters except TDS fall in allowable limits and is safe for drinking purpose while 76% of the water samples exceed allowable limit based on TDS. Thus there is need to check the water quality and necessitate appropriate actions for supply of safe drinking water.

Table 7: Drinking Water Standards of BIS (2003) and WHO (2005)

Parameters	Drinking Water Standards				Samples exceeding allowable limit	%
	BIS (2003)		WHO (2005)			
	Permissible	Allowable	Permissible	Allowable		
pH	7.0-8.5	6.5-9.2	7-8.5	6.5-9.2	-	-
TDS	NS	NS	500	1000	16	76.19
TH	300	600	-	1000	09	42.85
Ca	75	200	75	200	08	38.09
Mg	50	150	50	150	08	38.09
Cl	250	1000	200	600	09	42.85
SO ₄	200	400	200	400	08	38.09
F	1.0	1.50	-	1.50	07	33.33

4.4. Irrigational Quality

4.4.1. Sodium Absorption Ratio (SAR)

SAR is considered a better measure of sodium/alkali hazard in irrigation as it is directly related to the adsorption of sodium by soil and is an important criterion in determining the suitability of water for irrigation. The SAR is classified as shown in Table 8 and is calculated using:

$$SAR = \frac{Na^+}{(\sqrt{Ca^{2+} + Mg^{2+}})/2}$$

all values are in epm

According to classification (Table 8), it shows that 90% of water samples in the study area fall in excellent category while 5% each fall in good and fair category. Groundwater samples were also plotted in United States Salinity Laboratory diagram (Richard, 1954) to study its suitability for irrigation where plot of SAR vs EC is plotted (Figure 6) and it was found that, 42.85% of water samples fall in field of C1S1, indicating low salinity and low sodium, 23.80% of water samples fall in field of C2S1, indicating medium salinity and low sodium, 14.28% samples falling in field of C3S1, indicating high salinity and low sodium and 9.52% samples falling in field of C2S2, indicating medium salinity and medium sodium. Figure 8 shows the spatial distribution of SAR.

Table 8: Classification based on SAR

Class	SAR Range	No. of Samples	Percentage
Excellent	<10	19	90.47
Good	10-18	01	4.76
Fair	18-26	01	4.76
Poor	>26	-	-

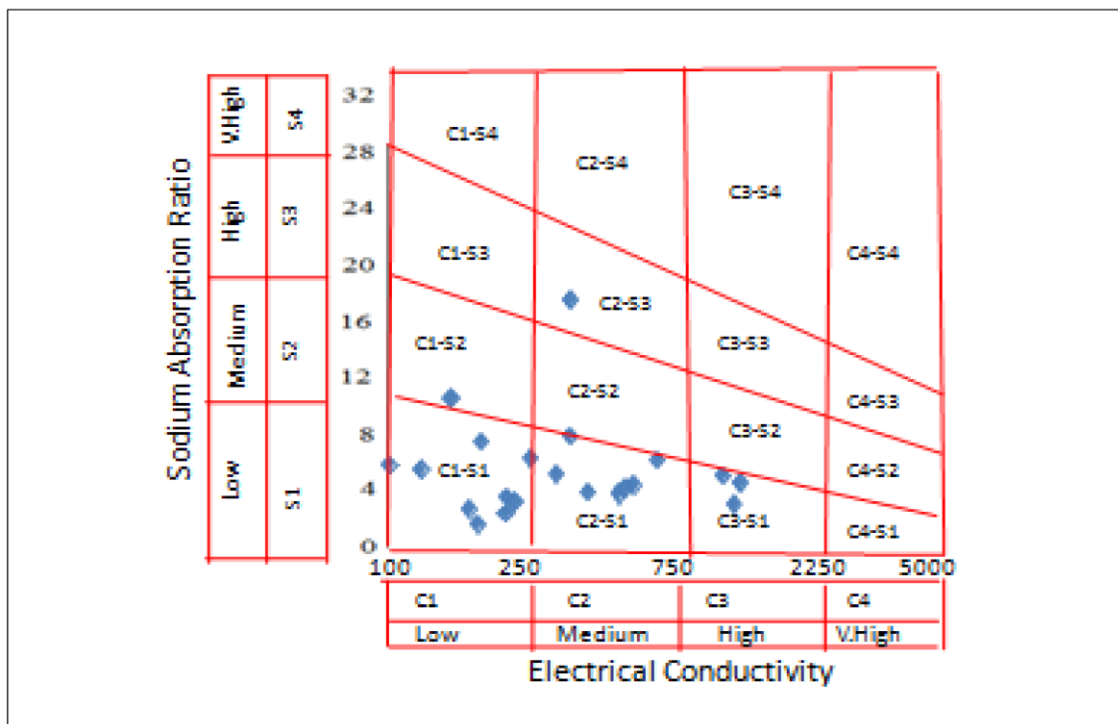


Figure 6: USSS Diagram for Classification of Irrigation Waters, 1950

5.4.2. Sodium Percent (Na%)

The suitability of the groundwater for irrigation depends on the minerals and its interaction present in water and its effect on plants and soil. When the concentration of sodium is high in irrigation water, sodium ions tend to be absorbed by clay particles which reduce soil permeability (Saleh, 1999; Arumugam and Elangovan, 2008). This can be computed using:

$$\%Na = \frac{(Na^+ + K^+) \times 100}{(Ca^{2+} + Mg^{2+} + Na^+ + K^+)}$$

all values are in epm

The classification for irrigation suitability based on sodium percent (Table 9) revealed that 66.66% of water samples from the study area fall in category excellent while 33.33% fall in good category. Similar comparison study to know the suitability of water for irrigation is done by plotting the plot of sodium percent vs EC i.e., Wilcox diagram (Wilcox, 1954) (Figure 7) which indicate 85% of the water samples falling in range excellent to good category and 15% of water samples fall in good to permissible category. Figure 9 shows the spatial distribution of sodium percent.

Table 9: Sodium Percent Classification for Irrigation Water

Class	Na%	No. of Samples	Percentage
Excellent	< 20%	14	66.66
Good	20-40	07	33.33
Permissible	40-60	-	-
Doubtful	60-80	-	-
Unsuitable	>80	-	-

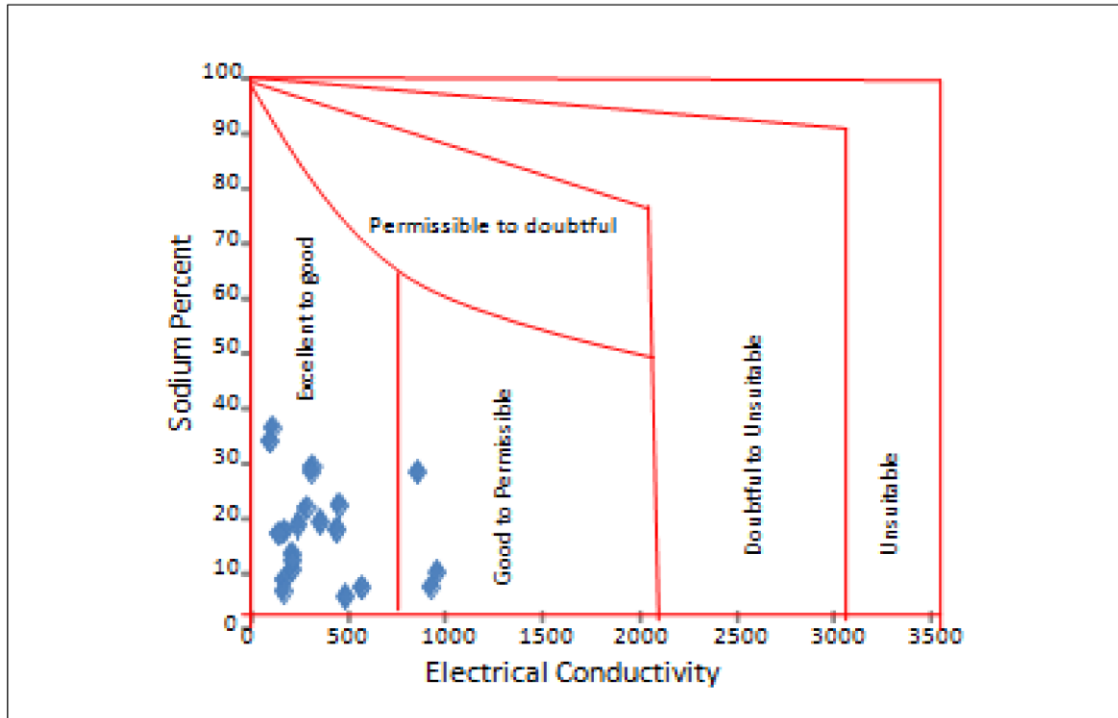


Figure 7: Classification of Irrigated Waters based on Wilcox, 1955

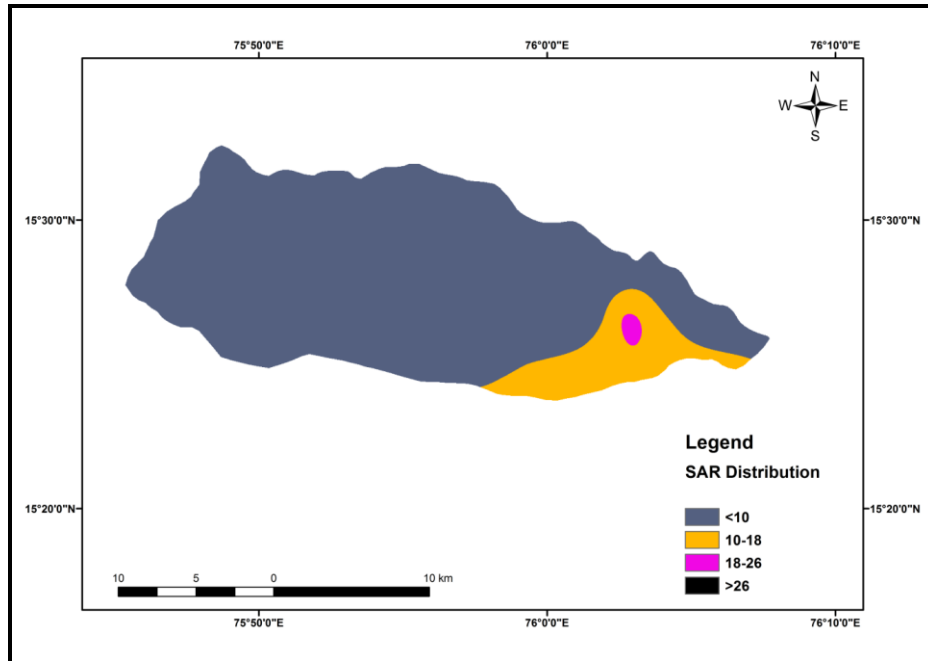


Figure 8: Spatial Distribution of Sodium Absorption Ratio (SAR)

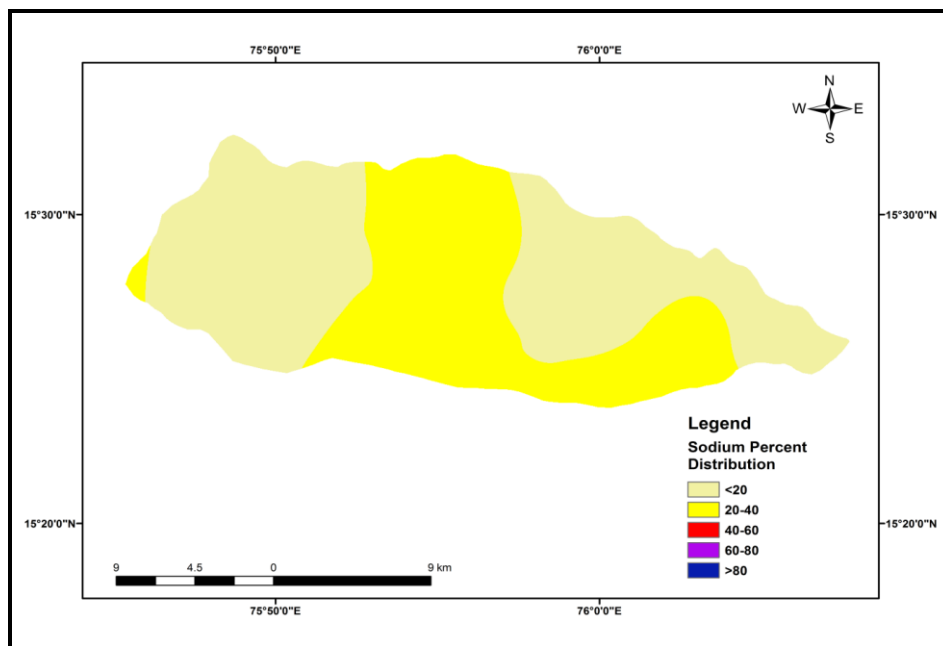


Figure 9: Spatial distribution of Sodium percent

6. Conclusion

GIS based approach has turned out to be very effective and efficient tool in determining the water quality of hard rock Hirehalla Sub-basin, Koppal district, Karnataka where water quality issues has been reported. Physico-chemical analyses result obtained revealed that, based on TDS 76% of the water samples are brackish and 85% hard based on hardness. Comparison of water samples with BIS and WHO standards for suitability for drinking purpose indicated approximately 35% of the water samples having water quality problem with respect to domestic use.

SAR classification for irrigational suitability showed 90% of the water samples in excellent category. Plot of SAR vs EC (USSL diagram) indicated the water samples to be in the field C1S1, C2S1 & C3S1. Based on sodium percent classification for irrigated waters it was found that 66.66% of water samples range in water class excellent and 33.33% in good. Wilcox diagram revealed the water samples to be ranging from excellent to permissible. Fluoride incidence was reported at some places which are due to geogenic processes. Further it is suggested to the authorities to keep a check on the water quality at regular intervals and necessitate actions for providing safe drinking water. Furthermore plan and manage for sustainable development of water resources.

Acknowledgement

The authors thank indepthly Dr. H.M. Jayasheela, Chairman, Dept. of Studies in Geology for providing all the necessary facilities to carry out this work. Thanks are due to the anonymous reviewers for their suggestions to uplift the quality of paper.

References

- American Public Health Association (APHA) 2005: *Standard Method for Examination of Water and Wastewater*. 21st Edn. APHA, AWWA, WPCF, Washington DC, USA.
- Arumugam, K. and Elangovan, K. *Hydrochemical Characteristics and Groundwater Quality Assessment in Tirupur Region, Coimbatore District, Tamil Nadu, India*. Environ Geol. 2008. 58; 1509-1520.
- BIS, 2003: *Drinking Water Specifications*. Bureau of Indian Standards IS: 10500.
- Cloutier Vincent, Lefebvre Rene, Therrien Rene and Savard Martine M. *Multivariate Statistical Analysis of Geochemical Data as Indicative of the Hydrogeochemical Evolution of Groundwater in a Sedimentary Rock Aquifer System*. Journal of Hydrology. 2008. 353; 294-313.
- Das Brijraj, K. and Kaur, P. *Geochemistry of Surface and Subsurface Waters of Rewalsar Lake, Mandi District, Himachal Pradesh: Constraints on Weathering and Erosion*. Journal Geological Society of India. 2007. 69 (5) 1020-1030.
- Eaton, EM. *Significance of Carbonate in Irrigation Water*. Soil Sci. 1950. 69; 123-133.
- Lakshmanan, E., Kannan, R., and Senthil Kumar, M. *Major Ion Chemistry and Identification of Hydrogeochemical Processes of Groundwater in a Part of Kancheepuram District, Tamilnadu, India*. Environmental Geosciences. 2003. 10 (4) 157-166.
- Prasanna, M.V., Chidambaram, S. and Srinivasamoorthy K. *Statistical Analysis of the Hydrogeochemical Evolution of Groundwater in Hard and Sedimentary Aquifers System of Gadilam River Basin, South India*. Jour of King Saud University (Science). 2010. 22; 133-145.
- Ravikumar, P. and Somashekhar, R.K. *Multivariate Analysis to Evaluate Geochemistry of Groundwater in Varahi River Basin of Udupi in Karnataka (India)*. The Ecoscan. 2010. 4 (2&3) 153-162.
- Piper, A.M. *A Geographic Procedure in the Geochemical Interpretation of Water Analysis*. Trans. Am. Geophysics Union. 1994. 25; 914-928.

Ragunath, H.M., 1987: Groundwater. Wiley Eastern, New Delhi. 563.

Rajesh Reghunath, Sreedhara Murthy, T.R., and Raghavan, B.R. *The Utility of Multivariate Statistical Techniques in Hydrogeochemical Studies: An Example from Karnataka, India*. Water Research. 2002. 36; 2437-2442.

Richard, L.A., 1954: *Diagnosis and Improvement of Saline Alkali Soils*. US Department of Agriculture, Hand Book. 60; 160.

Anbazhagan S. and Archana M. Nair. *Geographic Information System and Groundwater Quality Mapping in Panvel Basin, Maharashtra, India*. Environmental Geology. 2004. 45 (6) 753-761.

Saleh, A., Al-Ruwaih, F., and Shehata, M. *Hydrogeochemical Processes Operating within the Main Aquifers of Kuwait*. J Arid Environ. 1999. 42; 195-209.

Sarma, V.V.J., Prasad, N.V.B.S.S., and Rajendra Prasad, P. *The Geochemistry of Groundwater along Visakhapanam-Bhimilipatnam Coast with Regard to their Utility to Drinking Domestic and Irrigation Purposes*. Jour. Asso. Explo. Geophy. 1982. 2; 51-63.

Sreedevi, P.D., 2002: *A Case Study on Changes in Quality of Groundwater with Seasonal Fluctuations of Pageru River Basin, Cuddapah District, Andhra Pradesh, India*.

Srinivasa Rao, Y., Reddy, T.V.K., and Nayudu, P.T. *Groundwater Quality in the Niva River Basin, Chittoor District, Andhra Pradesh, India*. Environmental Geology. 1997. 32 (1) 56-63.

Srivastava Ajay. *Aquifer Geometry, Basement-Topography and Groundwater Quality around Ken Graben, India*. Journal of Spatial Hydrology. 2005. 2 (2) 1-7.

Subba Rao, N. and John Devadas, D. *Fluoride Incidence in Groundwater in an Area of Peninsular India*. Environ. Geol. 2003. 45; 243-251.

Subba Rao, N. *Seasonal Variation of Groundwater Quality in a Part of Guntur District, Andhra Pradesh, India*. Environ Geol. 2006. 49; 413-429.

Subramani, T., Rajmohan, N., and Elango, L. *Groundwater Geochemistry and Identification of Hydrogeochemical Processes in a Hard Rock Region, Southern India*. Environmental Monitoring and Assessment. 2010. 162; 123-137.

WHO, 2005: International Standards for Drinking Water, 3rd ed., Geneva. 2005.

Wilcox, L.V., 1955: *Classification and Use of Irrigation Waters*. USDA, Circular 969, Washington, DC, USA.

Water Quality Assessment in and Around Sandur Taluk, Bellary District, South India

B.V. Suresh Kumar, R.K. Sunil Kumar and K.N. Prakash Narasimha

Department of Studies in Earth Science, University of Mysore, Manasagangotri, Mysore, Karnataka, India

Publication Date: 15 March 2016

Article Link: <http://scientific.cloud-journals.com/index.php/IJAESE/article/view/Sci-420>



Copyright © 2016 B.V. Suresh Kumar, R.K. Sunil Kumar and K.N. Prakash Narasimha. This is an open access article distributed under the **Creative Commons Attribution License**, which permits unrestricted use, distribution, and reproduction in any medium, provided the original work is properly cited.

Abstract Assessment of surface and groundwater quality has been carried out in the parts of the Sandur taluk, Bellary district, Karnataka, South India. Surface and ground water samples collected from different villages in and around Sandur taluk. Sandur taluk is well known for iron ore deposits. At the same time, rigorous and unplanned mining methods causing intensive natural hazards like water pollution, air pollution, noise pollution dust pollution etc. Based on the analysis of these parameters, the villages are classified as safe and unsafe. Results show gradual decreasing of ground water quality and surface water pollution in the study area. GIS interpolation technique performed to represent the concentration parameters in the affected villages of the study area. Northern and central part of the taluk is more affected by mining activity whereas south eastern part of the taluk is well thought-out to be safe. Standard samples the following parameters analyzed as follows pH, Total Hardness (TH), Fluoride (F), Sulphate (SO₄), Nitrate (NO₃), Potassium (K), Magnesium (Mg). The tests carried out for characterization of surface waters and groundwater for the month of August and September 2012, Interpolation technique was performed using ArcMap 9.3.

Keywords *Geographical Information System; Water Analysis; Mining*

1. Introduction

The natural ecosystem of Sandur schist belt environments, in which the Sandur taluk is extremely sensitive to human interference. Open pits, mining dumps and tailing dams are a severe degradation of the environment. Due to the specific climatic and topographic conditions in environment, nature's self-healing capabilities are considerably reduced. Groundwater is the principal source of drinking water in our country and indispensable source of our life (Bajpayee et al., 2012). It is well known that no straight forward reasons can be advanced for the deterioration of water quality, as it is dependent on several water quality constituents (Jothi Venkatachalam et al., 2010; Bajpayee et al., 2012).

The quality of water resources is a subject of ongoing concern. The assessment of long-term water quality changes is also a challenging problem (Biswajeet Pradhan and Saied Pirasteh, 2011). The water required for domestic consumption should possess a high degree of purity and it should be free from suspended and dissolved impurities. The ground water account for nearly 100% of drinking

water supply. It has become an important water resource due to increasing trend of pollution in surface water (Alexander, 2008; Alexander et al., 2011).

According to Central Pollution Control Board, 90% of the water supplied in India to the town and cities in India are polluted, out of which only 1.6% gets treated. Therefore, water quality management is fundamental for the human welfare (Gupta, 1991; Navneet Kumar and Sinh D.K., 2010).

The groundwater is believed to be comparatively much clean and free from pollution than surface water. But prolonged discharge of industrial effluents, domestic sewage and solid waste dump causes the groundwater to become polluted and created health problems (Patil and Patil, 2010).

The Sandur Taluk mining activity has reached up to a depth of more than 500 feet and reached groundwater table. Hazardous chemicals which are used for the blasting purpose (Ammonium Nitrate) can directly interfere with ground water. Mitigative measures needed to be over take seriously in this location. Though the agricultural activity is dominates in Sandur Taluk rapid mining activity decreases agricultural production.

1.1. Study Area

The study area of Sandur taluk as shown in the Figure 1(a, b) is bounded by geo-coordinates 15°00' to 15°15' latitude and 76°15' to 77°00' Longitude within the Dharwar craton. The area fall under 57A/8, 57A/12, 57A/16 and 57B/9 topographical maps. The lowest elevation is 625m above the MSL and the highest elevation is 997m above the MSL. It covers an area of 1224.91 sq km. Hill ranges are cone shaped amphitheater formation and it is covered by dense vegetation.

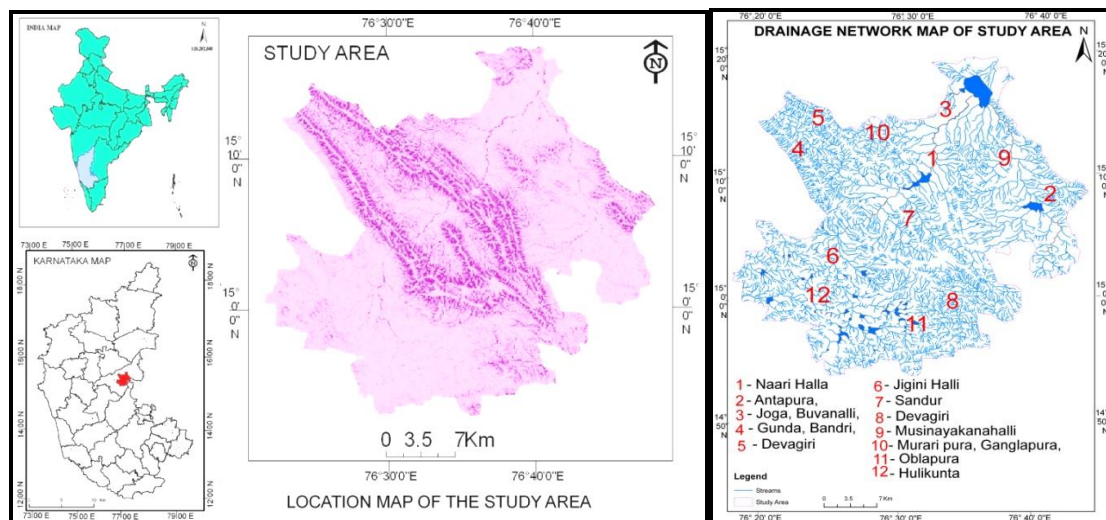


Figure 1a: Location Map of the Study Area; **Figure 1b:** Drainage and Village Location Map

2. Methodology

2.1. Standard Samples

The various parameters analyzed are as follows: pH, Total Hardness (TH), Fluoride (F), Sulphate (SO₄), Nitrate (NO₃), Potassium (K), Magnesium (Mg) as shown in the Table 1. The tests are carried out in the laboratories for characterization of surface waters and groundwater for the month of August and September 2012,

Interpolation technique was performed using ArcMap 9.3. Generation of maps done by attributing the values to the software.

3. Results and Discussion

Analysis of field samples carried out and results shows north, north-eastern part of the Sandur taluk is unsafe due to pollution. Southern part of the taluk is less affected by the mining activity. Central part of the taluk is highly affected area Interpolation technique was performed to show spatial distribution of pollutants within the Sandur taluk as shown in the Figure 2.

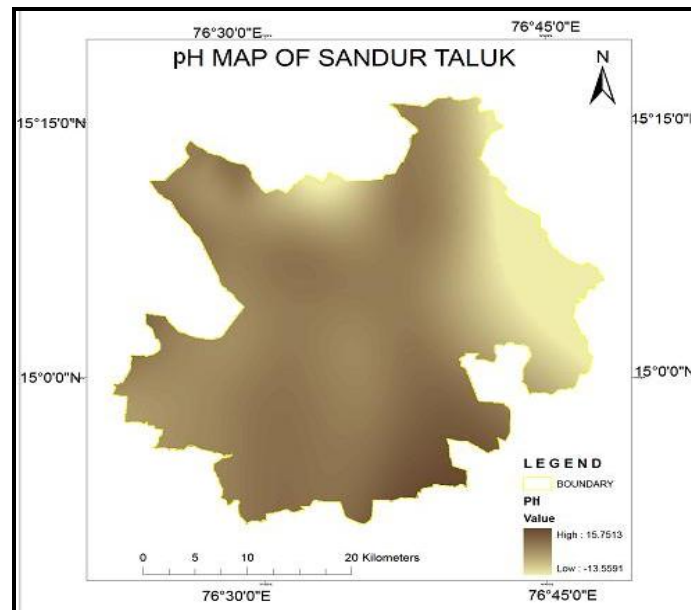


Figure 2: Map Showing Concentration of pH in the Sandur Taluk

As shown in Figure 2, Jaisigpur, Emmihatti, Siddapur, Rajapur, Radhanagar and Dhanapur of North, Sandur, Bhujanganagar, Dowlatpur, Susheel Nagar, Ramanmalai and Dharmapur of central and Devagiri, Swamyhalli south western parts of the taluk are showing high concentration in pH (Figure 2). It is because of the toxic chemicals used for mine blasting process. Central parts of the Taluk, mining activity is more, whereas north-eastern parts are literally thought out to be safe, less affected by mining activity.

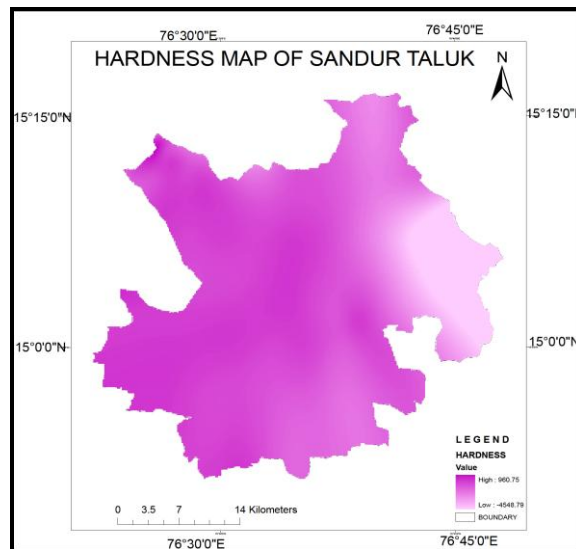


Figure 3: Map Showing Concentration of Water Hardness in the Sandur Taluk

Similarly, the hardness of the water is more in villages of Jaisingpur, Rajapur, Radhanagar and Emminahatti of North, and Sandur, Bhujanganagar, Dowlatpur, Susheel Nagar, Ramanmalai and Dharmapur of central, Devagiri, Swamyhalli, and Agrahara of South-western parts of the taluk as depicted in the Figure 3. More number of salts was induced by the mining activity to the ground water, which results in the high hardness.

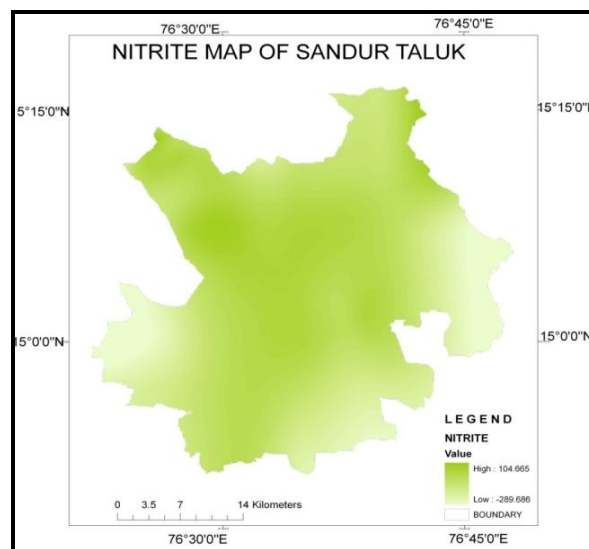


Figure 4: Map Showing Concentration of Nitrite in the Sandur Taluk

Figure 4, shows the nitrite distribution in the study area. As it indicates in the villages of Jaisingpur, Emmihatti, Sddapura, Rajapura, Radhanagar and Danapuram of North, Joga, Buvanahalli, Vaddu, Nagalapura, Muraripura and Gangalapura of North-eastern parts of the taluk and Sandur, Bhujanganagar, Dowlatpur, Shusheel nagar, Ramanmalai, Krishna Nagar and Dharmapura of central parts of the taluk are showing high concentration nitrite, because of the toxic chemicals like ammonium nitrite used for mine blasting process which directly contaminates ground water. Central parts of the taluk mining activity are more whereas northeastern parts are literally safe and less affected by mining activity.

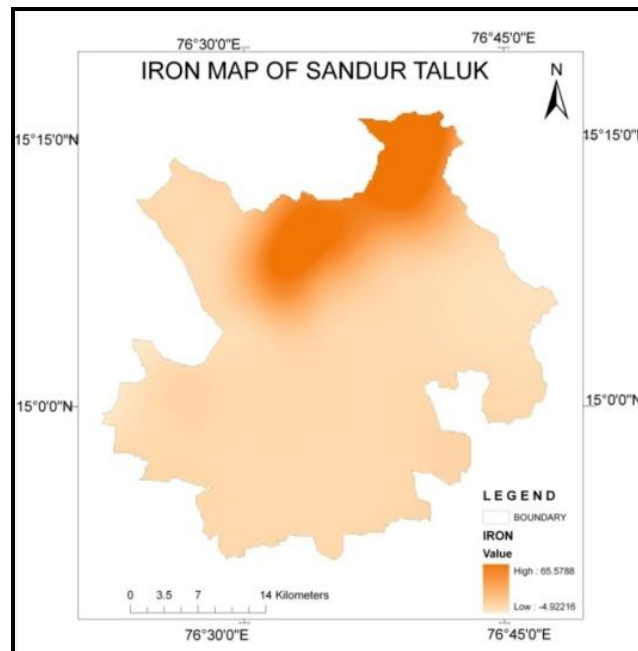


Figure 5: Map Showing Concentration of Iron in the Sandur Taluk

Even though the mining activity is more in central part of the taluk and because of the gradient towards villages of Joga, Buvanahalli, Vaddu, Nagalapura, Muraripura, and Gangalapura at North eastern part, the accumulation of the iron ore with runoff more as shown in Figure 5. This accumulated water with iron percolates deep in the ground and contaminates the ground water. The rest of the area is comparatively less affected.

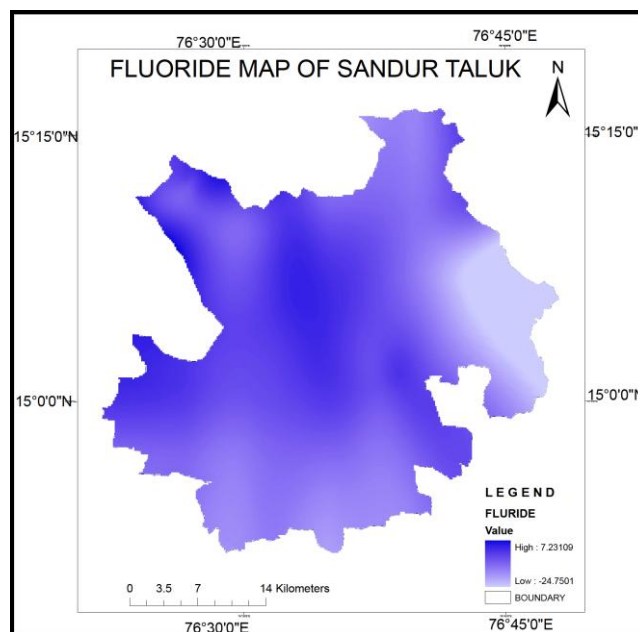


Figure 6: Map Showing Concentration of Fluoride in the Sandur Taluk

As shown in the Figure 6, the fluoride content is distributed in parts of Jaisingpur, Rajapur, Sandur, Bandri, B. Gollarahatti, Devagiri, Bommaghatta, Somalapura, Jambainatti, Toranagal and Siddanahalli. These villages spans in the north, Jiginihalli, Nidugurthi, Hulikunta, Chickerehalli of

western and Devagiri, Swamyhalli, Agrahara, Obalapura and Devarabudenahalli of southern parts of the Sandur taluk, which is unsafe.

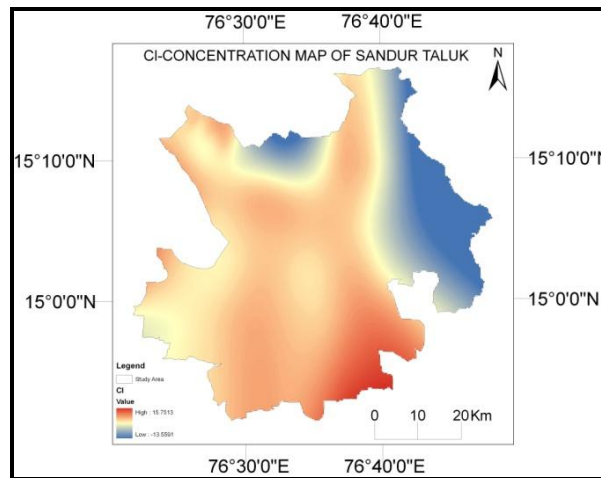


Figure 7: Map Showing Concentration of Chlorine in the Sandur Taluk

Figure 7, Describes the Chlorine content is distributed in parts of Jaisingpur, Rajapur, Sandur, Bandri, B. Gollarahatti, Devagiri, Bommaghatta, Somalapura, Jambainatti, Toranagal and Siddanahalli These villages spans in the north, and Devagiri, Swamyhalli, Agrahara, Obalapura and Devarabudenahalli of southern parts of the Sandur taluk.

Table 1: Analysis Report of the Villages in and Around Sandur Taluk

Sl. No.	Village Name	Location	Latitude	Longitude	pH	TDS	CI	F	NO ₃	Fe	Turbidity	Hardness	Remarks
1	Bommagatta	Hand Pump Near High school	14 ⁰ 59' 37.49	76 ⁰ 31' 21.8	7.9 8	300 0	298	1.5 5	50	0.2 0	10	620	Un safe
2	Jaisingpur	Hand Pump near field side	15 ⁰ 56' 11.8	76 ⁰ 34' 19.7	7.8 0	190 0	230	2.0 0	40	0.2 0	10	280	Un safe
3	Rajapur	Hand Pump Gowripura Road	15 ⁰ 55' 7.28	76 ⁰ 34' 34.0	7.5 0	130 0	190	1.6 0	30	0.2 0	10	160	Un safe
4	Bommagatta	Open well water Near Ag field	14 ⁰ 59' 41.2	76 ⁰ 30' 27.1	7.8 4	300 0	315	1.5 8	60	0.3 0	10	600	Un safe
5	Gollarahatti	Pond near Ag field	14 ⁰ 58' 9.11	76 ⁰ 34' 8.28	7.9 7	150 0	185	1.6 0	30	0.3 0	10	230	Un safe
6	Bandri	Hand Pump Giddi gurthu road side	14 ⁰ 59' 20.4	76 ⁰ 27' 10.8	7.0 0	102 0	98	1.5 1	25	0.2 0	10	200	Un safe
7	B. Gollarahatti	Hand Pump Karigunur chitappana house	14 ⁰ 59' 89.2	76 ⁰ 29' 20.2	7.5 0	100 0	96	1.5 1	25	0.5 0	10	310	Un safe
8	Kodihalli	Hand Pump near Durgamma temple	14 ⁰ 59' 07.2	76 ⁰ 27' 50.8	7.9 0	220 0	250	2.0 0	45	0.3 0	10	300	Safe
9	Swamyhalli	Hand pump near camp road	14 ⁰ 58' 31.4	76 ⁰ 36' 58.2	7.0 0	120 3	117	1.0 0	25	0.5 0	10	231	Safe
10	Chornur	Hand Pump Near kere	14 ⁰ 58' 44.6	76 ⁰ 31' 59.7	7.0 0	120 0	115	0.5 0	25	0.5 0	10	219	Safe
11	Chornur	Hand pump Near Bus stand	14 ⁰ 58' 46.5	76 ⁰ 32' 0.51	7.4 0	130 0	89	1.5 0	30	0.4 0	10	247	Safe
12	Hale vaddinakatti	Open well in village	14 ⁰ 55' 1.22	76 ⁰ 31' 0.42	6.8 0	123 0	113	1.5 0	60	0.3 0	10	290	Safe

13	Somalapur	Kudligi road side	14 ⁰ 54' 8.31	76 ⁰ 31' 0.07	8.5 0	120 0	210	2.0 0	25	0.4 0	10	250	Un safe
14	Swamyhalli	Hand Pump Key pumpu	14 ⁰ 58' 41.0	76 ⁰ 36' 51.3	8.0 0	800	78	1.0 0	40	0.2 0	10	150	Safe
15	Tumbaragud di	Kempa kere (Tank)	14 ⁰ 57' 20.5	76 ⁰ 34' 31.2	8.0 0	100 0	87	1.0 0	30	0.3 0	10	190	Safe
16	Siddanahalli	Open well near Hand Pump	14 ⁰ 55' 10.3	76 31 034	7.6 8	240 0	268	1.2 0	45	0.3 0	10	400	Safe
17	Hale vaddinakatti	Well in village	14 ⁰ 55' 28.0	76 ⁰ 31' 0.42	7.8 9	150 0	185	0.8 0	25	0.3 0	10	220	Safe
18	Vaderahalli	Open well near Tank	14 ⁰ 55' 31.4	76 ⁰ 30' 6.39	7.0 0	140 0	171	1.4 0	30	0.3 0	8	250	Safe
19	Devagiri	Hand Pump Kumarswami temple	15 ⁰ 00' 54.8	76 ⁰ 33' 29.4	8.0 0	800	411	1.0 0	40	0.2 0	10	150	Un safe
20	Devagiri	well near sahu kar marena land	15 ⁰ 06' 19.3	76 ⁰ 54' 9.20	8.5 0	140 0	130	1.5 0	30	0.2 0	10	220	Un safe
21	Jambainatti	mwss honakere road	15 ⁰ 06' 21.0	76 ⁰ 54' 14.9	7.5 0	170 0	316	2.0 0	40	0.3 0	10	295	Un safe
22	Kalingeri	Hand Pump in front of Govt. school	14 ⁰ 56' 15.5	76 ⁰ 31' 23.7	7.5 0	190 0	252	2.5 0	40	0.3 0	10	300	Un safe
23	Yeshwanthn agar	Hand Pump near hatti	14 ⁰ 56' 33.1	76 ⁰ 30' 20'4	7.5 0	200 0	319	2.5 0	40	0.3 0	10	360	Un safe
24	Sandur	Hand Pump near theater	15 ⁰ 05' 10.10	76 ⁰ 32'35.06	7.1 0	920	93	2.5 0	25	1.0 0	10	120	Un safe
25	Sandur	Borewell in Agri field	15 ⁰ 04' 45.90	76 ⁰ 32' 40.10	9.0 0	940	95	1.5 0	10	0.3 0	10	120	Un safe

4. Conclusion

Analysis of field samples carried out and results shows north, western, central and southern part of the Sandur taluk is unsafe due to contamination by unplanned mining activity. Sandur taluk environment facing severe problems such as water, air, dust and noise pollution. Agricultural crop yield gradually declined. Eastern part of that is less affected by the mining activity. Central part of the taluk is highly affected area. Village wise details of pH, TDS, Cl, F, NO₃, Fe, Turbidity and hardness were analyzed. The surface and ground water shows concentration of pH, Nitrite, Fluoride, Chlorine, Fe and Hardness of Water in the villages of Jaisingpur, Emmihatti, Sddapura, Rajapura, Radhanagar and Danapuram of North, Joga, Buvanahalli, Vaddu, Nagalapura, Muraripura and Gangalapura of North-eastern parts of the Taluk. Sandur, Bhujanganagar, Dowlatpur, Shusheel nagar, Ramanmalai, Krishna Nagar and Dharmapura of Central parts and Devagiri, Swamyhalli, Agraphara, Obalapura and Devarabudenahalli of southern parts of the Sandur taluk, because of the toxic chemicals like ammonium nitrite used for mine blasting process which directly contaminates ground water. At central parts of the taluk mining activity is more whereas eastern parts are less affected by mining activity and literally safe. The Narihalla stream flows from central part of the taluk to Naarihalla Dam at Taranagar is entirely polluted by the mining waste and is not suitable for drinking as well as agriculture purposes. Majority of the surface water bodies present around the Sandur, Torangallu and Taranagar are highly contaminated and silted by the mining waste.

Agricultural land is also gradually decreased due to mining activity, but fortunately it maintains the area statistics, because most of the waste lands (scrubland) are converted into agricultural land. The turbidity level increase drastically in surface water bodies due to sedimentation of mine wastes leads to disappearance of surface water bodies. GIS technologies coupled with spatial modeling are useful tools in providing a solution for future water resources planning.

References

- Alexander, P. *Quality Assessment of Groundwater of Mubi Town in Mubi South local Government Area of Adamawa State*. Anachem Journal. 2008. 2 (1) 214-220.
- Alexander, P., Maitera, O.N., and Kawuwa, B. *Quality Assessment of Ground Water in Vimtim Community in Mubi, Adamawa State, Nigeria*. 2011. 3; 34-40.
- Bajpayee, S., Das, R., Ruj, B., Adhikari, K., and Chatterjee, P.K. *Assessment by Multivariate Statistical Analysis of Ground Water Geochemical Data of Bankura, India*. 2012. 3; 870-880.
- Biswajeet Pradhan and Saied Pirasteh. *Hydro-Chemical Analysis of the Ground Water of the Basaltic Catchments: Upper Bhatsai Region, Maharashtra*. 2011. 5; 51-57.
- Gupta, S.C. *Chemical Character of Ground Waters in Nagpur district, Rajasthan*. Indian J. Environ. Hlth. 1991. 33 (3) 341-349.
- Jothi Venkatachalam, K., Nithya, A., and Chandra Mohan, S. *Correlation Analysis of Drinking Water Quality in and Around Perur Block of Coimbatore District, Tamil Nadu, India*. Rasayan Journal Chemistry. 2010. 3 (4) 649-654.
- Navneet Kumar and Sinh D.K. *Drinking Water Quality Management through Correlation Studies among Various Physico-Chemical Parameters: A Case Study*. 2010. 1 (2) 253-259.
- Patil, V.T., and Patil, P.R. *Physicochemical Analysis of Selected Groundwater Samples of Amalner Town in Jalgaon District, Maharashtra, India*. 2010. 7 (1) 111-116.

Satellite Remote Sensing Technologies for Biodiversity Monitoring and Its Conservation

Khare S. and Ghosh S.K.

Geomatics Engineering Division, IIT Roorkee, Uttarakhand, India

Publication Date: 6 April 2016

Article Link: <http://scientific.cloud-journals.com/index.php/IJAESE/article/view/Sci-429>



Copyright © 2016 Khare S. and Ghosh S.K. This is an open access article distributed under the **Creative Commons Attribution License**, which permits unrestricted use, distribution, and reproduction in any medium, provided the original work is properly cited.

Abstract Conservation of biodiversity is an essential issue due to increasing climate change and anthropological factors. Various rich biodiversity zones are greatly threatened and degrading with an alarming rate therefore it's required to safeguard these zones and their habitats at regional and local levels. In order to implement significant conservation schemes, exhaustive information on the distribution of species on a temporal basis are required. Recently, remote sensing and biodiversity communities have started coordinating their research ideas, problems and their solutions on a single platform. The likelihood of such type of co-operations has been significantly strengthened with the advancements in satellite remote sensing technology in last decade. Thus, this advancement has empowered the interdisciplinary research at regional and local scale with high temporal resolution to provide information about changes in species distribution, habitat degradation and fine-scale disturbances of forests. This paper presents the smart satellite remote sensing technologies, which can be very useful in retrieving relevant information about biodiversity present on earth surface. This paper emphasises on various advance remote sensing imageries and their utility in deriving relevant parameters and drivers required for biodiversity monitoring. This review paper incorporates the categorization of all important and advanced sensors with respect to the essential biodiversity variables required for its monitoring and conservation.

Keywords *Biodiversity; Satellite Remote Sensing; Conservation*

1. Introduction

In general, biological diversity, or in short, biodiversity has been defined by the leading Convention on Biological Diversity (CBD) as “the variability among living organisms from all sources including, inter alia, terrestrial, marine and other aquatic ecosystems and the ecological complexes of which they are part”. This includes diversity within species, between species and of ecosystems. Biodiversity may be divided into following components as shown in Figure 1.

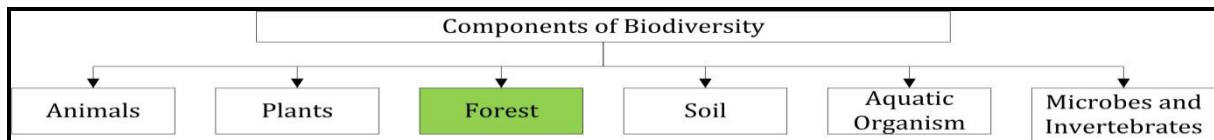


Figure 1: Components of Biodiversity

Conservation of biodiversity is proximately related to global environmental changes and globalisation issues, such as land use and land cover changes, climate change, and sustainable developments [45]. During the last century, human beings have caused changes to ecosystems more rapidly than in any comparable period in history due to rapid industrialization. As a result, biodiversity and their ecosystems are declining rapidly. This loss is further augmented by the lack of knowledge of biodiversity, especially amongst people with close relationship with the ecosystem. The global challenges relating to biodiversity include inventories to determine the magnitude and location of biodiversity existence and its change dynamics. At present, it is important to link biodiversity and human use of land in order to sustain biodiversity.

Remote sensing is a science of gathering information without coming in contact with earth [29], has wiped the fields of Ecology, Biodiversity and Conservation (EBC). Remote sensing has ability to provide consistent data of earth at various scales from global to local. In addition to this, remote sensing does not require labour and it also save time when compared to ground-based observations. The potential of synergies between remote sensing and biodiversity based research has been acknowledged by practitioners, researchers and data providers to better understand how remote sensing based studies can be utilised in bio diversity monitoring and its conservation [14, 20 & 34].

In this paper, smart technologies of satellite remote sensing have been highlighted. Satellite remote sensing incorporates three different prospects such as; satellite data, satellite data handling algorithms and software. In general satellite data can be obtained in the form of images, which includes low, medium and high resolution images. These satellite images contain variety of information of earth surface and level of details varies at different types of resolutions. To handle the complexity of information associated with these datasets various algorithms have been developed by researchers. These algorithms include statistical, probabilistic, artificial neural network and fuzzy based methods. Third prospect comprises of various types of commercial and open source softwares which take into consideration the algorithm and data handling. This paper presents the first prospect of satellite remote sensing i.e. different types of satellite remote sensing datasets and their utilities in biodiversity monitoring.

With this introduction, the aim is to highlight the importance of interdisciplinary perspective on satellite remote sensing and biodiversity monitoring and its conservation. This paper focuses on importance of space borne remote sensing in the field of biodiversity research from the angle of remote sensing specialists. It attempts to identify the specific remote sensing data set which may be applied to biodiversity monitoring.

2. Relevance of Remote Sensing Over Conventional Methods to Monitor Biodiversity

Biodiversity monitoring with traditional *in situ* methods normally requires as much effort as composing the initial inventory, as repeated measurements should be based on the same sampling methods and designs to explicitly detect changes. Some optimisation may be possible though using modeling and mathematical analysis [52]. Due to the inaccessibility of some habitats within a study region such as thick mangrove, steep slopes and practical considerations such as proximity to roads or observer populations may affect the inclusiveness of results obtained with traditional *in situ* methods.

Remote sensing cannot overcome traditional approaches for composing initial inventories of species, except in case of very large species identifiable on space-borne or airborne images. However, remote sensing is air replaceable large scale biodiversity monitoring tool at the level above species. If integrated with quality ground data and it can give more accurate results as compared to traditional methods. Remote sensing can be very advantageous for both planning surveys as well as monitoring biodiversity changes thereafter. To carry out repeated measurements under spatio-temporal conditions similar to the initial inventory, remote sensing is valuable tool in identifying when and where to monitor [7, 12, 31 & 49].

3. Remote Sensing Data Types and Their Applicability in Biodiversity

Remote sensing measures the electromagnetic waves reflected or emitted by distant objects present on Earth surface. Basically two types of sensors are attached with satellites: active or passive. The type of energy source required for both the sensors creates the basic difference between active sensors and passive sensors. Passive sensors, also known as optic sensors use Sun as an energy source and records reflected radiations of Sun from the Earth's surface. Multispectral scanners and Photographic cameras are passive sensors often used in satellite remote sensing Active sensors have their own energy source. They emit a signal that travels through the atmosphere, reflects on the Earth's surface and returns to the sensor, which measures the signal's travel time and strength. Synthetic Aperture Radar (SAR) is an example of an active sensor. Since it use signals with long-wavelength therefore, it can penetrate clouds or bad weather conditions [28].

3.1. Advanced Datasets in Remote Sensing of EBC

At present, remote sensing can provide data in different forms such as, hyperspectral, high spatial resolution, LIDAR and thermal infrared sensors. In order to avoid confusion between hyperspectral and high spatial resolution sensors, focus mainly given to medium spatial resolution hyperspectral sensors, such as Hyperion with 30m spatial resolution. Since radar sensors have their applications mostly in ice and snow, geology and agricultural domains therefore they have not selected in this discussion. Moreover, emphasis has been given to high spatial resolution sensors and their applications in biodiversity monitoring.

3.1.1. High Spatial Resolution

Normally in remote sensing high spatial resolution are also called as fine spatial resolution. The resolution is less than 10 m, and it ranges from 0.5 to 10 m in the commercial domain for environmental studies. Worldview-2 (WV-2), QuickBird, OrbView-3, IKONOS, and SPOT-5 (Satellite Pour l'Observation de la Terre-5) are the commonly used sensors. The advantage of high spatial resolution imagery is that it effectively increases the accuracy of characterization and identification of small objects at fine scales [20 & 59]. Gillespie et al. (2008) provided various examples for identification of plant species accurately based on the high spatial resolution imagery. Turner et al. (2003) revealed that it is viable and applicable to directly identify certain species and species assemblages at fine scale. In addition to this, fine scale imagery can be employed for the accuracy assessment of remote sensing derived from coarse or moderate spatial resolution imagery.

Wabnitz et al. (2008) has done the accuracy assessment for Landsat imagery of large-scale sea-grass mapping against patterns detectable with the help of fine resolution IKONOS images. In addition to this, security restrictions and data coverage is still a considerable constraint before easily acquiring fine resolution satellite data [46]. In addition to this, it is also observed out that fine spatial resolution imageries are still under-utilized and potential resources for biodiversity based research.

Harborne et al. (2008) highlighted intra-habitat variability in coral-reef fish by mapping heterogeneity among habitats. Fine resolution satellite data have opened the new gates for the development of species-level distribution maps along with structural information on canopy diameters, dominance, and distribution of age-class [54]. Moreover, some recent studies have revealed that the spectral bands of WV-2 ranging from 400 to 1040 nm are suitable for plant health analysis and it can also discriminate among various types of tree species [32 & 48]. Thus, WV-2 imagery may provide plenty of detailed information on a regular interval for various applications such as environmental, agricultural survey, ecological, geological, urban planning, and other areas.

Figure 2 is depicting the high spatial resolution satellite images of various sensors. Further, table 1 is showing the spatial and spectral information of various high spatial resolution sensors. The level of details present in the imageries and information associated with each object present on earth surface varies as the spatial resolution of sensors changes. Since these new generation sensors are playing a crucial role in biodiversity monitoring and its conservation by providing immense information of earth surface. Thus, these sensors are opening new dimensions in the field of biodiversity monitoring as discussed above.

Table 1: Satellite Sensors with Spatial Resolution and Spectral Information [66]

Sensor Name	Spatial Resolution		Spectral Bands		Area Coverage
	PAN	MS	PAN	MS	
Geoeye-1	0.46 m	1.84 m	1 band	4 bands	300 km x50 km (per strip)
Rapideye	NA	5 m	NA	5 bands	77 km x 1,500 km (per strip)
IKONOS-2	0.82 m	3.2 m	1 band	4 bands	4700 km square (per strip)
Quickbird	0.65 m	2.62 m	1 band	4 bands	18 km x 360 km (per strip)
WorldView-2	0.46 m	1.84 m	1 band	8 bands	138 km x 112 km (per strip)
Landsat-8	15 m	30 m	1 band	10 bands	185 kmx 180 km and can collect 500 scenes per day

PAN – Panchromatic, MS – Multispectral, NA – Not Applicable

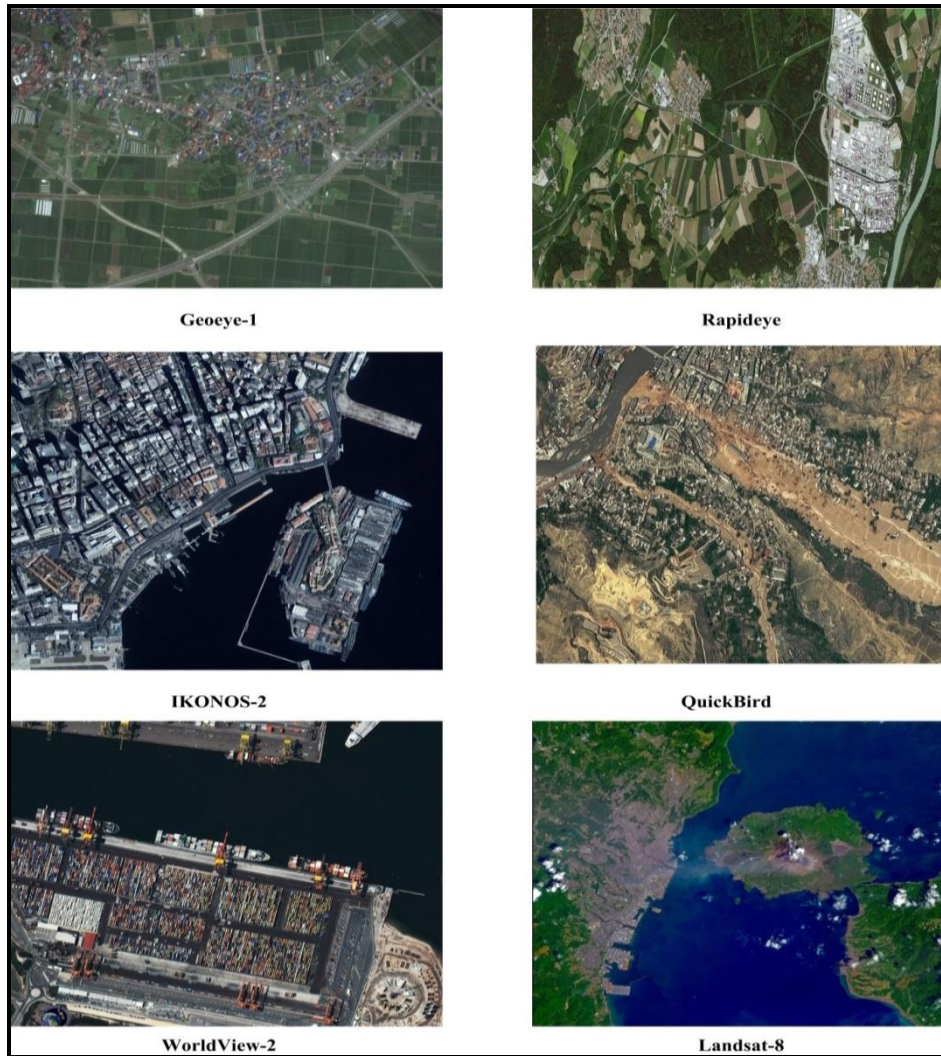


Figure 2: High Spatial Resolution Satellite Images [66]

3.1.2. Hyperspectral Data

Hyperspectral data have the capability to collect plenty of spectral information across a continuous spectrum normally with 100 or more contiguous spectral bands. It is somewhat dissimilar from multispectral sensors which incorporate relatively few discrete bands [46]. Due to the availability of hundreds of spectral bands with narrower width such as 10-20 nm spectral bandwidths offer new aspects to detect fine differences between objects of interest (Figure 3). The best instance is to distinguish fine-scale; species-specific land covers such as soil type's or vegetation categories which make incredible contribution to the biodiversity based studies. In addition to this, it was also found out that hyperspectral data can also be successfully applied in recording information of important plant properties such as water content, leaf pigment and chemical composition. Thus, it is possible to discriminate tree species in landscapes, and accurately identification between different species [59]. Similar to the case with fines spatial resolution imagery, hyperspectral imagery is also under-utilized resource and due to its high cost problem, it is putting it out of research for ecologists predominantly those in developing countries who keenly required the data [20 & 59].

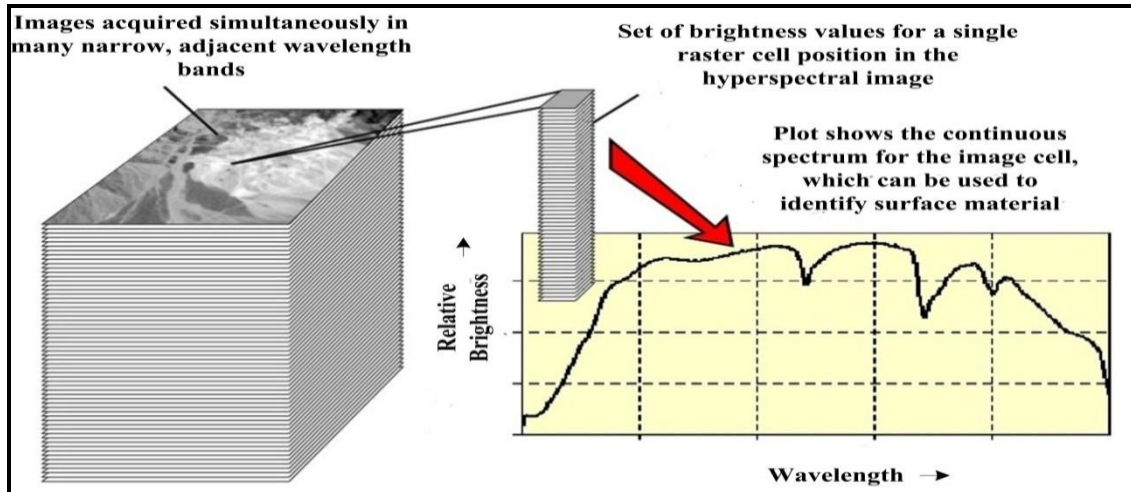


Figure 3: Basic Concept of Hyperspectral Imaging [46]

List of hyperspectral sensors is shown in Table 2:

Table 2: List of Hyperspectral Sensors

Sensor	Agency
Hyperion Sensor EO-1 (Earth Observing-1)	NASA (National Aeronautics and Space Administration)
CHRIS (Compact High Resolution Imaging Spectrometer)	European Space Agency
PROBA (Project for On-Board Autonomy)	US Air Force Research Lab
FTHSI (Fourier Transform Hyperspectral Imager)	US Air Force Research Lab

Among all these sensors, most commonly used and first civilian sensor is Hyperion, which is controlled by the EROS (Earth Resources Observation and Science) at a fairly low cost to the general public [53].

Hyperion hyperspectral imageries include applications in various fields such as forest biodiversity and ecology [21], vegetation, agriculture [3], fragmented ecosystem and coastal environment [37]. Recently in a Belgian heath land Natura 2000 landscape it was highlighted by the researchers that the potential and ability of airborne hyperspectral line-scanner radiometer (AHS-160) imagery was outstanding in mapping habitat extent and quality. Due to availability of 63 visual and near-infrared bands with a spatial resolution of 2.4 m, it became possible to map habitat extent, although the contrast was relatively low between heath land habitat types [22].

Hyperspectral imagery has numerous applications such as assessment of habitat degradation and stress [29]. Due to the availability of larger and narrower bands, it can also detect changes in structural and chemical traits. In addition to this, it can also detect changes in the level of nitrogen, phosphorus and other foliage compounds that could be linked with discrepancy in environmental factors such as quality of soil [58]. Further, comparison was also done between the field assessments and potential of airborne hyperspectral imagery to deliver information related to conservation status of two Natura 2000 heath land areas [56]. It was found that field based assessments estimated 43% of the variation in fine-scale indicators about habitat condition. While on the other side information obtained from remote sensing was less as compared to field based assessments and it was up to 39% only. In other studies such as assessment of invasive species, it was found that hyperspectral images are more useful for the mapping of individual species, whenever there is a low density scattered distribution of invader species [24].

3.1.3. Active Remote Sensing Sensors

Passive remote sensing data suffers cloud cover and haze related problems, however active remote sensing is not affected by atmospheric conditions. SAR is being used, with a number of new satellites such as, Terra SAR/Tandem-X. They are providing ample of opportunities for landscape monitoring at very high spatial resolution [20]. In particular, both SAR and LiDAR technologies have potential to gather information in different formats and it would be very useful for estimating above ground biomass and also the structure such as height and cover of woody vegetation. Further it can also be correlated to forest condition and biodiversity related issues. However, the usage of SAR and LIDAR data has been somewhat restricted in developing countries due to the technological and security challenges associated with them [5 & 26].

Active remote sensing data provides complementary information than passive sensors [57]. SAR data could be a best alternative to optical data for those areas which are more prone to cloud cover problems. The most important applications of Radar and also LiDAR is that it can provide three dimensional structure of any area which would be very useful in discrimination of different habitat types [35], which can be related to succession, age and species composition [9, 42 & 57]. RADARSAT-2 and ALOS PALSAR have shown immense potential for mapping wildlife habitat, especially when integrated with optical data through data fusion [64]. In brief, ALOS PALSAR L-band allows detection of non-forest and forest and retrieval of above ground biomass [50].

With its ability to penetrate below the top vegetation canopy, can be very useful for monitoring habitat degradation. An integration of SAR and Landsat data was used to differentiate among Amazonian forest patches during different stages of re-growth [37]. In a similar study, it was found that the Scots Pine and Norway spruce of Finland were classified to an accuracy of 83% and 90% respectively, on the other side birch trees were mixed with the other species [60].

3.1.4. High Resolution Digital Elevation Model (DEM)

Since forest biological parameters or attributes such as canopy density, tree height, canopy diameter and composition of species plays crucial role in biodiversity research. Thus, determination of these attributes is very important as they are required by forest planners, managers and policy makers for an estimation of forest conditions, volumes and biomass. At national and global levels, this information is required to estimate the existing carbon stock in the Earth's system, which would be very useful in deriving models for climate change studies, changes in biogeochemical cycling, and changes in wildlife habitats [18]. Traditionally in India we take field based survey of forest stock inventory which are tedious, costly, time-consuming and lack uniformity and accuracy [16 & 43].

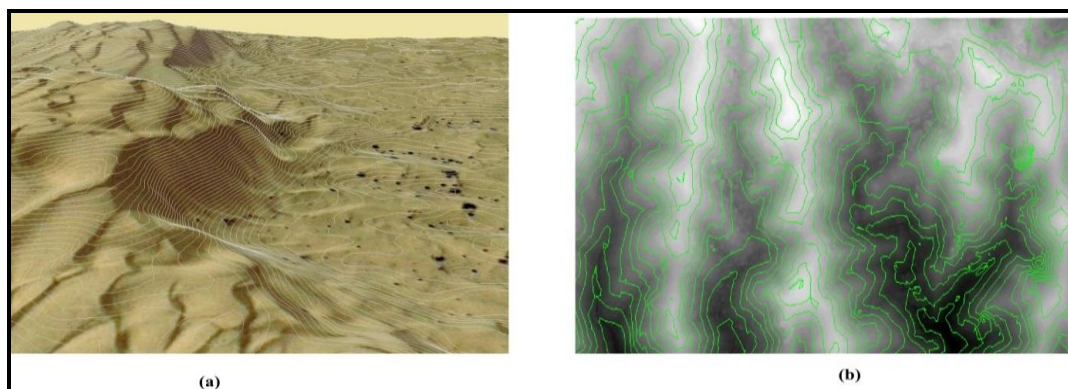


Figure 4: Example Images of Extracted DEMs (a) 1 m DEM from stereo IKONOS Satellite Image Data (b) 10 m DEM Extracted from Stereo Cartosat-1 Satellite Image Data [66]

Cartosat-1 with 2.5 m PAN stereo and Cartosat-2 with less than 1 m PAN stereo capability have opened up new gateways of applications in forest biodiversity studies. Due to the availability of fine resolution stereo data from satellites such as SPOT (Systeme Pour l' Observation de la Terre), IRS-1C/1D, IKONOS and Cartosat, it is becoming possible to create the fine quality DEMs. In addition to this, terrain variables required for many applications in natural resources management, including forest biodiversity studies [6 & 47]. Figure 4 depicts the extracted DEM from IKONOS and Cartosat satellite data. Various topographic variables such as height, slope, aspect and morphology can be derived from these DEMs, which would provide relevant information for biodiversity monitoring.

4. Monitoring Biodiversity Using Satellite Remote Sensing

Before proceeding to the various applications of satellite remote sensing in biodiversity research, it is essential to understand the possible approaches of remote sensing technologies to monitor biodiversity. Since, there are various components of biodiversity, thus remote sensing applications may vary as per the respective component. Suitability of approach depends upon the kind of environment in which biodiversity is to be monitored.

4.1. Advancement in Remote Sensing Methods for Biodiversity Monitoring

Recently, there is advancement in sensor technologies and digital image processing techniques, along with growing spatial detail. This led to challenge the remote sensing community to find out new methods of exploiting information present in these fine images more intelligently. Object Based Image Analysis (OBIA) is becoming a new paradigm in the field of remote sensing due to its ability to handle complex information associated with new generation satellite datasets mentioned above. This paper highlights the basic methodology of OBIA and its applicability in the field of biodiversity monitoring.

With the wide availability of fine resolution data, pixel-based classification algorithms seems to be not ideal to extract information desired from the data revealing high frequency components with high contrast and horizontal layover of objects [28]. Since, last several years, pixel based classification approaches are in vogue for classification of coarse and medium spatial resolution remote sensing data. However, the traditional pixel based classification approaches have limitations in incorporating the spectral, geometric, and contextual attributes such as shape, size, texture, shadow of land use features such as roads, buildings, trees etc., in the classification process [62]. Inclusion of these attributes may result in production of quality land use maps from high resolution data. This has given impetus to the development of OBIA recently.

OBIA is relatively a new concept applied for the extraction of meaningful objects of similar attributes from remote sensing images via a segmentation process. The classes involve a connection to nearby objects such as super and sub-objects in hierarchical order. Spatial relationship such as 'nearest neighbour' or statistical similarities can be applied on segmented image for assigning class. At its rudimentary level, OBIA involves image segmentation, attribute selection, classification and the ability to link individual objects in hierarchy. The basic flowchart is shown in figure 5. Basically, OBIA is based on the assumption that image objects provide a more appropriate scale to map environmental features and allows features with significant variations in their spectral reflectance signature to be mapped at specific scales [4].

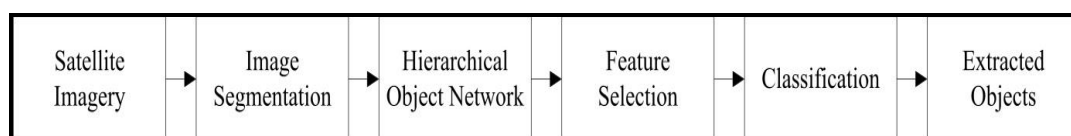


Figure 5: Basic Flow Chart of OBIA Methodology

A variety of studies have been carried using object based classification into the science of EBC. In a similar study it was proposed that object based classification may traverse the possible Landsat-gap on applications such as landscape pattern analysis or ecological models [64]. Moreover, biodiversity in an urban context in Bangalore was assessed and different challenges were found out in utilizing very high resolution GeoEye image for mapping of tree species and density estimation in human influenced urban areas. Here six different tree species were mapped using pixel-based and object based approaches and final comparison has been carried between the two approaches [1]. It is found that OBIA appears to have high potential over pixel-based approaches for monitoring changes in tree species distribution and tree felling in this highly data-poor, dynamic and fast developing city, which urgently requires better information on tree distribution for monitoring and management.

4.2. Application of Satellite Remote Sensing in the Field of Biodiversity Monitoring

Degradation and loss of habitat along with invasion of alien species are among the potential threats to biodiversity. Landsat imagery was mostly used to detect and map anthropogenic disturbances in desert environments and focus was also given to oil exploration in the Sahara in one of the case study [13]. In a similar study it was examined that the projected and current regional distributions of an invasive species in the United States, *Ailanthus altissima*, integrating ground-based measurements from the United States Forest Service's Forest Inventory and Analysis program with new data products from NASA's Terrestrial Observation and Prediction System [8]. Essential biodiversity variables (EBV) help in prioritizing by defining a minimum set of essential measurements to capture major dimensions of biodiversity change, complementary to one another and to other environmental change observation initiatives. Table 3 illustrates the relationship of EBVs with satellite images. Table 4 highlights the important research work carried out by remote sensing analysts in the field of biodiversity monitoring.

Table 3: Relationship among Essential Bio-Diversity Variables & Remote Sensing Measurement Scales [27& 63]

EBV (Ecosystem Structure)	Spatial Resolution satellite imagery with type of measurement scales (including available remote sensing sensors)	Relevance and related information for biodiversity
Temporal phenology metrics	Low/coarser spatial resolution (Global Scale) (MODIS, AVHRR etc.)	Phenology types, Forest / Non Forest, Deforestation and Biomass burning.
Habitat Structure, Ecosystem extent and fragmentation	Medium spatial resolution (Regional Scale) (Landsat, IRS, SPOT etc.)	Forest type distribution and agricultural expansion.
Habitat types and structures, and Ecosystem composition by functional type	High spatial resolution (Local scale) (IKONOS, QuickBird, Rapid Eye historic GeoEye, WorldView-2 etc.)	Species-level distribution, canopy diameters, stand-level analysis, individual tree detection, to differentiate species at a finer scale.
Habitat types and structures	Active remote sensing data	Habitat degradation monitoring by generation of 3D structures.

Table 4: Applications of Remote Sensing in Biodiversity Monitoring

Issues addressed	Data used	Focusing Area
1) Land-use and land-cover mapping and monitoring	IRS and Landsat	1) Landscape and regional dynamics of canopy damage in Eastern Amazon forest [2] 2) LULC identification in Nubra Valley [30] 3) Estimated the extent of forest habitat and loss over the last 20 years within and surrounding 198 of the most highly protected areas [10] 4) Bio-resource conservation study in Western Himalayas [36]
2) Biodiversity characterization and assessment	IRS, IKONOS and Landsat	1) Measured the structure and composition of tropical dry forests [15] 2) Predicted woody-plant species richness in tropical dry forests of South Florida, USA [19] 3) Mapped the species richness and composition of tropical forests [17] 4) Investigation of tree diversity mapping in the Hyrcanian forests of Iran [44] 5) Assessed the plant diversity in a dry tropical forest of central India [25]
3) Forest degradation and Species invasion	IRS, Landsat, QuickBird, IKONOS, Worldview-II	1) Forest management and land use/cover changes in the mid elevation zone of Central Himalaya, India [39] 2) QuickBird high resolution (2.8 m) satellite imagery was used to distinguish giant reed invasion along Rio Grande in southwest Texas [40] 3) Quickbird Satellite to estimate the flowering population of <i>Tabebuia guayacan</i> trees at Barro Colorado Island (BCI), in Panama [51] 4) Impact of anthropogenic pressure on forest cover has been analysed using satellite data and field observations [55]

5. Summary and Conclusion

Based on the above studies, it is now possible to use smart technologies such as satellite data, computing algorithms and techniques to analyse complex and difficult phenomenon such as biodiversity monitoring. Table 5 gives a summary of the different types of remote sensing data that is useful in biodiversity monitoring. Based on the type of application, it is possible to now select the appropriate satellite dataset in order to reach to possible monitoring scenarios.

On the basis of above discussions following conclusion can be drawn.

- i) Satellite remote sensing offers smart solutions for biodiversity monitoring and to prepare conservation strategies with less effort.
- ii) Due to the availability of multi-date, multi-resolution, multi-sensor datasets, it has become possible to acquire huge details of earth surface without making tedious field visit.
- iii) Since high spatial resolution datasets can acquire very fine details over small areas at a regular interval of time. Thus, this information will provide basis for regional scale monitoring of biodiversity.
- iv) This review primarily highlights the role that remote sensing can play in assisting environmentalists to characterize and map biologically rich zones, generating information on changes in biodiversity, alteration and distribution in species diversity.

Table 5: Summary of Active and Passive Remote Sensing Data Useful for Biodiversity Monitoring

Sensor	Biodiversity Monitoring
Coarse Spatial Resolution (MODIS, AVHRR)	Forest / Non Forest, Biomass burning studies at global scale.
Medium spatial resolution (Landsat, IRS, SPOT)	Indicators of overall species richness and diversity at regional scales, forest type distribution and agricultural expansion.
High temporal resolution data (Multi season data or images corresponding to specific seasons)	Information on invasion species and other species of interest (e.g. using images acquired corresponding to critical phenological stages of flowering or leaf senescence.

Very high spatial resolution (IKONOS, QuickBird, Geoeye, WorldView-2)	Indicators of overall species richness and diversity, identification of fine scale degradation in forests, fine scale monitoring of urban sprawl, Species-level distribution, canopy diameters, stand-level analysis, individual tree detection.
Hyperspectral (ASTER, HyMap, AVIS-2, AHS-160)	Differentiation of plant communities that are spectrally similar, mapping top canopy tree species or genus level and identification of invasive species, relating heterogeneities to species richness and diversity.
Active Remote sensing Data (SAR, LIDAR)	Floral and Faunal diversity in habitats (e.g. forests) with complex three dimensional structures.

References

- [1] Agarwal, S., Vailshery, L.S., Jaganmohan, M., and Nagendra, H. *Mapping Urban Tree Species Using Very High Resolution Satellite Imagery: Comparing Pixel-Based and Object-Based Approaches*. ISPRS International Journal of Geo-Information. 2013. 2 (1) 220-236.
- [2] Asner, G.P., Keller, M., Pereira, Jr, R., Zweede, J.C., and Silva, J.N. *Canopy Damage and Recovery after Selective Logging in Amazonia: Field and Satellite Studies*. Ecological Applications. 2004. 14 (sp4) 280-298.
- [3] Bannari, A., Khurshid, K.S., Staenz, K., and Schwarz J. *Potential of Hyperion EO-1 Hyperspectral Data for Wheat Crop Chlorophyll Content Estimation*. Canadian Journal of Remote Sensing. 2008. 34 (sup1) S139-S157.
- [4] Blaschke, T. *Object Based Image Analysis for Remote Sensing*. ISPRS Journal of Photogrammetry and Remote Sensing. 2010. 65 (1) 2-16.
- [5] Boyd, D.S., Phipps, P.C., Foody, G.M., and Walsh, R.P.D. *Exploring the Utility of NOAA AVHRR Middle Infrared Reflectance to Monitor the Impacts of ENSO-Induced Drought Stress on Sabah Rainforests*. International Journal of Remote Sensing. 2002. 23 (23) 5141-5147.
- [6] Carleer, A., and Wolff, E. *Exploitation of Very High Resolution Satellite Data for Tree Species Identification*. Photogrammetric Engineering & Remote Sensing. 2004. 70 (1) 135-140.
- [7] Chawla, A., Yadav, P.K., Uniyal, S.K., Kumar, A., Vats, S.K., Kumar, S., and Ahuja, P.S. *Long-Term Ecological and Biodiversity Monitoring in the Western Himalaya Using Satellite Remote Sensing*. Current Science (Bangalore). 2012. 102 (8) 1143-1156.
- [8] Clark, J., Wang, Y., and August, P.V. *Assessing Current and Projected Suitable Habitats for Tree-of-Heaven Along the Appalachian Trail*. Philosophical Transactions of the Royal Society B: Biological Sciences. 2014. 369 (1643) 20130192.
- [9] Costa, B.M., Battista, T.A. and Pittman, S.J. *Comparative Evaluation of Airborne Lidar and Ship-Based Multi-Beam Sonar Bathymetry and Intensity for Mapping Coral Reef Ecosystems*. Remote Sensing of Environment. 2009. 113 (5) 1082-1100.
- [10] DeFries, R., Hansen, A., Newton, A.C., and Hansen, M.C. *Increasing Isolation of Protected Areas in Tropical Forests over the Past Twenty Years*. Ecological Applications. 2005. 15 (1) 19-26.
- [11] Dodge, S., Bohrer, G., Bildstein, K., Davidson, S.C., Weinzierl, R., Bechard, M.J., and Wikelski, M. *Environmental Drivers of Variability in the Movement Ecology of Turkey Vultures (Cathartes Aura) in North and South America*. Philosophical Transactions of the Royal Society B: Biological Sciences. 2014. 369 (1643) 20130195.

- [12] Dubois, G., Clerici, M., Peedell, S., Mayaux, P., Grégoire, J.M., and Bartholomé, E. *A Digital Observatory for Protected Areas-DOPA, A GEO-BON Contribution to the Monitoring of African Biodiversity*. Proceedings of Map Africa. 2010. 23-25.
- [13] Duncan, C., Kretz, D., Wegmann, M., Rabeil, T., and Pettorelli, N. *Oil in the Sahara: Mapping Anthropogenic Threats to Saharan Biodiversity from Space*. Philosophical Transactions of the Royal Society B: Biological Sciences. 2014. 369 (1643) 20130191.
- [14] Duro, D.C., Coops, N.C., Wulder, M.A., and Han, T. *Development of a Large Area Biodiversity Monitoring System Driven by Remote Sensing*. Progress in Physical Geography. 2007. 31 (3) 235-260.
- [15] Feeley, K.J., Gillespie, T.W., and Terborgh, J.W. *The Utility of Spectral Indices from Landsat ETM+ for Measuring the Structure and Composition of Tropical Dry Forests*¹. Biotropica. 2005. 37 (4) 508-519.
- [16] Forest Survey of India, 1996: *Volume Equations for Forests of India, Nepal and Bhutan*. Dehradun, India: Forest Survey of India, Ministry of Environment and Forests, Government of India.
- [17] Foody, G.M., and Cutler, M.E. *Mapping the Species Richness and Composition of Tropical Forests from Remotely Sensed Data With Neural Networks*. Ecological Modeling. 2006. 195 (1) 37-42.
- [18] Franklin, S.E., Wulder, M.A., and Gerylo, G.R. *Texture Analysis of IKONOS Panchromatic Data for Douglas-Fir Forest Age Class Separability in British Columbia*. International Journal of Remote Sensing. 2001. 22 (13) 2627-2632.
- [19] Gillespie, T.W. *Predicting Woody-Plant Species Richness in Tropical Dry Forests: A Case Study from South Florida, USA*. Ecological Applications. 2005. 15 (1) 27-37.
- [20] Gillespie, T.W., Foody, G.M., Rocchini, D., Giorgi, A.P., and Saatchi, S. *Measuring and Modelling Biodiversity from Space*. Progress in Physical Geography. 2008. 32 (2) 203-221.
- [21] Guerschman, J.P., Hill, M.J., Renzullo, L.J., Barrett, D.J., Marks, A.S., and Botha, E.J. *Estimating Fractional Cover of Photosynthetic Vegetation, Non-Photosynthetic Vegetation and Bare Soil in the Australian Tropical Savanna Region Upscaling the EO-1 Hyperion and MODIS Sensors*. Remote Sensing of Environment. 2009. 113 (5) 928-945.
- [22] Haest, B., Thoonen, G., VandenBorre, J., Spanhove, T., Delalieux, S., Bertels, L., and Scheunders, P., 2010: *An Object-Based Approach to Quantity and Quality Assessment of Heathland Habitats in the Framework of NATURA 2000 Using Hyperspectral Airborne AHS Images*. GEOBIA 2010-Geographic Object-Based Image Analysis.
- [23] Harborne, A.R., Mumby, P.J., Kappel, C.V., Dahlgren, C.P., Micheli, F., Holmes, K.E., & Brumbaugh, D.R. *Tropical Coastal Habitats as Surrogates of Fish Community Structure, Grazing, and Fisheries Value*. Ecological Applications. 2008. 18 (7) 1689-1701.
- [24] He, K.S., Rocchini, D., Neteler, M., and Nagendra, H. *Benefits of Hyperspectral Remote Sensing for Tracking Plant Invasions*. Diversity and Distributions. 2011. 17 (3) 381-392.

- [25] Hernández-Stefanoni, J.L., Alberto Gallardo-Cruz, J., Meave, J.A., and Dupuy, J.M. *Combining Geostatistical Models and Remotely Sensed Data to Improve Tropical Tree Richness Mapping*. *Ecological Indicators*. 2011. 11 (5) 1046-1056.
- [26] Hyypä, J., Hyypä, H., Inkinen, M., Engdahl, M., Linko, S., and Zhu, Y.H. *Accuracy Comparison of Various Remote Sensing Data Sources in the Retrieval of Forest Stand Attributes*. *Forest Ecology and Management*. 2000. 128 (1) 109-120.
- [27] Innes, J.L., and Koch, B. *Forest Biodiversity and Its Assessment by Remote Sensing*. *Global Ecology & Biogeography Letters*. 1998. 7 (6) 397-419.
- [28] Jensen John, R., 2009: *Remote Sensing of the Environment: An Earth Resource Perspective 2/e*. Pearson Education India.
- [29] Joseph, S., Murthy, M.S.R., and Thomas, A.P. *The Progress on Remote Sensing Technology in Identifying Tropical Forest Degradation: A Synthesis of the Present Knowledge and Future Perspectives*. *Environmental Earth Sciences*. 2011. 64 (3) 731-741.
- [30] Joshi, P.K., Rawat, G.S., Padaliya, H., and Roy, P.S. *Land Use/Land Cover Identification in an Alpine and Arid Region (Nubra Valley, Ladakh) Using Satellite Remote Sensing*. *Journal of the Indian Society of Remote Sensing*. 2005. 33 (3) 371-380.
- [31] Jürgens, N., Schmiedel, U., Haarmeyer, D.H., Dengler, J., Finckh, M., Goetze, D., and Zizka, G. *The BIOTA Biodiversity Observatories in Africa—A Standardized Framework for Large-Scale Environmental Monitoring*. *Environmental Monitoring and Assessment*. 2012. 184 (2) 655-678.
- [32] Kanniah, K.D., 2011: *Worldview-2 Remote Sensing Data for Tropical Mangrove Species Classification*. Research Report submitted to DigitalGlobe Incorporated, USA for the Worldview-2, 8-Bands Research Challenge. Longmont, CO: DigitalGlobe.
- [33] Ke, Y., Quackenbush, L.J., and Im, J. *Synergistic Use of Quickbird Multispectral Imagery and LIDAR Data for Object-Based Forest Species Classification*. *Remote Sensing of Environment*. 2010. 114 (6) 1141-1154.
- [34] Kerr, J.T., and Ostrovsky, M. *From Space to Species: Ecological Applications for Remote Sensing*. *Trends in Ecology & Evolution*. 2003. 18 (6) 299-305.
- [35] Koch, B. *Status and Future of Laser Scanning, Synthetic Aperture Radar and Hyperspectral Remote Sensing Data for Forest Biomass Assessment*. *ISPRS Journal of Photogrammetry and Remote Sensing*. 2010. 65 (6) 581-90.
- [36] Kumar, Amit, Chawla, Amit, and Rajkumar, S. *Characterization of Solang Valley Watershed in Western Himalaya for Bio-Resource Conservation Using Remote Sensing Techniques*. *Environmental Monitoring and Assessment*. 2011. 179 (1-4) 469-478.
- [37] Kuplich, T.M. *Classifying Regenerating Forest Stages in Amazonia Using Remotely Sensed Images and a Neural Network*. *Forest Ecology and Management*. 2006. 234 (1) 1-9.
- [38] Lee, Z., Casey, B., Arnone, R., Parsons, R., Montes, M.J., Davis, C., and Goode, W. *Water and Bottom Properties of a Coastal Environment Derived from Hyperion Data Measured from the EO-1 Spacecraft Platform*. *Journal of Applied Remote Sensing*. 2007. 1 (1) 011502.

- [39] Lele, N., and Joshi, P.K. *Analyzing Deforestation Rates, Spatial Forest Cover Changes and Identifying Critical Areas of Forest Cover Changes in North-East India during 1972–1999*. Environmental Monitoring and Assessment. 2009. 156 (1-4) 159-170.
- [40] Lucas, R., Bunting, P., Paterson, M., and Chisholm, L. *Classification of Australian Forest Communities Using Aerial Photography, CASI and HyMap data*. Remote Sensing of Environment. 2008. 112 (5) 2088-2103.
- [41] Mahtab, A., and Narender, B. *Satellite Derived Digital Elevation Model and Terrain Parameters-Generation, Accuracy Assessment and Validation*. Journal of the Indian Society of Remote Sensing. 2003. 31 (1) 19-24.
- [42] Mallet, C., and Bretar, F. *Full-Waveform Topographic Lidar: State-of-the-art*. ISPRS Journal of Photogrammetry and Remote Sensing. 2009. 64 (1) 1-16.
- [43] Maslekar, A.R. *Remote Sensing and Its Scope in Indian Forestry*. Indian Forester. 1974. 100 (3) 192-201.
- [44] Mohammadi, J., and Shataee, S. *Possibility Investigation of Tree Diversity Mapping Using Landsat ETM+ Data in the Hyrcanian Forests of Iran*. Remote Sensing of Environment. 2010. 114 (7) 1504-1512.
- [45] Nagendra, H., Rocchini, D., Ghate, R., Sharma, B., and Pareeth, S. *Assessing Plant Diversity in a Dry Tropical Forest: Comparing the Utility of Landsat and IKONOS Satellite Images*. Remote Sensing. 2010. 2 (2) 478-496.
- [46] Nagendra, H., and Rocchini, D. *High Resolution Satellite Imagery for Tropical Biodiversity Studies: The Devil is in the Detail*. Biodiversity and Conservation. 2008. 17 (14) 3431-3442.
- [47] Navalgund, R.R. *CARTOSAT-1: The Latest from the Indian Remote Sensing Satellite Series*. ISPRS. 2005. 10 (3) 30-31.
- [48] Omar, H., 2010: *Commercial Timber Tree Species Identification Using Multispectral Worldview-2 Data*. Research Report submitted to DigitalGlobe Incorporated, USA for the WorldView-2, 8-Bands Research Challenge. Longmont, CO: DigitalGlobe.
- [49] Raes, N., Roos, M.C., Slik, J.W., Van Loon, E.E., and Steege, H.T. *Botanical Richness and Endemicity Patterns of Borneo Derived from Species Distribution Models*. Ecography. 2009. 32 (1) 180-192.
- [50] Rahman, M.M., and Sumantyo, J.T.S. *Mapping Tropical Forest Cover and Deforestation Using Synthetic Aperture Radar (SAR) Images*. Applied Geomatics. 2010. 2 (3) 113-121.
- [51] Sánchez-Azofeifa, A., Rivard, B., Wright, J., Feng, J.L., Li, P., Chong, M.M., and Bohlman, S.A. *Estimation of the Distribution of Tabebuiaaguayacan (Bignoniaceae) Using High-Resolution Remote Sensing Imagery*. Sensors. 2011. 11 (4) 3831-3851.
- [52] Sewell, D., Guillera-Arroita, G., Griffiths, R.A., and Beebee, T.J. *When is a Species Declining? Optimizing Survey Effort to Detect Population Changes in Reptiles*. PloS ONE. 2012. 7 (8) e43387.

- [53] Shippert, P. *Why Use Hyperspectral imagery?* Photogrammetric Engineering and Remote Sensing. 2004. 70 (4) 377-396.
- [54] Singh, J.S., Roy, P.S., Murthy, M.S.R., and Jha, C.S. *Application of Landscape Ecology and Remote Sensing for Assessment, Monitoring and Conservation of Biodiversity.* Journal of the Indian Society of Remote Sensing. 2010. 38 (3) 365-385.
- [55] Somodi, I., Čarni, A., Ribeiro, D., and Podobnikar, T. *Recognition of the Invasive Species Robinia pseudacacia from Combined Remote Sensing and GIS Sources.* Biological Conservation. 2012. 150 (1) 59-67.
- [56] Spanhove, T., VandenBorre, J., Delalieux, S., Haest, B., and Paelinckx, D. *Can Remote Sensing Estimate Fine-Scale Quality Indicators of Natural Habitats?* Ecological Indicators. 2012. 18; 403-412.
- [57] Strittholt, J., Steininger, M., Loucks, C., White, B., Wilkie, M.L., and Guariguata, M. *Trends in Selected Biomes, Habitats, and Ecosystems: Forests.* In Sourcebook on Remote Sensing and Biodiversity Indicators. Secretariat of the Convention on Biological Diversity, Montreal Technical Series. 2007. (32) 35-63.
- [58] Townsend, A.R., Asner, G.P., and Cleveland, C.C. *The Bio-Geochemical Heterogeneity of Tropical Forests.* Trends in Ecology & Evolution. 2008. 23 (8) 424-431.
- [59] Turner, W., Spector, S., Gardiner, N., Fladeland, M., Sterling, E., and Steininger, M. *Remote Sensing for Biodiversity Science and Conservation.* Trends in Ecology & Evolution. 2003. 18 (6) 306-314.
- [60] Vauhkonen, J., Korpela, I., Maltamo, M., and Tokola, T. *Imputation of Single-Tree Attributes Using Airborne Laser Scanning-Based Height, Intensity, and Alpha Shape Metrics.* Remote Sensing of Environment. 2010. 114 (6) 1263-1276.
- [61] Wabnitz, C.C., Andréfouët, S., Torres-Pulliza, D., Müller-Karger, F.E., and Kramer, P.A. *Regional-Scale Seagrass Habitat Mapping in the Wider Caribbean Region Using Landsat Sensors: Applications to Conservation and Ecology.* Remote Sensing of Environment. 2008. 112 (8) 3455-3467.
- [62] Walker, J.S., and Blaschke, T. *Object-Based Land-Cover Classification for the Phoenix Metropolitan Area: Optimization vs. Transportability.* International Journal of Remote Sensing. 2008. 29 (7) 2021-2040.
- [63] Walters, M., Pereira, H.M., Ferrier, S., Geller, G.N., Jongman, R., Scholes, R.J., and Reyers, B. *Essential Biodiversity Variables.* Science. 2013. 339 (6117) 277-8.
- [64] Wang, K., Franklin, S.E., Guo, X., He, Y., and McDermid, G.J. *Problems in Remote Sensing of Landscapes and Habitats.* Progress in Physical Geography. 2009. 33 (6) 747-68.
- [65] Wegmann, M., Santini, L., Leutner, B., Safi, K., Rocchini, D., Bevanda, M., and Rondinini, C. *Role of African Protected Areas in Maintaining Connectivity for Large Mammals.* Philosophical Transactions of the Royal Society B: Biological Sciences. 2014. 369 (1643) 20130193.
- [66] DigitalGlobe. *Satellite Imaging Corporation.* www.digitalglobe.com. 2001-2014.

Field Occurrence and Petrographic Characteristics of Tertiary Volcanic Rocks and Associated Intrusions in and around Taiz City, Yemen

Al-Qadhi Abdul-Aleam Ahmed A.D.¹, Janardhana M.R.¹ and Prakash Narasimha K.N.²

¹Department of Geology, Yuvaraja's College, University of Mysore, Mysuru, Karnataka, India

²Department of Studies in Earth Science, University of Mysore, Manasagangothri, Mysuru, Karnataka, India

Publication Date: 24 May 2016

Article Link: <http://scientific.cloud-journals.com/index.php/IJAESE/article/view/Sci-430>



Copyright © 2016 Al-Qadhi Abdul-Aleam Ahmed A.D., Janardhana M.R. and Prakash Narasimha K.N. This is an open access article distributed under the **Creative Commons Attribution License**, which permits unrestricted use, distribution, and reproduction in any medium, provided the original work is properly cited.

Abstract Geologic and petrographic studies of Tertiary volcanic rocks and their intrusive bodies such as plutons, dykes and sills were carried out in and around Taiz city, Yemen with an aim to document their field occurrence and distribution as well as to study their mineralogical composition. This has an important bearing on the town planning in the city of Taiz as the existing buildings are collapsing due to the foundation problems. Studies on 110 exposures, carefully selected after field traverses revealed that the Tertiary rocks in the study region are mainly represented by typical bimodal mafic-felsic associations in the form of flows, plutons and dykes. Tertiary volcanic flows are characterized by alternating sequences of basic and felsic rocks and varicoloured volcanoclastic deposits which were all extruded and fed from fracturing and fissuring in the old rocks through which magma emerged in successive pulses, flooding the surrounding region. The basic flows (Tb1, Tb2 and Tb3) consist of jointed/massive basaltic rocks and volcanoclastic deposits while the felsic flows (Tr1 and Tr2) are comprised of jointed/massive rhyolite/dacite rocks and also varicoloured felsic volcanoclastic deposits. All these rocks show wide variations in their geological and petrographical characteristics such as colour, texture, heterogeneity, macro/microfractures, weathering/alteration, thickness, horizontal attitude, and intercalation with volcanoclastic deposits, repetition with depth in both vertical and horizontal directions. Volcanoclastic deposits are also characterized with great diversity in their types, colours, textural features, thicknesses, grain sizes, matrices, and degree of roundness of rock fragments and alternating and/or interlocking as well as intercalation laterally and vertically with basalt/rhyolite lava rocks. Volcanoclastic rocks were classified for the first time in the study area based on their particle sizes into different types. They range from strong, compact, welded rocks to weak, altered soils. The younger Sabir granitic pluton is represented by alkaline or peralkaline granites that are white to greyish white coloured massive, medium to coarse-grained, grading up to granite porphyry. Petrographic examinations of 52 thin sections representing the samples of basaltic lava flows, rhyolitic/dacite lava flows and younger intrusives under polarizing microscope have been carried to study their mineralogy. The dominant minerals in basaltic rocks are plagioclase, augite and olivine whereas rhyolitic rocks contain quartz, orthoclase and biotite. The main mineral constituents of younger granitic rocks are k-feldspar, quartz, hornblende and biotite. The mafic and felsic dykes

almost resemble basalts and rhyolites/dacites respectively in their petrographical characteristics. XRD technique used for characterizing the minerals of volcanic soils revealed the presence of clay minerals namely montmorillonite and kaolinite as the major mineral phase in most of the samples whereas mica group of minerals such as muscovite, vermiculite and chlorite are present in minor amounts, in addition to talc, feldspar, calcite and halloysite.

Keywords *Taiz City in Yemen; Tertiary bi-modal Lava Flows; Volcaniclastic Characteristics; Colonnade Columnar Structures; Sabir Granite*

1. Introduction

In Yemen, during the Oligocene-Miocene period, stable conditions were persisted until the development of the Red Sea-Gulf of Aden which lead to a massive uplift along the rift boundaries, crustal thinning, extension and massive outpourings that resulted in the development of continental flood basalt provinces; Yemen Trap Series (YTS) and Yemen Volcanic Series (YVS). Obviously high heat flow was associated with crustal thinning and igneous intrusions. Extrusion and intrusive magmatic activity continued till the Quaternary. Yemen Trap Series (Geukens, 1966) are made up mainly of alternating lava flows (basalts, andesites or trachyte porphyries) and different types of tuffs. These basaltic, rhyolitic and ignimbritic successions attain a thickness in excess of 2500 m in the NE of Yemen (Al Subbary et al., 1993). The age of YTS ranges from Oligocene to Miocene (Al-Kadasi, 1994). Basalt of the Tertiary age is characterized by columnar, fine grained, porphyritic and intergrowth textures. The Quaternary Yemen Volcanic Series (YVS) are exposed bordering the Tertiary volcanics (YTS). Rhyolitic tuffs are of limited occurrence and the Quaternary basalts are fine grained and show porphyritic and intergrowth textures. Rhyolitic tuffs exhibit medium to fine grained porphyritic and myrmekitic textures. Earlier works on the bimodal volcanic rocks are largely limited to geological mapping of the Taiz and its surrounding areas (Kruck and Schäffer, 1991; DEY, 1997). Geology including petrogenesis of Sabir granitic rocks has been studied in detail than the surrounding volcanic rocks (Refaat et al., 1980; Shaalan et al., 1983; Youssef, et al., 1992; El-Gharbawy, 2011). Stratigraphy of a bimodal volcanic rocks and fault types present in Taiz area have been worked by Malek et al., (2014). The present paper documents geological and petrographical features of the Tertiary bimodal mafic-felsic suite represented by flows, plutons and dykes in addition to identification of mineral types in volcanic soils of Taiz and its surroundings.

2. Study Area

Taiz city is located in the southwestern part of Yemen in the watershed area of upper Wadi Rasyan. It lies mainly at the foot hill and slope regions of Sabir mountain in the northern highlands and bound by the latitudes 13°32' N - 13°44' N and longitudes 43°54' E - 44°10' E (Figure 1). The Taiz city and its vicinities are almost covered with product of the magmatism comprising mainly typical bimodal volcanic deposits, felsic plutonic rocks, mafic and felsic dykes as well as sills. The bimodal volcanic rocks encompass alternating sequences of volcanic lava flows and volcaniclastic deposits of varying composition from mafic to silicic types. The lava flows are believed to be extruded and fed from fracturing and fissuring in the old rocks through which magma emerged in successive pulses, flooding surrounding region. These sequences range in age from Oligocene to the lower Miocene (Beydoun et al., 1998). They form a part of the western volcanic margin of Yemen which is related to the Afar plume (Civetta et al., 1978; Capaldi et al., 1987; Chiesa et al., 1983, 1989).

During the field traverses, volcanoclastic materials and fresh rock surfaces exposed along the road cuttings as well as on quarry surfaces were observed and studied. Geological features were documented in the field note book. Compass-clinometer and GARMIN 12 channel GPS were used respectively to record the attitude and location of the different lithounits. The coordinates of the outcrops were converted to Universal Transverse Mercator (UTM) with Transfo and then plotted in Surfer 8. Geological map of Taiz area published by Kruck and Schaffer (1991) was verified and necessary corrections in the geological map were made based on the field study and satellite images. In the field various Tertiary volcanic and magmatic intrusive rocks were distinguished. Different rock samples from the study area were collected from the 110 exposures with the help of a field hammer. 14 representatives volcanic soils (volcanic ashes) found between the different lava flows were characterized for their mineralogy by XRD analysis.

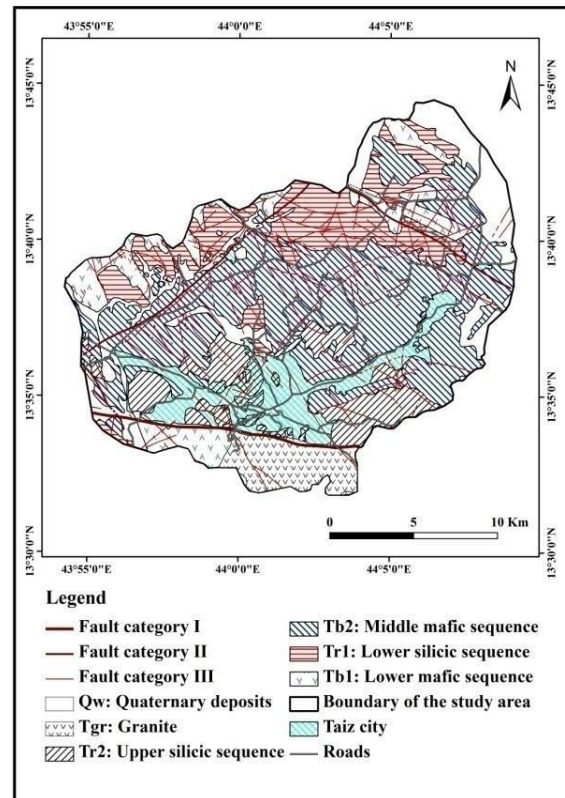


Figure 2: Geological Map of the Study Area (modified after Kruck et al., 1991; DEY, 1997; Malek et al., 2014)

Physical properties of the collected rock samples were studied with the aid of a magnifying lens. For the petrographic studies, 52 thin sections of different rock types were prepared in the laboratory by cutting the rocks using micro-cutting machine followed by reduction in the thickness of the rock slice to the required size using carborundum powder on a grinding wheel. The thin sections of the rocks were then mounted on a glass slide with the help of epoxy for their studies under petrological microscope. Photomicrographs were taken with digital camera to showcase the distinguishing and other optical characters of the minerals.

4. Results and Discussion

4.1. Tertiary Lower Mafic Sequence (Tb1)

Tb1 flows represent the lower most basaltic sequence of Tertiary volcanic rocks and the main activity which took place 29-20 million years ago (Civetta et al, 1978). This sequence is dated of Eocene age. In the study area, Tb1 comprises dominantly the basaltic lava flows and minor volcanoclastic deposits. They represent the volcanic products extruded primarily through the feeder dykes paralleling the axis of the Red Sea, and comprise either multiple or single cooling flow interbedded with centimeter to several meter thick basic volcanoclastic deposits. They are largely found scattered in the northwest border and to the west of Sabir mountain, covering 9% of the total area (see Figure 2). They occur deviated from horizontal attitude due to paleorelief peculiarities and/or riftogenic tectonic motions which are related to the development of the Gulf of Aden and opening of the Red Sea, or east African rift valley system. The basaltic lava flows which have developed joints owing to cooling have subsequently been filled with late hydrothermal alteration products. Further alterations have resulted in the development of angular fragments. Thus, the fresh to slightly altered basalt unit occurs as highly jointed, strong as well as very angular with sharp edges (eg, outcrop south of As-Salmani village). These jointed /massive rocks display varying colours ranging from dark grey in fresh surface to chocolate brown or dark reddish brown on outer weathered/alterated surface. The rocks, after extraction in the form of crushed stone/aggregate, are being used as concrete and asphalt mix. In the same location, this unit is intercalated with basic volcanoclastics.

Megascopically, the Tb1 rocks at places display porphyritic texture wherein plagioclase and/or olivine phenocrysts are visible to the naked-eye in the hand specimens (Figure 3a & b). They are with or without vesicles. Vesicles do sporadically show infillings with secondary minerals, thus exhibiting amygdaloidal structure. Chalcedony is one of the common infilling as seen at station 92, east of Al-Mulayh village, Al-Hawban area. Phenocrysts of pyroxene (clinopyroxene) are also seen. Thin section studies of Tb1 rock shows that both olivine and clinopyroxene represent the main components and other accessory minerals are represented largely by iron oxides. Also, the cracked coarse phenocrysts of olivine in the fine groundmass are observed (Figure 3c & d). Iddingsite and/or serpentine, as an alteration product of olivine, are/is seen at the rims and along the cracks of phenocrysts. The microscopic study revealed the nature of the Tb1 flow to represent the composition of olivine basalt.

Almost at the top of Tb1 sequence, a continuous horizontal intrusive body is seen and it is overlain by Tr1 (ignimbrite flows) (Figure 4). In some places, the rock appears to show pseudo-schistosity caused by horizons of compact fine-grained volcanics. It is resistant to weathering so, lithological scarps several meters in height are formed. The lower boundaries of Tb1 with the underlying rocks is generally not obscured in the studied area, while the upper boundaries with lower silicic rocks (Tr1) are well exposed and sharp, commonly irregular in most of the localities. The upper boundary of highly weathered Tb1 is encountered at a depth of 11m from the ground surface in one of the bore well section near, Al-Ikam Ajud village, wadi Al-Burayhi, north of the study area (Figure 5).

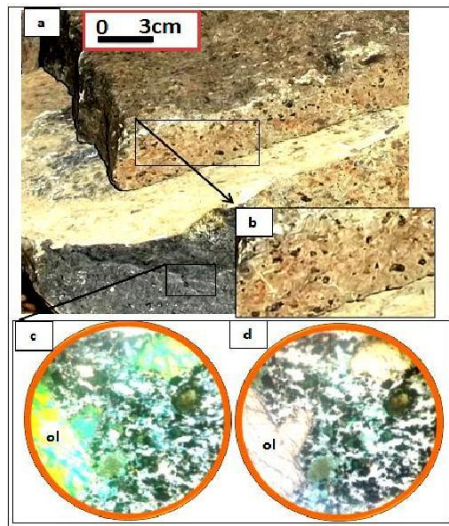


Figure 3: Field photograph of basalt of Tb1 showing porphyritic texture with olivine phenocrysts (a) and Olivine-filled amygdules (b). Also, photomicrographs displaying cracked coarse phenocrysts of olivine (ol) in the fine groundmass (Figures c and d) (XL and PPL; 10X).

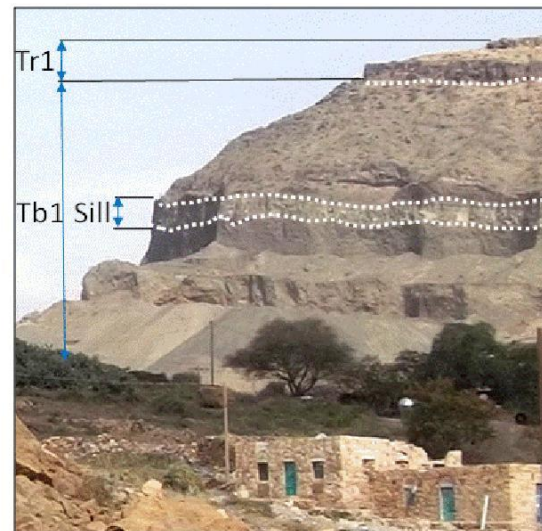


Figure 4: Field photograph showing basalt flow (Tb1) with a sub-horizontal sill and overlain by ignimbrite of Tr1 sequence



Figure 5: Upper boundary of highly weathered Tb1 as seen in a bore hole located near Al-Ikam Ajud village, wadi Al-Burayhi, north of the study area

4.2. Tertiary Lower Silicic Sequence Phase (Tr1)

The previous sequence (Tb1) is followed by Eocene - Oligocene felsic volcanic rocks (Tr1) which are exposed along the northern border of the study area with a dip of about 30° in SE direction. Thickness of these deposits reaches 200 m with an areal extent of 14.58% of the total investigated area. Topographically it forms high plateaus with escarpments or cliffs. In some places, Tr1 is forms cuesta-type almost horizontal morphology. Thus, Tr1 varies in its appearance from multi-sheet stratifications to domal mountains and hills (Figure 6).

Petrologically Tr1 is represented by jointed rhyolites/dacites, ignimbrites, rhyolitic tuffs, lapillistones, volcaniclastic breccias, and random pumice and obsidian. The higher amounts of volcaniclastic rocks

in Tr1 sequence indicate that initially volcanism of silicic volcanic rocks was more explosive (Malik et al., 2014). They are generally hard, massive rocks although flow structures may also be seen, showing foliation, and cooling discontinuities. In Tr1 sequence, vertically change in lithology and colonnade columnar jointing features was observed. This feature is best studied along a rhyolite quarry located in the cliff-face at long Al-Steen road, Ad Daraj village in the northern part of Taiz city (Figure 7a). Here, the Tr1 stratigraphic sequence consists of three main alternating layers viz., from bottom to the top: 1) whitish yellow coloured welded rhyolitic tuff, ranging from fine-grained ash to lapilli, 2) yellow to reddish brown coloured massive, fine grained, highly welded ignimbrite showing flow band structure and 3) reddish yellow coloured colonnade columnar jointed rhyolite. The yellowish brown coloured weathered/ altered basaltic dyke shows discordant relationship with layers 1 and 2 and does not cut layer number 3 implying, it is younger to these layers and layer 3 wasn't emplaced coevally with both 1 and 2 layers (Figure 7b). However, intensive field studies on the boundary between the volcanoclastic rocks and rhyolite/dacite in several locations indicate that they were emplaced at least in part simultaneously.

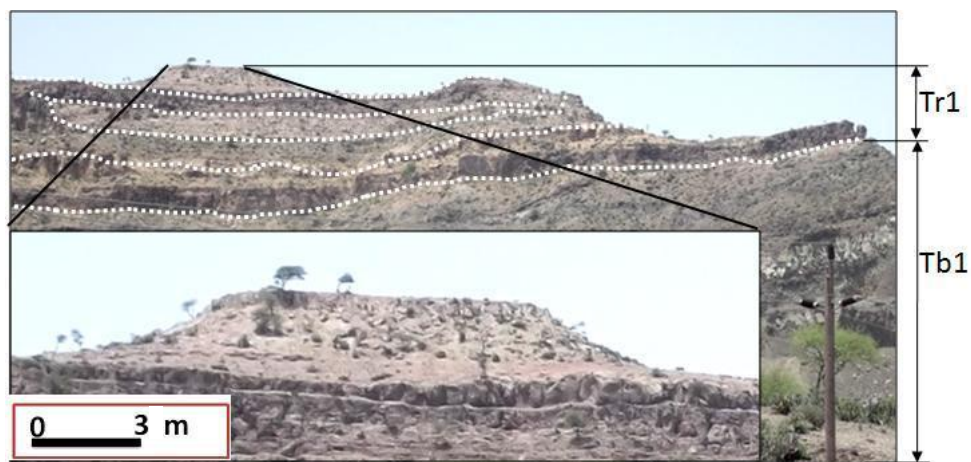


Figure 6: Cuesta topography with multi-sheet stratifications developed in the Tertiary lower rhyolite/ignimbrite flow (Tr1). Note the boundary between Tb1 and the Tr1

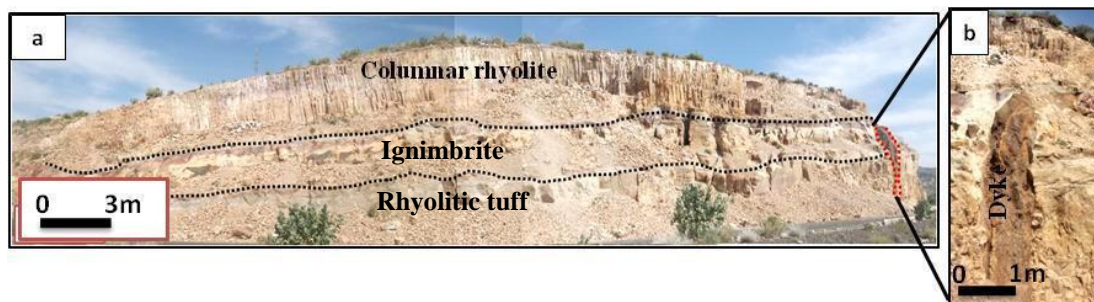


Figure 7: (a) Field view of rhyolite lava flows with well-developed colonnade columnar jointing in the upper flow; (b) altered basaltic dyke older to colonnade columnar joints, near Ad Daraj village, Al-Steen road, north of Taiz city

In some exposures, as at Aumam Mountain, the rhyolitic flows display colonnade shrinking joints which are varied in their shape and size along the flow direction than in the vertical section at the

same location (Figure 8a). In the present day urban planning, the rocks of Tr1 rhyolitic lava flows are extracted by quarrying to use them as building stones (Figure 8b). At places, spherical weathering in the columnar rhyolite has produced spheroids as big as 1.80 m diameter. In addition, exfoliation, blocky and cavernous weathering features were also found in the same location (Figure 9).

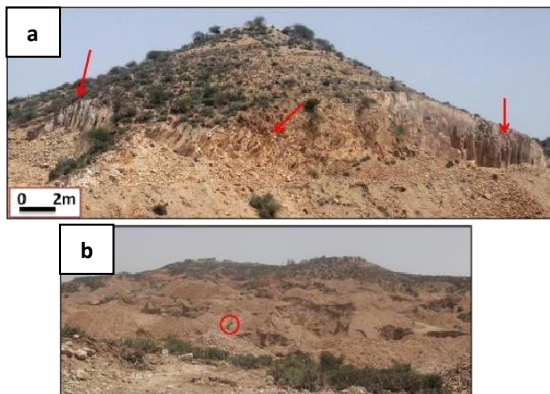


Figure 8: View of lower Tertiary rhyolitic lava flows (Tr1) with colonnade columnar jointing showing the variation in the shape, size and the diversion direction of the colonnade columnar joints in the Aumam mountain area, NE of Taiz city. (b) Displays quarry sites which are used for extraction of build stones, in the same location. The scale is the Pulverizer (red circle)



Figure 9: Spherical weathering feature in columnar rhyolite at Aumam mountain, NE of Taiz city

The Ignimbrites occur as flows and compact welded volcanoclastics with flattened and stretched fragments (Figure 10). At places, these rocks are seen as layer with columnar structure. Megascopically, the very important feature which was observed on most of the cut rock sample surfaces of the columnar rhyolites, ignimbrites and welded rhyolitic tuffs is the small pits or vesicles (1-7mm diameter); some of them are filled with powdery/hard white/black materials of secondary minerals. This feature is more frequent in the ignimbrites and welded rhyolitic tuffs than in the columnar rhyolites (Figure 11).

The ignimbrites at other places do not have pits or vesicles but contain flattened and stretched fragments known as fiammes. These fiammes are clearly visible in the hand specimens (see Figure 10) and their development is possibly due to the magmatic movement. The development of macrofractures on the surfaces of columnar rhyolite hand specimen are observed and these are filled with magnesium minerals (Figure 12a), while they are sometimes healed by hematite mineral as occurred in ignimbrite sample (Figure 12b).

In the field, clusters of thunder eggs (lithophysae) are also observed within welded rhyolitic lapillistone of the Tr1. This kind of clusters are clearly visible in the Ad Daraj village at Al-Steen road, to the north; where they form zones in the lower parts of rhyolitic lapillistone (Figure 13a & b) and near An Najaydah village in the northwestern part of the study area (Figure 13c). The size of concentric or star-shaped thunder eggs (lithophysae) varies from less than 1 cm to 8 cm. Another notable feature in most of Tr1 rocks is the stain like feature possibly created by iron oxides (hematization and limonite)

during the alteration of Fe-bearing minerals (Figure 14a & b).



Figure 10: *Fiammes* in welded ignimbrite, at middle of Aumam mountain, NE of Taiz city. Coin diameter 2.6 cm

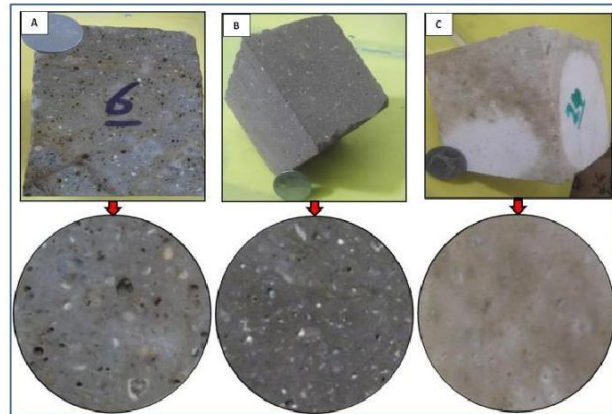


Figure 11: *Small pits or vesicles* on the cut rock sample surfaces of the Tr1 flows. Note the size and density of these features are reduced from ignimbrites (a) to welded rhyolitic tuffs (b) to the columnar rhyolites (c). Coin diameter 2.6 cm

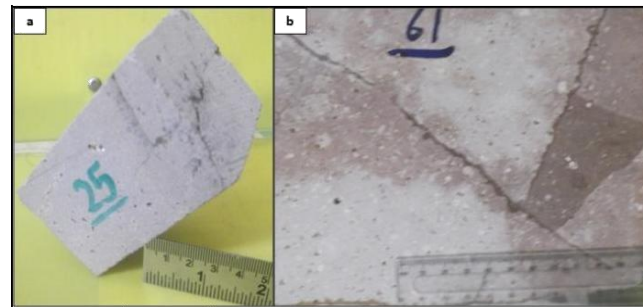


Figure 12: *Macrofractures filled with magnesium minerals* in the columnar rhyolite, (a) and *healed by hematite mineral* as occurred in ignimbrite sample (b)

Microscopic studies of jointed rhyolite/dacite of Tr1 reveal that most of the rock sections show porphyritic textures and on a minor scale, flow fabrics (Figure 15). They contain quartz grains, feldspar phenocrysts and biotite, opaque/Fe-oxide embedded in altered fine grained matrix of the same composition with or without clayey minerals. The ignimbrites in thin sections display pyroclastic textures and are composed of volcanic glass shards, rock fragments of vasicular basalt, quartz and opaque. These components are embedded in a glassy groundmass (Figure 16a & b).

Observed microfractures developed in the ignimbrites are normally filled with volcanic glass or/and secondary minerals while the vesicles or pits seen across the sections are either unfilled or partially filled with the secondary minerals (Figure 16 c & d).

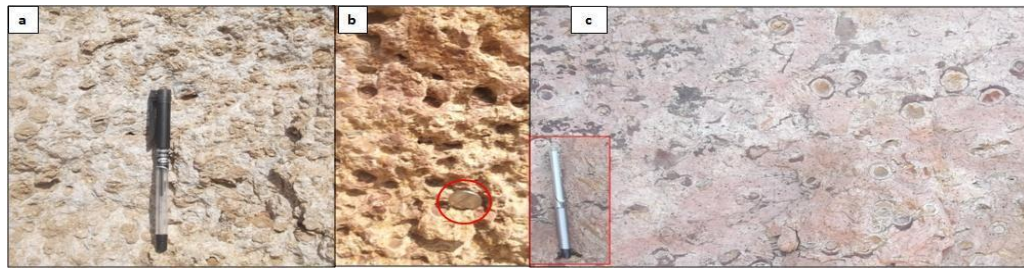


Figure 13: Rounded lithophysae "thunder eggs" in the lower part of welded rhyolitic lapillistone of the Tr1 found near the Ad Daraj village on Al-Steer road to the north of the study area (a and b) and near An Najaydah village to the northwest of the study area (c). Pen lengths 16.7 cm and 14 cm in Figure a and Figure c respectively. Coin diameter 2.6 cm

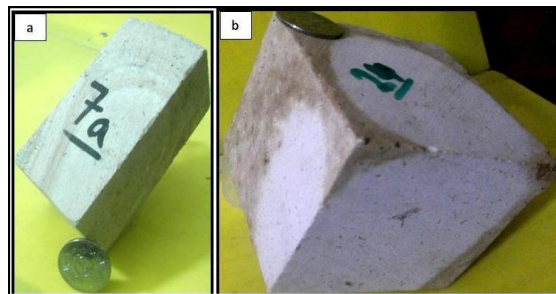


Figure 14: (a & b) Iron oxide coatings in Tr1 rocks

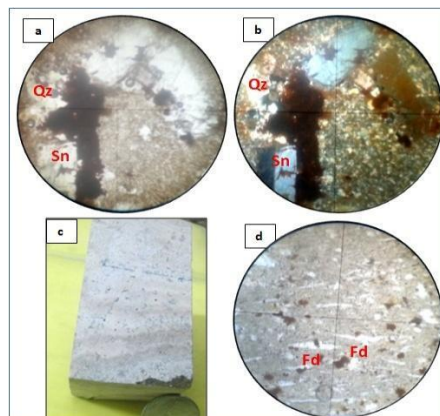


Figure 15: Porphyritic texture in jointed rhyolite/dacite flows (Tr1) in PPL and CPL respectively (a and b) (10X) and (c and d) are showing flow fabric in hand specimen of rhyolite and in its thin section respectively. (in PPL and 10X). Coin diameter 2.6 cm (Fd= Feldspar, Qz= Quartz, and Sn= Sanidine)

Mineralogy of tuffs of Tr1 sequence could not be made out as they are highly altered (Figure 17). They contain voids or vesicles which are at places filled with secondary minerals. In general, all thin sections studied of Tr1 rocks display the activity of hydrothermal solutions and consequent alteration of these rocks.

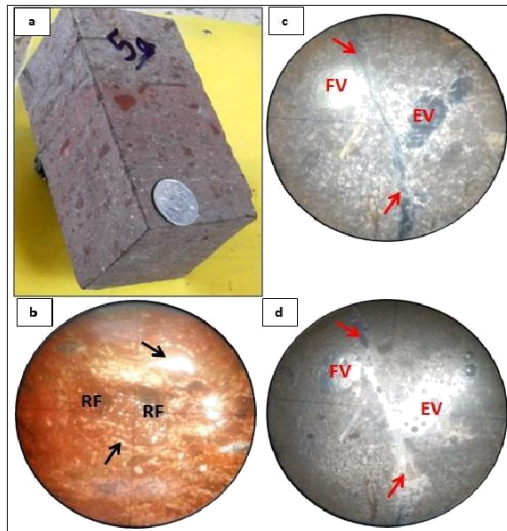


Figure 16: Hand specimen and photomicrograph (10X, CPL) showing pyroclastic texture in the Tertiary ignimbrites (Figures a and b). Note volcanic glass shards (black arrows), rock fragments (RF) of vascular basalt, quartz and opaque. Figures (c and d) exhibit microfractures filled with volcanic glass (red arrows), while the vesicles or pits are either unfilled (EV) or partially/fully filled (FV) with the secondary minerals (in PPL and CPL; 3.5X). Coin diameter 2.6 cm

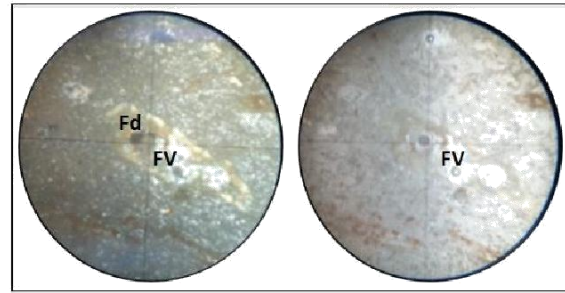


Figure 17: Photomicrographs (3.5X) in CPL and PPL showing alteration of feldspar phenocrysts (Fd) set in intensely altered groundmass and vesicles filled with secondary altered minerals (FV) in tuff belonging to Tr1 sequence due to permeation of hydrothermal solutions

4.3. Tertiary Middle Mafic Sequence Phase (Tb2)

The Middle basic volcanics (Tb2) of Cenozoic are represented in Taiz area by basaltic lava flows and volcanoclastic deposits. Similar to Tb1 and Tr1, these are also extruded primarily through the feeders like - dykes. Some of sub-vertical N-S to NW-SE trending basalt feeders are exposed along Al-Steen road in the investigated area. These lava flows came as a second basic phase and overlie the first acidic phase (Tr1). They are considered Oligocene-Miocene in age (Kruck and Schaffer, 1991). In the study area, the rocks and deposits of Tb2 have a greatest areal extent in comparison to all other units with an areal extent of 39.61 % of total area and a thickness of about 100 m. They are widespread on a long middle zone extending from east to west (see Figure 2), topographically forming undulating plains inside Taiz plain and are dissected by major Wadis. The most striking feature of Tb2 is its occurrence as alternating sequence of more than one lava flow. These lava flows show different physical characteristics (colour, heterogeneity, discontinuity, thickness, horizontal attitude, weathering/alteration, intercalation and repetition with depth) in both vertical and horizontal directions implying variation in eruption type, mode of transport, distance travelled from the vent, temperature of the deposits, particle size, water content and paleorelief of older Tr1 sequence.

In some places, Tb2 lava flows are poorly exposed due to high weathering and consequent soil formation. The thickness of the soil cover does not exceed 10 m on the slope side of hills and increases to reach more than 30 m in valley bottoms.

The fresh and clear exposures of basaltic lava flows (Tb2) are seen along road cuts and some are seen as natural outcrops. Generally, in these outcrops, Tb2 are comprised of jointed basalts, massive basalts and/or volcanoclastic deposits. According to Fisher (1966) and Gillespie and Styles (1999), the

volcaniclastic deposits can be classified as tuff-breccias, lapilli-tuffs, agglomerates and lapillistones based on their particles sizes. Locally, jointed basaltic lavas overlie volcanoclastic deposits of the same or different age and /or laterally intercalating with them. This kind of feature is observed in several places, particularly in the eastern parts of the study area such as NE Ash-Shu'ub village and in some outcrops occurring along Al-Rahidah road. For illustration of these features of Tb2, the excellent exposed section found near Al-Jibalah village in Al-Stein road was investigated. It consists of sequence of five layers (Figure 18) and from bottom to the top consists of the following: (1) reddish brown to dark greenish grey coloured massive basalt with more than 3 m thickness, (2) creamy white to reddish brown, unconsolidated to semi-consolidated volcanic ashes with a thickness of up to 6 m, (3) brown to dark grey colour jointed basalt flow with an irregular joint pattern (polyhedral blocks) and thickness varying from less than 1.5m to 5m, (4) brown to light grey colour poorly sorted volcanic agglomerates and (5) brown to greenish grey colour basalt flow with sub-vertical to irregular cooling joint pattern with a thickness of less than 1m to 2.40m.

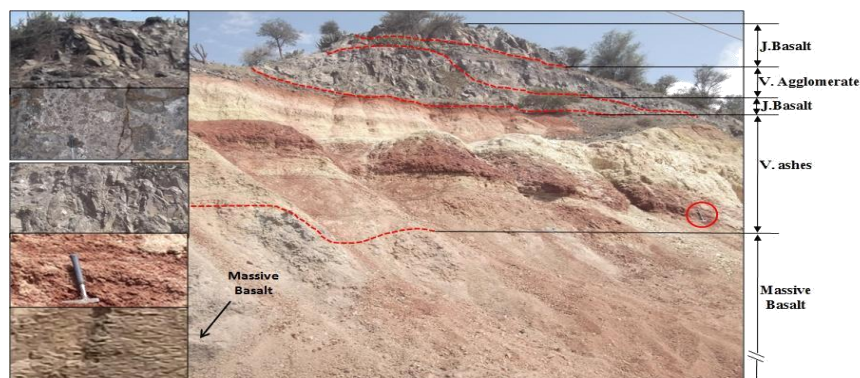


Figure 18: Exposure of the Tertiary middle mafic sequence (Tb2), near Al-Jibalah village, Al-Stein road. Length of hammer 32.5 cm (inside of red circle)

The second example has been taken to illustrate wide change in the physical characteristics of Tb2; vertically and laterally at the same location (Figure 19a-c). This example also includes correlation between the two sides, east and west of a road cut located to the west of Al-Mishhat village on Al-Stein road. For this reason, the representative vertical section at specified parts of the Tb2 sequence was taken on both trench sides for field description purpose. In the west side (Figure 19b, A-B section), the Tb2 sequence consists of the following from the bottom to the top: (1) Light reddish brown to dark grey coloured fine grained massive basalt flow with a thickness of about 3.5 m in this part and increases up to more than 10 m in other parts. These massive basalts have developed joints wherein the joint planes of the unfilled joints are stained by iron oxides. Some joints are filled with carbonate materials, quartz and angular fragments of basic rocks cemented by carbonate materials/calcite, especially near the dyke which cuts this layer (Figure 20).

In massive basalts, vesicles are small and tiny and vugs are of varied dimensions. These are partially or completely found filled with quartz and/or calcite minerals (Figure 21). The upper part of this layer has been subjected to weathering processes before the intrusion of the subsequent cycle basalt which formed the layer 2. The thickness of weathered zone ranges from 15 cm to 60 cm. (2) light reddish brown to dark grey coloured fine grained jointed basalt; this layer is injected through the sub-vertical feeder dyke and displays concordant relationship with the surrounding rocks. The angle of dip

of this lava sheet ranges from few degrees to 47° in the SE direction and the lava sheet is obscured under the layer 3, with thickness ranging from 30cm to more than 3.5m. This lava sheet laterally shows change from randomly jointed basalt (close to dyke) to columnar basalt (in the SE direction). (3) Grey coloured welded and compacted volcanic pyroclastic rocks (lapilli-tuff) with 50 cm to 1.40 m thickness; it consists of angular to sub-angular basic rock clasts embedded in a matrix of volcanic ash and iron oxides. This layer is laterally interlocked with jointed basalt in other parts of this layer. (4) Light reddish brown coloured fine grained jointed basalt with a thickness ranging from 60 cm to 1.5 m is noticed at a distance from the current location. This flow is laterally discontinuous; where in, the jointed basalt may be laterally intercalated with volcanoclastics in some parts.

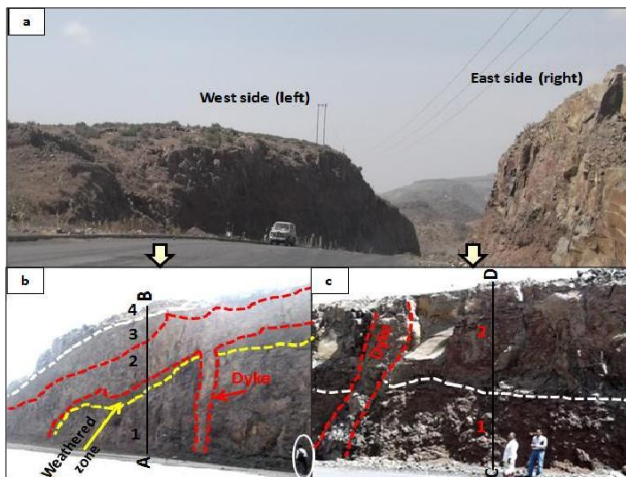


Figure 19: a) The trench cut for laying road shows diverse features of Tb2 flow on either side. b) Western part consists of massive basalt (1); fractured basalt (2), lapilli tuff (3) and fractured basalt (4) Eastern side displays basaltic tuff breccia (c) (1) and fractured basalt (2) Note the presence a dyke and a sill on the western side

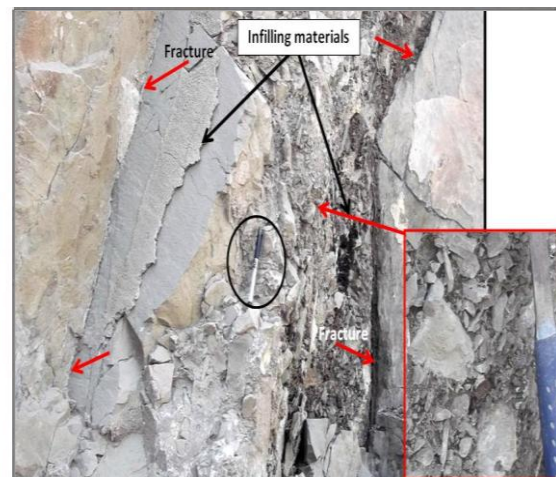


Figure 20: Field photo showing carbonate formed along the joints of Tb2 rocks of western side of the trench

The east side section of the road cutting displays a sequence of two layers (Figure 19c, C-D section) which are from bottom upwards are as follows: (1) Dark grey to light reddish brown coloured welded and/or interlocked, strong to medium strong volcanic pyroclastic rocks (tuff breccia); it is composed of small to medium, vesicular/ massive, angular, sub-angular to sub-rounded, intact to fractured clasts of basic rocks. These clasts are cemented by volcanic ashes, iron oxides and carbonate and silicate minerals (Figure 22). This layer is intercalated laterally with jointed basalt with thickness more than 2.50m. (2) Light reddish brown to light grey coloured fine-grained, highly jointed basalt; this layer is interbedded laterally with volcanoclastic deposits. The fractures are irregular, most of them stained with iron oxides and a few are filled with calcite and/or quartz or with admixture of these minerals and angular basic rock fragments.

Generally, in the investigated exposures of Tb2, the basaltic lava flows can be described as chocolate-brown to/or dark greenish grey coloured fine-grained, slightly to highly weathered, vesicular and porphyritic, in places with plagioclase and/or olivine phenocrysts as the dominant mafic minerals and pyroxene as a minor constituent. The jointed basalts are affected by the development of relatively

random fractures in different directions. Locally, jointed basalts exhibit well-developed columnar jointing structures.



Figure 21: Vugs lined with quartz and calcite on the eastern side of the trench



Figure 22: Tuff breccia, in the Tertiary middle mafic sequence (Tb2), on the eastern side (right) of the road trench. Pen length 16.7 cm (inside red circle)

Highly fractured columnar basalt is seen near Uqush village (Figure 23), where the columns are of major discontinuous form and each column is highly fractured in different directions. The maximum and minimum spacings of columnar structures were measured between 1.38 m and 0.12 m south Qusaybah village, Al-Hamseen road and near Uqush village, Al-Stein road respectively. The columnar basalt, with persistence reaches to 3 m as seen in Wadi Al-Fula, North West of Al-Hawban area.

In most locations, the vesicles and cavities found in jointed basalt are either unfilled or entirely/partially filled with secondary minerals such as calcite/crystallized quartz. The diameter of these cavities or vesicles varies from <2mm to as large as 35 cm.



Figure 23: Exposure of columnar basalt (Tb2) located near Uqush village. Note (inset) each column is affected by fractures in different directions

The discontinuities in the basalt flows are either stained by iron oxides and/or filled with iron oxides and/or rock fragments. Sometimes, these materials take the form of thin sheets ranging in its thickness from <1mm (iron oxides in the form of films) to more than 20mm (carbonates and other minerals) (Figure 24a-c).

In some places, the carbonate materials which have filled the fractures are weathered and appear as white powdery materials in some fractures and weak thin sheets in other. The surfaces of fractures with a thin layer of micro or cryptocrystalline silicate minerals are rarely observed (Figure 24d). The fractures filled with angular rock fragments cemented by carbonate material/calcite are commonly found especially near dykes. The laminated jointed basalts are seen in the eastern part of Al-Mulayha village located in Al-Hawban area, and on the side of Taiz-Sana'a road nearly 300 m far from Hail's biscuit factory (Figure 25a). While the crushed jointed basalt was seen in the southern part of Al-Qurf village in Al-Howban area (Figure 25b).

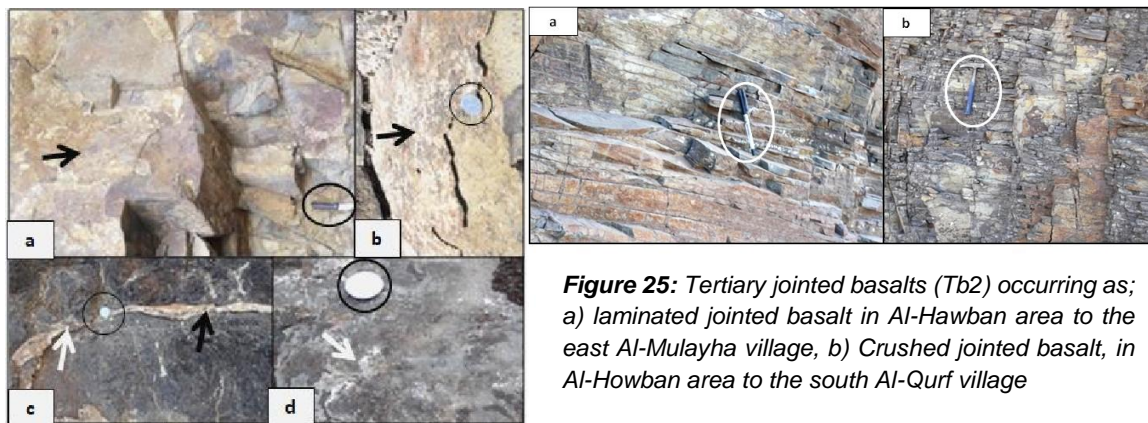


Figure 24: Types of infilling material in the joints of basalt flows (Tb2); a) Iron oxide in the form of stain b) Iron oxides, carbonates minerals and fine soil found as sheets, c) Carbonate minerals, d) Cryptocrystalline silicates/ quartz. Knife length 14.6 cm (inside black circle), coin diameter 2.6 cm

Basalts which show high density macro joints along horizontal and vertical directions join or cross each other. At places major joints have resulted in forming the tabular blocks. At times, these tabular blocks move down under the influence of gravity for which the term wedge slide is used. In general, the type of release surfaces which were identified in the jointed basaltic rocks are plane surfaces, concave surfaces, convex surfaces and inter-crossed surfaces. Small calcite veins, up to 1 mm thick were observed in both the hand specimens and thin sections of crushed basalts (Figure 26). These locations represent sites for extraction of crushed stone/aggregate which are being used for construction purposes. Megascopically; basalt in the hand specimens is greenish grey or light greenish black colour, generally show porphyritic texture with plagioclase and/or olivine as phenocrysts in a fine-grained groundmass (Figure 27). Rare occurrences of fine-grained aphyric basalts have been found in the study area.

Massive trachybasalts with trachy structure and aphanitic texture are seen in the upper Nqeel Al-Epil located to the southeast of the study area, where this lava flow is overlain by Tr2. In trachy basalts, assemblages of secondary calcite and/or quartz are found in small pockets. The amygdalae are filled with glass, chalcedony/quartz, calcite, and zones of quartz-calcite while other vesicles are emptied

due to weathering of feldspar crystals (Figure 28). Massive trachy basalts of Tb2 in Taiz area show pseudo-pillow structure at places implying the intensity of sub-aerial weathering (Figure 29).

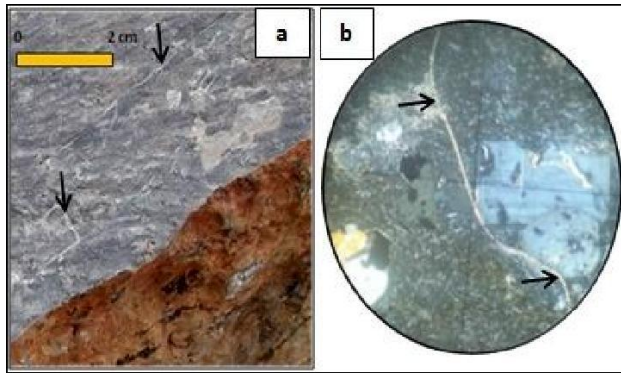


Figure 26: Calcite vein in Tertiary Crushed jointed basalt in Al-Howban area to the south Al-Qurf village; a) In hand specimen, b) In thin section. (CPL and 3.5X)



Figure 27: Porphyritic texture in Tertiary jointed basalt flows showing olivine phenocrysts (black arrows) embedded in a fine-grained groundmass

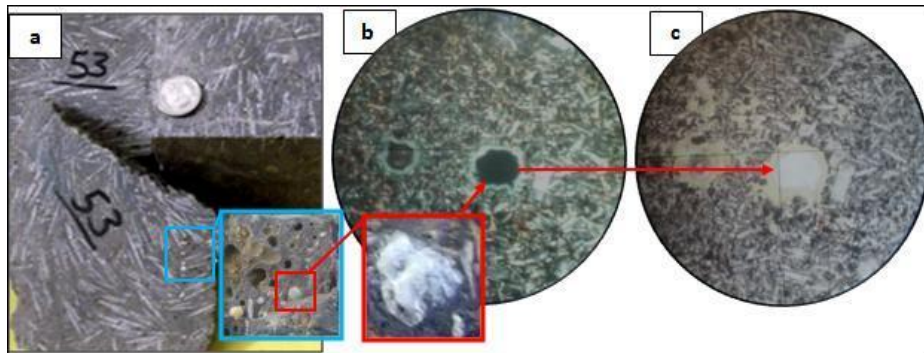


Figure 28: Massive trachybasalt lava flow (Tb2) exposed at upper Nqeel Al-Epil to the southeast of the study area; a) Trachy structure and aphanitic texture in hand specimen. Note emptied vesicles due to release of feldspar /quartz/ calcite crystals by weathering. The amygdales filled with glass, chalcedony/quartz, calcite, or zones of quartz-calcite in thin sections (b and c and insets) (CPL and PPL; 10X). Coin diameter 2.6 cm



Figure 29: The pseudo-pillow structure in massive trachybasalt lava flow (Tb2) near upper Nqeel Al-Epil to the southeast of the study area

In addition, the spherical weathering phenomenon is also observed in the basaltic lava flows as well as in some basic dykes at different sites. The highly spherical weathered basalt is seen in wadi Al-Qula, Al-Hawban area (Figure 30a), while moderately spherical weathered basaltic dyke is observed in Wadi Al-Malih, west of the study area (Figure 30b). The basaltic volcanoclastic deposits are also classified into tuff-breccias, lapilli-tuffs, agglomerates, lapillistones and volcanic ashes. These deposits are different in their types, colour, thickness, grain size, matrix, and degree of roundness of rock fragments and are interlocked laterally and horizontally. They range from strong, compacted, welded rocks to weak altered soils. This large diversity is a direct consequence of the wide range of emplacement and post-emplacment processes operation on volcanic flows (del Potro and Hürlimann, 2008).

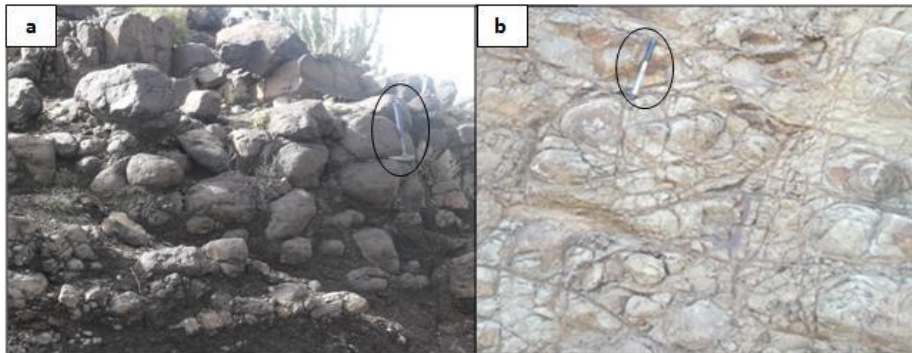


Figure 30: a) Tertiary basaltic lava flows (Tb2) in the form of boulders due to spherical weathering phenomenon seen at wadi Al-Qula, Al-Hawban area, b) Onset of spherical weathering phenomenon in basaltic dyke, Wadi Al-Malih, west of the study area. Hammer length 32.5 cm, and the pen length 16.7 cm

Tuff-breccias are dark grey to light reddish brown in colour welded and/ or interlocked, strong to medium weak. It is composed of small to large, vesicular/massive, angular, sub-angular to sub-round, intact to fractured clasts of basalt rocks. The bomb and/or block clasts range in volume from 25% to 75% (Figure 31a). They are cemented by volcanic ashes, iron oxides and carbonate minerals. Tuff-breccias often occur under jointed basalts or intercalated laterally with them within the Tb2 sequence.

Basaltic lapilli-tuffs are white, grey to reddish brown in colour, welded, strong to medium weak and compacted pyroclastic deposits. The bomb and/or block clasts (>64mm) represent <25% by volume, while lapilli (64-2mm) and ash (<2mm) together constitute less than 75% (Figure 31b). These deposits consist of angular to sub-angular and sub-round, vesicular/ amygdaloidal to massive clasts of basic rocks cemented by volcanic ash and iron oxides. Volcanic agglomerates are brown to light grey in colour, welded volcanic pyroclastics. The basic clasts are poorly sorted angular to subangular, rounded to sub-rounded, vesicular/amygdaloidal to non-vesicular, irregular interlocked and moderately strong. The size of these clasts is > 64mm (Figure 31c).

Basaltic lapillistones are pyroclastic rocks in which lapilli (64-2mm) constitutes > 75% (Figure 31d1). These are grey/light reddish brown in colour, welded and compacted, moderately strong pyroclastic rocks. They consist of angular to sub-angular and sub-rounded interlocked mafic clasts, cemented by volcanic ash and iron oxides/ or silicates and contain irregular voids between them. Some void surfaces are coated with silicates and carbonates as the lining material (Figure 31d2). Generally, in

the study area, the volcanic ashes and iron oxides are more frequent matrix materials in the volcanoclastics.

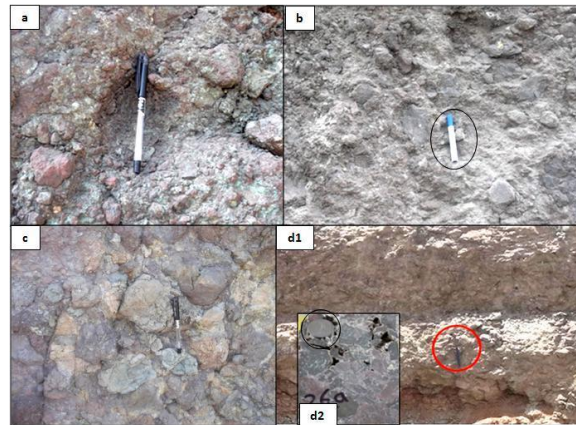


Figure 31: Basaltic volcanoclastic deposits of Tb2; a) Tuff-breccia b) Lapilli-tuff, c) Volcanic agglomerate, d1) Lapillistone; Inset in Fig. d2 irregular, voids in rock clasts are emptied or partially lined with quartz. Hammer length 32.5 cm, pen length 16.7 cm, marker pen length 14.2 and the coin diameter 2.6 cm

The volcanoclastics composed from un-welded and irregular interlocking clasts of two or more of volcanic materials are found at different sites such as, western side of Raheedh -Aden road, near intersection of Sana'a road with Aden road. In the exposures located near Nashit village and Al-Harrir areas, volcanoclastics are laterally and vertically intercalated with jointed basalt of Tb2. Usually, the jointed basalt occurs as lens in volcanoclastics. In the most investigated exposures of Tb2, the basalt flows are underlain by semi-consolidated volcanoclastic materials are found sandwiched between the volcanic sequences (Figure 32).

Due to this situation, the subsidence and landslides were observed in several locations in the study area such as near Al-Thawrah hospital and east of Al-Mulayh village, Al-Howban. In some places, the debris landslides have taken place as a consequence to the high degree of weathering volcanoclastics (Figure 33).



Figure 32: Semi-consolidated volcanoclastic deposits sandwiched between the volcanic sequences



Figure 33: Field photographs showing the debris landslide in intensely weathered basic volcaniclastics-Tb2 located in the southeast NWRA, Ussayfra area. Note the horizontal displacement (about 1.4m) and the movement direction (EW) of landslide. Field notebook height 20 cm (inside white circle)

Microscopically the jointed basalts of Tb2 flow show several features. They are generally porphyritic, where abundant feldspar and olivine and/or pyroxene phenocrysts are set in a fine groundmass of the same composition (Figure 34a). Most thin sections prepared from the samples of jointed basalt flows of Tb2, display glomeroporphyritic texture where crystal clots of varying sizes composed of plagioclase and /or olivine are found in fine groundmass (Figure 34b)

Occasionally, some phenocrysts define a flow fabric. The crystal phenocrysts of olivine are often altered at their rims and along fractures into iddingsite (Figure 34c). The microfractures intersecting the phenocrysts and the fine groundmass are also observed. They are filled with secondary minerals produced by alteration processes (Figure 34d).

Growth zoning in plagioclase with oscillatory variations in composition characterises is seen in some thin sections of these rocks (Figure 34e). Plagioclase with characteristic simple and lamellar and polysynthetic twins also is observed. Massive basalt in thin section shows trachytic texture or flow structure where the plagioclase phenocrysts are almost parallel in defined direction and embedded in fine-grained ground mass of plagioclase and iron oxides (Figure 35).

The vesicles/amygdales are observed within the trachytic-textured groundmass. The amygdales are filled with glass, chalcedony/quartz, calcite, or zones of quartz-calcite. The volcaniclastics in thin section are often consisting of clasts of trachybasalt cemented by volcanic ashes, iron oxides, malachite, glass or silicates (Figure 36). They contain emptied or filled vesicles and microfractures and veins also filled with secondary minerals.

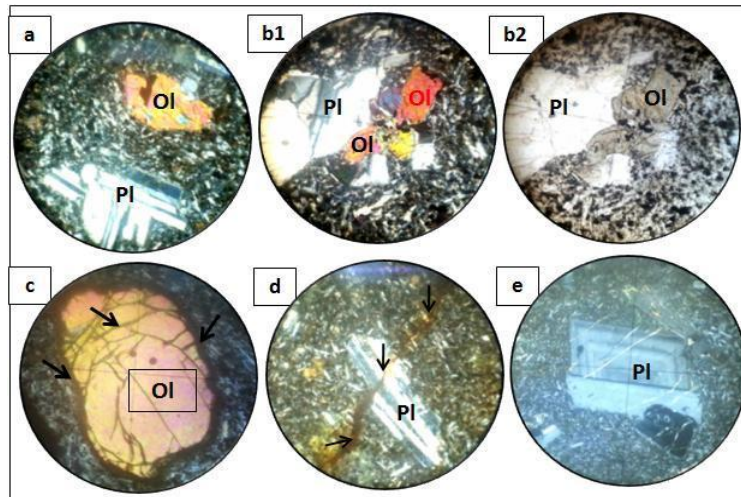


Figure 34: Photomicrographs of Tertiary jointed basaltic rocks (Tb2); a) Porphyritic texture showing abundant feldspar and olivine phenocrysts in a fine groundmass of the same composition, b) Glomeroporphyritic texture, where crystals clots of different sizes composed of plagioclase and olivine are clustered in fine groundmass (in CPL (b1) and PPL (b2); 10X), c) Alteration of phenocryst olivine into iddingsite at its rims and along fractures (in CPL; 10X), d) Microfracture intersecting plagioclase phenocryst and the fine groundmass (in CPL; 10X) filled with iron oxides and e) Growth zoning in plagioclase with oscillatory variations in composition characterises (in CPL; 3.5 X). (Pl= Plagioclase, Ol= Olivine)

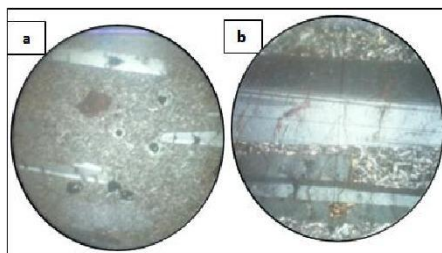


Figure 35: (a and b) Photomicrographs show trachytic texture (flow structure) of Tertiary massive basalt (Tb2) (CPL; 3.5 X and 10X in respectively)

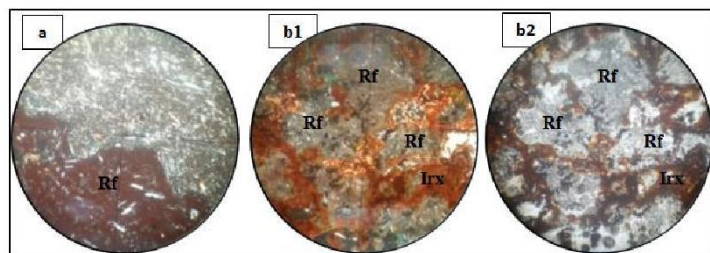


Figure 36: Photomicrograph of Tertiary basaltic volcaniclastic rock Showing a) Large rock fragment of trachybasalt in volcanic agglomerate (CPL; 10X), (b1 and b2) Rock fragments of trachybasalt cemented by iron oxides and volcanic ashes in basaltic tuff-breccia (in CPL (b1) and PPL;10X). (Rf= Rock fragment, Irx= iron oxides)

4.4. Tertiary Upper Silicic Sequence Phase (Tr2)

The Oligocene-Miocene upper silicic volcanic rocks (Tr2) are exposed along the northern part of E-W Sabir fault system as isolated domal mountains and plugs of different sizes and shapes. They cover an area of 14.47 sq.km of the total area (10.6%). Tr2 are represented by fine-grained porphyritic, yellow to gray, white, red, green and pink coloured jointed/massive rhyolites/dacites and/ or varicolored volcaniclastics of rhyolitic composition. Here, the volcaniclastic materials are also

classified based on their particle sizes (Fisher, 1966; Gillespie and Styles, 1999) into ignimbrites, rhyolitic tuffs, rhyolitic lapilli-tuffs and rhyolitic lapillistones.

The most characteristic feature of Tr2 is its occurrence as alternating sequence of more than one lava flow with lateral and vertical variations as in the case of Tb2. Here, a number of exposures of Tr2 were selected and studied in detail. For example, the exposure of Tr2 sequence, located at Al-Hamseen road consists from the bottom to the top (Figure 37a): (1) white to reddish brown colour, un-welded to semi-welded felsic volcanic accumulated materials, including ash, random pumice and obsidian and lapilli tuff with more than 4.5m thickness. The semi-welded lapilli-tuff is laterally interbedded with un-welded other volcanic components. The lapilli-tuff is lithologically composed of fragments derived from sub-angular to sub-rounded silicic and basic surrounding volcanic rocks. Internal texture of the fragments, generally 2–64 mm in size, is homogenous; e.g. silicic and basic fragments are weak and they have been exposed to the same degree of weathering (Figure 37b), (2) light grey coloured massive welded rhyolitic lapilli-tuff with 0.50-1.6m thickness, (3) light grey to white coloured colonnade columnar jointing rhyolite with 0.60-3.80 m thickness, (4) reddish grey to white coloured massive welded rhyolitic tuff with 2-6 thickness and (5) chocolate colour in outer surfaces to light grey and white in inter surfaces, irregular colonnade columnar jointing rhyolitic lava with thickness ranging between 2-2.60 m. In this site, colonnade columnar jointing rhyolite shows porphyritic texture wherein the phenocrysts of quartz and plagioclase are embedded in altered fine-groundmass of the same composition and clay minerals. The minerals of this rock are highly affected by alteration hence the identifiable minerals for these components remains more difficult (Figure 38).

Reddish brown coloured, slightly weathered columnar ignimbrite bed is crossed by moderately to closely spaced vertical to sub-vertical columnar joints. This is emplaced on volcanic ash and tuff accumulations, with different colours, on the north east of the Al-Kahirah volcanic cone and it dips 42° in NE direction. The volcanic accumulated materials often occur welded by reddish brown to brown and gray coloured iron oxides with sandy size grained texture.

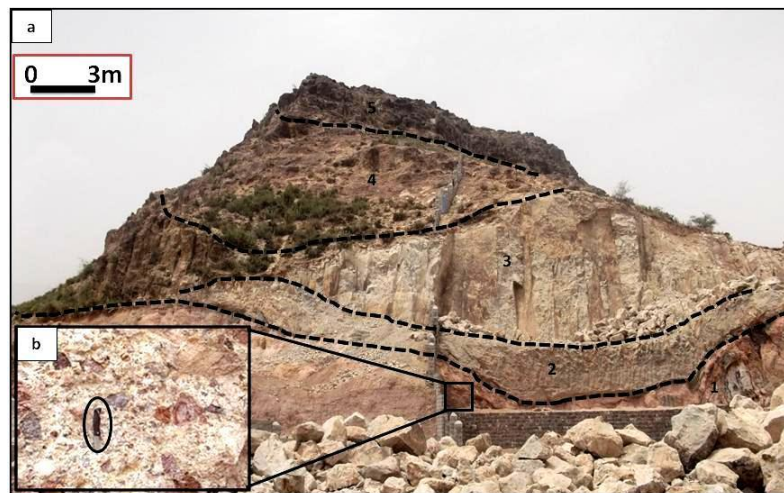


Figure 37: Outcrop of the Tertiary upper silicic sequence phase (Tr2). Note a) Its occurrence as alternating sequence of more than one lava flow, b) Inset-the lapilli -tuff composed of fragments derived from surrounding sub-angular to sub-rounded silicic and basic volcanic rocks. Knife length 14.6 cm (inside black circle)

Gabal Amid area located to the north of Taiz university exposes light grey (reddish brown on outer surface) coloured highly jointed voluminous rhyolite /dacite flow over the whitish grey coloured semi-volcanic tuff. In this site, the thickness of flow is various with an average of 7 m. The big blocks are formed by major joints and each block has also minor joints cutting each other thus forming small blocks of different sizes and shapes.

The columnar and tabular block shapes are more frequent. Rocks of this flow show porphyritic texture. Feldspar phenocrysts are fractured and the flow fabric is visualized. These crystals are affected by alteration and some minerals are totally altered into iron oxides. Most of the groundmass is generated from the produce of alteration process.

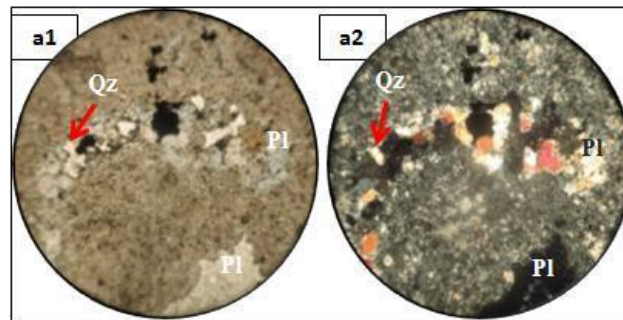


Figure 38: Photomicrographs of porphyritic texture in columnar jointing rhyolite (Tr2), where the phenocrysts of quartz and plagioclase are embedded in altered fine-groundmass of the same composition and clay minerals (in PPL (a1) and CPL (a2); 10X), (Pl=Plagioclase, Qz= Quartz)

The Tr2 sequence found at 0.5 km south of Al-Qurayn village, south east of the study area consists of the following sequence from bottom to the top (Figure 39a): (1) whitish grey coloured, massive, friable rhyolitic tuff with thickness exceeding more than 3m (Figure 39b).

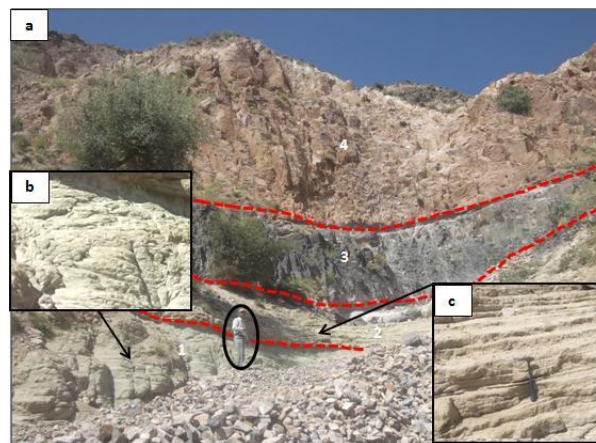


Figure 39: Field photo of the Tertiary upper silicic sequence (Tr2) (a) near south of Al-Qurayn village, south east of the study area displaying massive, friable rhyolitic tuff (b), Tabular, saccharoidal textured rhyolitic tuff (c) and the black coloured volcanic flow (layer3) represented by Pitchstone overlaid by columnar rhyolite (layer 4). Hammer length 32.5 cm.

This layer overlies Tb2 as observed in the surrounding region of the study area, (2) light greenish grey coloured, tabular, sand size grained texture, 1.40m thickness coarse rhyolitic tuff (Figure 39c). The most grain sizes are between 2 mm and 1/16 mm. The clasts composed of basic rocks with size more than 2mm are also found. Microscopically, it consists of quartz grains, k-feldspar and rock fragments. The matrix is composed of glassy and iron oxide minerals (Figure 40), (3) black to dark grey coloured fractured pitchstone with 3.5m thickness in this part and extended to more than 0.5 km and becomes obscured in the north east of this exposure. Microscopically, it shows perlitic fractures in the matrix of the glassy material (Figure 41). Other components are k-feldspar and sanidine, and (4) reddish brown (light grey inner) coloured, sub-vertical irregular columnar rhyolite. Folded flow bands in rhyolite are observed in this rock type.

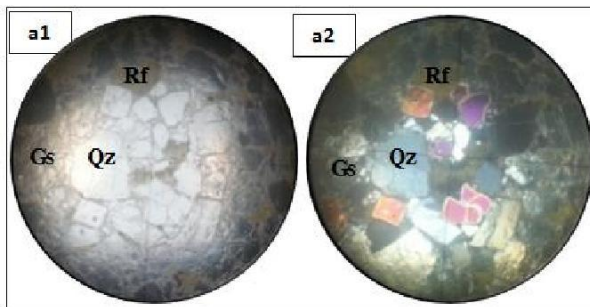


Figure 40: Photomicrograph of tabular, saccharoidal texture, coarse rhyolitic tuff consisting of quartz grains, k-feldspar and rock fragments. The matrix is composed of glassy and iron oxide minerals. (PPL (a1) and CPL (a2); 3.5X). (Gs=Glass, Qz= Quartz, Rf=Rock fragment)

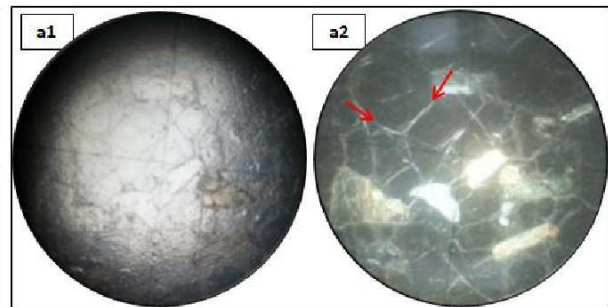


Figure 41: Photomicrograph of the volcanic pitchstone showing perlitic fractures (red arrows) in the matrix of the glassy material. (in PPL (a1) and CPL (a2); 3.5X)

In Jabal Zanikh located west Al-Kharabah village, the Tr2 flow is represented by light grey coloured rhyolite/dacite as big blocks of sub-vertical columns and exhibit more resistance for weathering forming ridges and steep slopes. In some parts of this exposure, the rhyolite/ dacite of Tr2 appears laterally change into white to reddish grey coloured, massive ignimbrite, while in other parts, some blocks of rhyolite/ dacite are unstable due to their occurrence over relatively weak, tabulated volcanic tuff. In hand specimen, this rock shows porphyritic texture, where feldspar phenocrysts are embedded in fine-grained groundmass. The small vesicles (not exceeding 7mm) are filled with secondary minerals. In most places, especially near fault zones the fractures developed in these rocks are stained by iron oxides generated by the dissolution of Fe and Mg bearing silicates (Figure 42). Folded flow bands in rhyolite were also observed (Figure 43).

Tr2 flows appear as light grey to reddish grey coloured, porphyritic columnar rhyolite in the south east of medical College, Al-Habil area (Figure 44a). Microscopically, it shows porphyritic texture and consists of phenocrysts of quartz and k-feldspar which are clustered to show glomeroporphyritic texture (Figure 44b). The groundmass is glassy, opaque and mainly composed of fine k-feldspars and quartz. The microfractures filled with iron oxides and called as transgranular fractures are travelling through some grains and groundmass (Figure 44c).

The vesicles filled with minerals (glass and calcite) are also seen. In the upper wadi Hasanat, south of the study area, the greenish grey to white colour rhyolite occurs overlying thin layer (average thickness 70 cm) of grey volcanic soil found over the thick layer of black to dark grey colour volcanic pitchstone.



Figure 42: Permeation of Mg- and Fe- bearing solutions through fractures developed in Tr2 sequence of rocks. Pen length 16.7 cm (inside white circle)

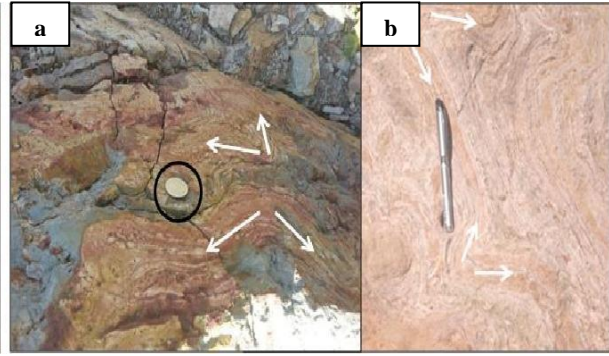


Figure 43: (a & b) Folded flow bands in Tertiary rhyolitic lava flows (Tr2). Pen length 14 cm. Coin diameter 3.1

The pitchstone contains inclusions of basic and acidic xenoliths from the neighboring country rocks and also crossed by basic dyke trending S60°E. Whole sequence of Tr2 in this location is dipped 41° SW. This sequence is laterally changed into light grey bedded semi-welded to welded volcanoclastics; this clearly appears in the east side of the investigated exposure. Microscopically, the rhyolite flow shows micrographic texture in granophyres, where crystal intergrowth is between quartz and k-feldspar (Figure 45a). The radiate intergrowths of quartz and k-feldspar is also seen, where these components are arranged about euhedral, equant plagioclase crystals (Figure 45b).



Figure 44: Fe-oxide stained Tertiary columnar rhyolite (Tr2) showing porphyritic texture (a), and is composed of phenocrysts of quartz and k-feldspar that are clustered to form glomeroporphyritic texture (b in CPL; 10X) and (c) The transgranular microfractures filled with iron oxides (in CPL; 10X). (K-f=K-feldspar, Qz= Quartz). Knife length 14.6 cm

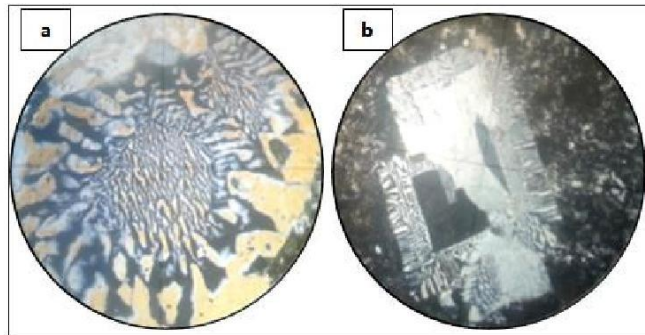


Figure 45: a) Micrographic texture in granophyres in the Tertiary rhyolitic flow. Note the crystal intergrowth between quartz and k-feldspar. (in CPL; 10X), b) The radiate intergrowths of quartz and k-feldspar are arranged about euhedral, equant plagioclase crystals (in CPL; 10X)

The pitchstone in thin section shows hypocrySTALLINE with perlitic cracks. The crystals of quartz, biotite and magnetite are embedded in glass which has spherical fractures and appear as circles. In Thabat area, at the north foot of Sabir mountain, white to chocolate colour, massive rhyolite appears overlaying the white welded rhyolitic tuff. It forms steep slope and hazardous zone dipping 46° to the NW. The welded rhyolitic tuff is massive and shows laminated structure vertically in some parts. This tuff laterally changes to light greenish grey, massive, weak rhyolitic lapilli-tuff with thickness more than 10 m (Figure 46). In the later, the basic clasts are cemented by volcanic ashes. In its upper part, the semi-stabled granitic blocks which have been rolled from Sabir Mountain are found.



Figure 46: Shows Tertiary rhyolitic lapilli-tuff of Tr2, Thabat area, south of Taiz city. Hammer length 32.5 cm

This location represents the northern fault contact zone which is called as Sabir fault system trending E-W and separates the Jabal Sabir granitic mass from the surrounding Tertiary stratified volcanic rocks (see Figure 2). The reddish brown rhyolitic lava flows at Adanah village, to the south east of the study area occur as cap above white welded rhyolitic lapilli-tuff conical hill with slopes having dip angles ranging between 31° and 47° and thickness more than 60m (Figure 47a & b). This feature is also observed in several places at Adanah village. Macroscopically, in the hand specimens of Tr2 flow, the small vesicles are seen; some of them are found as having replaced other minerals (quartz or iron oxides) due to hydrothermal alteration while some other are empty (Figure 47c). Microscopically, the thin section of the rhyolitic lava flow-Tr2 shows vitrophyric and spherulitic textures (Figure 48). It is composed of phenocrysts of plagioclase, quartz, volcanic glass and opaque. These components are assembled in glassy groundmass. Also, the microfractures and vesicles are filled with quartz, glass or/and iron oxides.

The white welded rhyolitic lapilli-tuff forming the lower part of this sequence is composed of angular to sub-angular volcanic clasts of basic rocks and black volcanic obsidian embedded in volcanic ash (Figure 49a). In this location, welded rhyolitic lapilli-tuff appears in massive state, with scarce joints, appearing as homogenous deposit, while at other places, lapilli-tuff occurs as bedded layers (Figure 49b).

At places, the lapilli-tuff/ignimbrite is reddish brown in colour and contains some fragments which are fattened and stretched forming so-called fiammes. Often it contains rectangular shaped vugs which reach up to 4cm in diameter filled with yellowish white coloured friable powdery material as seen in

hand specimens. In some sites, the rhyolitic rocks occur as separated blocks forming instability zones on slope sides. They also exhibit variation in colour from chocolate on outer surfaces to white colour on the inner surfaces. These rocks are brittle, with rough outer surfaces. In the hand specimens of the rhyolitic rocks, some features like corrosion, macrofractures and alteration are observed. Generally, the rhyolitic tuffs display also lateral changes in their colour (creamy-white, whitish grey, yellowish grey and reddish brown), grain size, structure and hardness due to the changes in their components and the conditions of environmental deposition.

The rhyolitic tuffs form the middle or bottom of the Tr2 sequence in the most the investigated exposures and overlain by lava flows of rhyolitic/dacitic composition.

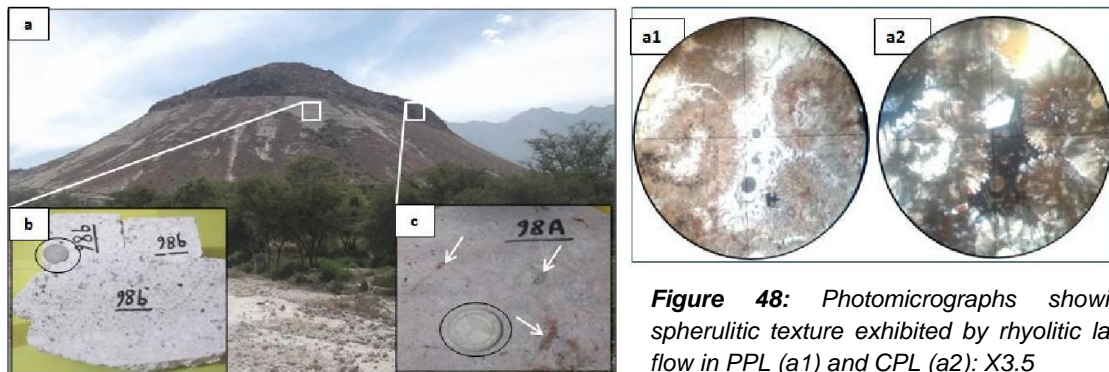


Figure 48: Photomicrographs showing spherulitic texture exhibited by rhyolitic lava flow in PPL (a1) and CPL (a2): X3.5

Figure 47: a) Tertiary rhyolitic lava flows (Tr2), near Adanah village, to the south east of the study area consisting welded rhyolitic lapilli-tuff at the bottom (b) overlaid by rhyolitic flow containing small vesicles some of which emptied (white arrows in c). Coin diameter 3.1 cm

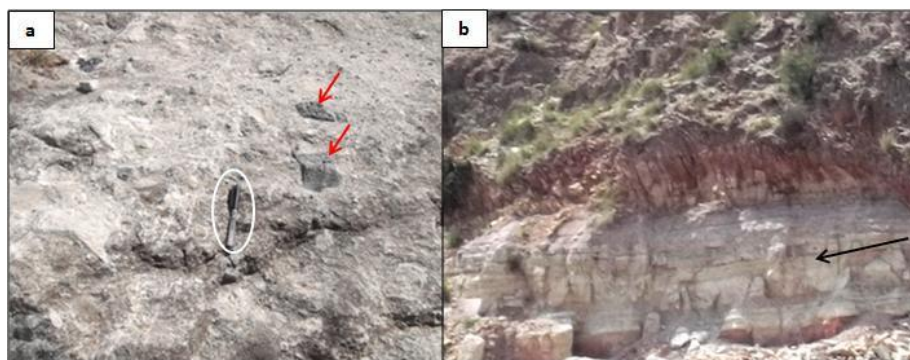


Figure 49: a) Welded massive rhyolitic lapilli-tuff forming the lower part of the Tr2 sequence. Note angular to sub-angular volcanic clasts of basic rocks and obsidian (red arrows) embedded in volcanic ash; b) the rhyolitic tuff occurrence as bedded layers, near Al-Lasab village, south east of Taiz city.

In south face of Gabal Al-Darbah, Al-Masbah area located in Taiz city, the welded rhyolitic tuff (grains size is <math><2\text{mm}</math>) appears as big blocks separated by sub-vertical discontinuities and emplaced on white, reddish brown and dark grey un-welded to semi-welded volcanoclastic deposits. In the lower

volcaniclastics, very weakly cemented coarse grains of quartz mineral are aggregated formed friable layer in some zones. They are also occurred alternating with thin layers formed of sandy grain size of volcanic material in other parts (Figure 50a & b). This weak layer nearly extended horizontal formed unstable base and actually hazardous zone due to the nature this layer and the poor and unplanned construction on it (Figure 50c). The basic clasts and obsidian are also observed in volcaniclastics. In other locations, the welded rhyolitic tuffs display folded structures (Figure 51) and cavities with <10cm up to more than 7m in diameter (Figure 52).

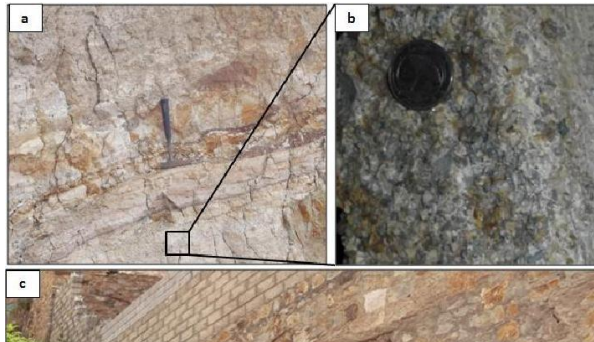


Figure 50: Field photos showing un-welded to semi-welded volcaniclastic deposits (a) with a friable zone consisting dominantly quartz (b). This zone extends into human settlement area (c) causing instability to the civil structures

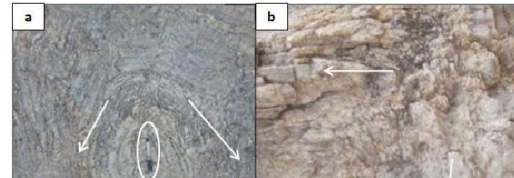


Figure 51: (a, b) Folded structures in the welded rhyolitic tuffs belonging to Tr2. The pen length 14.3 and Coin diameter 3.1 cm

In thin section, they show porphyritic rhyolitic texture where feldspar, quartz, subhedral biotite phenocrysts and iron oxides are embedded in the fine groundmass with same composition. Microfractures filled with iron oxides are seen and also vesicles/amygdales emptied or filled with minerals are observed. The flow structure was also seen.

Megascopically, the small vesicles commonly are observed on the surfaces of cut samples of rhyolitic volcaniclastic rocks, some of them are emptied and other are filled with white minerals (such as carbonate, glass, iron oxides minerals). These minerals can be/or cannot be peeled with a pocketknife such as sample 47p1 (Figure 53a) and sample 23 respectively (Figure 53b).

In places, the rhyolitic tuff is light greenish yellow to white grey in colour. It contains on crystals of quartz mineral in sandy grains size, and black, grey, light yellow rock fragments. The tuff in the block sample appears white or grey to white on the outer surface or brown material as stain, while on the fresh cut sample is white in colour. In other sites, the tuff appears the flow-structures composed from alternating bands of hard brown flows with relatively weak white detritus flows (Figure 54). These layers are intervened by friable brown dust material or emptied voids. Bands can be from few mms to 3 cm thick. In some places, the tuff appears as light reddish brown, massive blocks, compacted with grain sizes ranging between 2 to 64mm, corresponding to lapilli-tuff size. Black to dark grey sub-angler to sub-round clasts of basaltic rocks with diameters > 64 mm were also observed. The cavities with different sizes are found, particularly at the bottom of these blocks formed high potential of collapse hazard zone, especially, the blocks separated by discontinuities.

In thin section, rhyolitic tuff shows the pyroclastic texture, where it consists of basic rock fragments and shards of glass. The vesicles filled with minerals were also seen. The tuff can be contains

different sizes of volcanic rock clasts such as lithic rhyolite /dacite and basalt; this indicating to the violent explosive nature of the felsic volcanism as observed that in wadi Al-Qadhi (Figure 55).



Figure 52: (a, b) The cavernous structure developed in welded rhyolitic tuffs of Tr2. Hammer length 32.5 cm

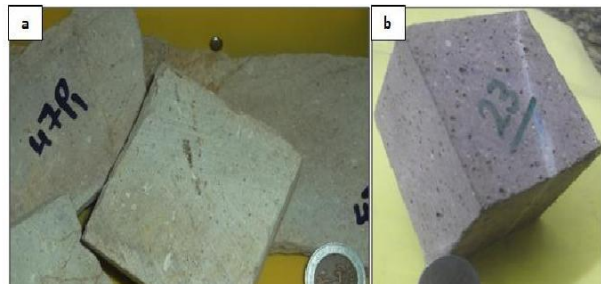


Figure 53: Tiny vesicles in rhyolitic tuff and ignimbrite in respectively are filled with (a) white minerals which can be peeled with a pocketknife and (b) iron oxides minerals which cannot be peeled with a pocketknife. Coin diameters are 3.1 cm and 2.6 cm respectively

The white rhyolitic tuff is exposed with average thickness more than 15 m in the north Hasanat, overlain by rhyolitic lava flow. Generally this tuff is welded, massive but may be contains on parts are either laminated (thickness <50cm) or have irregular joint systems. The block sample of this tuff is exhibited intact but after cut it; the macrofractures may be seen in its inner (Figure 56).

From alteration point of view, the effect of hydrothermal solutions on the joint surfaces is almost very less; this generally indicates that effect near the Sabir fault system or other fault systems is more and decreasing with increasing the distance far from those faults. Microscopically, the thin section of welded rhyolitic tuff reveals that sample primarily consists of plagioclase phenocrysts, quartz crystals and opaques embedded in highly altered fine grained groundmass.



Figure 54: The flow-structures in rhyolitic tuff showing alternate bands of hard brown flows with relatively weak white detritus. Hammer length 32.5 cm. The pen length 14.3

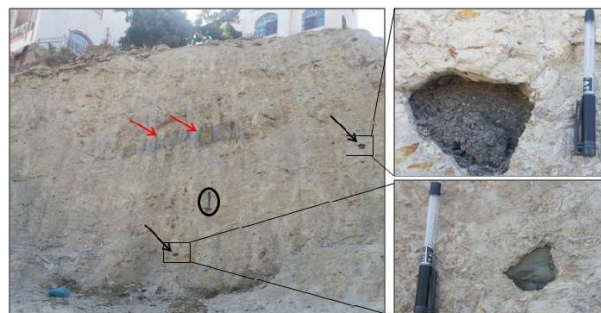


Figure 55: Different sized volcanic rock clasts of rhyolite (red arrows) and basalt/andesite rocks (black arrows), in the Tertiary rhyolitic tuff (Tr2). The pen length 14.3

The radiate intergrowths of quartz and k-feldspar are arranged about euhedral plagioclase crystals formed the granophyric texture. These textures are commonly observed in the rhyolite and rhyolitic tuffs belonged to Tr2. The pyroclasts-poor rhyolite is characterized by abundant feldspar and quartz phenocrysts in fine - grained matrix in comparison to pyroclasts-rich rhyolite (Malik, 2014).



Figure 56: Macrofractures inside of the cut block sample of Tertiary rhyolitic tuff (Tr2) of Thabat area, south of Taiz city. Coin diameter 2.2 cm

The effect of the weathering condition on Tr2 rocks is more clear through forms a number of accentuated ridges and knobs of pyroclasts-poor rhyolite and exhibiting cavities and spheroidal features which are observed in Gabal Al-Birarah, Madinat Al-Noor, wadi Al-Dehi and Gabal Al-Kahirah Castle.

4.5. Tertiary Upper Mafic Sequence Phase (Tb3)

The Tb3 represents the youngest and the uppermost lithological unit of Tertiary volcanic rocks which are confinedly exposed to the south eastern part, outside of the studied area. This sequence is erupted through re - novation of the old faults and fractures, mainly those in the NE-SW direction (DEY, 1997). It mostly comprises on compact basaltic lava flows, but also includes intercalated andesite, mafic conglomerate, tuff layers and red and white ash. It occurs as dykes and sills intruded into the various Tertiary rocks (e.g. volcanic rocks and granite intrusions). Microscopic observations show that most of the Tb3 are fine grained, nonporphyritic and rarely contains plagioclase phenocrysts (Malek et al., 2014).

4.6. Volcanic Soils

In Taiz area, Tertiary volcanic units are underlain or intercalated with varicoloured semi-unconsolidated accumulated volcanic materials. The powder X-ray diffraction (XRD) studies on volcanic ash (volcanic soils) reveal sharply defined reflections (Figures 57-60). The mineralogical search carried out by adopting the standard procedure revealed that clay minerals namely montmorillonite and kaolinite as the major mineral phase in most of the samples with minor amounts of mica group of minerals such as muscovite, vermiculite and chlorite, in addition to talc, feldspar, calcite and halloysite. Quartz is present in almost all the soil samples.

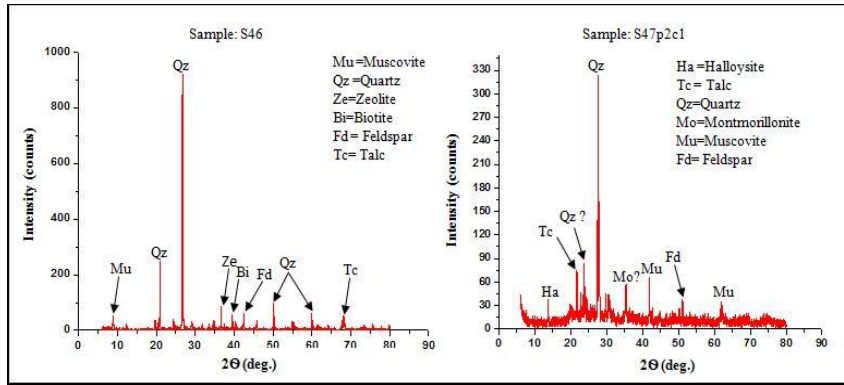


Figure 58: XRD patterns of S46 and S47p2c1 volcanic soil samples

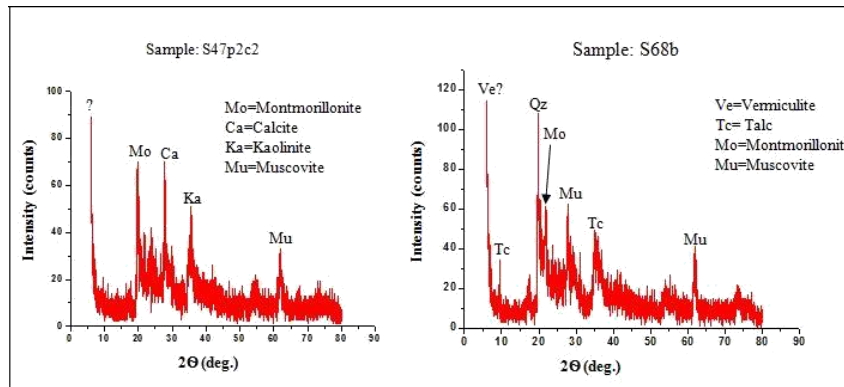


Figure 59: XRD patterns of two volcanic soil samples (S47p2c2 and S68b)

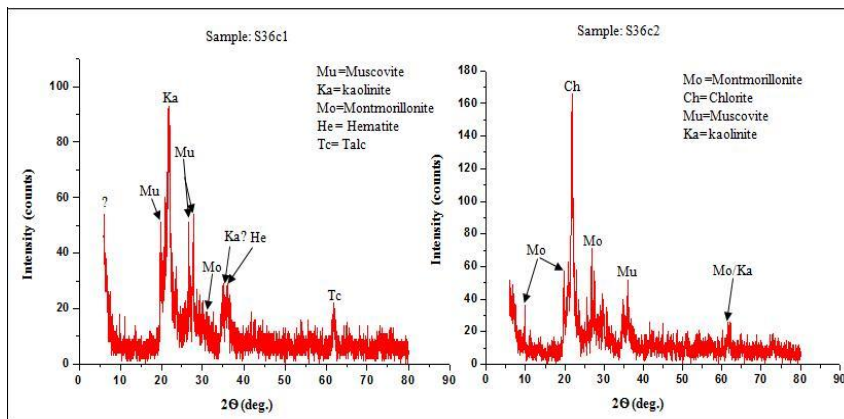


Figure 57: XRD patterns of two volcanic soil samples (S36c1, S36c2)

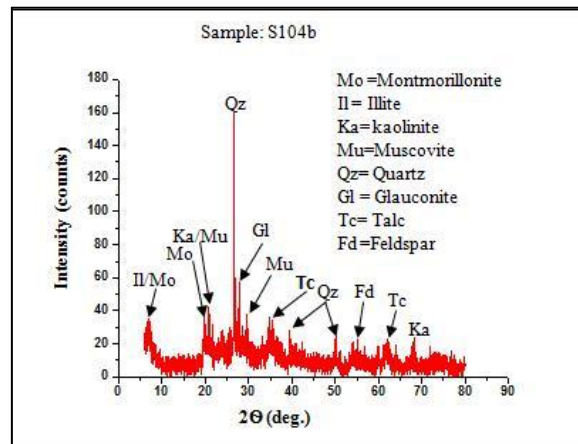


Figure 60: XRD pattern of S104b volcanic soil sample

4.7. Younger Intrusives

Sabir Granitic Pluton

Jabal Sabir granite body dated to Miocene age (Shaalan and Zalata, 1983) is one of the Tertiary intrusive bodies exposed in various locations, especially in the south and along the western escarpment slopes of Yemen highlands, parallel nearly to the general trend of the Red Sea. The Jabal Sabir granite is emplaced as laccolithic body inside the older stratified Tertiary Yemen volcanic rocks, forming the dominant morphological feature (Sabir Mountain) overlooking the city of Taiz in the southern part of the study area (see Figure 2). It is characterized by high lands, steep slopes and deep valleys. Physical weathering of varying intensities has produced different sizes of granitic blocks and boulders along the slope sides. At places deep valleys have been filled by the granitic boulders. The waterfalls and channels are the dominant features in the Sabir area. Tertiary granite contacts with the surrounding Tertiary volcanic rocks covered by the Quaternary deposits are although sharp, it is distinct in some places. Along northern contact, the fault breccia is observed. It is composed of angular to sub-angular and sub-rounded blocks of basic and granitic clasts which are cemented by carbonate material (Figure 61).

The Tertiary granitic masses consist mainly of alkaline or peralkaline granite, white to greyish white coloured, massive, medium to coarse-grained with grading up to granite porphyry and almost < 5% of dark minerals. They belong to the alkaline or peralkaline suite of A-type granites (El-Gharbawy, 2011). These are produced by fractional crystallization in the basic magmas (Capaldi et al., 1987; Chazot and Bertrand, 1995).

Microscopic studies of Sabir granitic rocks reveal that the main rock forming minerals are k-feldspar (orthoclase, perthite, and perthitic microcline), quartz, hornblende and biotite with accessory minerals zircon and other opaque minerals (Figure 62a). K-feldspars are the most common and occur as subhedral to lath-shaped crystals. It shows narrow lamellae of albite forming a braided pattern in an orthoclase host. In some thin sections, the microperthitic texture is observed (Figure 62a & b).

The micrographic texture is also seen where the intergrowth is between quartz and plagioclase minerals. Quartz appears as anhedral to subangular grains.



Figure 61: (a) Field photo shows part of the E-W Sabir fault system along the northern contact between Tertiary Sabir granite and the surrounding Tertiary volcanic rocks (Tr2) and (b) The occurrence of fault breccia composed of angular to sub-angular and sub-round rock fragments of basic and granitic clasts which are cemented by carbonate material, Hammer length 32.5 cm.

In some thin section, interlocked aggregations of quartz grains, biotite, hornblende crystals and opaque minerals are seen. Most of the feldspar and quartz crystals are large in size. This is characteristic of almost all the different granitic samples. Biotite is less common and present as subhedral to anhedral grains and shows pale to dark brown pleochroism.

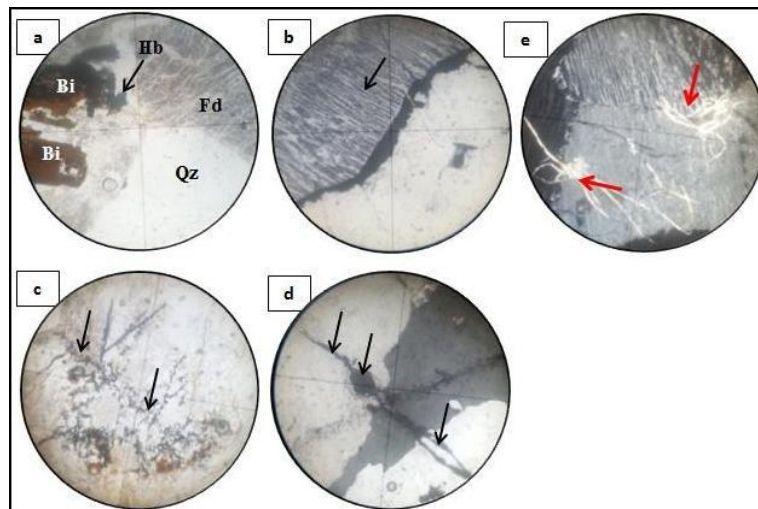


Figure 62: Photomicrographs of Sabir granitic rock (a) containing k-feldspar(Fd), quartz (Qz), hornblende (Hb) and biotite (Bi) with opaque minerals under plane polarised, 10X, (b) showing microperthitic texture, under crossed nicol, 10X, and microfractures, veins and cavities that are filled with calcite and iron oxides (c, d) under crossed nicol 10X. The microviens are filled with calcite (red arrows) under crossed nicol (e) 10X

Usually, it occurs as elongated irregular skeleton and contains small inclusions of quartz grains. Locally, the biotite crystals are partly magmatically corroded. In some thin sections, the muscovite has also been seen.

The zircons are present in some thin sections, occurring as rounded grains. Generally, Sabir granitic rock samples in these sections are characterized by microfractures, veins and cavities that are nearly filled with minerals especially calcite, iron oxides and quartz (Figure 62c & d). The microveins are filled with calcite and are seen almost in all the thin sections (Figure 62e). The granite (syenite) hand specimens taken from Thabat area appear to be relatively coarser than some of the other samples. Granite of this area is characterized by coarse grained texture with phenocrysts of white plagioclase and quartz.

Individual grains of both the plagioclase and quartz measure a length of about 2cm. Biotite and hornblende grains are visible to the naked-eye in the hand specimens (Fig.63a). The miarolitic cavities occupied by euhedral crystals of quartz, alkali feldspar and chalcedony are also found in hand specimens of granite (Figure 63b).

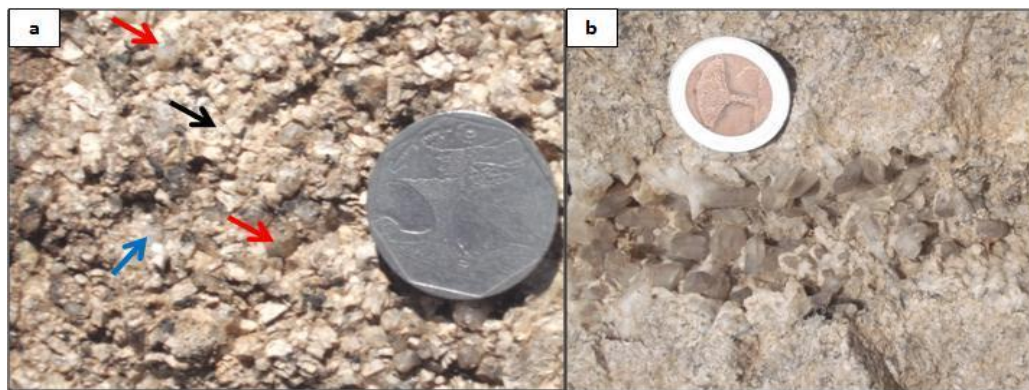


Figure 63: Coarse grained texture with phenocrysts of white plagioclase (black arrow) and quartz (red arrows) with lengths up to 2cm and 2.1cm, respectively in the granite hand specimen (a) (Coin diameter 2.6 cm). Note the biotite is also observed (blue arrow) and the miarolitic cavity occupied by euhedral crystals of quartz, alkali feldspar and chalcedony in hand specimen (b) miarolitic cavities occupied by euhedral crystals of quartz, alkali feldspar and chalcedony, Sabir granite. Diameter of coin is 3.1cm

Megascopically, biotite is the main ferromagnesian mineral. Microscopically, the syenite samples are characterized by myrmekitic texture (intergrowth texture) where intergrowth is seen between quartz and plagioclase. This forms embayments in the microcline crystal. Generally, the granitic rocks are easily identifiable in the study area by their macro features such as texture in situ, structure, joint discontinuities and degree of weathering. The texture varies from medium to coarse-grained and often graded up to granite porphyry. In the hand specimens the pinholes (<1mm to 1cm in diameters) are observed; some of them are empty and others are filled with secondary minerals.

In places, the granite appears as beds alternating with basic dykes or layers of same composition (Figure 64). In other sites, these beds of granite appear slightly deformed wherein cataclinal joints have developed well and granitic body is altered, especially near the dykes (Figure 65). Granites are disjointed, which occur either as systematic sets of joints or occur randomly. The orientation of these discontinuities with different spacing, are planar and curved. In each investigated site, the

discontinuities display various geometrical relationships to each other. These relationships define the size and shape of the blocks formed between those discontinuities. The discontinuities in the granitic blocks have produced different sizes and shapes including triangular and rectangular blocks as seen in the north of Al-Mihal village (Figure 66a).

Granite occurring in the form of domes show pile of disjointed boulders and have suffered intense alteration along the fractures resulting in the oblate form of the boulders (Figure 66b). Here the effect of the weathering doesn't extend into the rock but is restricted to the surface. However, brown coloured coatings due to iron oxide has extended into the inner parts of the rock along the fractures and weak planes Figure (67a & b). The effect of this phenomenon has reduced the strength of the rocks (Figure 67c). Granites contain xenoliths of various rocks as seen in different locations (Figure 68).

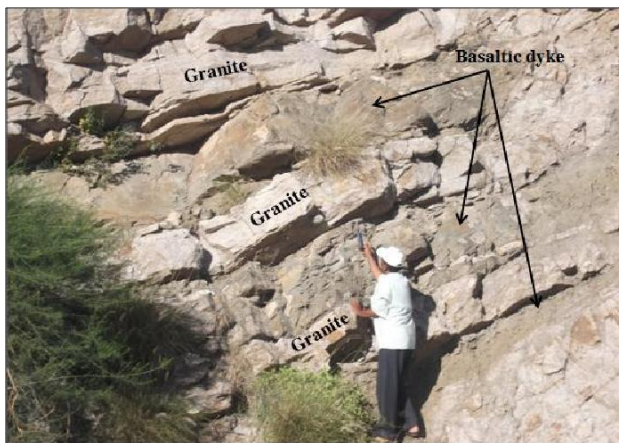


Figure 64: Granite showing cataclinal joints and alternated with basic dykes or layers of same composition, east of Dar Al-Nasr, Sabir area. Hammer length 32.5 cm



Figure 65: Granite exposed as slightly deformed layers which may be caused by intrusion of the basic dyke through them (red arrow). Note highly alteration of granite near the basic dyke

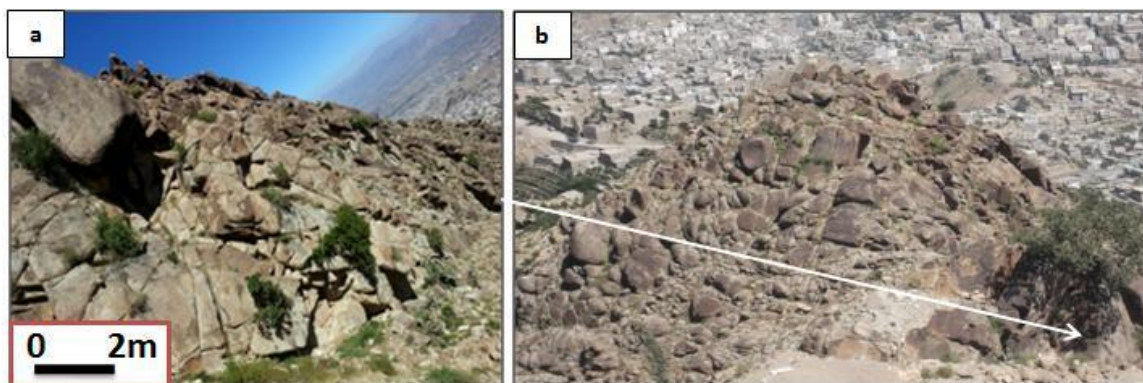


Figure 66: (a) Shows the variation in the sizes and shapes of granitic blocks formed by discontinuities and (b) Dome formed of granitic boulders of granite. Note concentration of weathering processes along the fractures and eliminating the block edges, north of Al-Mihal village, Sabir area.

The abundance of xenoliths from the neighbouring country rocks and porphyritic texture of the Jabal Sabir granite body indicate shallow depths of intrusion (El-Gharbawy, 2011). Generally, granites are almost affected by all weathering grades e.g. from fresh weathering to complete weathering (Figure 69). The spherical and cavernous weathering is one of characteristic features of Sabir granitic rocks. The caverns with various sizes and shapes were observed in different locations. They have spherical or elliptical shapes, arched-shaped entrances, concave inner walls, overhanging edges and gently sloping-covered floors (Figure 70).

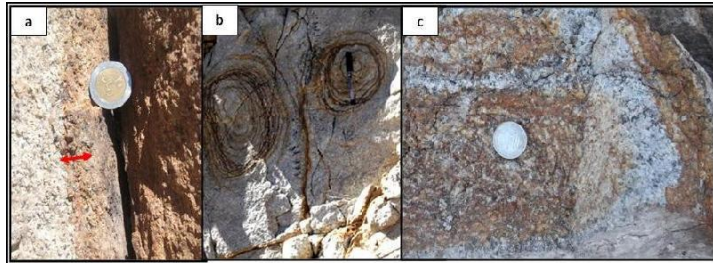


Figure 67: Photographs showing the effect of weathering/alteration on granite in Sabir area; (a) The effect is restricted to the surface of granitic rock (diameter of coin is 3.1cm), (b) The extension of iron oxide solutions effect into interior of rock. Note the whirling paths for the injected iron oxide solutions through fractures and weak parts of rock (pen length 14.3cm) and (c) The strength and hardness of granitic rock is reduced by alteration caused by hydrothermal solutions. Diameter of coin is 2.6cm



Figure 68: Xenolith of basalt in granite rock exposed in the north west of Zaid's Hotel, Sabir area. Pen length 14.3 cm



Figure 69: Weathering grades in granite; (a) Fresh granite, in Salah area and (b) Highly weathered granite at the foot of the Gabal Sabir, near Al Damkha area. Hammer length 32.5 cm



Figure 70: Field photograph shows the spherical and cavernous weathering on Sabir granitic rocks

4.8. Mafic and Felsic Dyke and Sill Intrusions

Numerous basic and felsic dykes cut through the concordant and discordant bodies represented respectively by flows (basalts, rhyolites/dacites and volcaniclastic deposits) and Sabir granitic pluton. These are injected during different volcanic phases and along fault trends, the majority of them trend in the NW-SE and NE-SW directions, and few in the E-W direction. The dykes with basic composition

are more predominant than acidic dykes in the study area (Al-Qadhi, 2007). The basic and felsic dykes show resemblance to basalts and rhyolites/dacites respectively in their petrographical characteristics. In some places, the dykes followed Tr2 form i.e., occur in the form of blocky ridges, often rising more than 10m above the surrounding landscape and with an areal extent of more than 8 km in length. For example, a large NE-SW dacitic dyke located at Al-Sufi village, Al-Hawban area is seen like a pillar as it has been left standing after softer Tb2 country rock eroded away. It is well jointed and appears as bedded layers.

The dyke contains cavities of various sizes and shapes and these are concentrated along bedding planes (weak planes) (Figure 71a). Microscopically, the dyke rock shows porphyritic texture where feldspar and quartz phenocrysts are embedded in holocrystalline groundmasses of same composition and opaques. Opaque minerals in matrix are altered to hydrous Fe-oxides (Figure 71b).

In the most investigated exposures (in more than 10 stations) especially along Al-Steen and A-Hamseen roads, the younger dykes are characterised by fractures and/or features of weathering/alteration, particularly the basic types. In some places the dykes of basalt have been weathered to form trenches (Figure 72a). The composite basic dykes were also observed in the Wadi Al-Malih and west of Nashit village, located in the northern part of the study area (Figure 72b).

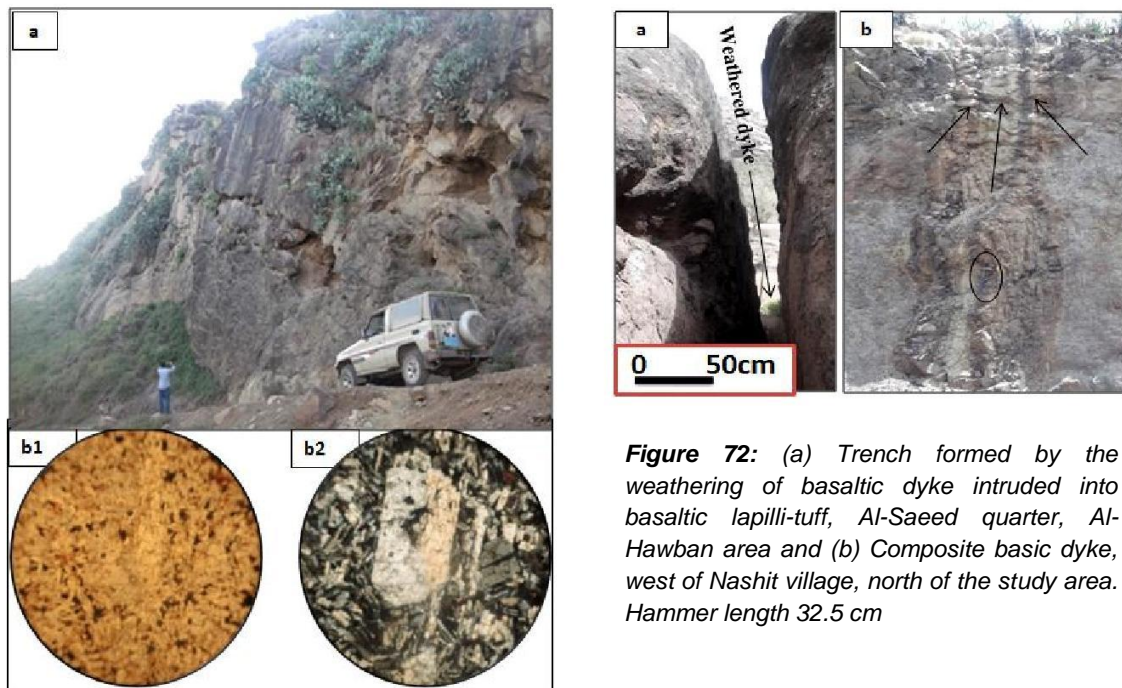


Figure 71: (a) Large NE-SW trending dacitic dyke intruded through Tertiary basaltic rocks (Tb2) and forms prominent, blocky ridge, rising more than 10m above the surrounding landscape, near Al-Sufi village, Al-Hawban area and (b) The porphyritic texture in dacitic dyke, where feldspar and quartz phenocrysts are embedded in holocrystalline groundmasses. (in PPL (b1) and CPL (b2) 3.5X)

Figure 72: (a) Trench formed by the weathering of basaltic dyke intruded into basaltic lapilli-tuff, Al-Saeed quarter, Al-Hawban area and (b) Composite basic dyke, west of Nashit village, north of the study area. Hammer length 32.5 cm

Some dykes with fault displacement were found in granite (Figure 73). The sills are also observed in many locations and these are injected through feeder-like dykes.



Figure 73: Basic dyke cut the highly weathered granite of Sabir, displaced by small normal fault, east of Al-mihwar village, Sabir area. Hammer length 32.5 cm

5. Summary and Conclusions

Taiz city and its surrounding areas in Yemen are largely covered with product of the Tertiary magmatism comprising typical bimodal mafic-felsic associations and are represented by flows, plutons, dykes and volcanoclastic deposits of variable composition. The magmatism is related to the continental rifting and break up processes associated with Afar mantle plume. All lava flow sequences are believed to be extruded and fed from fracturing and fissuring in the old rocks through which magma emerged in successive pulses, flooding the surrounding region. The occurrence of the Tertiary volcanic rocks as bimodal mafic-felsic with alternating sequences (Tb1, Tr1, Tb2, Tr2 and Tb3) and with distinctive lithological and stratigraphic characteristics and separated from one another by well-developed unconformities is the characteristic geological feature of these rocks. The alternating layers have widely different characteristics such as colour, heterogeneity, discontinuity, thickness, horizontal attitude, intercalating with volcanoclastic deposits, repetition with depth even within the same site, in both vertical and horizontal directions, depending on eruption type, mode of transport, distance travelled from the vent, temperature of the deposits, particle size, water content and paleorelief or riftogenic tectonic motions which are related to the development of the Gulf of Aden and opening of the Red Sea, or east African rift valley system.

Generally, in the study area, the Tb1 and Tb2 sequences are represented by jointed/massive basalt lava flow rocks which are interbedded/ alternated/ intercalated with volcanoclastic deposits. The Tertiary upper mafic sequence phase (Tb3) is exposed outside the investigated area and is also represented by the basaltic rocks. Megascopically, these rocks are characterized by porphyritic textures due to the presence of the plagioclase and/or olivine phenocrysts which are visible to the naked eye on the hand specimens. Presence of calcite veins, trachy structure and aphanitic texture are characterized features for massive trachybasalt. Microscopically, a variety of textures have been observed in the Tb1 and Tb2 thin sections including porphyritic, glomeroporphyritic and trachytic texture or flow structure. The microfractures intersected the phenocrysts and the fine groundmass, the alteration of olivine phenocrysts at their rims and along cracks into iddingsite, growth zoning in

plagioclase with oscillatory variations in composition characterises and the vesicles/ amygdales structures all these features were seen in thin sections.

The Tr1 and Tr2 sequences are comprised of jointed/massive rhyolitic/dacitic/ pitchstone lave flows and domes which are also intercalated or interbedded/ alternated with the silicic volcanoclastic materials. Felsic volcanic rocks (Tr1 and Tr2) are exposed to forms characteristic geomorphological features as ridge of domal mountains and hills, high plateaus with escarpments or cliffs sides and resistant cuestas. Petrographically, the jointed rhyolites/dacites show various textures; porphyritic, micrographic, radiate, glomeroporphyritic, vitrophyric and spherulitic textures. Identification of minerals present in the Tr1 and Tr2 was not possible due to the effect of hydrothermal solutions and alteration. The pits and/or vesicles of varying sizes with or without secondary minerals are found in the hand specimens of the columnar rhyolites, ignimbrites and welded rhyolitic tuffs. The microfractures filled with volcanic glass or/and secondary as iron oxides and called as transgranular fractures travel through some grains and groundmass.

The volcanoclastic deposits are characterized with great diversity of their type, colour, textural features, thickness, grain size, matrix, and degree of roundness of rock fragments and interlocking, intercalating laterally and vertically with basalt/rhyolite rocks. They range from strong, compacted, welded rocks to weak, altered, soils. In the investigated exposures, the basaltic volcanoclastic deposits are represented by tuff-breccias (>64mm wherein bomb and/or block clasts ranges from 25% to 75 %), lapilli-tuffs (a mixture of both lapilli (64-2mm) and ash (< 2mm) put together <75% and the bomb and/or block clasts are <25%) from 25% to 75 %), lapillistones (lapilli is >75 %), agglomerates (bomb and/or block clasts volume is >75 %), tuffs (ash grains<2mm) and volcanic ashes. The Ignimbrites are also common in the study area. Microscopically, the basic volcanoclastics in thin section are often consisting of clasts of trachybasalt cemented by volcanic ashes, iron oxides, malachite, glass or silicates. They contain emptied or filled vesicles and microfractures and veins also filled with secondary minerals. The silicic volcanoclastic materials consist of ignimbrites, rhyolitic tuffs, rhyolitic lapilli-tuffs and rhyolitic lapillistones.

The volcanic ashes and iron oxides are more frequent matrix materials in the volcanoclastic materials. Both mafic and acidic types are underlain or /and intercalated with varicoloured volcanic ashes (soil). In the volcanic soils, the major clay minerals namely montmorillonite and kaolinite are identified by XRD analysis in addition to minor amounts of mica group of minerals such as muscovite, vermiculite and chlorite. Other minerals found in volcanic soils are talc, feldspar, calcite and halloysite.

The felsic plutonic rocks are represented by alkaline or peralkaline granites called Jabal Sabir granites. It consists of, white to greyish white, massive, medium to coarse-grained with grading up to granite porphyry and almost <5% of dark minerals. The main minerals constituted these granitic rocks are k-feldspar, quartz, hornblende and biotite. Petrographically, the study of thin sections of Sabir granitic rocks indicates that the main minerals are k-feldspar (orthoclase, perthite, and perthitic microcline), quartz, hornblende and biotite with accessory minerals zircon and other opaque minerals. The spherical and cavernous weathering is one of characteristic features of Sabir granitic rocks. The caverns with various sizes and shapes were observed in different locations. Numerous basic and felsic dykes cut through the surrounding older Tertiary igneous rocks represented by flows (basalts, rhyolites/dacites and volcanoclastic deposits) and Sabir granitic pluton. They are injected during different volcanic phases and along fault trends. The dykes with basic composition are more

predominant than acidic dykes in the study area. The basic and felsic dykes show resemblance to the basalts and to the rhyolites/dacites respectively in their petrographical characteristics. The Tertiary rocks of Taiz area have been affected by the permeation of magnesium and iron-bearing solutions along their discontinuity surfaces implying the instability of the rocks caused due to the intensity of alteration the rocks.

Acknowledgment

The authors thank the Chairman, Department of Studies in Physics, University of Mysore for the X-ray analysis of the soil samples.

References

- Al Subbary, A.A., Nicols, G.M., and Bosence, D. *Cretaceous to Tertiary Pre-Rift Fluvial to Shallow Marine Sedimentation in Yemen*. Geo. Soc. of Egypt, Cairo. 1993. 1; 383-407.
- Al-Kadasi, M., 1994: *Temporal and Spatial Evaluation of the Basal Flow of the Yemen Volcanic Group* (Unpublished Ph.D. Thesis). Royal Holloway Collage, Landon University, UK.
- Al-Qadhi, Abdul-Aleam, A., 2007: *Preliminary Engineering Geological Studies of Taiz City, Yemen Republic* (Unpublished M. Sc. Thesis). Sana'a University, Yemen.
- Beydoun, Z.R., As-Saruri, M.A.L., El-Nakhal H., Al-Ganad, I.N., Baraba, R.S., Nani, A.O., and Al-Awah, M.H., 1998: International lexicon of Republic of Yemen. Second Edition. IUGS, Republic of Yemen Publication, 34, 245.
- Capaldi, G., Chiesa, S., Manetti, P., Orsi, G., and Poli, G. *Tertiary Anorogenic Granites of the Western Border of the Yemen Plateau*. Lithos. 1987. 20; 433-444.
- Chazot, G. and Bertrand, H. *Genesis of Silicic Magmas during Tertiary Continental Rifting in Yemen*. Lithos J. 1995. 36; 69-83.
- Chiesa, S., Civetta, L., De Fino, M., La Volpe, L., and Orsi, G. *The Yemen Trap Series: Genesis and Evolution of a Continental Flood Basalt Province*. J. Volcanol. Geotherm. Res. 1989. 36; 337-350.
- Chiesa, S., La Volpe, L., Lirer, L. and Orsi, G. *Geological and Structural Outline of Yemen Plateau, Yemen Arab Republic*. N.Jb. Geol. Paläont. Mh. 1983. 11; 641-656.
- Civetta, L., Lavalpe, L., and Lirer, L. *K-Ar Ages of the Yemen Plateau*. J. Volcanol. Geotherm. Res. 1978. 4, 307-314.
- del Potro, R. and Hürlimann, M. *Geotechnical Classification and Characterization of Materials for Stability Analyses of Large Volcanic Slopes*. Eng. Geology. 2008. 98; 1-17.

DEY and UN/DDSMS, 1997: Hydrological and Land-Use Studies in Taiz Region (Upper Wadi Rasyan Catchment) (TCD CONTARCT NO: YEM/93/010-3) Dar El-Yemen Hydro Consultants DEY & SOAS. Vol.1: Main Report.

El-Gharbawy, R.I. *Petrogenesis of Granitic Rocks of the Jabal Sabir Area, South Taiz City, Yemen Republic*. Chin. J. Geochem. 2011. 30; 193-203.

Fisher, R.V. *Rocks Composed of Volcanic Fragments*. Earth Sci Rev. 1966b. 1; 287-298.

Geukens, F.S., 1966: *Geology of the Arabian Peninsula, Yemen*. Professional Paper. Report. U.S. Geol. Survey, Washington D.C., Series No. 560, B1-B23.

Gillespie MR, Styles MT., 1999. Classification of igneous rocks. British Geological Survey Research Report RR 99–06. BGS Rock Classification Scheme, vol 1.

Kruck, W. and Schaffer, U., 1991: *Geological Map of Republic of Yemen (ROY)*. Taiz Sheet, Ministry of Oil and Mineral Resources, Sana'a, Yemen, Federal Inst. of Geosci. and Natural Resources, Hanover (FRG), Scale 1:250,000.

Kruck, W., Schäffer, U., and Thiele, J., 1996: *Explanatory Notes on the Geological Map of the Republic of Yemen- Western Part*. Geologisches Jahrbuch, Hannover.

Malek, Abdul-Hamid, Janardhana, M.R., and Al-Qadhi, Abdul-Aleam. *Cenozoic Eruptive Stratigraphy and Structure in Taiz Area of Yemen*. Earth Sciences. 2014. 3; 85-96.

Njue Muthoni, L., 2010: *Geological Field Mapping*. Presented at Short Course V on Exploration for Geothermal Resources, Organized by UNU-GTP, GDC and KenGen, at Lake Bogoria and Lake Naivasha, Kenya, Oct. 29-Nov. 19.

Refaat, A.M., El-Odyia and Kabesh, M.L. *The Chemistry of Arfvedsonites and Riebeckites from Sabir alkali granites, Taiz area, Yemen Arab Republic*. Chem. Erde. 1980. 39; 37-45.

Shaalan, M.M.B. and Zalata, A.A., 1983: *Petrography of the Tertiary Alkaline Granite of Gabal Sabir and the Associated Dykes, Y.A.R. [Z]*. Geol. Soc. of Egypt 21st Annual Meeting (Abstract).

Youssef, M. El-Shatoury and Al-Kadasi, M., 1992: *Geology of Gabal Sabir Granitic Mass, Taizz, Yemen Republic*. Geology of the Arab World, Cairo University, Vol. 1, 433-447.

Investigating the Impact of the BP Deepwater Horizon Oil Spill on Trace Metal Concentrations in Bottom Sediments Retrieved from the Outer Continental Shelf (OCS) of Alabama and Western Florida, Gulf of Mexico

David Steffy, Alfred Nichols and Joe Morgan

Department of Physical and Earth Sciences, Jacksonville State University, Alabama, USA

Publication Date: 10 June 2016

Article Link: <http://scientific.cloud-journals.com/index.php/IJAESE/article/view/Sci-452>



Copyright © 2016 David Steffy, Alfred Nichols and Joe Morgan. This is an open access article distributed under the **Creative Commons Attribution License**, which permits unrestricted use, distribution, and reproduction in any medium, provided the original work is properly cited.

Abstract The changes in the metal concentrations in sediments from the eastern Gulf of Mexico OCS can be explained by the presence of a new source for these metals. These metals were released from the damaged Macondo Well which resulted in the BP Deepwater Horizon Oil Spill during the spring of 2010. One-hundred and twenty sediment samples were collected during the fall months for the years 2008-2012 from the eastern OCS. The Tukey range test was used to compare measurement six metal concentrations between the relict sand deposits of the northern Gulf of Mexico OCS to the relict carbonate sediments off of western Florida OCS. Tests indicated that nickel (Ni), and lead (Pb) were significantly higher ($p < 0.05$) in the seasonal average concentrations in the relict sand deposits after the spill. These higher concentrations are also reflected in the V to Ni ratio being at its lowest value in the relict sand (0.82) in the north, which is closer to the damaged well.

Keywords *Deepwater Horizon; Vanadium; Nickel*

1. Introduction

Between April 20 and July 15, 2010, approximately 686,000 metric tons of crude oil was accidentally released from the British Petroleum (BP) Deepwater Horizon well located in the Gulf of Mexico (Figure 1; Hoch, 2010). The damaged wellhead released between 1,670 to 2,670 metric tons of crude oil per day (Johnson and Torrice, 2010). BP sprayed over 4,670 metric tons of chemical dispersants on the sea surface and injected 2,600 metric tons at the well head to alleviate the spread of crude oil slicks in the Gulf of Mexico (Kujawinski et al., 2010). The concentration of the dispersant as it was incorporated in the marine system was not controllable. The spray resulted in dispersant being delivered at various concentrations throughout the surface and the upper water column. These environments range from an open marine system to the ever changing coast line.

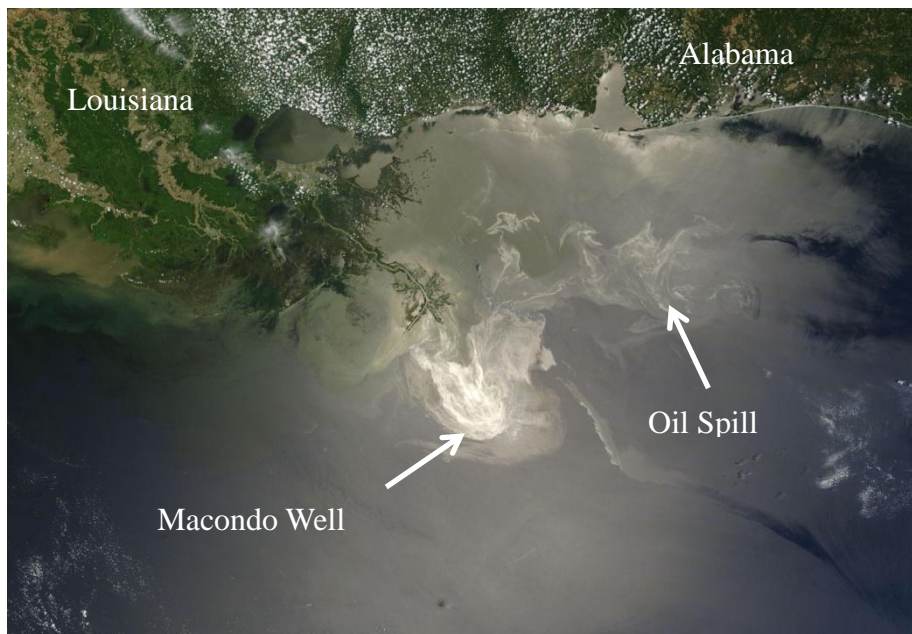


Figure 1: NASA's Terra Satellite Image of the Oil Spill on May 24, 2010

Liu et al. (2012) reported the following metals concentrations ($\mu\text{g g}^{-1}$) of concern for this report found in the crude oil released: V (0.2); Cr (9.4); Ni (1.5); and Pb (0.3). For V and Ni, Lui et al. (2012) found that the concentrations increased to 1.0 and 4.2 ($\mu\text{g g}^{-1}$) as the crude oil was degraded into oil mousse. Wise et al. (2014) measured Cr and Ni to range from 0.24 to 8.46 ($\mu\text{g g}^{-1}$) in crude oil from the wellhead, and oil from slicks on surface waters and tar balls from Gulf of Mexico beaches.

This study investigated the presence of trace metal concentrations found in sea bottom sediments along the relict sand deposits off of Alabama-Florida shelf and the relict carbonate sand off of western Florida (Figure 2). One-hundred and twenty sea bottom sediment samples were collected over a 5-year period (2008-2012) covering the time before and after the spill.

The study area is the OCS of the western Florida and Alabama. The shelf consists of an inner shelf (<40 m in depth), a middle shelf (40-100 m in depth), and the OCS (100-200 m in water depth). The 200-m bathymetric contour line is given in Figures 2 and 3. The shelf area is formed by an extensive carbonate platform along the west coast of Florida, and layers of lithogenous sediment north of Apalachicola Bay, Florida (Figure 2; Hine et al., 2003). To the west of the carbonate platform shelf (the study area) gives way to the continental slope which extends down to water depths of 1500 m and the Florida escarpment. To the east, the carbonate platform rises to form the inner shelf. By the early Cenozoic Period, the west coast of Florida became a drowned carbonate shelf (Hine et al., 2003). At this time, the shelf became deeper than the photic zone which resulted in a pelagic zone with reduced carbonate accumulation. This deepening occurred between depths of 100 and 200 m and extended over 100 Km between shelf and slope (Hine et al., 2003). Presently, the seafloor carbonates content ranges from 10% north of Apalachicola Bay to over 75% on the shelf south of bay (Balsam and Beeson, 2003).

By the middle Cenozoic Period, siliciclastic sediment eroded from the Southern Appalachian Mountains and was delivered to the inner shelf region (Balsam and Beeson, 2003; Hines et al., 2003).

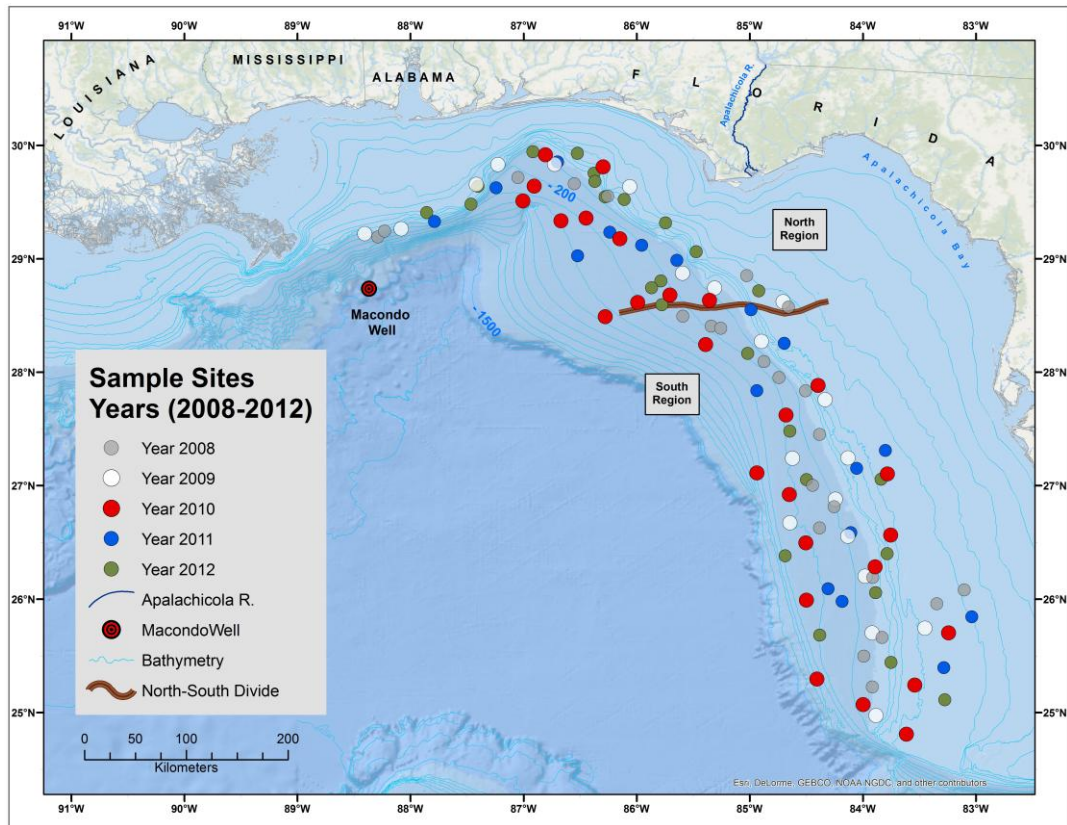


Figure 2: Bottom sampling sites occupied during 2008 through 2012 along the Alabama and Florida outer continental shelves. The division between North and South Regions is also located

Nineteen watersheds drain the western Florida coastline. The largest fresh-water outflow is from the Apalachicola River Watershed which drains 19,500 square miles of west-central Georgia, northwest Florida, and southeastern Alabama (Figure 2). Land use of this watershed is diverse and includes agricultural, residential, and industrial regions and the extensive Atlanta metropolitan area. Delivery of trace-metal laden sediment by this outflow to the inner shelf is likely. Sediment released is distributed by longshore currents in a northwest to a southeast direction parallel to the west Florida coastline. Quartz sand ridges parallel to the coast are formed by these currents and do not occur beyond 20 Km from shore (Figure 2; Balsam and Beeson, 2003; Hine et al., 2003).

Chemical analysis by the US EPA (Environmental Protection Agency) (2010) (Table 1) and studies by Steffy et al. (2013, 2014) (Table 2) indicate that V is lost during the decomposition process of crude oil, and Ni concentration is reduced to a lesser extent by these processes (Figure 3). Steffy et al. (2014) proposed that the retention of the Ni by the weathered oil and the resulting tarballs along the Alabama beaches indicate the Ni is being held tightly, probably by porphyrin rings as described by Yen (1975). Further studies of these metals have been advanced to recognize areal extent of the spilled oil's impact on sea bottom sediment. This is found to have a significant impact on the active abyssal ecosystem (Landers et al., 2015; Nichols et al., 2014).

As elements, trace metals do not degrade. Once deposited on marine sediment as a component of a nonvolatile fraction of crude oil, the metals could remain after the organic fraction has been metabolized by microbes or otherwise decompose (Steffy et al., 2014). A complete list of metals found in MC252 spilled oil was listed by Liu et al. (2012).

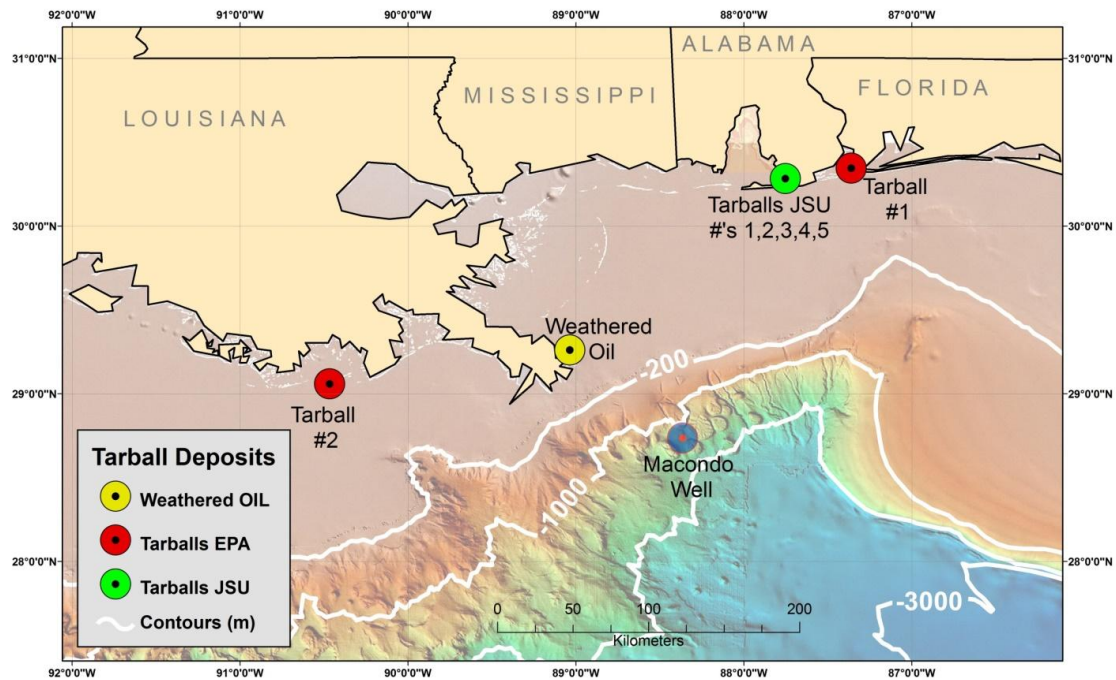


Figure 3: Location of tarballs and weathered oil analyzed by US EPA (2010) and tarballs sampled by this study, both associated with the BP Deepwater Horizon oil spill released from the damaged Macondo well

Table 1: Trace metal content of tarballs and weathered oil measured in μg of metal per g of tarball or weathered oil associated with the oil spill (US EPA, 2010)

Trace Metal	Tarball #1	Tarball #2	Weathered Oil
Cr	0.06	ND	ND
Ni	0.32	0.32	0.079
Pb	16.4	ND	0.240
Tl	0.07	ND	ND
V	0.20	ND	ND
Hg	0.06	ND	0.00024

ND indicates not detected

2. Methodology

The following methods were used to analyze for each of the 5-years' worth of sediment samples collected and analyzed by the authors. The methods are described previously by Steffy et al. (2014; 2013), and also are provided below.

Table 2: Trace metal content of tarballs measured in μg of metal per g of tarball associated with the oil spill collected along the Alabama coastline by Steffy et al. (2014)

Trace Metal	Tarball #1	Tarball #2	Tarball #3	Tarball #4	Tarball #5
Cr	ND	0.18 ± 0.32	0.45 ± 0.77	ND	ND
Ni	0.20 ± 0.18	0.38 ± 0.04	0.16 ± 0.28	0.10 ± 0.18	0.48 ± 0.55
Pb	0.64 ± 0.50	0.71 ± 0.18	0.56 ± 0.19	1.27 ± 1.36	0.59 ± 0.14
Tl	0.10 ± 0.09	0.14 ± 0.12	0.23 ± 0.11	0.06 ± 0.10	0.12 ± 0.11
V	0.12 ± 0.20	ND	ND	ND	ND
Hg	ND	ND	ND	ND	NA

ND indicates not detected. NA indicates not analyzed.

2.1. Field Methods

Sediment samples were collected in the fall during 2008-2012 as part of the NOAA (National Oceanographic and Atmospheric Administration) Small Pelagics Survey (Figure 2). One-hundred and twenty bottom samples were collected using a Shipek grab sampler operated from the decks of the NOAA R/V *Pisces* and R/V *Gordon Gunther*. The sediment is retrieved from the upper 10 cm (~0.32 foot) of the sea bottom. The sampler was returned to the ship's deck and a 40-ounce clear glass jar was filled with water-saturated sediment. The jar was labeled, sealed with a Teflon-lined lid and the sample placed in a 4°C walk-in cooler. Samples were transported to laboratory facilities at Jacksonville State University for processing and metal analysis (Steffy et al., 2013). The 2012 samples analyzed by this study supplements earlier data reported by Steffy et al. (2014).

2.2. Granulometric Analyses

A modified USGS method for granulometric analysis of marine sediment as described by Poppe et al. (2000) was used to measure the grain-size distribution. The modified method produced, a percent of the following fractions: gravel and larger size (>2mm), coarse sand (2mm–500 μm), medium sand (500 μm –250 μm), fine sand (250 μm –125 μm), very fine sand (125 μm –63 μm), silt/ clay (<62 μm), and the organic fraction. Data was statistically evaluated using Microsoft Excel and data plotted by a geographic information system was visually assessed to recognize areal trends.

2.3. Metal Analyses

Air dried sediment samples were subsampled into one gram triplicates and processed for metal analysis. Samples weighing approximately one gram were measured to ± 0.001 g and placed into acid washed 150 mL beakers for digestion. All reagents used in sample preparation and metal analyses were trace metal grade. Ultra-pure water (17 megaohm resistance) was used to prepare all solutions. All glassware was acid washed prior to each assay. Samples were digested using 15 mL of concentrated nitric acid, and further oxidized by the addition of 1 mL of hydrogen peroxide. The digested samples were diluted with 2 M sulfuric acid and filtered through a 45 mm filter into a 50 mL volumetric flask. The addition of 2 M sulfuric acid brought the total volume to 50 mL.

2.4. Mercury Analyses

For Hg analysis, a 10 mL aliquot of the digested solution was pipetted into a BOD (Biological Oxygen Demand) bottle and 0.25 mL of nitric acid, 0.5 mL of sulfuric acid, 0.8 mL of potassium persulfate,

and 2 mL of potassium permanganate were added. This solution was then heated for one hour at 95°C. Cooled samples received 1 mL of hydroxylamine prior to analysis. Standard Hg solutions were prepared from Fisher Certified Mercury Reference Solution, Lot No. 055614-24. Samples were analyzed for total Hg using US EPA Method 245.1, Manual Cold Vapor Technique (US EPA 1983). Hg analysis was conducted using a CETAC Quick Trace Mercury Analyzer M-6100 cold vapor atomic absorption Hg analyzer with an ASX-400 AutoSampler.

2.5. ICP Analyses

Digested sediment and tarball samples were submitted to Southern Environmental Testing, Inc. (Florence, AL) for ICP analysis using US EPA *Methods for Chemical Analysis of Water and Wastes*, EPA-600/4-79-020, revised May 1994.

2.6. Quality Control

Triplicates of each sediment sample were analyzed. All specimens were run in batches that included blanks (reagent and instrument) and spiked samples as part of the quality control for this study. All glassware was acid washed prior to each assay. All reagents used in sample preparation and metal analyses were trace metal grade. For Hg sample analysis, all samples were run in batches that included blanks (reagent and instrument), a five point standard calibration curve (standards of 0.0, 5.0, 10.0, 16.0, 24.0, and 32.0 mg/L with a linear correlation of 0.995 or better), and spiked specimens.

3. Results and Discussion

We hypothesize that the release of crude oil and the use of dispersants during the summer of 2010 associated with the BP Deepwater Horizon Well oil spill temporarily increased the trace metal concentrations in the sea bottom along the outer continental shelf of the Gulf of Mexico off of Florida and Alabama (Figure 1).

The study area is divided into North and South Regions with the boundary located on Figure 1. The boundary is based on several physical characteristics, which include: proximity to the damaged Deepwater Horizon well, water circulation pattern of the OCS, and known sea bottom sediment depositional pattern on the OCS. Figure 1 locates the damaged Macondo Well founded in 1,500 m water depth of the continental slope south of the Alabama – Mississippi state border. The surface oil spill depicted in Figure 1 indicates flow is clockwise along the OCS of Alabama and Florida. Long-shore currents of the inner shelf parallel the coast and flow clockwise as well (northwest to southeast). North of Apalachicola Bay, relict lithogenous sediment dominant the OCS of the North Region. South of Apalachicola Bay relict carbonate sediment the OCS of the South Region. This transition in the sea bottom sediment of the OCS from relict carbonate to relict lithogenous sediment defines the North-South boundary and is concurrent to the transition from carbonate to quartz sand of Balsam and Beeson (2003) and Distribution of Heavy Minerals (2015).

3.1. Granulometry

Granulometry data measured for 112 of the 120 sample sites from 2008-2012 collected from the OCS (Figure 1) have an average clay/silt content of $12.7 \pm 9.3\%$, an average sand content of $76.2 \pm 10.5\%$, an average gravel content of $8.4 \pm 9.9\%$, and an average dissolvable organic content of $3.9 \pm 4.2\%$. According to the Folk (1954) classification scheme, the sediment would be classified as a gravelly muddy sand, as would most of the samples collected from the carbonate platform. Table 3 provides separate granulometry data for the South and North Regions. There is no significant

statistical difference between the Regions. No distinction has been made in this study between hydrogenous, biogenous, or lithogenous components of the sediment samples. However, the geological history of the Floridian continental shelf (South Region) would indicate that the carbonate material is biogenous in origin (Balsam and Beeson, 2003; Hines et al., 2003). The South Region includes the Tyner et al. (n.d.) carbonate Middle Ground having an estimated overall carbonate depositional rate of $103 \text{ (g CaCO}_3\text{/m}^2\text{)/yr}^{-1}$. Most of the carbonate mass is from foraminiferal contribution. In contrast, the inner shelf of the South Region consists of a mixture of unconsolidated fine siliciclastic sand, and gravel size marine biogenic carbonate deposits $< 3\text{m}$ (Hine et al., 2003). In Tampa Bay located on a coastal area of South Region, the Holocene accretion rate ranges from 1.4 to 4.1 mm yr^{-1} based on Pb-210 measurements (Trimble et al., n.d.).

The delivery of lithogenous sediment to the Florida OCS is unlikely because the longshore currents restrict the movement of sediment to the inner shelf being delivered by erosion of the adjacent continental margin. In contrast, The North Region covers the Alabama OCS which is more likely to receive lithogenous sediment delivered by the Mobile River (Emery, 1968), and by the Apalachicola River on the Florida OCS north of Apalachicola Bay (Figure 2). The eastern continental shelf of the Gulf of Mexico is a dynamic depositional system with reactivation and amalgamation occurring throughout its Holocene history (Anderson and McBride, 1996). Brooks et al. (2015) cite the sedimentation rate on the continental shelf at $\sim 10 \text{ cm/1,000 yr}$ northeast of the Deepwater Horizon well (North Region), and at $\sim 17 \text{ cm/1,000 yr}$ southeast of the well (South Region). They document rate based on Th-234 content could have received a pulse of sediment caused by a marine oil “snow” generated by the spill. This pulse of sediment is estimated to have been deposited within a 4-5 month period after the spill.

Table 3: Granulometry results for the South and North Regions of the study area. Values are the mean percent of the sediment sample

Year	South Region (n = 91)				North Region (n = 21)			
	Granule	Sand	Silt/Clay	Organic	Granule	Sand	Silt/Clay	Organic
2008	15.6	78.1	6.1	0.01	6.3	60.4	32.6	0.03
2009	10.7	78	4.6	6.7	33.1	63.2	3.6	0.1
2010	4.6	81.7	13.7	0.01	1.5	88.5	10	0.01
2011	0.2	88.7	9.8	6.3	0.4	77.8	20.2	8.7
2012	6.8	62.5	21	9.8	4.4	82.3	5.6	7.7
Mean	7.6	77.8	11.0	4.6	9.1	74.4	14.4	3.3
stdev	5.9	9.6	6.6	4.4	13.6	12.2	12.0	4.5

n is the number of sample sites

Steffy et al. (2013) reported that metal concentrations increases as grain size decreases. Metal concentrations also increase with ion exchange capacity increases, surface area increases and clay mineral content increases. There is no significant statistical difference between the regions in the silt/clay content of the sea bottom samples; however, there is a higher dissolvable organic content measured in the samples of the North Region.

3.2. Seasonal Mean Metal Concentrations Comparison

Seasonal mean (\pm standard deviation) metal concentrations for five metals present in sea bottom sediment samples collected from 53 of the 120 sites during 2008-2012 (Figure 2) are given in Table 4. Seasonal means are based on all samples collected and analyzed for the designated year. Seasonal mean metal concentrations of Ni, V, Pb, and Tl are at their highest concentrations in 2010. Seasonal mean sediment levels of V in 2010 were seven times as large as those from 2009 (Table 4), although this difference was not statistically significant due to the amount of variation among samples.

Seasonal mean sediment levels of Ni in 2010 were five times larger than those in 2009. Seasonal mean sediment levels of Pb in 2010 were six times larger than those in 2009. Seasonal mean sediment levels of TI in 2010 were eight times larger than those in 2009. For Ni, V, and TI mean concentrations for the years following 2010, showed lower concentrations.

Table 4: Seasonal mean (\pm standard deviation) are shown for all metals. Values are measured in μg of metal per g of sediment

Trace Metal	Mean (\pm standard deviation)	2008	2009	2010	2011	2012
Cr	8.01 \pm 2.90	8.55 \pm 4.73	5.66 \pm 0.56	7.07 \pm 3.86	8.58 \pm 2.94	10.20 \pm 0.17
Ni	6.07 \pm 3.86	2.52 \pm 1.13	1.93 \pm 0.19	11.42 \pm 5.42	7.49 \pm 4.74	7.00 \pm 0.09
Pb	3.48 \pm 2.69	1.45 \pm 0.40	0.71 \pm 0.06	4.22 \pm 2.17	3.09 \pm 3.02	6.80 \pm 0.17
TI	0.24 \pm 0.52	NA	0.06 \pm 0.00	0.52 \pm 0.85	0.14 \pm 0.18	NA
V	7.27 \pm 5.21	3.00 \pm 1.93	2.08 \pm 0.16	15.00 \pm 7.05	7.07 \pm 5.42	9.20 \pm 0.25
Hg	0.15 \pm 0.03	NA	0.03 \pm 0.01	0.37 \pm 0.01	0.05 \pm 0.06	NA
Sites Sampled	53	10	7	12	18	6

NA indicates not analyzed

The seasonal mean concentrations (Table 4) are greater than for Ni, V, and Pb; and at the same order of magnitude for Cr present in the crude oil released from MC252 well as reported by Liu et al. (2012) and Wise et al. (2014). In comparison, the tarballs (Table 4) has less Cr and Ni than the crude oil, whereas the Pb reported by EPA (2010) exceeded both our measurements of tarballs and the crude oil value. It should be noted that Liu et al. (2012) and EPA (2010) did not report a standard deviation associated with their measurement. Wise et al. (2010) was not specific in the measurement and the standard deviation of the metals found. With respect to all three references, the lack of specific means and standard deviations prevented a statistical comparison.

3.3. Comparison of Seasonal Mean Metal Concentration Variations in North Region v. South Region

Figure 4 depicts seasonal mean concentrations for Ni, V, Pb, and Cr for the North and South Regions. These mean values are given as column \pm standard deviations for each year. The 2010 means for Ni, V, and Pb appear to peak during 2010, which were sampled after the Deepwater Horizon Oil Spill. The Tukey range test was used to compare these four metal mean concentrations between the relict sand deposits of the North Region to the relict carbonate sediments of the South Region. Tests indicate that Ni, V, and Pb found in the North Region were significantly higher ($p < 0.05$) than the South Region (Table 5).

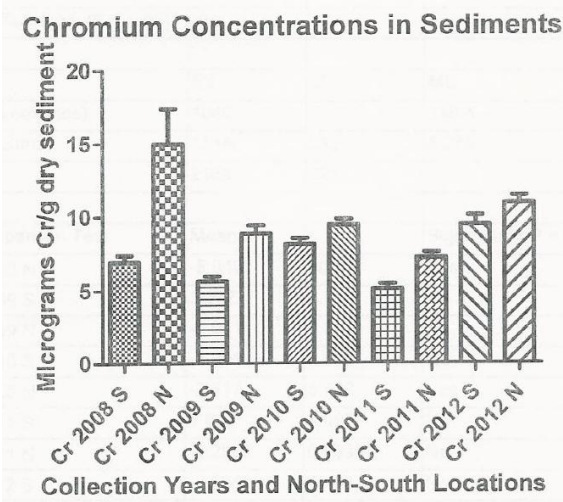


Figure 4(a): Chromium

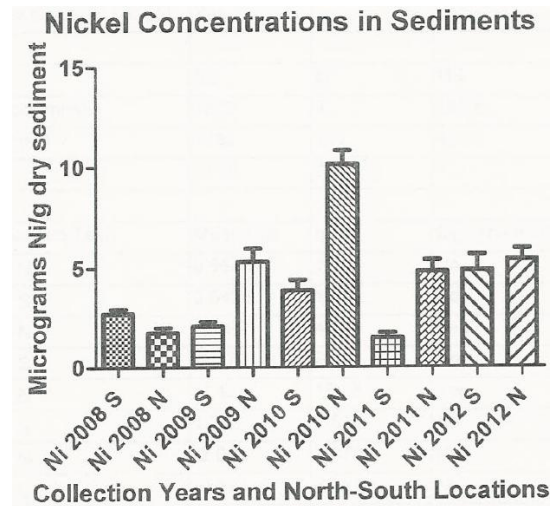


Figure 4(b): Nickel

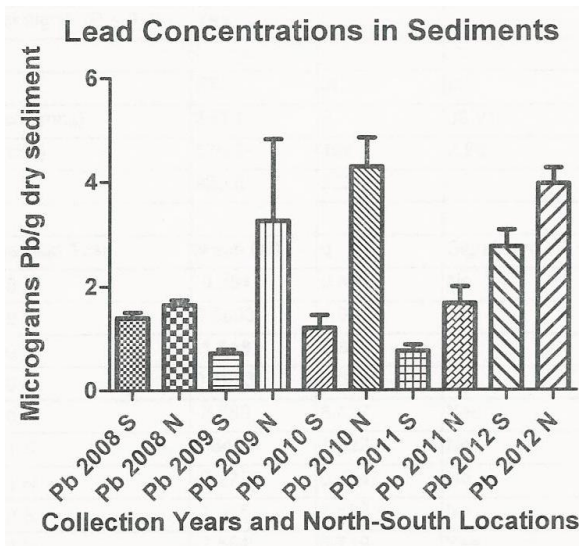


Figure 4(c): Lead

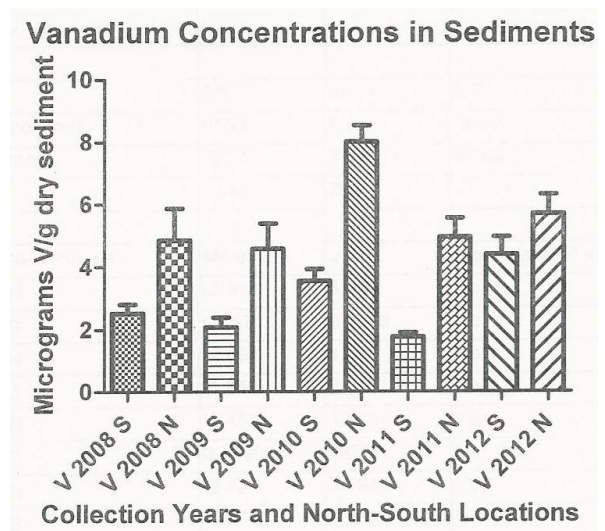


Figure 4(d): Vanadium

Figure 4: Column plots of metal mean (\pm standard deviation) concentrations segregated for North and South Regions

For all metals except for Pb in the study area, appear to have returned to pre-spill levels in the sea bottom sediment (Figure 4). These increases are statistical significant (Table 5). This natural recovery may be attributed to water currents or storms redistributing the metals present in the upper centimeters of sediment. The cause for the increasing level of Pb after the 2010 is unknown. It could indicate a new source of Pb is present, such as the effluence from Apalachicola Bay. The effluence and any accompanied sediment would be redirected by longshore currents in a northwest to a southeast direction parallel to the west Florida coastline (water depth <40 m), however. This needs to be investigated to confirm that a new source is present.

Table 5: North vs. South Regions sea bottom sediment concentrations were compared for four metals during the fall of 2008-2012. Statistical significance was determined using one-way ANOVA with Tukey's multiple comparisons post-test

Metal	Year									
	2008		2009		2010		2011		2012	
	Mean Diff	q value	Mean Diff	q value	Mean Diff	q value	Mean Diff	q value	Mean Diff	q value
Cr	-6.143	5.276*	-3.217	2.816*	-.9200	0.9444 ns	-1.728	2.078 ns	-1.468	2.605ns
Ni	0.911	0.7113 ns	-4.413	3.512*	-5.100	4.760*	-2.618	2.863 ns	-0.525	0.730ns
Pb	-0.2495	0.2987 ns	-2.536	3.095ns	-3.663	5.241*	-0.5499	0.9216 ns	-1.206	2.416ns
V	-1.246	1.091 ns	-4.690	5.246*	-3.728	3.901 ns	-2.549	3.125 ns	-1.299	1.929ns

Statistical significance indicated at * ($p < 0.05$), and "ns" is not significant

3.4. V-Ni Ratio Comparison of North Region v. South Region

We modified Yen's (1975) technique of fingerprinting crude oil with the V-Ni ratio by calculating V/Ni. Table 6 lists the average values of V-Ni ratios for each Region and for each year. For the 5 year time frame, the North Region has a lower average ratio of 1.09 ± 0.32 compared to the South Region's value of 1.54 ± 0.66 . No statistical significance was determined to be present between the years when comparing North to South Regions, or when comparing North to South Regions for each year. These tests were conducted by using one-way ANOVA with Tukey's multiple comparisons post-test. For 2008, 2010, and 2011, the V to Ni ratios (Table 6) are higher, but not statistically, for carbonate sediment found in the South Region when compared to relict sand found in the North Region, which is closer to the damaged well. Also, in the North Region, the V-Ni Ratios are at its lowest value during 2010. This would suggest some of the trace metals measured in the 2010 samples were higher in concentration and derived, in part, from the oil spill.

Table 6: Vanadium to Nickel ratio characteristic as it varies with year and area

Year	South Region (Relict Carbonate Sediment)	North Region (Relict Lithogenous Sediment)
2008	2.61	0.91
2009	1.19	NA
2010	1.34	0.82
2011	1.66	1.09
2012	0.90	1.54
Mean	1.54	1.09
Stdev	0.66	0.32

NA indicates not analyzed

4. Conclusions

There appears to be a discernable rise and fall of trace metal concentrations in the sea bottom sediment in the eastern portion of the Gulf of Mexico OCS (Figure 4). The trace metals, Ni, V, and Pb, demonstrate this fluctuation during 2008-2012. We propose that the rise was caused by the presence of a new source of metals during the spring and summer of 2010 that being the Deepwater Horizon Oil Spill. The 2011 values approach pre-spill values, which represents natural remediation or dilution of metal concentrations in the sea bottom shelf sediment. The relict carbonate sediment of the South

Region has a statistically different V to Ni ratio compared to the relict sand of the North Region, which is closer to the damaged BP Macondo well.

On the west Florida carbonate shelf, the seafloor sediment seasonal concentrations of Ni and V, the two metals most strongly associated with crude oil, have a ratio that is significantly higher after the oil spill than before the oil spill in samples collected. This indicates that the spilled oil and the dispersants used to remediate the oil are new sources of trace metals to the Gulf of Mexico region.

The OCS is composed of gravelly muddy sand. Tarballs and weathered oil generated from the spilled oil that were analyzed from the Louisiana, Alabama, and Florida coastline indicate that Ni is being held tightly by the porphyrins in the oil while V tends to be lost. This would explain the trend measured in this study's North Region of the V-Ni ratio decreasing to its lowest value immediately after 2010 the Deepwater Horizon Oil Spill. Two years after the spill, the V-Ni ratio continued to increase.

Based on the limited number of sampling sites that have been processed to date, we believe that sediment concentrations of Ni and V could be indicative of an area north of Apalachicola Bay of the eastern Gulf of Mexico continental shelf contaminated by crude oil from the BP spill. As we continue to process sediments from additional collection sites, we will develop a better case for or against this hypothesis.

Acknowledgments

We would like to thank the Laboratory of Environmental and Applied Chemistry at Jacksonville State University for the use of equipment during this investigation. Special thanks to the NOAA scientists at the Pascagoula facility and to the crew and officers of the NOAA R/V *Pisces* and the R/V *Gordon Gunther*.

References

- Anderson, L.C. and McBride, R.A. *Taphonomic and Paleoenvironmental Evidence of Holocene Shell-Bed Genesis and History of Northeastern Gulf of Mexico Shelf*. *Palaios*. 1996. 11; 253-263.
- Balsam, W.L. and Beeson, J.P. *Sea-floor Sediment Distribution in the Gulf of Mexico*. *Deep Sea Research Part I*. 2003. 1421-1444.
- Canevari, G.P. and Fiocco, R., 1997: *Crude Oil Vanadium and Nickel Content Can Predict Emulsification Tendency*. In *Proceedings International Oil Spill Conference: Progress, Challenges, Responsibilities*, Fort Lauderdale, Florida. 309-314.
- Distribution of Heavy Minerals in the Gulf of Mexico.
Available from <http://geology.uprm.edu/Morelock/resou.htm> (Accessed on 15 December 2015).
- Emery, K.O. *Relict Sediments on Continental Shelves of World*. *Bulletin of the American Association of Petroleum Geologists*. 1968. 52 (3) 445-464.
- Folk, R.L. *The Distinction between Grain Size and Mineral Composition in Sedimentary Rock Nomenclature*. *Journal of Geology*. 1954. 62; 344-359.

- Gong, Y., Zhao, X., Cai, Z., O'Reilly, S.E., Hao, X., and Zhao, D. *A Review of Oil Dispersed Oil and Sediment Interactions in the Aquatic Environment; Influence on the Fate, Transport and Remediation of Oil*. Marine Pollution Bulletin. 2014. 79, 16-33.
- Hine, A.C., Brooks, G.R., Davis Jr., R.A., Duncan, D.S., Locker, S.D., Twichel, D.C., and Gelfenbaum, G. *The West-Central Florida Inner Shelf and Coastal System: A Geologic Conceptual Overview and Introduction to the Special Issue*. Marine Geology. 2003. 200; 1-17.
- Hoch, M., 2010: *New Estimate Puts Gulf Oil Leak at 205 Million Gallons*. Arlington, VA: PBS News Hour MacNeil/Lehrer Productions.
- Johnson, J. and Torrice, M. *BP's Ever-Growing Oil Spill*. Chemical and Engineering News. 2010. 15-24.
- Kujawinski, E.B., Kido-Soulet, M.C., Valentinéz, D.C., Boysent, A.K., Longneckert, K., and Redmond, M.S. *Fate of Dispersants Associated with the Deepwater Horizon Oil Spill*. Environmental Science & Technology. 2011. 45(4); 1298-1306.
- Landers, S.C., Nichols, A.C., Schimmer, C.A., Stewart, P.M., Ramroop, S., Steffy, D.A., and Romano, F.A. *Meiofauna and Trace Metals from Sediment Collections in Florida following the Deepwater Horizon Oil Spill*. Gulf of Mexico Science. 2015. 32 (1) 1-10.
- Liu, Z., Liu, J., Zhu, Q., and Wu, W. *The Weathering of Oil after the Deepwater Horizon Oil Spill: Insights from the Chemical Composition of the Oil from the Sea Surface, Salt Marshes and Sediment*. Environmental Research Letter. 2012. 7 (3)
- Nichols, A.C., Steffy, D.A., Morgan, L.J., and Gardner, S.T., 2014: *Concentrations of Metals Associated with Crude Oil from the BP Macondo Spill in Fish Collected from the Northeastern Gulf of Mexico Across A Four Year Period*. In Proceedings of Society of Toxicology Annual Meeting, Phoenix, Arizona. 23 March 2014.
- Poppe, L.J., Eliason, A.H., Fredericks, J.J., Rendings, R.R., Blackwood, D., and Polloni, C.F., 2000: *Chapter 1: Grain-Size Analysis of Marine Sediments: Methodology and Data Processing*. U.S. Geological Survey Open-File Report 00-358. Available from: <http://pubs.usgs.gov/of/2000/of00-358/text/chapter1.htm> (Accessed on 25 May 2016)
- Steffy, D.A., Nichols, A.C., Morgan, L.J., Bonner, B., and Gibbs, R., 2013: *Increase in Nickel and Vanadium Concentrations in Sea Bottom Sediment Collected From the Continental Shelf Off Western Florida after the Deepwater Oil Spill, Gulf of Mexico*. In Proceedings of Oil Spill & Ecosystem Science Conference Gulf of Mexico Research Initiative, New Orleans.
- Steffy, D.A., Nichols, A.C., Morgan, L.J., and Gibbs, R. *Evidence that the Deepwater Horizon Oil Spill Caused a Change in the Vanadium and Nickel Average Seasonal Concentrations Occurring in Sea Bottom Sediment Collected from the Eastern Gulf of Mexico Continental Shelf between the Years 2009 and 2011*. Water, Air, & Soil Pollution. 2014. 224; 1756.
- Trimble C.A., Hoenstine, R.W., Highley, A.B., Donoghue, J.F., and Ragland, P.C. *Baseline Sediment Trace Metals Investigation: Steinhatchee River Estuary, Florida, Northeast Gulf of Mexico*. Marine Georesources and Geotechnology. 1999. 17 (2-3) 187-197.

Tyner, E., Blake, N.J., and Doyle, L.J. (n.d.) *Carbonate Production on the Central West Florida Continental Shelf*. USGS Open-File Report 03-303, Available from: http://coastal.er.usgs.gov/wfla/ofr/ofrframework/fr_link8.html (Accessed on 22 March 2016)

US EPA Response to BP Spill, 2010: Available from: www.epa.gov/bpspill (Accessed on 18 November, 2010).

Wise Jr., J.P., Wise, T.F., Wise, C.F., Wise, S.S., Gianios Jr., C., Xie, H., Thompson, D., Perkins, C., Falank, C., and Wise Sr., J.P. *Tar Balls, Oil Slicks, and Released Oil from the Gulf of Mexico in the Immediate Aftermath of the Deepwater Horizon Oil Crisis: Is Genotoxic Metal Exposure Part of the Deepwater Horizon Legacy?* Environ. Sci. Technol. 2014. 48 (5) 2997-3006.

Yen, T.F., 1975: *The Role of Trace Metals in Petroleum*. Ann Arbor, MI: Ann Arbor Science Publishers.

Determination of Zeta Calibration Constant for Fission Track Analysis

Amal Kumar Ghosh, Virendra Kumar Sharma and Rajeev Kumar Singh

Department of Physics, Bhagwant University, Ajmer, Rajasthan, India

Publication Date: 21 July 2016

Article Link: <http://scientific.cloud-journals.com/index.php/IJAESE/article/view/Sci-468>



Copyright © 2016 Amal Kumar Ghosh, Virendra Kumar Sharma and Rajeev Kumar Singh. This is an open access article distributed under the **Creative Commons Attribution License**, which permits unrestricted use, distribution, and reproduction in any medium, provided the original work is properly cited.

Abstract Zeta constant has been determined for calibration in fission track dating. Three apatite age standards have been used for the calibration. The zeta value against a dosimeter glass IRM-540R has been calculated. A single weighted-mean zeta constant is given as 250 ± 1.40 (16).

Keywords Fission track; IRM-540R; Neutrons fluence; Zeta constant

1. Introduction

The Ambiguity of age calibration constants including (the spontaneous fission decay rate of ^{238}U), and the “B-value” encountered in thermal neutron dose measurements has been a controversial problem for a long time in fission track dating (FTD) (Bigazzi, 1981; Hurford and Green, 1981). To circumvent the problem, an alternative way of system calibration, named the zeta calibration, was proposed, in which a calibration constant zeta is determined experimentally against a series of age standards that are well established (Fleischer and Hart, 1972; Hurford and Green, 1982, 1983). The first systematic attempt at calibration was carried out against four zircon standards by Hurford and Green (1983). For determining on unknown AFT age using age standard approach, first the ζ value must be determined. According to Hurford (1900 a-b), a good ζ value requires a calculation of five pair of standard samples which are derived from five different irradiation cans. In this Study, three samples from Durango were counted. The track density on the dosimeter glasses is related to the neutrons fluence. The magnitude of the neutron fluence depends upon the position of the samples during irradiation; the closer a sample is to the radiation source, the larger its track density is derived from a linear regression line of several track numbers of each dosimeter glass in one can.

2. Experimental Procedure

The samples for this study were processed in the laboratory of the Geological Survey of India, Kolkata, after obtaining permission from the Director General, GSI, Kolkata, West Bengal. The samples were prepared using standard separation, grinding and polishing techniques. All the samples were prepared for the external detector method. AFT mounts were etched with 70% HNO_3 at room temperature for 30 s and were irradiated in the thermal facilities of FRM II at Garching, Germany

together with dosimeter glass IRMM-540R (15ppm). Mica sheets were etched using 48% HF at room temperature for 19 min. The fission tracks were counted under a total magnification of 1000x (Figure 1). The calibrated area of one grid is $0.64 \times 10^{-6} \text{ cm}^2$. Durango apatites were used as the age standard mineral, which was provided by Prof. Barry Paul Kohn, University of Melbourne, Australia.

Table 1: Fission track analytical data for zeta calibration and sample weighted mean zeta (SWMZ) value for age standard. Weighted Mean Value of Zeta $\approx 250 \text{ Ma}$
Standard Age of Durango Apatite = $31.4 \pm 0.5 \text{ Ma}$ (McDowell and Keizer, 1977)

Sample Name	N	N_s	N_i	$\rho_s \times 10^6$	$\rho_i \times 10^6$	N_d	ρ_d	Age(Ma) $\pm 1\sigma$	$P(\chi^2)\%$
DUR-1	16	98	750	0.266	2.034	1232	1.925	250 \pm 1.40	9.64
DUR-2	16	96	735	0.260	1.99	409	2.045	235.40 \pm 1.42	18.81
DUR-3	16	100	767	0.271	2.08	1168	1.820	265.49 \pm 1.39	7.8

All of the standard samples were analyzed using the external detector method, with a geometry factor $G=0.5$, N_s and N_i are numbers of spontaneous and induced tracks respectively, ρ_s and ρ_i are the density of spontaneous and induced tracks per cm^2 , N_d is the amount of induced tracks on the mica, and ρ_d is the density of induced tracks on mica per cm^2 . $P(\chi^2)$ – probability for obtaining χ^2 value for n degrees of freedom, where $n = \text{no. of grain} - 1$.

3. Results and Discussion

Zeta was determined empirically by analyzing a set of standard mineral of known age, and it is given by inputting the measured data of standard (i.e., ρ_s , ρ_i and ρ_d) and the reference age t into the following equation:

$$t = \frac{1}{\lambda_D} \ln \left\{ 1 + \lambda_D \zeta \rho_d \left(\frac{\rho_s}{\rho_i} \right) QG \right\}$$

Where λ_D is total decay constant of ^{238}U , viz. $1.55125 \times 10^{-10} \text{ yr}^{-1}$, G is the geometry factor, taken to be 0.5; t is the reference age of the standard sample. The statistical error of zeta was calculated by the “conventional analysis” described by Green (1981). ρ_s was counted on the etched internal surface of each mineral grain, ρ_i was counted on the external detector surface (mica) attached to the mineral grain, whereas ρ_d was counted on mica firmly attached to the dosimeter glass. Table 1 shows the results of repeated measurements on three apatite age standard samples. The presented zeta value in Table 1 does not contain an error component from the reference age at this stage. All the repeated analyses for individual samples show high consistency and sample weighted mean zeta (SWMZ) values were calculated. The consistency of repeated measurements ensures the reproducibility of the FTD analysis in our experiment. The overall weighted mean zeta (OWMZ) value was calculated as 250 ± 1.40 (16).

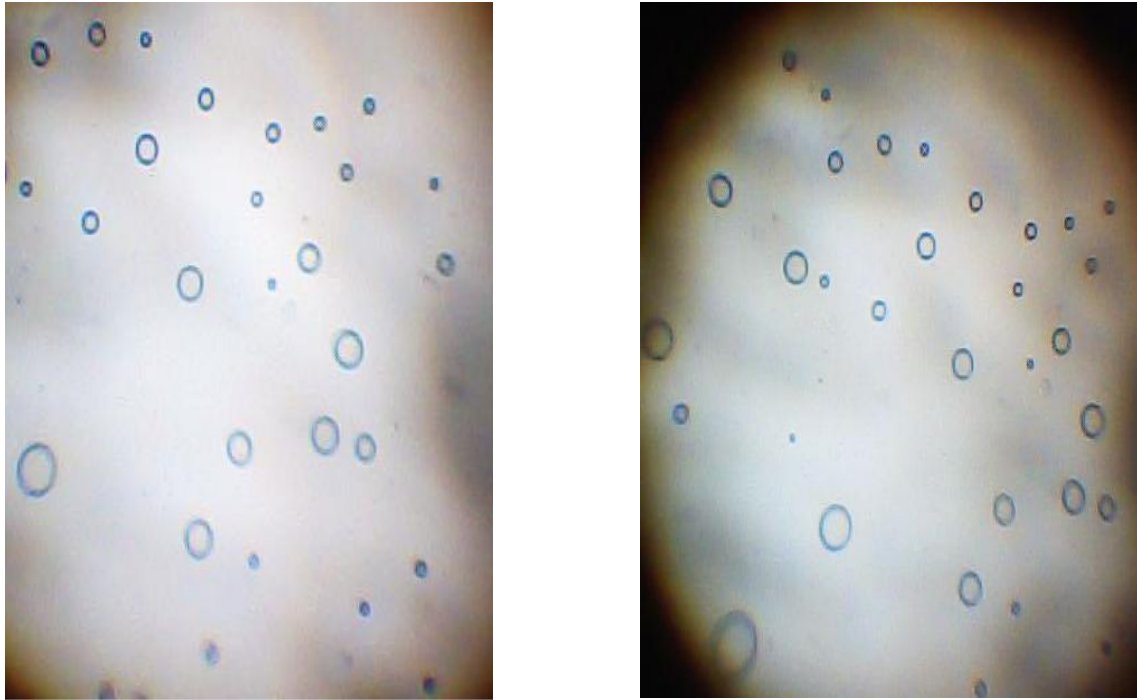


Figure 1: Induced Tracks on Dosimeter Glass (IRM-540R)

4. Conclusion

The personal zeta factor was calculated from three standard samples. The zeta value itself is counted as a weighted mean of individual zeta values of all standard samples (Table 1). Using the Zeta Mean program by Brandon (2001), the weighted mean is determined and yield the zeta value of 250 ± 1.40 with 1σ error.

Acknowledgement

I thank Prof. Barry Paul Kohn, “University of Melbourne”, Australia for his overall support and advice throughout my time as a Ph.D. student. He also sent me age standard minerals (Durango apatite) for zeta calibration. Without his contribution, my work would have never been possible.

I thank Prof. Richard Ketcham “University of Texas”, U.S.A., who kindly reviewed my AFT models and provided valuable guidance for the improvement of the models. Prof. Ketcham also kindly extended his help to offer the important interpretations of my AFT models and the offset AFT age. Prof. Ketcham sent me the copy of the most recent versions of the HeFTy (Ketcham, 2013, Version 1.8.1), I thank Prof. Paul B.O’ Sullivan, Apatite to Zircon, Inc., U.S.A., who kindly initiated my idea into the importance of obtaining the AFT data in the correct form. Prof. O’Sullivan also kindly advised me to contact Prof. Richard Ketcham. My indebtedness to these professors knows no bounds.

I am highly indebted to the Director General of Geological Survey of India, Kolkata for his kind permission to perform my work in the laboratory of G.S.I, Kolkata.

I thank Mr. Partha Nag, Officer-in-Charge, WBMTDC, Purulia for his dedicated help with the field work. I thank Mr. T. Ray Barman, Ex-Scientist, G.S.I, Kolkata, for his constructive advice. Many thanks are due to the entire family of G.S.I., Kolkata, for their help and encouragement.

References

Belton David, X., Brown Roderick, W., Gleadow, A.J.W., and Kohn Barry, P. Fission Track Dating of Phosphate Minerals and the Thermochronology of Apatite. *Reviews in Mineralogy and Geochemistry*. 2002. 48 (1)

Bigazzi, G. The Problem of the Decay Constant λ_f of ^{238}U . *Nuclear Tracks*. 1981. 5 (1-2) 34-44.

Gleadow, A.J.W. Fission Track Dating Methods: What are the Real Alternatives? *Nuclear Tracks*. 1981. 5 (1-2) 3-14.

Green, P.F. Comparison of Zeta Calibration Baselines for Fission-Track Dating of Apatite, Zircon and Sphene. *Chem. Geol.* 1985. 58 (1-2) 1-22.

Hurford, A.J. and Green, P.F. The Zeta Age Calibration of Fission-Track Dating. *Isotope Geosci.* 1983. 41; 285-317.

Delineation and Characterization of Geomorphological Features Studies of Muguru Addahalla Watershed, Mysore and Chamarajanagar Taluks of Southern Part of Karnataka, India

Nagaraju D., Siddaraju K., Shivaswamy, Bhanupraksh H.M., and Balasubramanian A.

Department of Studies in Earth Science, University of Mysore, Mysuru

Publication Date: 19 October 2016

Article Link: <http://scientific.cloud-journals.com/index.php/IJAESE/article/view/Sci-484>



Copyright © 2016 Nagaraju D., Siddaraju K., Shivaswamy, Bhanupraksh H.M., and Balasubramanian A. This is an open access article distributed under the **Creative Commons Attribution License**, which permits unrestricted use, distribution, and reproduction in any medium, provided the original work is properly cited.

Abstract In the present study an attempt has been made to delineate and characterize the different geomorphic units of Muguru Addahalla watershed located in the southern part of Karnataka State, India. The drainage network and topographic elevation contours have been delineated using toposheets. The geological units have been overlaid on the Indian Remote Sensing (IRS)-1D LISS-111 satellite imagery. The study area is basically a drainage-controlled region wherein the fluvio-geomorphological processes dominate on the surface. Based on the interpretation of satellite data, the hydrogeomorphic units like linear ridges, shallow moderate and deeply buried slopes, shallow valley fills and deep valley fills have been demarcated. These zones have been generated as vector layers using GIS and the geological and geomorphological maps of the study area have been compared. This integrated approach demonstrated that the IRS data used in conjunction with geology, drainage and topographic parameters helped in the evaluation of different geomorphological units and their characteristics. These features were also verified based on the field observations. The geomorphological units can be utilized for the management of natural resources.

Keywords *Fluvio-Morphology; GIS, Drainage; Contour Geomorphological Units; Natural Units*

1. Introduction

Geomorphology deals with the study of the landforms. A systematic study of landforms can reveal the signatures of the past and ongoing geological processes. The geomorphic features of a region have a great bearing on the water resources of that region. Certain geological agents like rivers, glaciers, winds, etc relentlessly operate on the earth's crust to bring about the changes of degradation and aggradation. These features are important from the point of understanding the surface and subsurface water movements. Landforms like plateaus, residual hills, pediments, pediplain, piedmont zones, valleys and other landscape features are suitable for the occurrence of the water resources of any basin or region. Similarly, rainfall pattern is yet another influencing factor in the landform evolution. Rainfall pattern will also be playing a key role in terrain development and for water storage and replenishment. Analysis of rainfall pattern is vital for predicting droughts, cycles of surplus rainfall

and runoff pattern, which are ultimately necessary for a comprehensive planning of water resources in a watershed. This study aims to evaluate all these aspects on an integrated approach.

2. Study Area

The Muguru Addahalla watershed spreads in two districts viz. Chamarajanagar and Mysore in southern part of Karnataka (Figure 1). The spatial extent of the study area is 248.827 sq km. The area is covered in Survey of India toposheet numbers 57d/16, 58A/13 and 57H/4. It is bound by north Latitude of 11° 58' 20.78" N to 12° 12' 33.67" N and East longitude of 76° 52' 50.34" E to 76° 59' 25.68" E. The topomap of the area is shown in (Figure 2). The area is well connected with all-weather roads (Figure 1 and 2). Physiographically, Muguru Addahalla watershed forms the 'Southern Maidan' region of Karnataka. It is bound by the Doddasampige Reserve Forest area in the east and Suttur village in the west. The River Cauvery drains in the North and city Chamarajanagar is located at the south. The Muguru Addahalla stream originates at Ummathur Gudda ("Gudda" means mound, in the regional language) in the south and it joins the Cauvery River near the village Ayyanurhundi. The maximum elevation of the area is 900 m (MSL) at Ummathuru Gudda and minimum is 540m (above Mean Sea Level) seen at Muguru Addahalla, where it joins the Cauvery River. The rest of the area constitutes very gently dipping plains, dissected by shallow rivulets. Much of the area is under cultivation.

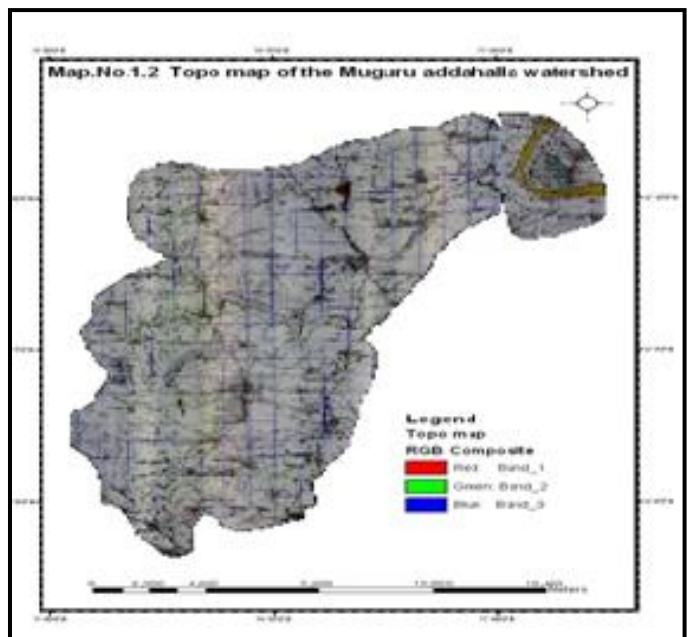
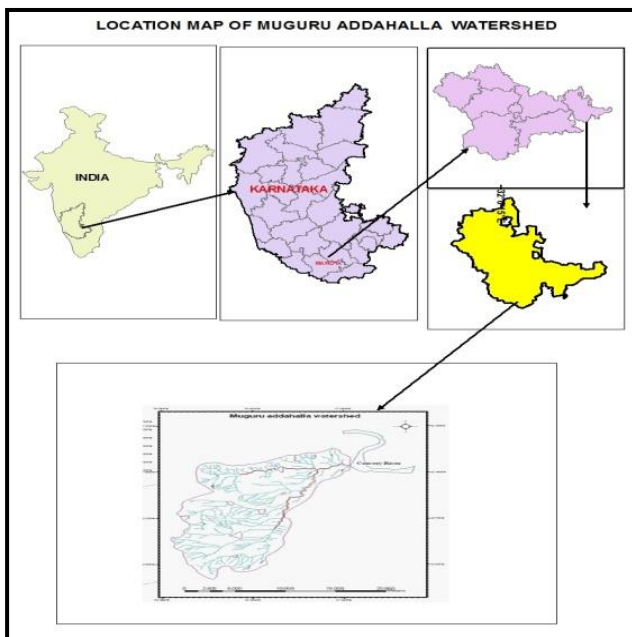


Figure 1: Location map of the Muguru Addahalla watershed

Figure 2: Topo map of the Muguru Addahalla watershed, (Merged toposheets of 57D/16, 58A/13 and 57H/4)

3. Methodology

The different thematic maps of the study area were prepared by making use of a base map. This base map was prepared using Survey of India toposheets bearing nos. 57D/16, 58A/13, 57H/4 in 1:50,000 Scale. Pan+LISS merged data was used for preparing various thematic maps. Visual interpretation and validation with field checks were carried out. In all these interpretations, software's like AutoCAD-2000, ERDAS IMAGINE 8.7, and Arc GIS 9.0 were used. For image and topomap mosaicking and subsetting of different scenes, these software were used.

4. Results and Discussion

4.1. Land use/ land cover

Using Remote Sensing and GIS techniques, the study area is classified into different categories from the point of utility and natural cover, as double crop, kharif, plantations, land with scrub, settlement, stream, tank, gullied land and forest plantations. These are shown in Figure 3, and their aerial extension is shown in (Figure 4). The relevant data is given in the Tables 1 and 2.

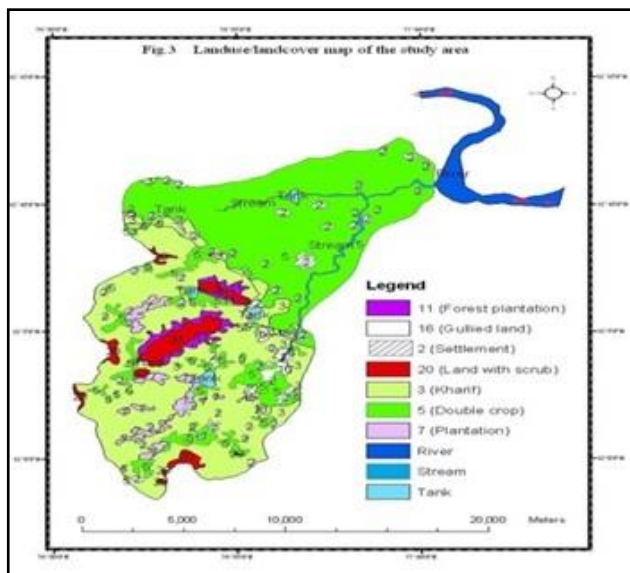


Figure 3: Landuse / landcover map of the study area

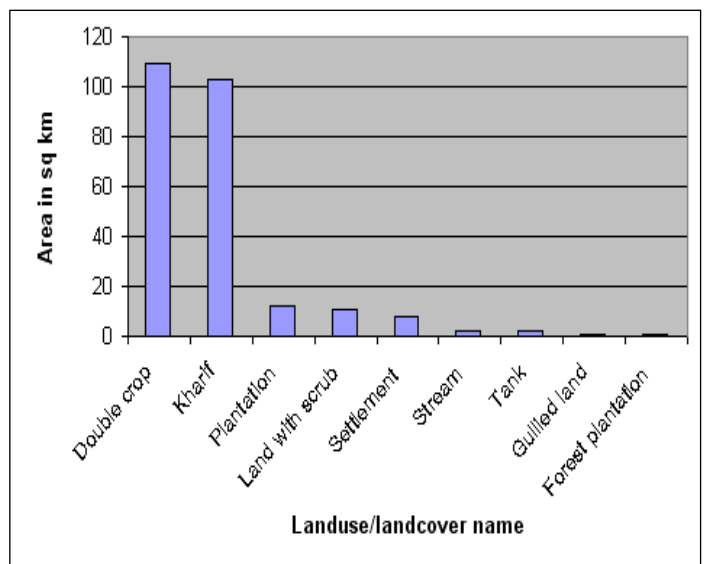


Figure 4: Graphical representation of Landuse / landcover

Table 1: Landuse/landcover Classification

Serial. no	Lu / Lc	Code	Area in sq.km	Area in Percentage
1	Double crop	5	109.6015	44.16
2	Kharif	3	103.0153	41.51
3	Settlement	2	7.5624	3.05
4	plantation	7	12.031771	4.85
5	Forest plantation	11	0.6333	0.26
6	Gullied land	16	0.7034	0.28
7	Land with scrub	20	10.5286	4.24
8	Stream	Stream	2.2349	0.9
9	Tank	Tank	1.8544	0.75

Table 2: Hydrosol unit of the study area (In sq.km)

Run off potential	Area in sq. km
Habitation mask	6.72
Highest	1.19
Low	111.21
Moderately high	90.45
Moderately low	34.52
Water body mask	4.74

4.2. Slope

Slope aspect and altitude are very important terrain parameters from land utilization point of view. For evaluating various ground features of a basin and to prepare different thematic maps, the slope analysis is important. In the present study, the slope map has been prepared on 1:50,000 base map using the guidelines of All India Soil and Land use Survey (AIS & LUS, 1995). The categories of slopes were classified (Table 3). The general classification of slope, following the above guidelines, is shown below:

Table 3: Criteria used for classifying the slope categories

Sl. No.	Slope category	Slope (%)
1	1- Nearly level	0-1
2	2-Very gently sloping	1-3
3	3-Gently sloping	3-5
4	4-Moderately sloping	5-10
5	5-Strongly sloping	10-15
6	6-Moderately steep to steep sloping	15-35
7	7-Very steep sloping	>35

For general slope analysis, the survey of India toposheet in 1:50,000 scales has been used which gives 20 meter contour interval. The closely spaced contours indicate higher order slopes. The slope categories observed are given in the Table 4.

Table 4: Slope category obtained from Contour spacing on 1: 50,000 base maps (IMSD tech. guideline 1995)

Slope category	Lower and Upper limit of slope percentage	Lower and Upper limit of contour Spacing
1.	0-1 %	More than 4 cm
2.	More than 1% upto 3%	More than 1.33 cm and upto 4 cm
3.	More than 3% upto 5%	More than 0.8 cm and upto 1.33 cm
4.	More than 5% upto 10%	More than 0.4 cm and upto 0.8 cm
5.	More than 10% upto 15%	More than 0.26 cm and upto 0.4 cm
6.	More than 15% upto 35%	More than 0.11 cm and upto 0.26 cm
7.	More than 35%	0.11 cm and less

Table 5: Slope area of the study area in sq.km

Slope Code	Slope area/in sq km	Slope area/in Percentage
1	212.07	85.21
2	19.06	7.66
3	2.29	0.92
4	3.97	1.59
5	2.33	0.94
6	3.78	1.52
7	5.37	2.16

Using topographic maps, all the contours of the study area have been updated to understand the altitudinal variations of the watershed. These are shown in Figure 4. Based on these contour maps and comparing with Table 5, and employing the remote sensing and GIS techniques, the slope map has been generated. The area of each category of the slope were determined. The highest slope is

represented by level 1. The level 1 area is more in the study area (85.21 %) and it covers about 212.07 sq km. The directions of slope are found to be along NW, SE, NE, SSE and NNE. The lowest slope area covers 0.92% percentage and is a gently sloping land and covers an area of about 2.29 sq km. The direction of the slope is NW and NNE. Very gently sloping (slope no. 2 is 1 to 3%) covers an area of 19.06 sq km and trending along NE, NNE and SSE directions. Moderately sloping land (Slope no 4 is 5 to 10%) covers an area of 3.97 sq km. Its direction is N, NE and NNE. Strongly sloping (slope.no. 5 is 10 to 15%) area covers about 2.33 sq km (0.94%). It's slope is trending towards SSE and NNE directions. Moderately steep to steep sloping (slope no. 6 is 15 to 35%) covers an area of 3.78 sq km (1.52%). Its slope direction is towards NW and NNE. Very steep sloping (slope no. 7 is >35%) zone covers an area of 5.37sq km (2.16% with a trend towards NNW, SSE and NNE

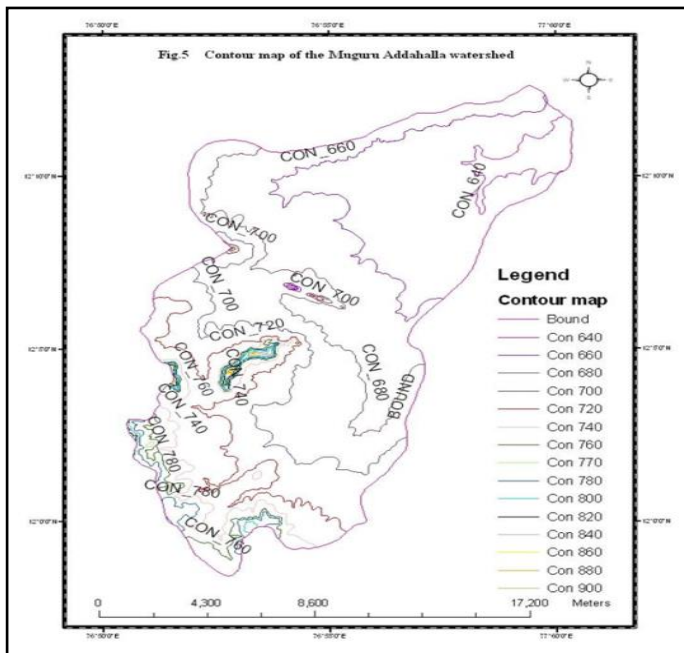
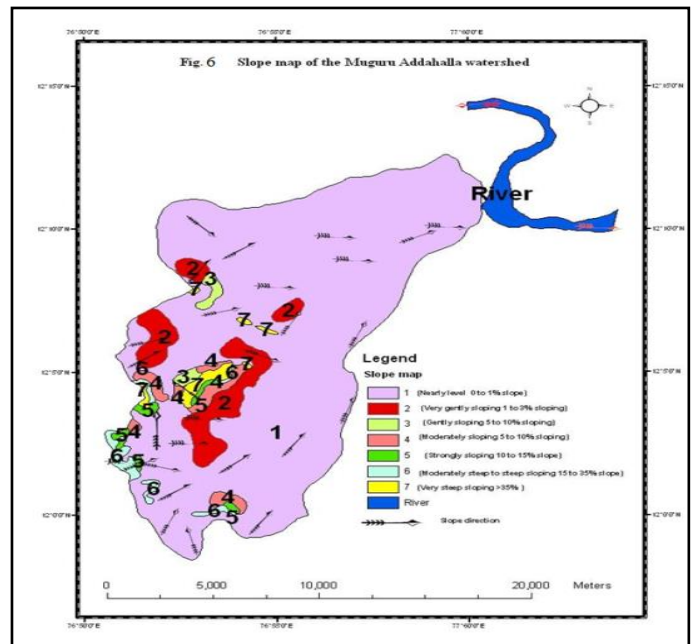


Figure 5: Contour map of the Muguru Addahalla watershed



directions.

Figure 6: Slope map of the Muguru Addahalla watershed

4.3. Morphometric Characteristics

Stream drainage development is a natural dissection of the land surface created by flowing water along the slopes. It's vertical, horizontal and length of depression depends on bedrocks, topography, geological structure and the nature of the soil etc. Many other factors like slope, rainfall and vegetation etc, also contribute for the development of a drain. The study area is represented by dendritic to subdendritic type of drainage pattern. The dendritic drainage pattern is the most common drainage pattern characterized by branching or tree like drainage pattern. Drainage network in the present study was prepared by toposheets and Pan+LISS merged data, in which the spatial resolution of the data is 5.8 m. For this interpretation keys like tone, texture, pattern and association were used. After visual interpretation of the drainage map of the study area, it was scanned and digitized using AutoCAD 2000 and ERDAS IMAGINE and finalized after field validation for the doubtful drainages. Some of the drainage paths were updated near Thottavadi village, northeast of Hallikerehundi, southwest of Vatalupura, near Kannahallimole, southeast of Ayyanurhundi, east of Honnegowdanahundi, south of Halakathurhundi and west and southwest of Karya.

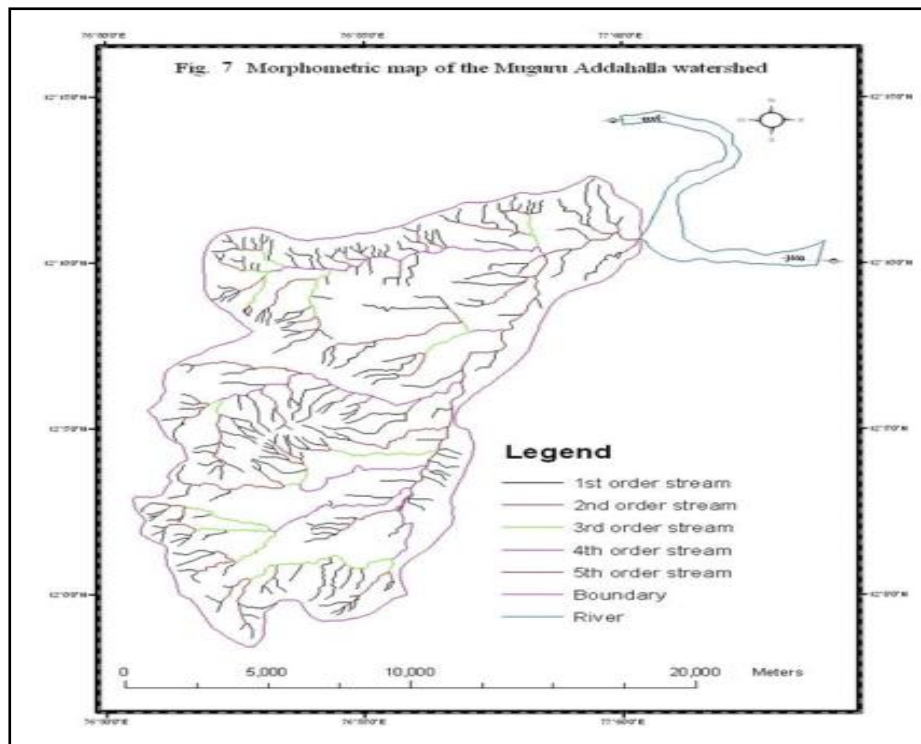


Figure 7: Morphometric map of the Muguru Addahalla watershed

4.4. Lithological Characteristics

The lithological units have been mapped for their spatial extent, and contact relationships have been marked out based on both field observation and satellite imagery studies. The categorization of lithological units was attempted based on Quadrangle map of Geological Survey of India (GSI), Using remote sensing and GIS. The characteristics of various structural patterns were also enumerated. The middle infrared region of the electromagnetic spectrum with the wave length range between 2.08 to 2.35 micrometer is more suitable to differentiate the contact zones between various lithological boundaries.

Table 6: Categories of various lithological units and their spatial extents

Sl. No.	Lithology Code	Area/sq km	Percentage Area Cover
1	GTGN	247.0975	99.28
2	DYKE	0.9647	0.39
3	UM	0.2144	0.09
4	AMP	0.6084	0.24

GTGN :	Gneisses Granodiorite, Tonalite and Migmatite gneiss
AMP :	Amphibolite and Hornblende schist
UM :	Metaultramafics, Metapyroxenite, Serpentinised dunite and Peridotite
Dyke :	Dolerite\Gabbro dyke
GSI :	Geological Survey of India
GIS :	Geographical information system

Among the different lithologies, granitoids cover the largest area of 99.28% followed by dyke (0.39%) and amphibolites (0.24%). The ultramafics occupy the least area (0.09%)

Gneisses, Granodiorite, Tonalite and Migmatite Gneiss (GTGN)

The major rock types of this study area include Tonalite, Trondhjemite and Granodiorite (TTGs). These rocks occur as slightly weathered zones and found at ground level exposures. However, much of the TTG area has been under soil cover. Some isolated outcrops are seen intermittently. Generally, these are well foliated rocks. The strike of the foliation trends along N-S with steeply dipping configurations. Some mafic enclaves and hornblende schists are commonly noticed within these gneissic rocks. The mafic enclaves are hornblende rich, schistose to amphibolite in character. They also show sharp to diffused contacts with the gneisses. The gneisses commonly show migmatitic character at several places. The migmatitic gneisses are pinkish to grayish on the surface and display wavy and banding structures. The migmatitic gneisses also contain wide variety of mafic enclaves. The observations also suggest that many phases of TTGs have been formed episodically.

Amphibolite and Hornblende schist (AMP)

In the southern part of the study area, amphibolite and hornblende schists occur within the gneissic country rocks. They are dark grey to green in colour. Amphibolites range in fabrics with granular to schistose. It is traversed by infrequent thin quartz veins. Hornblende schist is medium to coarse grained and slightly schistose and display strong green colour. They commonly show trends along NE-SW. They normally occur as lenticular patches and linear bodies. Their boundaries with gneisses are normally found to be tectonised. They are more weathered than the surrounding gneisses. They mostly represent the older mafic remnants, but intense deformation and metamorphism defines the clear cut relationships between the larger gneisses and minor mafic units.

Metaultramafics, Metapyroxenite, Serpentinised dunite and Peridotite (UM)

Minor occurrences of metaultramafic rocks like metapyroxenite, serpentinised dunite and peridotites occur in southern part of the study area. These constitute about 0.09% of the spatial extent of the terrain. They generally trend as elongated enclaves within the gneissic terrain. They display strong fabric pattern along N-S similar to that of the fabric pattern in TTG gneisses. They are seen as dark greenish coloured sub-weathered outcrops. They are also more strongly weathered than the surrounding gneisses.

Dolerite / Gabbro Dykes

These are frequently noticed in the study area. They are medium to coarse grained very narrow to slightly wider bodies. They cover an area of 0.9647 sq/km. They mainly trend in the direction of NW-SE, but some also trend in different directions. They have varying width with mainly doleritic in composition and are coarse to medium grained. They normally play an important role in ground water movement and storage. Ground water prospective zone maps have been prepared keeping this as an important factor because, the upstream of the dyke normally stores good amount of water and conversely the downstream side of the dyke will be poorer in ground water.

4.5. Structural Features

Structurally, the area displays shears, joints, faults and lineaments. They are small to moderate in extent with variable dipping configurations. They too play some significant role in ground water percolation. As joints, fractures, and shears are smaller and localized, they could not be quantified through remote sensing data. However, the linear features like lineaments have been quantified. Most of the drainage network in the study area is controlled by these lineaments. Many structural features like folds axis, faults and shears, besides dyke bodies normally appear on remote sensing data

products as lineaments. Often the lineaments develop in a systematic way and hence a spatio-statistical analysis of lineament pattern provides information regarding their tectonogenesis and relevance to ground water movement. The term lineament was originally used by Hobbs (1904), to describe linear features that are “significant lines of land scape” although linear features have been discussed since 1800’s (Hodgson, 1974). Lineaments are both local and regional features. Bhavé et al., (1989) opined that the term lineament is preferentially used to define the unidirectional earth features of larger magnitude. The other synonyms related to lineament that is linear, lineation, geofracture, suture, mega fracture and shear. Several tectonic process and related parameters are involved in the formation of lineaments (Rakshit and Prabhakara Rao, 1989) and they act as neotectonic windows (Ramaswamy, 1997). Lineaments have major tectonic, magmatic, economic and neotectonic significance, and their role in surface and sub surface hydrology is assuming more and more importance. From the point of their origin Sonder (1947) has developed global shear pattern. It envisages lineaments as regular fracture patterns that pervade the globe, generated by the forces of the rotation of the body on its axis. Flattening of the earth in north-south along its axis would produce a set of north-trending tensional and east-trending compressional weakness zones and northwest and northeast trending shears. These would be propagated throughout the life of the planet. Katterfield and Charushic (1970) later recognized such a pattern on satellite imagery of the moon and other planets, and visualized similar dynamics. Lineaments of the study area investigated and interpreted in the background of their regional studies carried by early workers. Based on their characteristics they are grouped into 4 categories by Ganesh Raj (1987) viz. (a) Continuous, (b) Discontinuous, (c) Simple and (4) Composite. Lineament which show uninterrupted linear scarp is termed as continuous lineament. In discontinuous lineaments the discrete features are aligned along a contact path and are relatively closely spaced, such as a linear stream valley or a series of aligned topographic escarpments. A composite lineament consists of more than one type of feature, such as a combination of aligned tonal features and stream segments. Kowalik and Gold (1976) suggested a classification of lineaments based on their lengths as shown in Table 7.

Table 7: Classification of Lineaments (Based on Kowalik and Gold, 1976)

Sl. No.	Lineament Class	Length(km)
1	Short /Minor	1.6 to 10
2	Intermediate	10 to 100
3	Long / major	100 to 500
4	Mega	>500

5. Nature of the Lineaments in the Study Area and Their Classification

In the study area, lineaments are both continuous and discontinuous. As briefed earlier, uninterrupted linear scarp is an example of continuous lineaments. In discontinuous lineaments, the surface feature aligns in a consistent direction and is relatively closely spaced. Both simple and composite lineaments are also observed in this area. Simple lineament is characterized by single type of feature, such as a linear stream or valley. Composite lineaments consist of more than one type of feature. Generally the lineaments of any area are classified as confirmed lineaments and inferred lineaments. Confirmed ones are those which have been identified in satellite imageries and also by field validation, whereas the inferred ones are neither visible on the imageries nor could be recognized in the field. In the study area, most of the lineaments have been confirmed through the imagery and field studies. However, there is a possibility of concealed lineaments and they too could have played important role in ground water accumulation.

Following Kowalik and Gold (1976) the lineaments of the study area have been classified and the pie diagram shows the total number of lineaments in which less than 1 km ones are found to be 188 in number and the 1 to 2 km lineaments are 51 and 2 to 3 km lineaments are 12 and the total length of the lineaments is contributed by lineaments of 2-3 km length followed by 1 to 2 km and <1 km lineaments. It depicts that lineaments of < 1 km account for 113.80 km cumulative length and 1 to 2 km lineaments occupy 67.43 km. Lineaments of 2 to 3 km length account for 137.47 km cumulative strike length.

Table: Spatial Distribution of Lineaments in the study area

Lineament range in km	Total length of lineament in each class(km)	Total no of lineaments
Less than 1Km	113.80	188
1 to 2km	67.43	51
2 to3 km	137.47	12

6. Total length wise distribution of lineaments in the Pie diagram

The lineaments are running in N-S, E-W, NW-SE, NE-SW, NNE-SSW, NNW-SSE directions. It can be seen that 2 to 3 km lineaments are align along the stream course, shears and less frequently along the contacts of different litho units. 1-2 km and less than 1 km lineaments are found along and sides of the drainage segments. Joints, fracture and fissure zones and contact zones of litho boundary. All these characteristics are identified on the satellite imageries, based on parameters like colour, tone, texture, pattern and association. Lineaments, especially the geotechnical ones are known to be excellent sites for groundwater movement and storage. The ground water potential of the study area has been appraised from this angle, because good net-work of lineaments, as is found here, contribute significantly for ground water potential. As such, the bedrocks of the study area are not so favorable for ground water movement, due to their inherent properties, but are rendered considerably favorable due to the existence of lineaments.

7. Geomorphology

7.1. Residual hills

It is formed due to differential weathering and erosion and a more resistant formation (controlled by rock type) stand as hills. The structures which control their formation are joints and fractures. The lithology in residual hill area is dominant with granodiorite, tonalite and migmatitic gneiss. They are the prominent and elevated features in the study area. Such hills are noticed in northwest and adjacent areas of Hanumanapura. They are also noticed around Karya and also west and northwest of Ummatturu village. Residual hills cover an area of 3.0958 sq km (1.24% of the watershed). The tributary Muguru Addahalla originates at Ummathur Gudda at an altitude of 300m from MSL as a first order stream.

7.2. Pediments

Gently sloping smooth surfaces of eroded bedrocks between hills and plains with veneer of detritus lithologies like granodiorite, tonalites and migmatitic gneisses, constitute the pediment zones. Fractures play an important role in their formation. These pediments are situated west and northwest of Ummathuru village, west of Paduvalamarahalli, southwest of Hanumanapura and west and northwest of Bagali village. The total area covered by pediments is 5.715 sq km (2.3% of the watershed).

7.3. Pediment Inselbergs

The isolated low relief hills surrounded by gently sloping, smooth, erosional bed rocks constitute the pediment inselbergs. Bedrocks like granodiorites and migmatitic gneisses are the lithologic units controlling the pediment inselbergs. Again here also joints fracture, and lineaments have controlled their formation. Prominent pediment inselbergs are situated in northeast of Hallikerehundi. The area occupied by them is 0.1461 sqkm (0.06% of the total area).

7.4. Pediment Inselberg Complex

These are isolated low relief hills surrounded by gently sloping smooth bed rocks. As the dominant lithologic unit of the area is granitoids, this pediment inselberg complex is also encompassed by granodiorite, tonalitic and migmatitic gneisses. These are controlled by structures like joints, fractures and lineaments. The only difference between the pediment inselberg complex and pediment inselberg is, in the case of pediment inselberg, it is a single isolated low relief hill but in the case of pediment inselberg complex it is more than one isolated low relief hill but occurring very closely. These land forms are observed in the northeast of Badanaguppe village. The area covered by them is around 1.607 sq km (0.65% of the total area).

7.5. Pediplain (Shallow)

They are formed by coalescence of buried pediments, where a thick overburden of weathered materials accumulate. The intensely weathered areas of granitoids constitute these landforms. Varying thickness of shallow overburden are observed in such areas. Weathering of the bedrocks has been initiated by fractures, joints and minor lineaments. The area covered by such land forms is very vast, and account for about 107.81 sq km (43.31% of the total area). These land forms are spread over the villages namely, Hosahalli, Badanaguppe, Hanumanapura, Honnegowdanahundi, Karya, Kuderu, Demahalli, Hallikerehundi, Dasanuru, Ummatturu, Jennuru, Jennuru Hosuru and Bagali, Hosuru Hundi.

7.6. Pediplain (Moderate)

Flat and smooth buried pediplain and pediment with moderately thick overburden are called pediplain moderate. Thickness of weathered material is high when compared to pediplain shallow. The weathered materials are chiefly constituted by gneisses and migmatites. They are extended towards southwest of Demahalli upto Dasanua, Ankushayyanahalli, Badanaguppe, Karya and Hanumanapura villages covering a total area of 34.1008 sq km (13.7% of the total area).

7.7. Pediplain Shallow Command Area

These are the Pediplain shallow land forms but occurring in the irrigated command area. Like in other areas, they are formed by coalescence of buried pediments where a thick overburden of weathered materials occurs to form pediplain shallow. Here, the overburden is a weathered mantle of granodiorite, tonalitic and migmatitic gneisses, with varying thickness. The weathering is controlled by fracture, faults and lineaments. This zone is extended towards north, northeast and northwest of Bagali, Hyakanur and Vatalu villages and the areal extent is 66.0929 sq km (26.56% of the total area).

7.8. Pediplain Moderate Command Area

Flat and smooth buried pediplain and pediment with moderate thickness of overburden occurring in irrigated command area are termed as pediplain moderate command area. The lithology here includes granodiorite, tonalitic and migmatitic gneisses. They are controlled by fracture here and lineaments. Thickness of the weathered mantle is high when compared to pediplain shallow command area. It is extended towards west and southwest of Ayyanurhundi, and extends up to Hanumanapura. They are also observed close to Marahallipura, Badanaguppe, Karapura and Ankushayyanapura, Dasanuru, Ummatturu and Kuderu. The aerial extent of the landform is 25.553 sq km (10.28% of the total area). Besides mapping and delineating the above land forms, the water bodies have also been delineated using toposheets updated with imageries. These surface water bodies influence the surrounding bore wells and ground water recharge conditions. Out of the total surface water bodies, the streams occupy 2.23 sq.km (0.9% of the total area) and the lakes (tanks) occupy about 2.51 sq.km (1.01% of the total area).

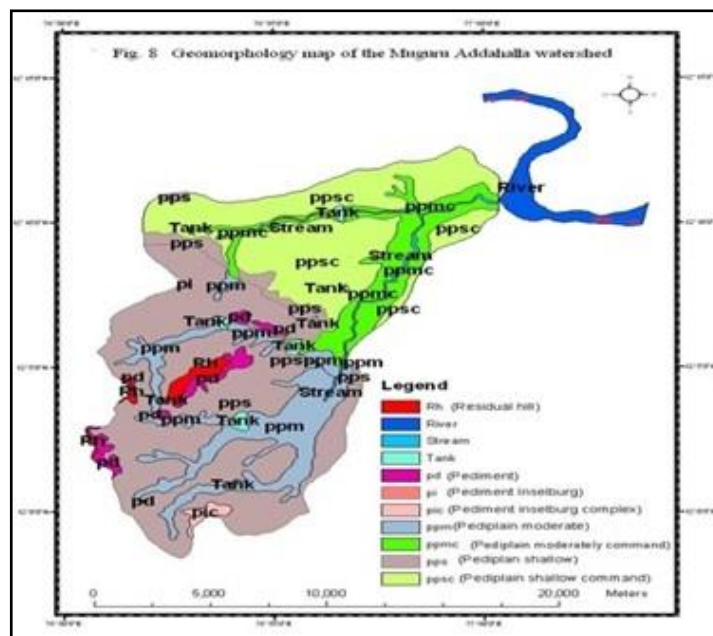


Figure 8: Geomorphological map of the Muguru Addahalla Watershed

Table 8: Geomorphomic units of the study area (In sq .Km)

Serial No.	Geomorphomic unit	Area in sq.km	Percentage
1	PI	0.1461	0.06
2	PD	5.712	2.3
3	PIC	1.607	0.65
4	PPM	34.1008	13.7
5	PPMC	25.553	10.28
6	PPS	107.8075	43.31
7	PPSC	66.0929	26.56
8	RH	3.0958	1.24
9	STREAM	2.2349	0.9
10	TANK	2.5141	1.01

PI : Pediment Inselberg
 PD : Pediment

PIC	:	Pediment Inselberg Complex
PPM	:	Pediplain Moderate
PPMC	:	Pediplain Moderate Command
PPS	:	Pediplain Shallow
PPSC	:	Pediplain Shallow Command
RH	:	Residual Hill

8. Hydrogeomorphological Characterization of the Study Area

The geomorphic unit-wise ground water prospect zones, their subsurface phenomenon, their identification and distribution were done based on the analysis of directly observable terrain features like geological structures, geomorphic features and their hydrological significances. Remote sensing techniques also helped for a better understanding and more systematic analysis of various geomorphic units.

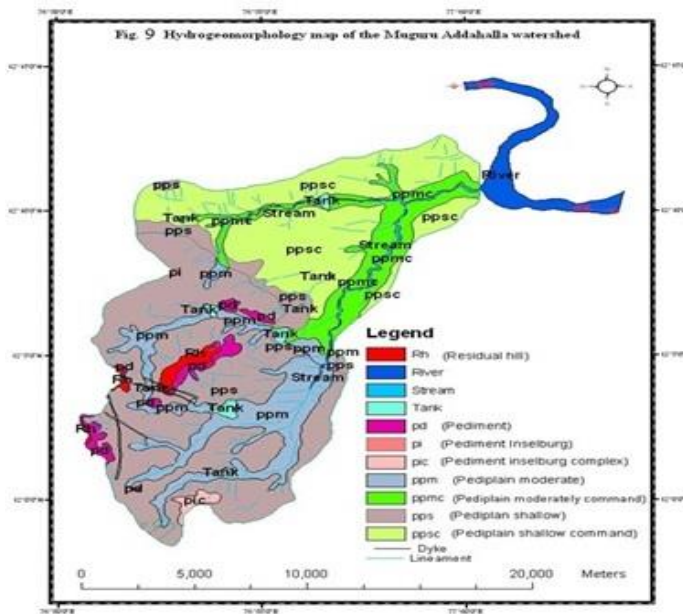


Figure 9: Hydrogeomorphological map of the Muguru Addahalla Watershed

Table 9: Ground water prospect of Hydrogeomorphic unit

Sl. No	Map Symbol	Geomorphic Unit	Structure	Description	Ground Water Prospect
1	Rh	Residual hill	Joints, fractures, Lineaments	Isolated low relief formed due to differential erosion so that a more resistant formation and as residue like small hills.	Poor to nil
2	Pd	Pediment	Sometimes Fracture controlled	Gently sloping, Smooth surface of erosional bedrock between hill and plain with veneer of detritus.	Moderate to poor, varies with underlying Lithology; presence of fracture lineaments.
3	Pi	Pediment Inselberg	Sometimes Controlled by joints, fracture lineaments etc.	Isolated low relief/hill surrounded by gently Sloping smooth erosional bedrock with veneer of detritus.	Moderate to poor
4	Pic	Pediment Inselberg comple	Same as that of Pediment Inselberg complex	Isolated low relief/hill surrounded by gently Sloping smooth erosional bedrock with veneer of detritus and coalescence of group of Pediment Inslberg.	Moderate to poor
5	Pps	Pediplain shallow	Joints, fracture Lineaments etc	Coalescene of pediments marked by a large area and shallow soil depth.	Moderate to poor varies With underlying Lithology and structure.
6	Ppm	Pediplain moderate	Joints fracture lineaments etc	Coalescene of pediments marked by a large area and moderate soil depth.	Good to moderate varies with underlying Lithology and structure.
7	Ppsc	Pediplain shallow Comman	Joints fracture and lineaments	Coalescene of pediments marked by a large area and shallow soil depth and recharge the ground water by Canal water.	Moderate to poor varies With underlying Lithology and Structure and sometimes moderate to good depending On structure and the amount of ground water Recharge by the canal.
8	Ppmc	Pediplain moderate	Joints fracture and lineaments	Colaescene of pedinents marked by a large area and moderate soil depth and recharge the ground water by the canal water.	Good to moderate varies With underlying Lithology and Structure and sometimes good to very good depending on structure, the amount of ground water recharge by canal.
9	Dyke	Dyke	Dyke	It is the discordant type of Igneous body having wall type of structure.	Acts as a ground water barrier water is available on the upstream of the dyke.
10	Lineament		Lineament	It represents joints, fracture, Shear zones	Good to very good

8.2. Recharge Geomorphc Unit of the Study Area

Residual hill (RH), Pediment (PD), Pediment Inselberg (PI) and Pediment Inselberg Complex (PIC) are the regions of medium to high slope gradient (slope category 4-7). In these regions, infiltration is expected to be less and hence the runoff is expected to be more. Water gets collected from these regions, but moves towards pediplain shallow (PPS), pediplain moderate (PPM), pediplain shallow command (PPSC) and pediplain moderate command (PPMC) regions. All these land forms come under the slope category 1 to 3.

8.3. Discharge-prone Geomorphc Unit of the Study Area

The Pediplain shallow (PPS) and Pediplain Shallow Command Area (PPSC) landforms come under 1st to 3rd order stream regions. Here, the ground water potential is expected to be poor to moderate. It will be moderate to good depending on the existence of fractures, fissures and jointed zones. Pediplain Moderate (PPM) and Pediplain Moderate Command (PPMC) land forms come under 1st to 5th order streams. Here, the ground water potentiality is expected to be moderate to good. It will be very good depending upon the existence of fractures, fissures and jointed zones. Such studies have been carried out for different river basins based on remote sensing and GIS techniques by various workers (Krishnamurthy 1991 & 1996; Gupta and Ganeshraj, 1992; Gupta 2002; Travaglia et al., 1987).

9. Conclusion

Remote sensing and GIS proved to be efficient tool in drainage basin analysis. In this study, the integrated method adopted by using topographic and drainage details, lithologic units, hydrogeomorphic units and other parameters was focused to identify the groundwater potential zones. The landforms like plateaus, residual hills, pediments, pediplain, piedmont zones, valleys and

other landscape features are suitable for the occurrence of the water resources of any basin or region. The geomorphic unit-wise ground water prospect zones, their subsurface phenomenon, their identification and distribution were done based on the analysis of directly observable terrain features like geological structures, geomorphic features and their hydrological significances. Remote sensing techniques also helped for a better understanding and more systematic analysis of various geomorphic units.

References

Agarwal, C.S. Study of Drainage Pattern through Aerial Data in Naugarh Area of Varanasi District. *U.P. Jour. Indian Soc. Remote Sensing*. 1998. 26 (4) 169-175.

AIS & LUS, 1990: *Watershed Atlas of India, Department of Agriculture and Co-operation*. All India Soil and Land Use Survey, IARI Campus, New Delhi.

Clarke, J.I., 1966: *Morphometry from Maps*. Essays in Geomorphology. New York: Elsevier Publ. Co. 235-274.

GSI, 1981: Geological and Mineralogical Map of Karnataka & Goa. Geological Survey of India.

Gottschalk, L.C., 1964: *Reservoir Sedimentation*. In: Chow, V.T., (ed.), *Handbook of Applied Hydrology*. New York: McGraw Hill Book Company. Section 7-1.

Horton, R.E. *Drainage Basin Characteristics*. *Trans. Am. Geophys. Union*. 1932. 13; 350-361.

Horton, R.E. Erosional Development of Streams and their Drainage Basins; Hydrophysical Approach to Quantitative Morphology. *Geol. Soc. Am. Bull.* 1945. 56; 275-370.

Langbein, W.B. Topographic Characteristics of Drainage Basins. *U.S. Geol. Surv. Water-Supply Paper*. 1947. 986 (C) 157-159.

Miller, V.C., 1953: A Quantitative Geomorphic Study of Drainage Basin Characteristics in the Clinch Mountain Area, Virginia and Tennessee, Proj. NR 389-402, Tech Rep 3, Columbia University, Department of Geology, ONR, New York.

Nag, S.K. Morphometric Analysis Using Remote Sensing Techniques in the Chaka Sub-Basin, Purulia District, West Bengal. *J. Indian Soc. Remote Sensing*. 1998. 26 (1&2) 69-76.

Nag, S.K. and Chakraborty, S. Influence of Rock Types and Structures in the Development of Drainage Network in Hard Rock Area. *J. Indian Soc. Remote Sensing*. 2003. 31 (1) 25-35.

NRSA, 1995: Integrated Mission for Sustainable Development Technical Guidelines. National Remote Sensing Agency, Department of Space, Government of India, Hyderabad.

Reddy, P.R.R. and Rangaswamy, C.Y., 1989: Groundwater Resources of Pavagada Taluk, Tumkur District. Groundwater Studies No. 240. Department of Mines and Geology, Government of Karnataka, Bangalore.

Singh, S. and Singh, M.C. Morphometric Analysis of Kanhar River Basin. *National Geographical J. of India*. 1997. 43 (1) 31-43.

Schumm, S.A. Evolution of Drainage Systems and Slopes in Badlands at Perth Amboy, New Jersey. *Geol. Soc. Am. Bull.* 1956. 67; 597-646.

Smith, K.G. Standards for Grading Textures of Erosional Topography. *Am. Jour. Sci.* 1950. 248; 655-668.

Srivastava, V.K. Study of Drainage Pattern of Jharia Coalfield (Bihar), India, through Remote Sensing Technology. *J. Indian Soc. Remote Sensing.* 1997. 25 (1) 41-46.

Srivastava, V.K. and Mitra, D. Study of Drainage Pattern of Raniganj Coalfield (Burdwan District) as observed on Landsat-TM/IRS LISS II Imagery. *J. Indian Soc. Remote Sensing.* 1995. 23 (4) 225-235.

Strahler, A.N. Quantitative Analysis of Watershed Geomorphology. *Trans. Am. Geophys. Union.* 1957. 38; 913-920.

Strahler, A.N., 1964: *Quantitative Geomorphology of Drainage Basins and Channel Networks*. In: Chow, V.T. (ed.), Chapter, *Handbook of Applied Hydrology*. New York: McGraw-Hill. 4-39/4-76.

Analysis and Evaluation of Groundwater Quality in Periyapatna Taluk, Karnataka State, South India

Nagaraju D., Kouhsari M., Bhanupraksh H.M., Siddaraju K., Shivaswamy and Balasubramanian A.

Department of Studies in Earth Science, University of Mysore, Mysuru

Publication Date: 19 October 2016

Article Link: <http://scientific.cloud-journals.com/index.php/IJAESE/article/view/Sci-485>



Copyright © 2016 Nagaraju D., Kouhsari M., Bhanupraksh H.M., Siddaraju K., Shivaswamy and Balasubramanian A. This is an open access article distributed under the **Creative Commons Attribution License**, which permits unrestricted use, distribution, and reproduction in any medium, provided the original work is properly cited.

Abstract An attempt has been made for the first time in this region to assess the groundwater quality and the suitability of groundwater for drinking and irrigation purposes systematic studies which are significant for assessment of water quality have been carried out to find out the area for sources of dissolved ions in groundwater of Periyapatna taluk, part of upper basin, which is one of the sub basins of Cauvery River, Karnataka. One hundred and twenty samples have been collected from different bore wells for two seasons (Pre-monsoon and Post-monsoon.) The physico chemical parameters such as hydrogen ion concentration (pH) and Total Dissolved Solids (TDS) were measured in addition to major cation and anion concentrations. A comprise of ground water quality is relation to drinking water standards was made. The pH values of ground water for pre monsoon season in this area range from 7.20 to a maximum of 9.50 and for Post monsoon season is 7.56 to 9.85.(from 6.50 to 8.50 for dug wells and bore wells receptively). The average pH value for the groundwater of the region is 7.20 which indicates slightly alkaline nature of water and are suitable drinking purpose. About 92% of groundwater samples fall in hard water category and there is a need for softening these waters if it is to be used for drinking and domestic purposes. All the samples are within the permissible limits as per standards proposed by WHO. In the most of the samples alkaline earths ($Ca^{2+}+Mg^{2+}$) exceeds alkalies 44.30% for pre monsoon and 56.40% for post monsoon season and strong acids exceeds weak act 3.50% for pre monsoon and 1.80% for post monsoon season as per Pipers trilinear diagram based interpretation

Keywords *Hydrogeochemistry; Groundwater; Physico Chemical Parameter; Periyapatna Taluk; Karnataka*

1. Introduction

Water is the most essential natural resource for sustaining life and environment. The quality of water plays an important role in promoting the agricultural production and human health. The available water resources are under severe pressure due to increased demands; the time is not far when the water, which we have always thought to be available in abundance and free gift of nature, will become a scare commodity. In Karnataka majority of the water supply schemes are dependent on

ground water. The number of wells and bore wells has increase fivefold during the last fifty years. Groundwater levels are declining at the rate of one meter or more per year on account of several reasons. Over exploitation in the form of excessive withdrawal either locally or over a large area has been observed in several parts in order to meet the increasing demand of water. The use of water for various purposes has significantly risen during the last century and the trend continues. This has led to focus the attention on sustainable use of water resources and maintenance of environmental quality. The first and necessary step in this endeavor is inventory of water resources of a region. The total amount of water which is present in hydrosphere is classified into different forms which include free water in liquid, solid, or gaseous state. These forms of water are spread all along the atmosphere, earth's surface and in crust down to a depth of 2000 meters. The Hydrogeochemical study alone reveal can the quality of water and its suitability for drinking and irrigation purposes. Therefore an attempt made to discuss the various hydrogeochemical parameters of the groundwater of Periyapatna taluk, Karnataka in this work.

2. Study Area

The study area is bounded in the north by Hassan district, in the south by Hunsur taluk, in the east by K.R. Nagar taluk and in the west by Kodagu district. Periyapatna is located at 12.34°N 76.1°E with the geographical area extent of 815 SqKm covering 203 villages (Figure 1). All the villages are well connected by all weather roads. A southern railway broad gauge line connects the headquarters passing through the eastern part of the study area. This area falls into the western block of Proterozoic basins of Southern Karnataka and comes under the semi-arid type of climate with gneisses occupying the total area and has limited recharge facilities. The study area belongs to one out of seven taluks of Mysore district.

2.1. Geology and Climate

The study area is underlain by hard rock terrain consisting peninsular gneiss, ultramafics, hornblende-biotite gneiss, charnockites and intruded by dolerite dykes of Proterozoic era. Charnockite is the wide spread formation of the study area. Peninsular gneiss comprises of migmatites, gneisses and granitoids. These forms a backdrop to the scattered Schist belts of Karnataka, which are mainly covered by thick black cotton soil (Figure 2). The Periyapatna taluk is moist during the winter and rainy season. There are 7 rain gauge stations in this taluk. The average annual rainfall is 696mm. About 37% of the annual rainfall is received during the SW monsoon (June – September) and is 36% during the post monsoon or NE.

3. Methodology

Groundwater samples have been collected in dry and clean one liter plastic cans. The samples have been collected from 115 locations during two seasons pre monsoon and post monsoon in 2014 and location of villages used for collecting samples are shown in Figure 3. The samples were collected from all available bore wells which are being used for drinking and irrigation purposes. The physico-chemical analysis was performed following standard methods (APHA, 1995). TDS was determined by multiplying the EC value (Todd, 1980). The analytical results of chemical analysis of groundwater for Periyapatna taluk are provided in Table 1. These data were processed by using computer software named as HYCH in BASIC which is written by Balasubramanian et al. (1991). Figure 4 shows the Flow chart of the program "HYCH".

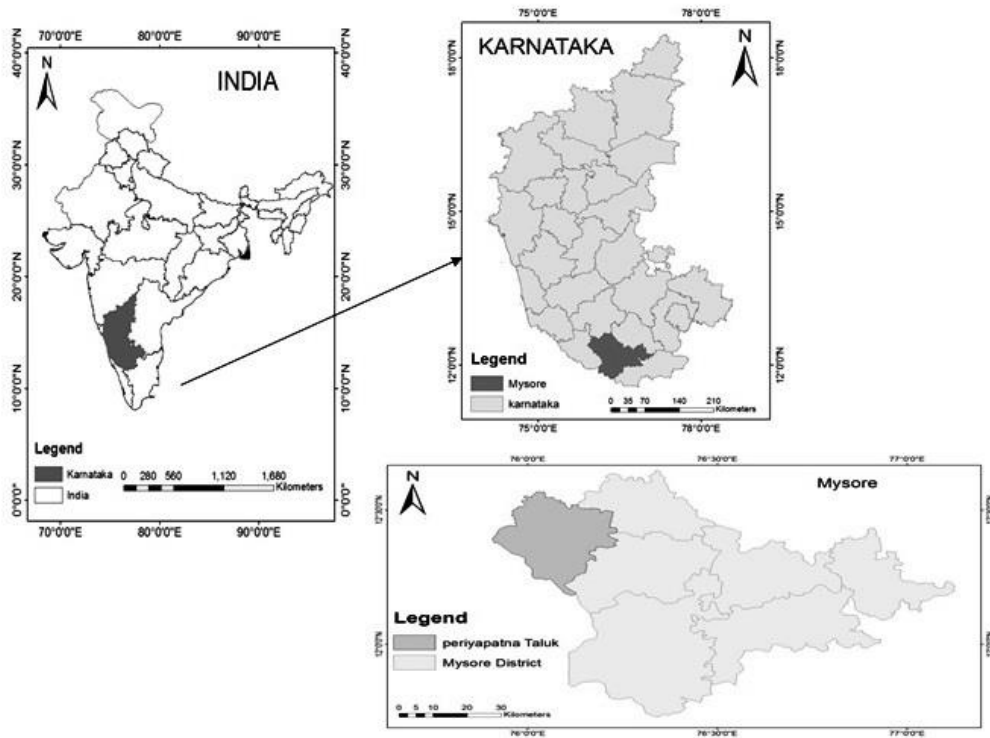


Figure 1: Location of the study area

The mean maximum temperature is 34°C in April and mean minimum temperature 16°C in December, so generally the climate is not humid.



Figure 2: Lithology of the study area

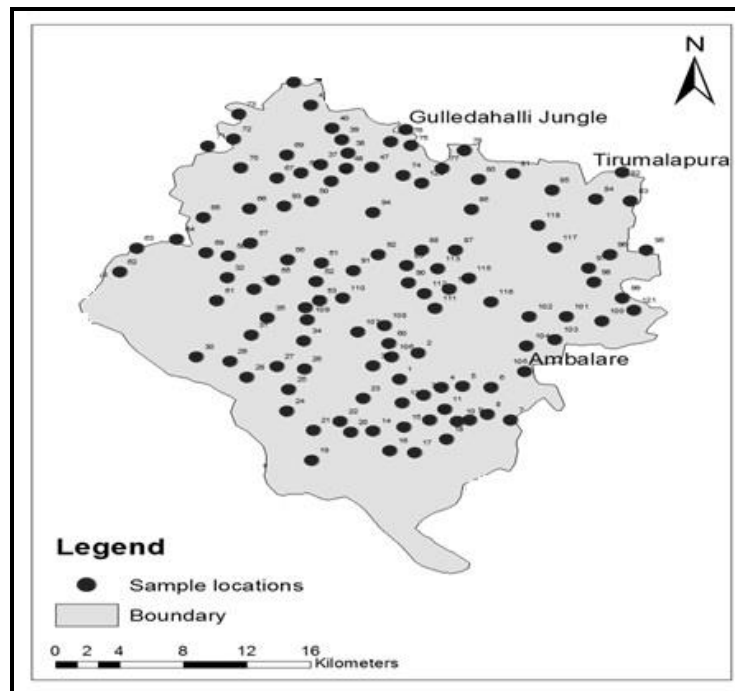


Figure 3: Sample locations of the study area

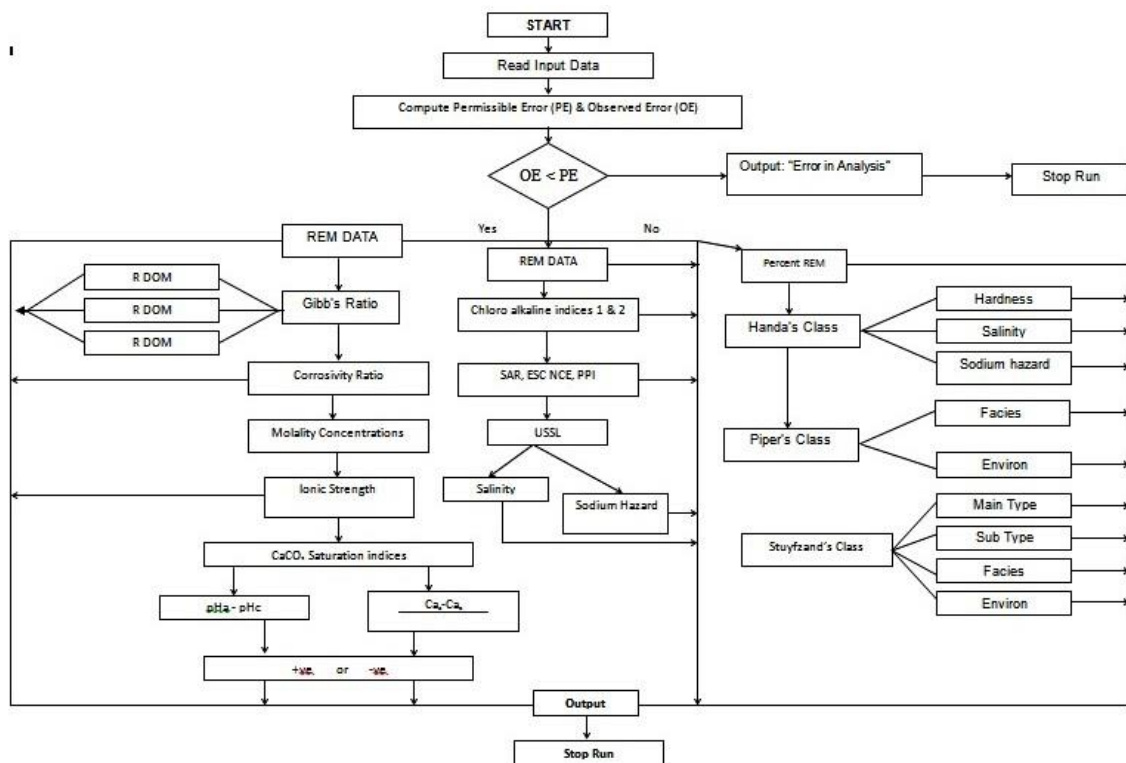


Figure 4: Flow chart of the program "HYCH"

5. Results and Discussions

5.1. Hydrogen Ion Concentration (pH)

The present investigation reveals that the pH values of groundwater in this area for Pre monsoon season range from minimum 7.20 to a maximum of 9.50 and for Post monsoon season is minimum 7.56 to a maximum of 9.85.(from 6.50 to 8.50 for bore wells receptively). The average pH values for the groundwater of Periyapatna taluk is 7.98 for Post monsoon and in pre monsoon season 8.89 and for post monsoon season it is 8.30.This indicates slightly alkaline nature and not suitable it is drinking purpose according to the WHO (1971) and BIS (1991) standards is shown in Figure 5.

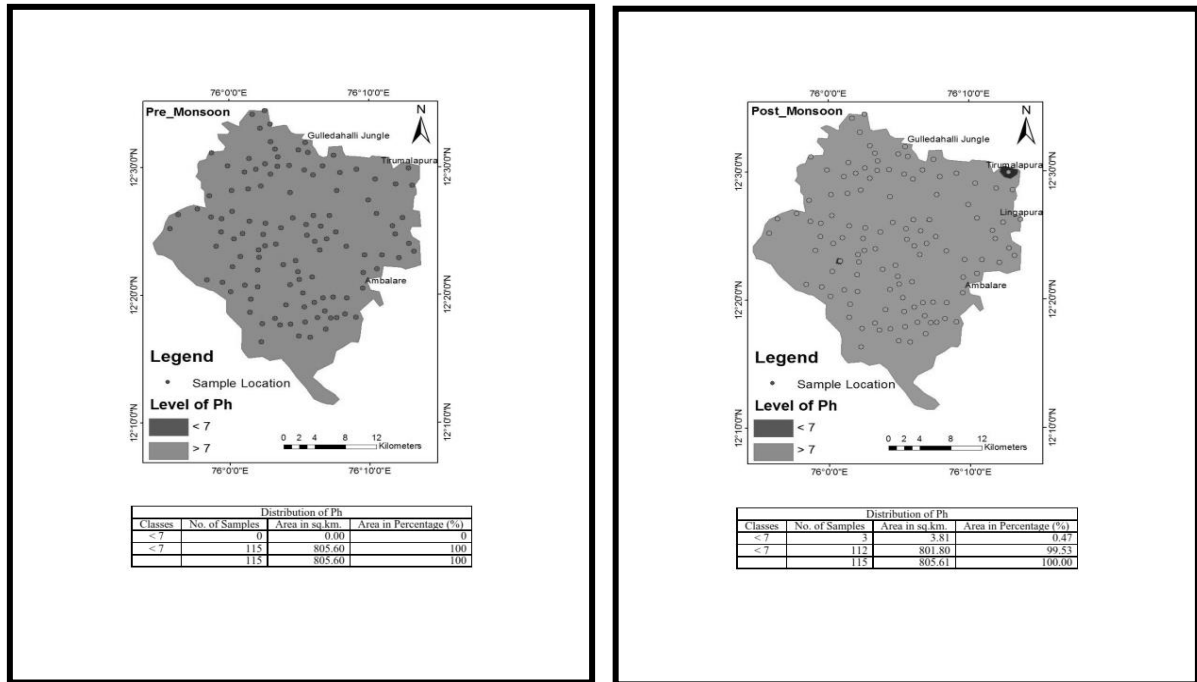


Figure 5: Hydrogen ion concentrations of the area

5.2. Total Dissolved Solids (TDS)

TDS was determined by multiplying the electrical conductivity value with factor of 0.64 (Todd, 1980). Water containing less than 500 mg/l of dissolved solids is generally considered satisfactory for domestic and many industrial purposes. Water with more than 2000mg/l of dissolved solids usually contains minerals that give a distinctive taste or make it unsuitable for any other purposes. U.S Geological survey has classified groundwater based on concentration of TDS as given below.

Description	Dissolved Ion Concentration (mg/l)
Non Saline	< 1,000
Slightly Saline	1,000 to 3,000
Moderately Saline	3,000 to 10,000
Very Saline	10,000 to 35,000
Brine	>35000

TDS percentage for both pre and post-monsoon season are given in the following table. Based on the above classification 10.80% to 20.80 % of the groundwater in the study area falling in the desirable for drinking and 70.80 to 77.50 % of the groundwater samples for permissible for drinking.

TDS (mg/l)	Class	Number of samples		In percentage	
		Pre-monsoon	Post-monsoon	Pre-monsoon	Post-monsoon
up to 500 mg/l	Desirable for drinking	25	13	20.80	10.80
500-1000 mg/l	Permissible for Drinking	80	88	70.80	77.50
Up to 3000 mg/l	Useful for drinking and irrigation	10	12	8.33	10.00
Above	Unfit for drinking and irrigation	-	02	-	1.66

5.3. Electrical Conductivity (EC)

Electrical conductivity is an index of the degree of mineralization which varies with temperature. Using the classification of Wilcox (1955), the Periyapatna taluk could be divided into 3 horizons with stray pockets of high values of conductivity. A major part of the area containing water with an Ec less than 700 micro mhos /cm at 25°C covers the percentage of 1.7% observed in northern portion of the study area. The second horizon with >-1000 micro mhos/cm at 25°C are observed in middle portion of the area with 33.70%. Ec is predominant in the middle and upper reaches of the area.

Table 2: EC spatial changes pre to post monsoon

Classes	No. of Samples	Area in Sq.km	Area in%
<700 to <700	03	14.1	1.7
>1000 to >1000	33	274.7	33.70
700-1000 to >1000	13	135.2	16.65
700-1000 to 700 -1000	50	321.5	39.44
>700 to 700-100 0	09	68.01	8.34
<700-1000 to >1000	02	0.80	0.09
700 -1000 to <700	02	0.25	0.03
>1000 to 700-1000	03	0.44	0.05
	115	815	100

5.4 Sodium Adsorption Ratio (SAR)

The sodium or alkali hazard in groundwater for irrigation is determined by the absolute and relative concentration of cations and is expressed in terms of Sodium Adsorption Ratio (SAR). There is a significant relationship between SAR values of irrigation water and the extent to which sodium is absorbed by the soil. If groundwater used for irrigation is high in sodium and low in calcium, the cation-exchange complex may become saturated with sodium. Table 3 depicts the Periyapatna taluk based on SAR values 95% the groundwater of the area belong to excellent irrigational water quality and rest of the 5% fall under the locations of 18, 27 and 21. Since the urban area is growing very fast the utility of the water for irrigation is out of question.

Table 3: SAR Spatial changes of Periyapatna Taluk

SAR	No. of Samples	%
> 4	112	95.00
< 4	03	5.00
Total	115	100.00

5.5. Doneen’s Permeability Index (PI)

Permeability of the soil influenced by sodium content of the irrigation water. The permeability index (PI) is obtained by considering the ions (epm), which influence permeability (Domenico and Schwartz, 1990). Permeability index is defined as

$$PI = \frac{Na^+ + HCO_3^- + 100}{Ca^{++} + Mg^{++} + Na}$$

The concentrations of cations and anions are in epm.

The groundwater samples of the study area fall in class-I and class-II of Doneen chart (Figure 6). 104 Samples fall in class I and 11 samples are plotted in class II. Therefore, in the study area Class I of 90.40% and Class II of 9.60%.

It is inferred on the basis of the study area is of good quality for irrigation purposes. The increased percentage of groundwater samples under class- I was due to dilution and subseque lower values of permeability index.

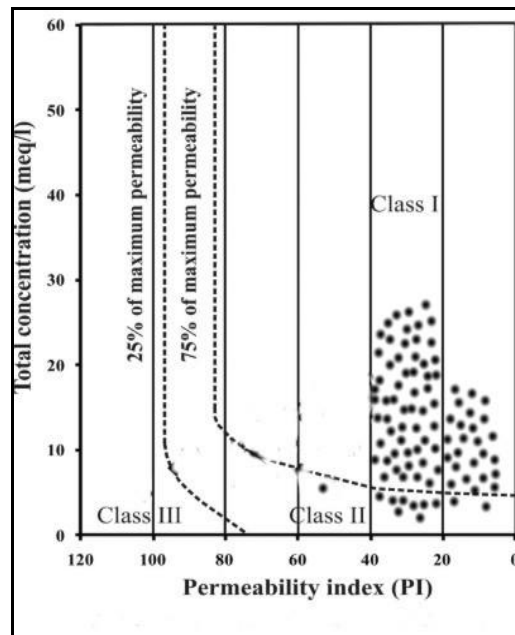


Figure 6: Classification of Irrigation Waters for Soils of Medium Permeability (Doneen, 1948)

Table 4: Permeability Index Classification of Groundwater’s Periyapatna Taluk

Type	No. of Water Samples	Percentage %
Class I	104	90.40
Class II	11	9.60
Class III	NIL	Nil
Total	115	100=00

5.6. Wilcox Diagram

Percentage of sodium content in natural water is an imperative parameter to assess its suitability for agricultural use. A maximum of percentage sodium in groundwater is plotted for agricultural purposes (Wilcox, 1948, 1967; USSL, 1954). Sodium percentage can be defined in terms of epm of the common cations (Wilcox, 1948).

$$\text{Na}\% = \frac{(\text{Na}^+ + \text{K}^+)}{\text{Ca}^{++} + \text{Mg}^{++} + \text{Na}^+ + \text{K}^+} \times 100$$

The concentrations of cations and anions are in epm.

The sodium percentage (Na %) in the study area ranges from % to %. The highest percentage of sodium is found in the bore well water sample. The minimum value of Na% is located in the bore well water samples. Plotting the data of the area on Wilcox diagram (Wilcox, 1948) relating to electrical conductivity and sodium percentage (Figure 7) show different water classes for irrigation for both season on the basis of Na% value and are presented in the Table 5 and 6. Excellent can be used for the purpose of irrigation.

Table 5: Water classes for irrigation on the basis of Na% for Pre monsoon Season

Water class for irrigation	%Na	No of sample
Excellent to Good	Up to 20	53
Good to Permissible	20-40	42
Permissible to Doubtful	40-60	14
Doubtful to Unsuitable	60-80	5
Unsuitable	>80	1

Table 6: Water classes for irrigation on the basis of Na% for Post monsoon Season

Water class for irrigation	%Na	No of sample
Excellent to Good	Up to 20	55
Good to Permissible	20-40	40
Permissible to Doubtful	40-60	13
Doubtful to Unsuitable	60-80	6
Unsuitable	>80	1

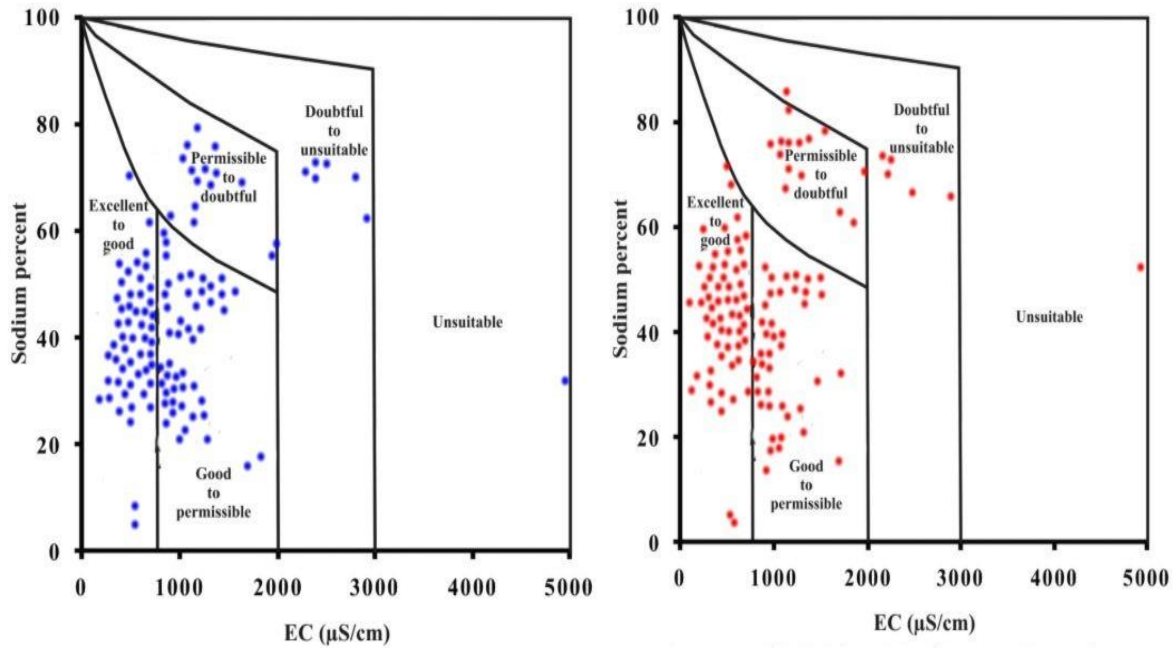


Figure 7: Wilcox diagram showing Na% for both pre monsoon & post monsoon season

5.7. USSL Diagram

In the U.S. Salinity Laboratory diagram based on sodium Absorption Ratio (SAR) vis a vis specific conductance values (USSL, 1954), the two most significant parameters of sodium and salinity hazards determine the suitability of water for agricultural purposes (Table 7, 8 and Figure 8).

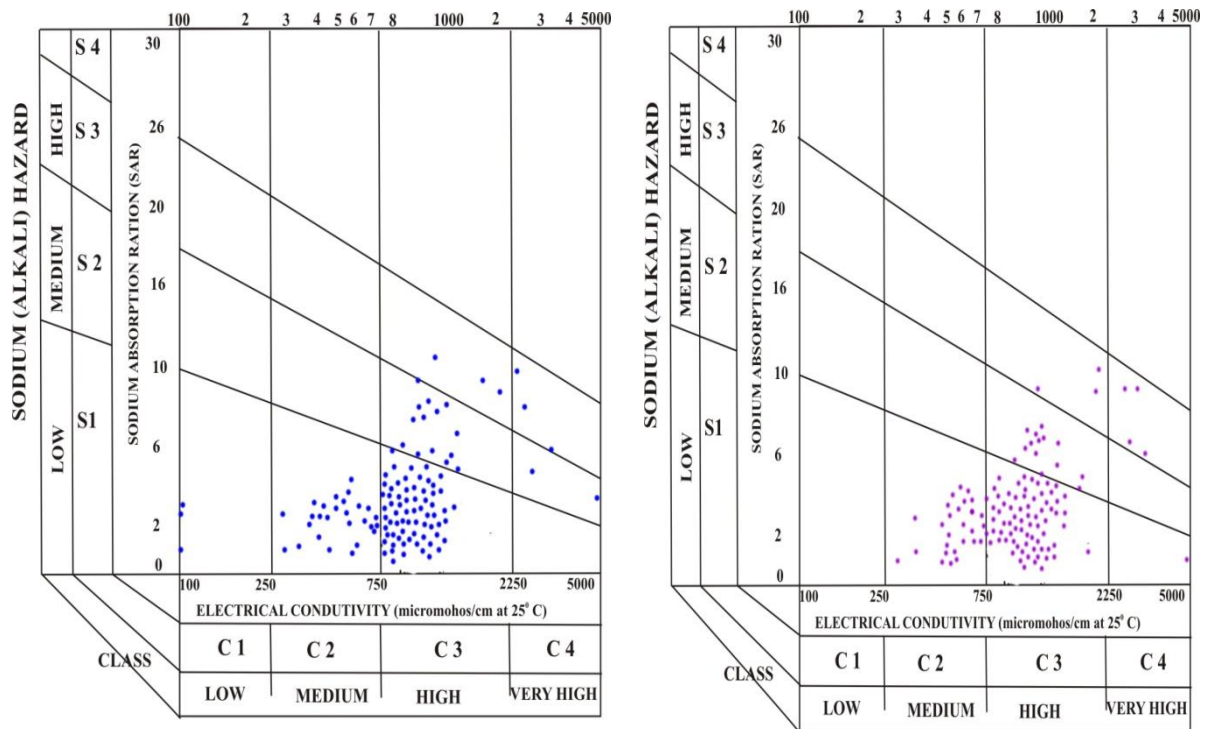


Figure 8: USSL salinity diagram of pre monsoon & post monsoon season

Table 7: Groundwater classification based on USSSL, diagram for Pre monsoon season

Category	No. of samples	Water quality
C ₁ S ₁	3	Low salinity and lower alkali water
C ₂ S ₁	25	Medium salinity and lower sodium water
C ₃ S ₁	70	Moderate to high salinity and less alkaline water
C ₂ S ₂	Nil	Moderately alkaline and medium salinity
C ₃ S ₂	14	Moderate to high salinity and moderate alkaline
C ₃ S ₃	3	Highly alkaline and have moderate to high saline
C ₄ S ₁	Nil	Very high alkaline and saline
C ₄ S ₂	2	
C ₄ S ₃	3	

Table 8: Groundwater classification based on USSSL, diagram for Post monsoon season

Category	No. of samples	Water quality
C ₁ S ₁	0	Low salinity and lower alkali water
C ₂ S ₁	27	Medium salinity and lower sodium water
C ₃ S ₁	71	Moderate to high salinity and less alkaline water
C ₂ S ₂	Nil	Moderately alkaline and medium salinity
C ₃ S ₂	14	Moderate to high salinity and moderate alkaline
C ₃ S ₃	3	Highly alkaline and have moderate to high saline
C ₄ S ₁	1	Very high alkaline and saline
C ₄ S ₂	Nil	
C ₄ S ₃	4	

5.8 Corrosivity Ratio (C.R.)

Ryzner (1944) proposed a ratio to evaluate corrosive tendency of groundwater towards metallic pipes. Badrinath et al., (1984) have used this index to evaluate corrosive tendency of Sabarmathi river waters. Earlier Balasubramanian (1986), Venugopal (1988), Siddaraju (1966), Chandrashekar (1988) Indira (1988), Nagaraju (1996), Mahadevaswamy (2004), H.S. Mahadeshwara (2004), and M.P. Dharmesh (2004) used this ratio for the groundwater chemistry to evaluate its effect on metallic pipes during the transport of water from the source to the consumers.

$$\text{Corrosivity Ratio} = \frac{0.028 \text{ Cl} + 0.021 \text{ SO}_4}{0.02 (\text{HCO}_3 + \text{CO}_3)}$$

Where all ionic values are in ppm concentrations

The distribution of the area having corrosivity ratio less than one value is indicates that corrosivity and more than one values is non corrosive. In the pre monsoon, the 1.19 in Halasuru to 0.1 Thammadahalli, Hitnahebbigilu village, with an average of 0.41 ppm this season corrosivity ration domestic and some area are non-corrosive. In the post monsoon season, 1.44 Haralapura to 0.1 in Shanbaganahalli with an average 0.49, here is corrosive ratio all most all same of the pre monsoon so there is no corrosive point both season used the metallic and polyvinyl chloride pipes. Corrosivity greater than one has a tendency to corrode the metallic pipes. In such areas where corrosivity ratio is greater than one, non-corrosive PVC pipes may have to be safely utilized.

Table 9: Statistics data of Corrosivity ratio of study area

Corrosivity Value	Pre monsoon		Post monsoon	
	Samples no	%	Samples no	%
>1	8,10,42,66,68,70,102 =07	6.08	8,10,18,55,66,68,70,102,111, 115=10	8.70
<1	1,2,3,4,5,6,7,9,10,11,12,13,14,15 ,16,17,18,19,20,21,22,23,24,25,2 6,27,28,29,30,31,32,33,34,35,36, 37,38,39,40,41,43,44,45,4,47,48, 49,50,51,52,53,54,55,56,57,58,5 9,60,61,62,63,64,65,67,69,71,72, 73,,74,75,76,77,78,79,80,81,82,8 3,84,85,87,88,89,90,91,92,93,94, 95,96,97,98,99,100,101,103,104, 105,106,107,108,109,110,111,11 2,113,114,115=108	93.92	1,2,3,4,5,6,7,9,10,11,12,13, 14,15,16,17,,19,20,21,22,23,24,25,2 6,27,28,29,30,31,32,33,34,35,36,37, 38,39,40,41,42,43,44,45,4,47,48,49, 50,51,52,53,54,56,57,58,59,60,61,6 2,63,64,65,67,69,71,72,73,74,75,76, 77,78,79,80,81,82,83,84,85,87,88,8 9,90,91,92,93,94,95,96,97,98,99,10 0,101,103,104,105,106,107,108,109 ,110,112,113,114,=105	91.30

Above Table 9, it indicates that the more one value of corrosivity samples are 7 and 6.08% during the pre-monsoon, in the same way post monsoon samples are 10 and 8.70%. It is very less values or places of the study area. The not less than one values are the majority of the area it found that condensed and interpretation of the Table 9 are in the pre monsoon samples are 108 and 93.92% & 105 samples, 91.30% of the areas are post monsoon. This concludes that areas are 92% of corrosive.

5.9. Groundwater Hardness

The normal range is 300 (desirable) to 600 ppm (permissible) in the values of the total hardness not determine the available in the laboratory. In the (Table 10) Utilizing Handa’s classification the groundwater of the study area have been classified into permanent (A₁, A₂, A₃) and temporary hard water (B₁, B₂, B₃) areas respectively. It is found that water belonging to temporary hardness occupies 81.7% during the pre-monsoon and 83.53% in post monsoon of the study area and there is a gradual change of hardness from temporary to permanent hardness depending upon the time of residency of groundwater in the subsurface. But there is no/little changes the temporary hardness in the case of both seasons. It is of interest to note that 18.3% of the groundwater of the area belonging to permanent hard water (Pre monsoon) and 16.47% of permanent hard water (Post monsoon) indicating that the water can be used with happiness in the domestic or industrial sectors and 94 samples of occupies the temporary water can be used with domestic or industrial sector in the both seasons.

Table 10: Handa’s Classification of Periyapatna Taluk

Classes	Pre monsoon			Post mon soon		
	Samples No.	No. of Sample s	%	Samples No.	No. Samp les	%
B1C3S1	1,4,5,7,11,14,15,19,20,22 ,23,25,26,27,28,33,34,36, 37,41,43,50,56,58,59,61, 62,63,67,71,74,75,79,80, 82,83,84,85,86,87,88,96, 97,98,101,103,108,110,1 14	48	41.73			

B2C3S1	2,13,32,44,45,46,47,48,53,73,78,104,105,106,107	15	13.04	1,2,4,5,14,16,18,43,44,45,46,47,61,62,65,73,75,78,103,104,105,106,107	23	20.00
B1C2S1	3,17,38,77	04	3.5	3,17,26,30,38,63,77,86,90,98	10	8.70
B1C5S3	57	01	0.90			
B1C3S1	64,65,92,93,94,113	06	5.20	7,8,12,15,19,20,22,23,24,25,27,28,32,34,36,37,41,48,50,53,54,55,56,58,59,64,67,71,74,79,80,82,83,84,85,87,88,92,94,96,97,108,110,113,11	44	38.30
A2C3S1	6,55,66,102,115	05	4.35	6,42,57,66,102	05	4.30
A3C3S3	51	01	0.90			
B3C5S3	8,68	02	1.70	68	01	0.90
B3C5S2				09	01	0.90
B2C5S3	52,112	03	2.60	52,112	02	1.70
B2C3S2	9,12,40,60,69,72,21,76,81,109	10	8.70	10,11,13,16,40,49,60,69,70,72,76,109	12	10.43
B3C3S2	10,16,70	03	2.60			
A2C3S2	18	01	0.90			
A1C3S1	24,29,30,31,35,39,54,89,90,91,95,99	12	10.43	29,31,33,35,39,89,91,93,95,99	10	8.70
A2C5S3	42	01	0.90			
B2C3S3	49,100	02	1.73	21,81,100	03	2.60
A3C3S2	111	01	0.90	51,111	04	3.50
TOTAL		115	100.00		115	100.00

5.10. Groundwater Salinity – Sodium Hazard

Based on the degree of salinity - sodium hazard the groundwater of the area gets divided into 8 horizons (C2S1, C3S1, C1S1, C4S2, C4S1, C3S2, C3S3, and C4S3), with a maximum predomination of C3S1 class (68) in pre monsoon and 71 samples of C3S1 in post monsoon and among these all the water upto C₃ type could be suitably used for crops, similarly S₂ category water is suitable for soils with good drainage.

Table 11: Statistics data of salinity sodium hazard of study area

Quality Parameter	Pre monsoon		Post monsoon	
	No. of Samples	%	No. of Samples	%
C2S1	1,3,4,5,14,17,30,38,44,51,62,63,64,65,66,75,78,80,83,84,91,99,105,109,115=25	21.70	1,3,4,5,14,17,19,24,30,39,44,48,50,61,63,64,65,74,77,79,82,84,90,98,104,107,108=27	23.50
C3S1	2,6,7,11,12,13,18,19,21,22,23,24,25,26,27,28,29,31,32,33,34,35,36,37,39,41,42,43,45,46,47,48,49,54,55,56,57,58,59,60,67,68,72,74,76,79,81,86,87,88,89,90,92,93,94,95,96,97,98,100,102,103,104,106,107,108,111,114,=68	59.10	2,6,7,11,13,15,18,20,22,23,25,26,27,28,29,31,32,33,34,35,36,37,41,43,45,46,47,53,54,55,56,57,58,59,62,66,67,71,73,75,78,80,83,86,87,88,89,91,92,93,94,95,96,97,99,101,102,103,105,106,110,113,114,115=71	61.70
C1S1	15,20,85=03	2.60		
C4S2	112=01	0.90	9,51,111=03	2.60
C4S1	8,10,52=03	2.60	08=01	0.90

C3S2	9,16,50,61,70,71,73,77,82 110=10	8.70	10,12,16,21,40,42,49,60, 69,70,72,76,81 =13	11.30
C3S3	40,53,101,113=04	3.50		
C4S3	69=01	0.90		
Total	115	100	115	100.00

6. Cation Geochemistry

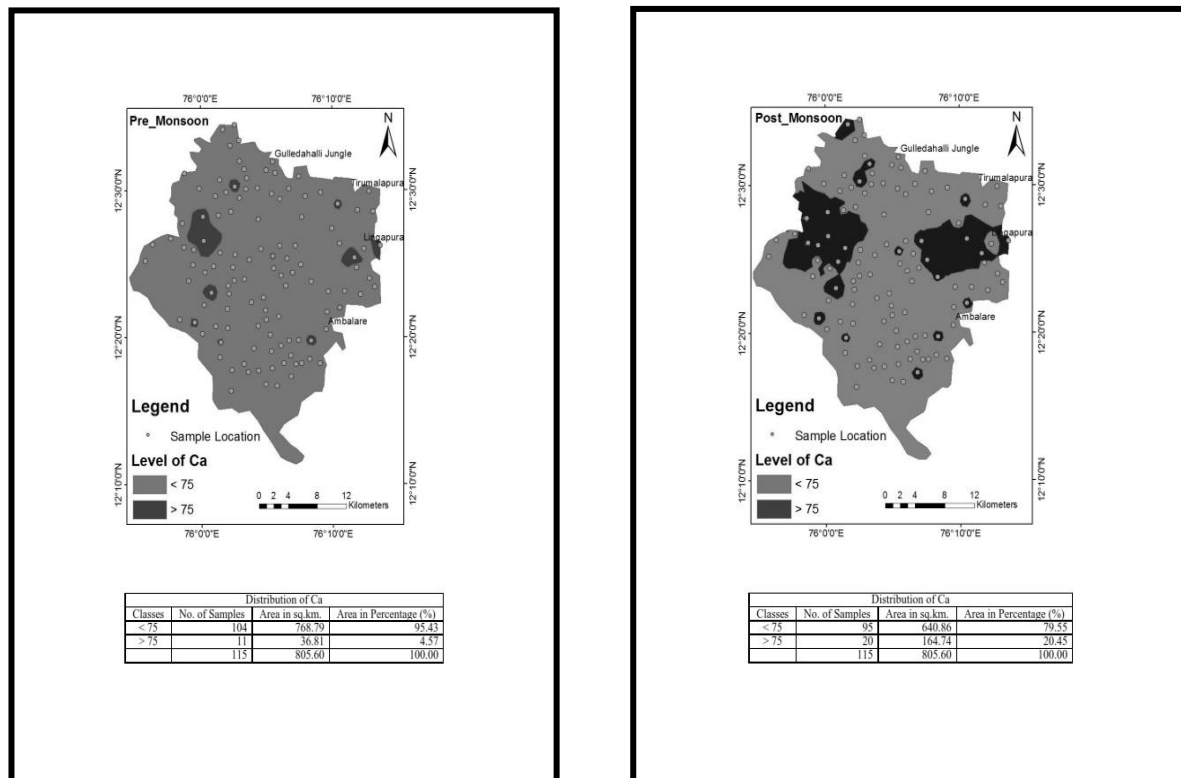
The main cations found in the groundwater of study area are Ca, Mg, Na, and K.

6.1. Calcium

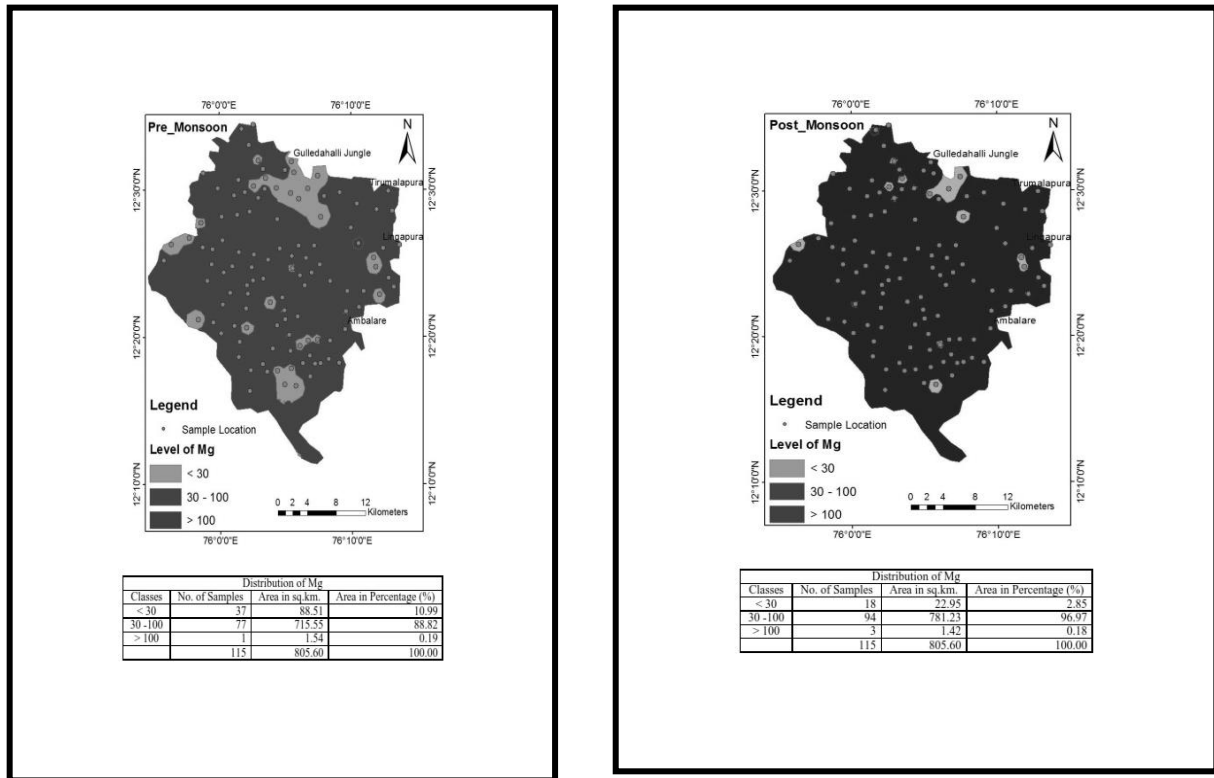
The calcium content in the groundwater of study area range from 8 to 139 ppm for pre monsoon season and range of 9 to 951ppm for post monsoon season and from 75 to 200 ppm for bore wells respectively (Figure 9). Most of the samples for both seasons are within desirable limit as per standards prescribed by WHO, (1971). 2 samples are having the Ca concentration beyond the permissible limits. Water with higher concentration of calcium may cause kidney stones and liver ailments

6.2. Magnesium

Magnesium usually occurs in less concentration in groundwater than calcium it's commonly associated with calcium and causes hardness of water. Mg content in the study area varies from 14 to 125 ppm with an average of 40.73 mg/l and 15 to 362 ppm with an average of 49.76 mg/l during pre-monsoon and post-monsoon respectively (Figure 10). Most of the samples are within limits, except 5 samples. Magnesium exceeding the permissible limit in potable water may cause laxative effect.



Figures 9: Spatial distribution of Calcium of Periyapatna Taluk



Figures 10: Spatial distribution of Magnesium of Periyapatna Taluk

6.3. Sodium and Potassium

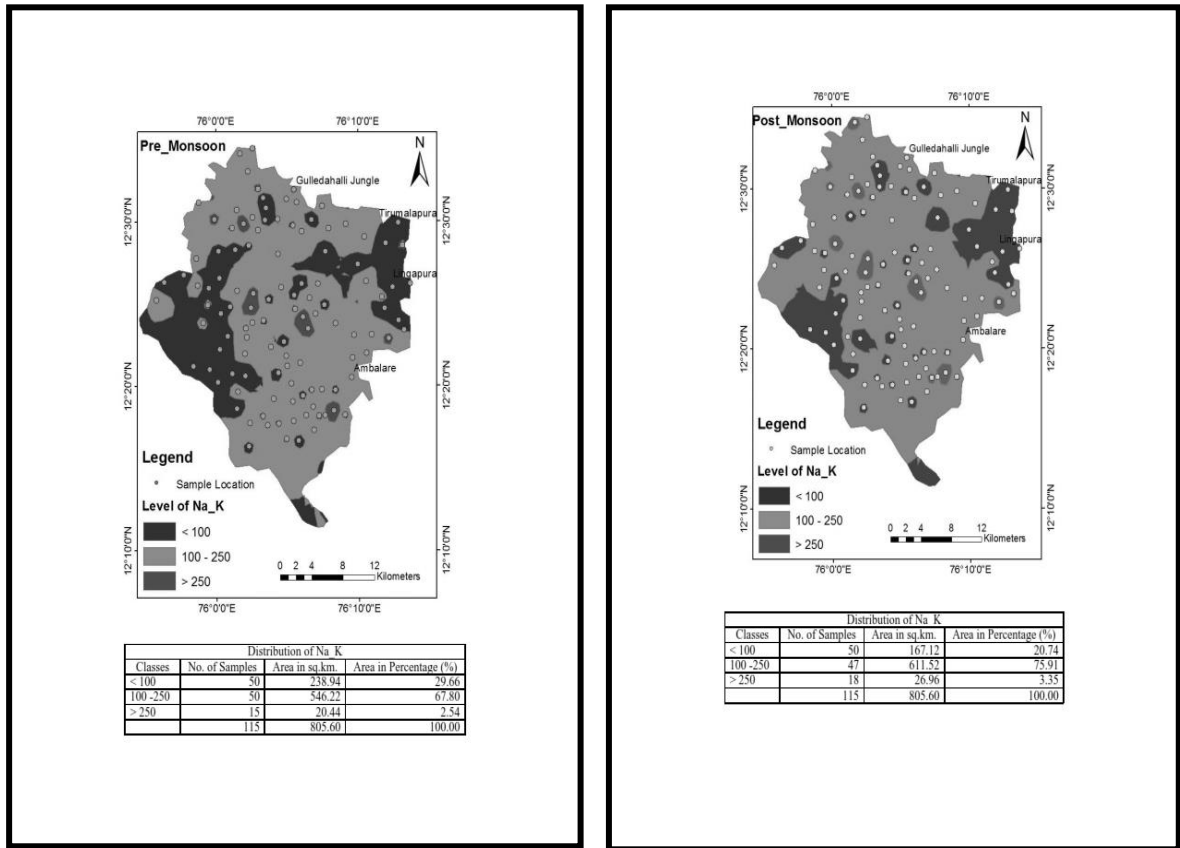
For determination of sodium, the samples should be stored in polyethylene bottles to check the leaching of sodium from the glass. High sodium concentration in irrigation water results in adsorption of Na⁺ ion by the clay particle resulting in reduced permeability of soil such soil become hard when dry (Collins and Jenkins, 1996). In the present study, the Na and K concentration varies from 9.0 to 545 ppm with an average of 135.79 and 13 to 536 ppm with an average of 144.26 mg/l in pre-monsoon and post-monsoon respectively (Figure 11)

7. Anion Geochemistry

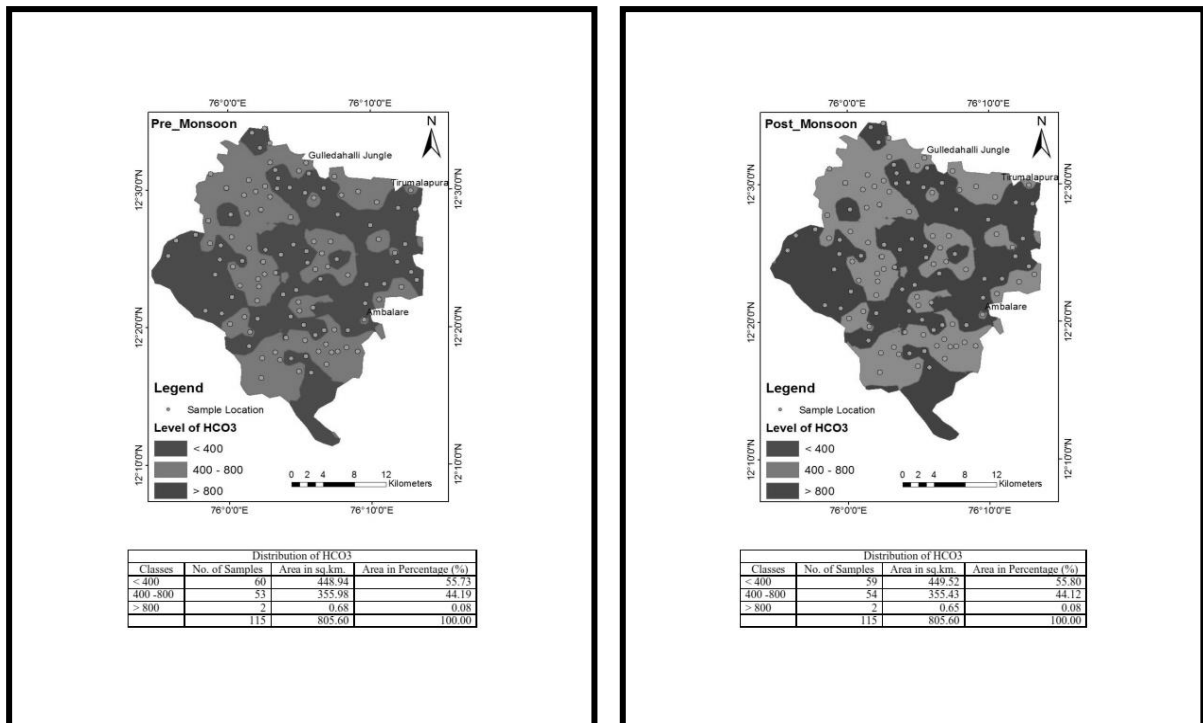
The negatively charged ions or anions usually determined in routine water analysis are carbonates, bicarbonates, sulphates and chlorides.

7.1. Bicarbonates and Carbonates

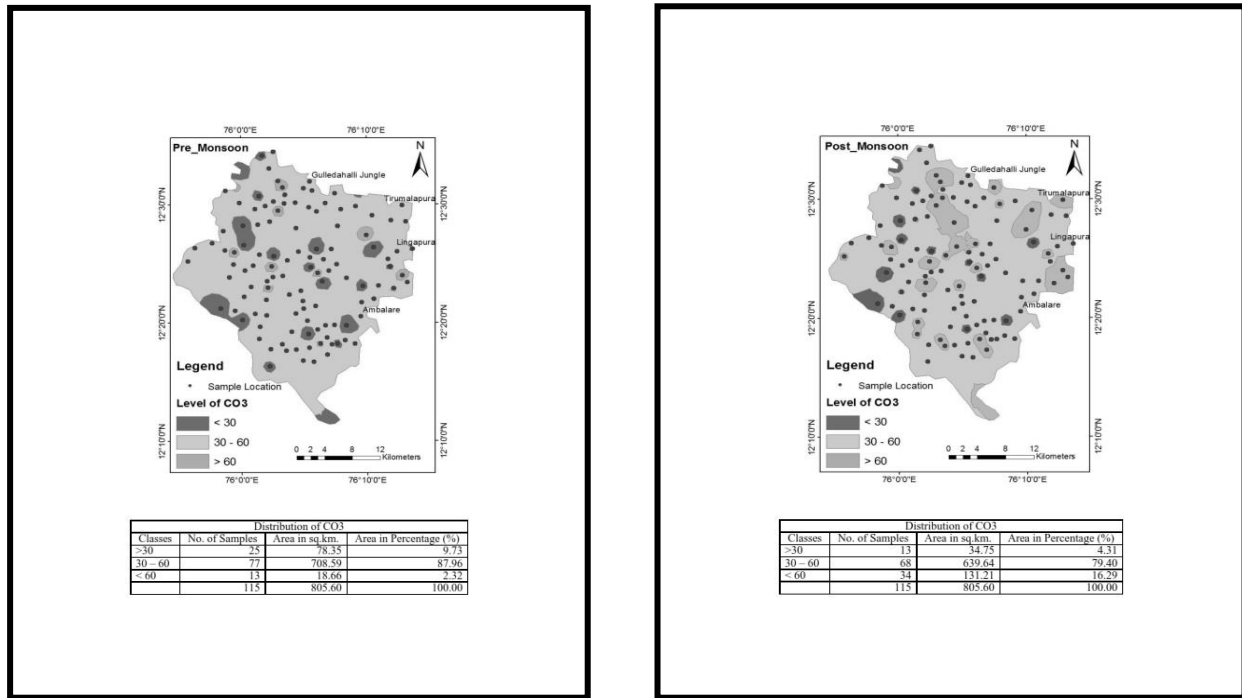
The Total Alkalinity of water is a measure of ability of water to neutralize a strong acid. Commonly, alkalinity is reported as bicarbonates (HCO₃⁻) or calcium carbonate (CaCO₃), (Ritcher B. Chrsitan and Charles W., Kreitler, 1993). It is a measure determined by how much strong acid will lower pH of a water sample to a specific level; most of the carbonate and bicarbonates ions in groundwater are derived from the carbon dioxide in the atmosphere, carbon dioxide in soil and solution of carbonate rocks. The relative amount of these two anions depends on PH of water and other factors. Usually, bicarbonates increase as pH decreases. In the study area carbonates are found to be nil in all samples since the pH value in none of the seasons were above 8.5, and the concentration of bicarbonates varied from 152 to 902 ppm with an average of 403.95 and 342 to 905 ppm with an average of 559.85 for pre-monsoon and post-monsoon seasons respectively (Figure 12 and 13)



Figures 11: Spatial distribution of Sodium and Potassium of Periyapatna Taluk



Figures 12: Spatial distribution of Bicarbonates of Periyapatna Taluk



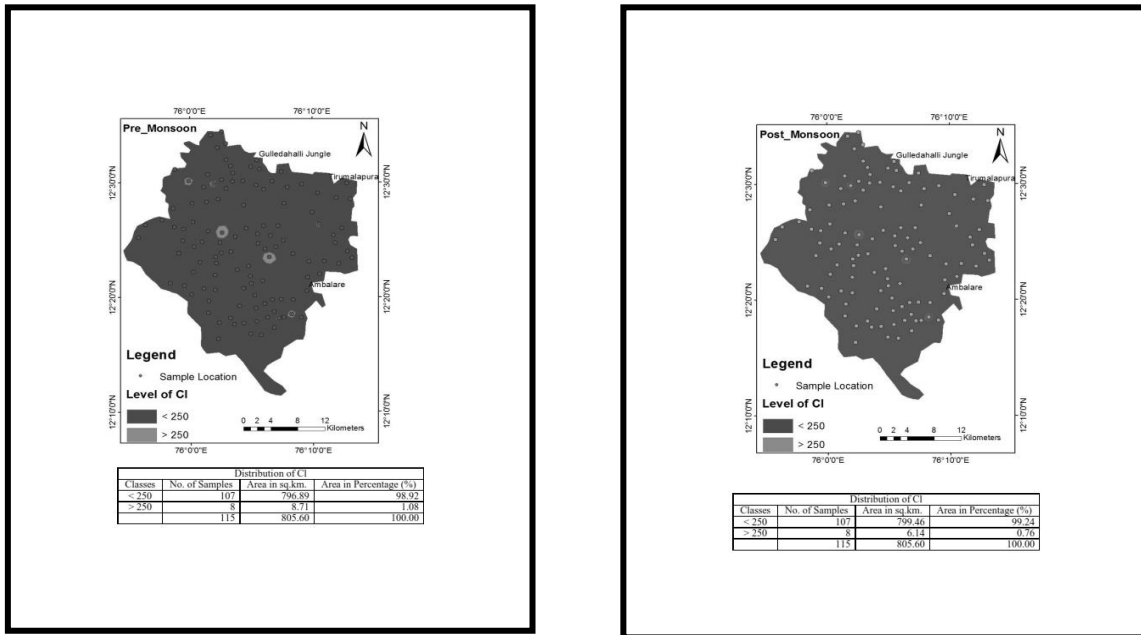
Figures 13: Spatial distribution of Carbonates of Periyapatna Taluk

7.2. Chloride

Chloride is a minor constituent of the earth. Chloride salts are highly soluble and are rarely removed by precipitation except by freezing and evaporation of water. The dominant chloride sources in groundwater include rain water, anthropogenic sources, solution of halites and evaporate. Waters, high in chloride, are normally also high in sodium. In general, the chloride content of water is less than 10 mg/l and it can be as high as 30,000 mg/l in sea water (Davis, J.C., 1973). The concentrations of chloride ion have direct proportionality with salinity. Chloride concentration in groundwater is high where salinity is high. Chlorine can be contributed by dissolution of halite that is present in aquifer rocks either as rock salt or as vein crossing other rocks (Edmunds, W.M and Smedley, P.L., 1996). The Cl concentration varies from 14 to 437 ppm with an average of 81.74 mg/l and 19 to 443 ppm with an average of 86.68 mg/l during pre-monsoon and post- monsoon seasons respectively (Figure 14). If water containing less than 150 ppm of chloride is satisfactory for most of the purposes. A chloride content of more than 250 ppm is generally objectionable for municipal water supply. And more than 350 ppm is objectionable for irrigation and industrial uses. Most of the samples are within the permissible limit and samples are suitable for drinking purpose as per standards by WHO.

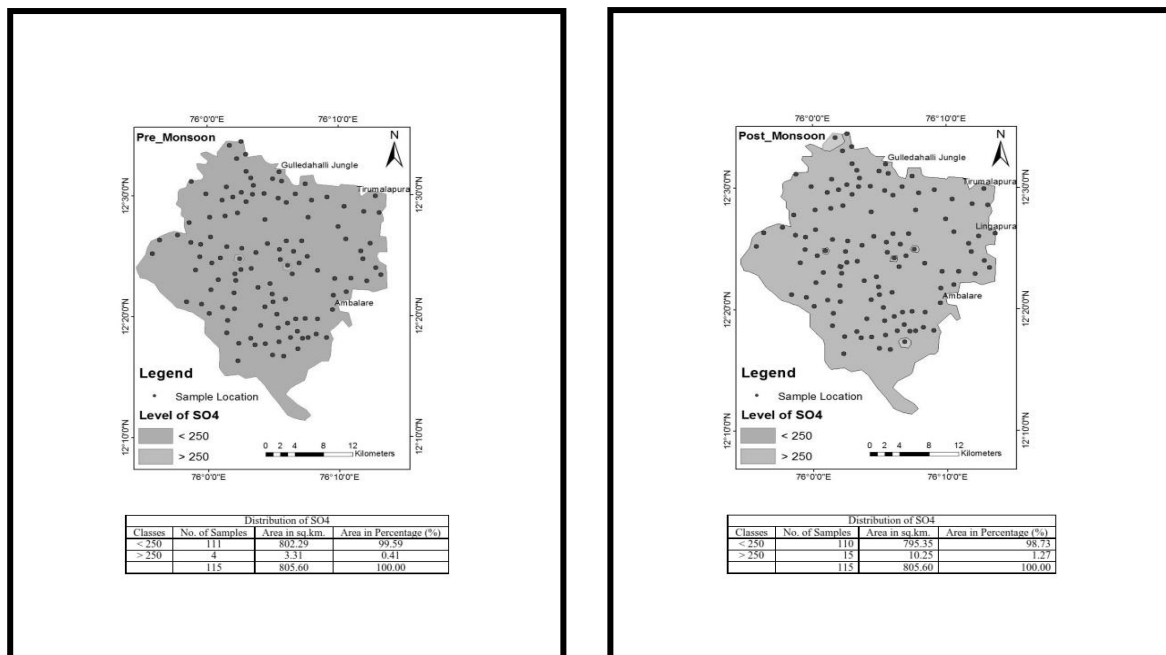
7.3 Sulphate

Sulphate is dissolved from most sedimentary rocks. Large quantities may be derived from beds of gypsum, sodium sulphate deposits and some types of shale (Brown et al., 1970). Soils absorb sulphate ions to some extent and it can be lost by reduction due to bacteria. Groundwater traversing through the zone of oxidation of sulphide ore bodies, pyrite-bearing shales, lignites, and coal and gypsiferous beds are characterized by anomalously high concentrations of sulphates (Hem, 1989). The concentration of sulphate ions in water can be affected by sulphate-reducing bacteria, the products of which are hydrogen sulphide and carbon dioxide.



Figures 14: Spatial distribution of chloride in Periyapatna taluk

Hence, a decline in sulphate ion frequently is associated with an increase in bicarbonate ions. Higher concentration of sulphate could cause a cathartic action on human beings and also cause respiratory problems (Maiti, 1982; N. Subha Rao et al., 2002). The SO₄ content of the water samples of the study area varied between 0.0 to 340 ppm with an average of 18.0 mg/l and 10 to 430 ppm and an average of 73.79 mg/l for pre-monsoon and post-monsoon seasons respectively (Figure 15). The higher concentration of sulphate in the water samples may be attributed to its lithogenic sources and also could be attributed to the excessive use of fertilizers. Five samples contain more than permissible limit which is not suitable for drinking purposes. Remaining samples are within the permissible limit proposed by WHO, (1971).



Figures 15: Spatial distribution of sulphate in Periyapatna taluk

8. Conclusions

The result of geochemical analysis of water samples from bore wells of the study area indicate that water is lightly alkaline in nature due to pH values of more than 7 and are suitable for drinking purpose according to the WHO, (1971) standards. Generally, on the basis of TDS classification 20.8% of total samples belong to drinking and fresh water and 92% useful for drinking purposes. The groundwater samples when compared to drinking water standards indicate that the chemistry of the water samples associated with study area are well within the permissible limits except a few samples.

References

- APHA, 1995: *Standard Methods for the Estimation of Water and Wastewater*. American Public Health Association, 20th edn. Washington DC.
- Balasubramanian, A., Firugnana Sambadam, R., Chellasamy, R., and Ramakrishnan, V., 1991: Electrical Resistivity Studies in the Coastal Aquifers of Tuticorin, Tamilnadu, proc. Vol. Nat Sem. On water, Govt. of Kerala. 318-323.
- BIS, 1991: Bureau of Indian Standards IS: 10500, Manak Bhavan, New Delhi, India.
- Brown, E., Skougstad, M.W., and Fishman, M.J., 1970: *Methods for Collection and Analysis of Water Samples for Dissolved Minerals and Gases*. Techniques of Water Resources Investigation of the U.S. Geological Survey, Book 5, Chap. Al. 160.
- Collins, R., and Jenkins, A. The Impact of Agriculture and Land Use on Stream Chemistry in the Middle Hills of the Himalayas. *Nepal Journal of Hydrology*. 1996. 1 (85) 71-86.
- Davis, J.C., 1973: *Statistics and Data Analysis in Geology*. John Wiley & Sons, New York. 646.
- Edmunds, W.M., and Smedley, P.L., 1996: Groundwater Geochemistry and Health: An Overview. In: Appleton, Funge and McCall (eds.) *Environmental Geochemistry and Health*, Geological Society Special Publication No. 113. 91-105.
- Hem, J.D., 1989: *Study and Interpretation of the Chemical Characteristics of Natural Water*. 3rd edn. U.S Geological Survey Water-Supply Paper. 2254-263.
- Maiti, T.C. The Dangerous Acid Rain. *Sci Report*. 1982. 9 (6) 360-363.
- Richter, B. Christan and Charles W . Kreitler, 1993: *Geochemical Techniques for identifying Sources of Groundwater Stalination*.
- Subba Rao, N. Geochemistry of Groundwater in Parts of Guntur District, Andhra Pradesh, India. *Environ Geol*. 2002. 41; 552-562.
- Todd, D.K., 1980: *Ground Water Hydrogeology*. Joh and Sons, Hoboken.
- WHO, 1971: *International Standards for Drinking Water*.

Impacts of the Reservoir on the Navigation Conditions of the Downstream Channel: Taking the Three Gorges Reservoir in the Middle Reaches of the Yangtze River as an Example

Xingying YOU^{1,2}, Jinwu TANG³, Jing Xu², and Meng Chen²

¹State Key Laboratory of Water Resource and Hydropower Engineering Science, Wuhan University, China

²Hubei Institute of Survey & Design for Water Resources & Water Power Engineering, Wuhan, China

³Changjiang Institute of Survey Planning Design and Research, Wuhan, China

Publication Date: 15 October 2016

Article Link: <http://scientific.cloud-journals.com/index.php/IJAESE/article/view/Sci-505>



Copyright © 2016 Xingying YOU, Jinwu TANG, Jing Xu, and Meng Chen. This is an open access article distributed under the **Creative Commons Attribution License**, which permits unrestricted use, distribution, and reproduction in any medium, provided the original work is properly cited.

Abstract The flow and sediment condition in the middle and lower reaches of Yangtze River (MLYR) was changed a lot after the impoundment of Three Gorges Reservoir (TGR), and further, the evolution process of the sandbars and shoals were affected, both of which have obvious influence on the navigation in the MLYR. Based on the field data, the analysis shows that the changes of flow and sediment favored the waterway condition, which includes the elevation of the lowest water level, the extension of the scour time of shoals, the increase of the erosion speed of shoals caused by the reductive sediment. After the operation of TGR, the frequency of the bank collapse and the sandbar cutting is increasing, and the shoal tends to shrink. However, not all the deformation of sandbars and shoals will obstruct the waterway, only the Critical Width of Returning to Channel (CWRC) is more than the critical river width, the channel will not be unimpeded. The CWRC is about 900–1900m, varying with the navigation base surface and the channel dimension.

Keywords *Navigation Condition; Three Gorges Reservoir; the Middle and Lower reaches of Yangtze River; Channel evolution*

1. Introduction

The main stem of the Yangtze River is a transportation artery communicating East part – West part of China, known as the golden waterway (Gao et al., 2013; Chen et al., 2010; Zhang et al., 2006; Xu et al., 2011). In 2011, striving to build a unimpeded, efficient, safe, green system of modern inland navigation was put forward by the State Council, marking the accelerating development of the inland waterborne and the Yangtze River development has risen to the national strategy. The impoundment of TGR changes the downstream flow and sediment condition and has an influence on the navigation condition of MLYR (Dai et al., 2013; Xia et al., 2014).

The existing studies mainly have three viewpoints about this: Firstly, the navigation condition changes better because of the riverbed's erosion and downcut, the increment of flow in dry seasons and the

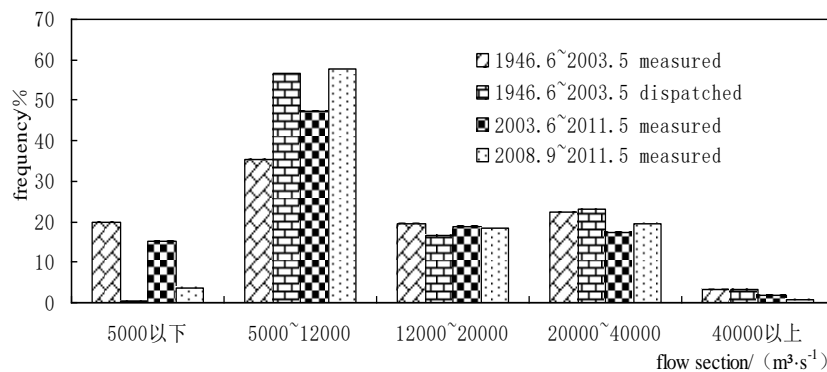
reinforcement of shoal scouring caused by reductive sediment after the flood (XIONG et al., 2000). The second view is that the riverbed downcuts meanwhile the bank collapses and the channel broadenings, making the averagely scouring depth of riverbed is not more than the decline amplitude of water level when the flood recedes quickly, and then the navigation depth diminishes and the migration amplitude of the channel increases, all of which cause the navigation condition deteriorates (LI et al., 2004; CAI et al., 2006). The last point is that TGR has both advantages and disadvantages on the navigation condition. On the one hand, with the riverbed scouring and the discharge increasing in dry season, the channel deepens; on the other hand, with the central bar and point bar scouring, the bank collapses and broadens (LIU et al., 2005).

The field data shows that the channel condition in the MLYR turns better as a whole after the impoundment of TGR, though part of them deteriorates. The deformation of sandbars and shoals takes the form of the low sandbar downcut and the bank collapse, but not all of them will cause the navigation obstruction. Thus the evolution process in the MLYR before and after TGR actually still needs further analysis. Based the analysis of the changes of flow and sediment condition and the deformation of sandbars and shoals, combining with the field data before and after the operation of TGR, dissect their impact on the channel condition, so as to provide a reference for the waterway remediation and the upstream reservoir regulation.

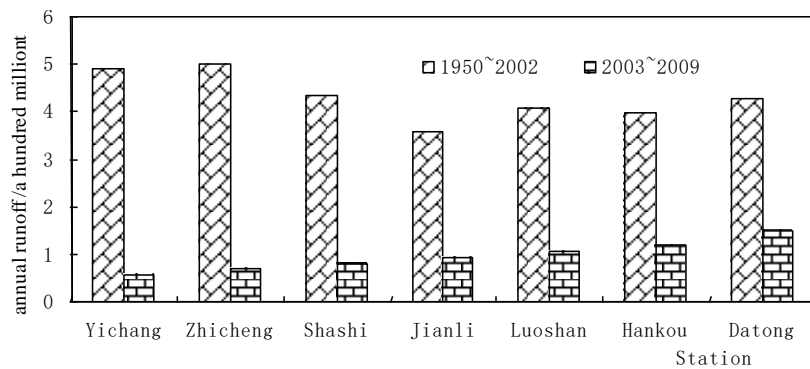
2. The Impact on Flow & Sediment Condition & Sandbar Deformation by Impoundment of TGR

2.1. The Impact on the Flow and Sediment Condition by the Impoundment of TGR

The TGR adopts the mode of ' storing clear and discharging muddy water '. After the impoundment, the flow occurrence frequency at different water levels has adjusted, for instance, the outflow slightly adjusts in the flood period, decreases in the storage period and increases in the dry period. Based on the field flow at Yichang station in the period from June, 1946 to May, 2003, according to the Flood dispatching plan of TGR, the flow occurrence frequency at different levels before and after dispatching is calculated as shown in Figure 1 (a). As can be seen from the graph, the occurrence frequency below 5000 m³/s falls from 20% to less than 1%, the frequency of 5000–12000 m³/s increases from 35% to 57%, the frequency above 12000m³/s decreases slightly. At the same time, the statistical data in the period from June, 2003 to May, 2011 shows that, the frequency below 5000 m³/s falls from 20% to 15%, the frequency of 5000–12000 m³/s increases from 35% to 47%, the frequency above 12000 m³/s decreases significantly.



(a) Change of water flow



(b) Change of sediment load

Figure 1: Changes of flow and sediment before and after the operation of TGR

The main reason for the greater difference between before and after TGR has two aspects: Firstly, the watershed has less rainfall after TGR and the flow reduces correspondingly, especially the annual runoff at Yichang station in 2006 is only 284.8 billions m^3 , which is accounted for 65% of the average runoff over many years. Secondly, in the period from June, 2003 to September 2008, TGR respectively operates with 135–139m and 144–156m mode, resulting in the lower impounded level and the restricted compensation ability for the flow in dry season. However, the statistical flow process from September 2008 to May, 2011 (operating with 155–175m mode) is basically consistent with the dispatched result. In a word, after TGR the frequency below 5000 m^3/s decreases by a large margin, the frequency of 5000–12000 m^3/s increases evidently, the frequency above 12000 m^3/s decreases slightly.

Under the influence of that the reservoir intercepts sediment, the sediment discharge in the MLYR declines sharply since 2003, descending from 490 millions tons / year before TGR to 57 million tons / year at Yichang station, descending from 430 million tons / year to 150 million tons / year at Datong station, which reduced respectively by 88% and 65%. According to the correlative analysis, in the 40–50 years after TGR, the riverbed of MLYR basically reaches the equilibrium of erosion and deposition. If a series of high dams built in upstream of main Yangtze River are considered, the riverbed of MLYR will be subjected to the erosion effected by the unsaturated water more than 300 years at least.

2.2. The Impact on the Sandbar Deformation by the Impoundment of TGR

With the significant change of the flow and sediment in the MLYR after impoundment of TGR, the sandbars and shoals also have an obvious trend of deformation. Mainly for the more frequent bank collapse and sandbar cutting, also for the low sandbar substantial shrink.

Bank collapse is a common phenomenon in the MLYR, 35.7% of the shoreline in the MLYR has a collapse before TGR. According to statistics, the bank collapse in Jingjiang river happens 15 times per year in 1998–2003, accordingly the collapse length is about 6.6 kilometers per year. Yet there are 26 times per year in 2003–2005, correspondingly the length is about 17.4 kilometers. Compared with 1998–2003, the bank collapse frequency in 2003–2005 is 1.7 times as much as the former, and the length is 2.6 times as much as the former.

Not only the river bank collapses, but also the left or right edge of the central bar collapses. The reason for this phenomenon is that, the river bank collapse, which mainly due to that the actual slope ratio is larger than the stability slope ratio caused by the nearshore water erosion (TANG et al., 2012). After impoundment of TGR, the sediment concentration declines sharply, the riverbed erosions

generally, the slope ratio increases, so the frequency and the length of bank collapse all increase.

The sandbar cutting is also a pervasive phenomenon in the MLYR. According to statistics, in the Shashi – Chenglingji river reaches, the sandbars in the Majiazui, Zhoutian, Ouchikou, Jianli waterway accumulated are cut 7 times, averagely once two years in 1990–2003. However in 2003–2011 the sandbars accumulated are cut 6 times, averagely twice three years. In addition, some sandbars, such as in the Chibakou waterway, Longkou waterway or Huguang waterway, have remained relatively intact more than 50 years (1950–2002), nevertheless they are all cut after impoundment of TGR. In short, the cutting frequency of sandbar in the MLYR increases and the low shoal is more prone to be cut after the impoundment of TGR.

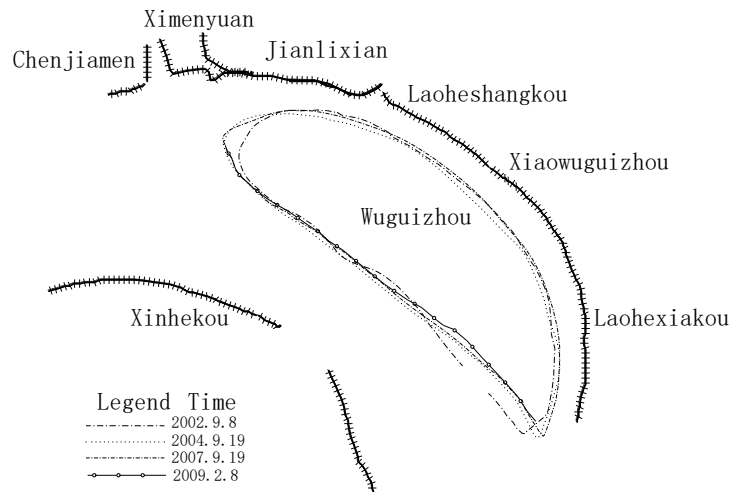


Figure 2: Bank collapse of Wuguizhou during 2002–2009

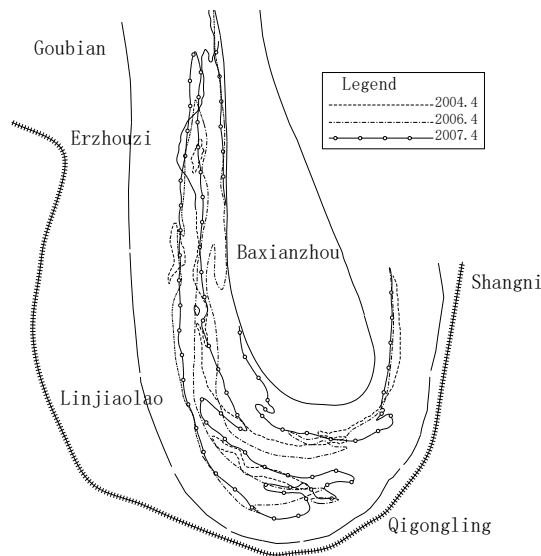


Figure 3: Cutting of the convex bank sandbar in Chibakou

The substantial shrink of low shoal is a common phenomenon since the impoundment of TGR. Before the impoundment, because of the fluctuation of flow and sediment and the translocation between the main branch and the second branch, the point bar and central bar scours and deposits frequently, but in a whole they maintains a balance, such as Guniusha bar had no a consistent change trend in

nearly 50 years before the TGR (Figure 4). However various types of point bar and central bars all shrink significantly after the impoundment of the TGR.

In the single-thread river reaches, such as the Guangxingzhou bar of the Tiepu waterway, the Luoshan bar of the Jiepai waterway, the Zhaojiaji bar of the Huguang waterway (Figure 5), are substantially shrinking while cutting after TGR. With the upper point bar in Jiepai reach scours promptly, its '0 m' line (Sailing base surface) has washed back to the head of the spur dike in 2010. In curved rivers, such as the Tiaoguan, Fanzui, Hanjinguang, Guniusha waterway, whose convex bars all show greater amplitudes of shrink (Figure 4). In the braided rivers, the concave bars and the low shoals of the sandbar head shrink markly, in some tributary arms the concave bars almost wash over, such as the Bahe bar of the Daijiazhou waterway and the Hongyangshu bar of the Tuqiao waterway.

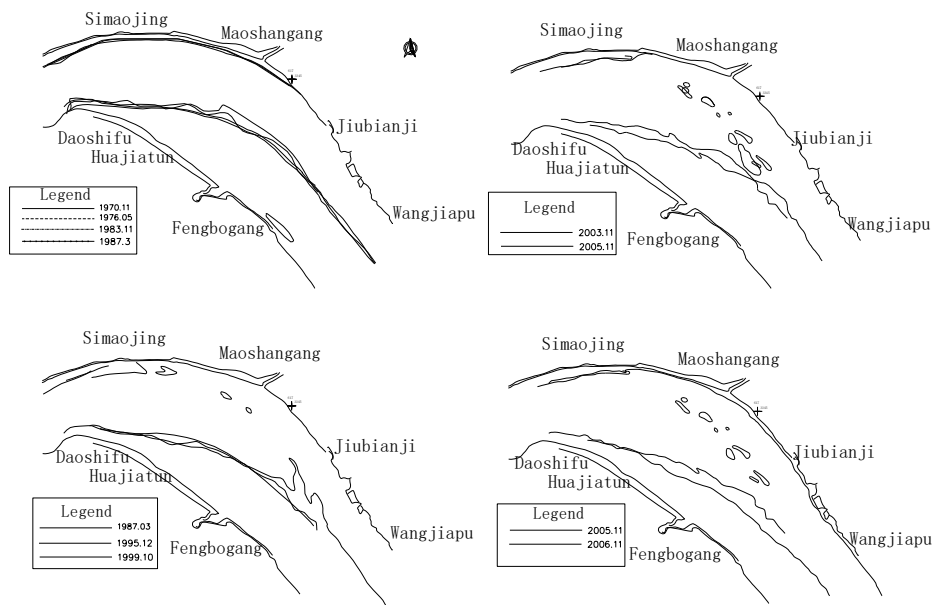


Figure 4: Changes of convex bank sandbar in Guniusha

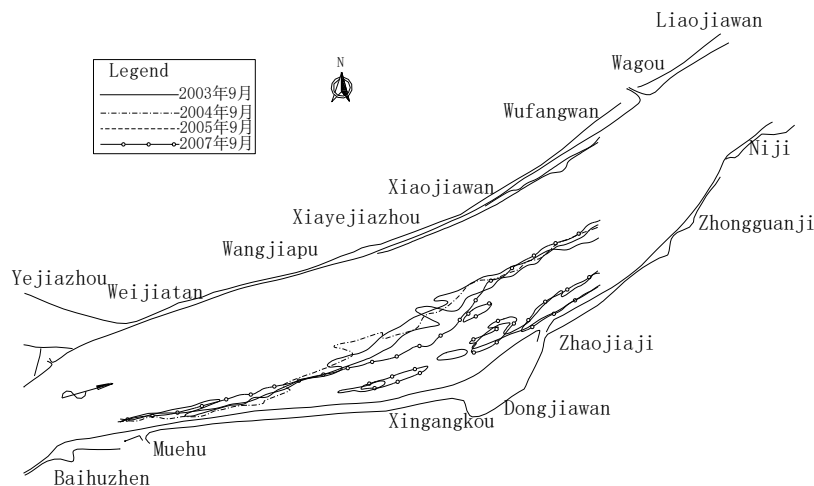


Figure 5: Changes of Zhaojiaji Sandbar in Huguang

3. The Impact of the Impoundment of TGR on the Channel in the MLYR

The impoundment of TGR changes the flow and sediment process in the MLYR, and then causes the collapse, sandbar cutting, substantial shrink of low shoal. The former changes the flow and sediment condition of the shoals, the latter changes the boundary condition of the shoals, both of them will affect the channel condition. The followings analyse the changes of channel condition firstly, then inquire into the impact on channel by the change of flow and sediment condition and the sandbar deformation.

3.1. The Impact on the Flow and Sediment Condition by the Impoundment of TGR

The shoal obstruction phenomenon in the MLYR mostly appears in the dry season, and compared with other levels, the change of the shoal depth at the lowest water level within a certain period more reasonably reflects the change of channel condition. Collecting the terrain data of typical shoals in the Jingjiang River in dry season, verifying the depth at the lowest water level of different period within a channel wide range of 150m, the result is shown as Figure 6. From this graph, the shoal depths in the Taipingkou, Majiazui, Zhougongdi, Tianxingzhou, Ouchikou, Jianli waterway increase, yet in Chibakou decreases, that is to say, most shoal depths increase while the channel condition improves, but individual shoal depth decreases.

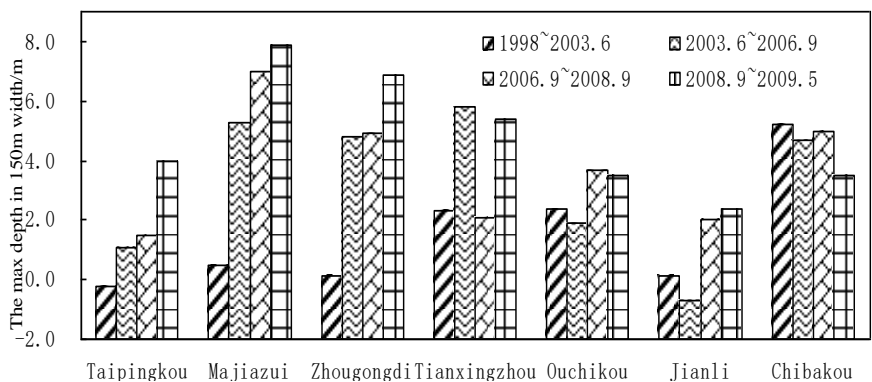


Figure 6: Changes of shoal water depth in Jingjiang Reach

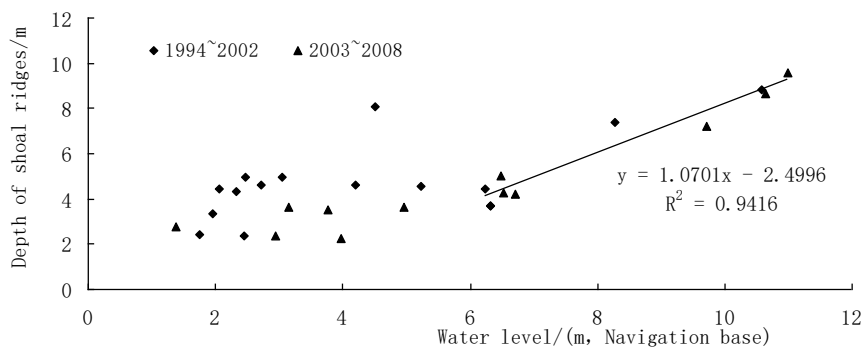


Figure 7: Relationship between the water depth and the water level at the shoal

3.2. The Impact of the Change of the Flow and Sediment Condition on Channel

1) *The impact on channel by the change of flow process*

A large number of field data shows that, the most shoals in the MLYR follow the evolution process of “depositing in the flood but scouring in the dry season” within a year. Obviously there is a critical flow. In the flood receding process, when the flow is less than the critical flow, the water returns to deep groove, the shoal begins to scour, the critical flow is called the critical flow of returning to channel (CFRC). Correspondingly the water level and the river width are respectively called the critical water level of returning to channel (CLRC) and the critical river width of returning to channel (CWRC).

Statistics on the relation between the water depth and the water level at the shoal ridges shows that (the relation in Jianli waterway shown as Figure 7), the CLRC in the MLYR is 6 m above the “82” sailing base surface. Further statistics on the relation between the water level and the flow shows that, the CFRC in the Shashi station, Jianli station, Luohan station, Hankou station is respectively 12000 m³/s, 11000 m³/s, 14000 m³/s, 16000 m³/s (TANG Jinwu et al., 2012). According to the definition, the longer the duration of the CFRC, the more fully the shoal scouring, the better the channel condition will be. Combining with the dispatching calculation result of TGR, the occurrence frequency of the CFRC (the flow below 12000 m³/s) in the Shashi station increases from 55.2% to 57.1% (Figure 1a). That's to say the flood recedes more slowly after the impoundment of TGR, the scouring time of the shoal increases averagely 7 days per year.

The scouring of shoal is not only related with the during time of CFRC, but also related with the size of channel flow in dry season. The average value of the flow in the dry channel is defined as the channel average scouring flow, which is average value between the CFRC and the lowest flow level, representing the riverbed deformation effect on channel by flow. According to the dispatching calculation result of TGR, statistics and analysis show that, the channel average scouring flow in various reaches of the MLYR increases by about 400 m³/s–1000 m³/s after the TGR's regulating, which is about 6%–8% of the channel average flow before TGR. Obviously, this change is favorable for the navigation condition.

In addition, owing to the replenishing water function of TGR in dry season, the driest flow increases, the lowest level raises in the downstream of the dam, so as the channel depth. The driest flow at the Shashi station is 3200 m³/s in the period from May, 1998 to 2003, the lowest level is 30.02 m, but in the period from September, 2008 to August, 2011 after TGR, the driest flow is 5300 m³/s increased by about 2000 m³/s, the lowest level is 31.08 m raised by about 1.0 m.

2) *The impact of the sediment discharge on channel*

The change of sediment discharge affects the channel condition by changing the shoal scouring speed. According to the riverbed deformation equation, when the sediment concentration declines, the shoal scouring thickness increases in unit time, the deposition thickness decreases, that's to say the scouring is accelerating but the silting is slowing down, which is undoubtedly advantageous to the navigation condition of MLYR. Numerous field datas also prove this point, like that the duration of the CFRC is basically equal to the channel average flow in the Jianli waterway in the flood receding process of 2001 and 2005, nevertheless the average sediment concentration after the flood is about 0.87 kg/m³ in 2001, but is only 0.26 kg/m³ in 2005, correspondingly the shoal scours 0.8 m in 2001, yet 2.0 m in 2005.

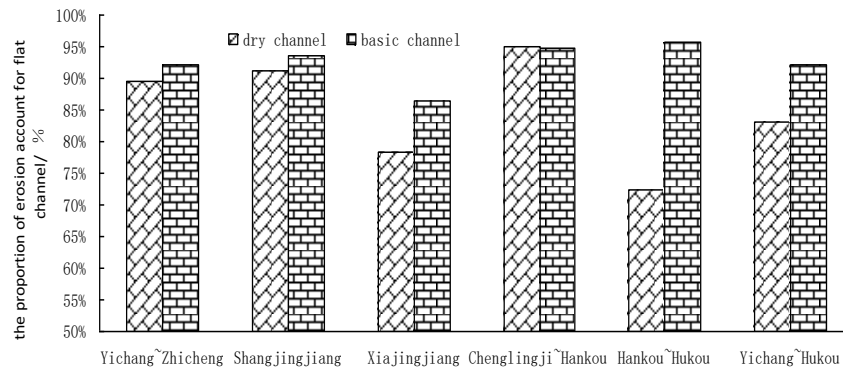


Figure 8: The percentage of the channel erosion at bankful water level

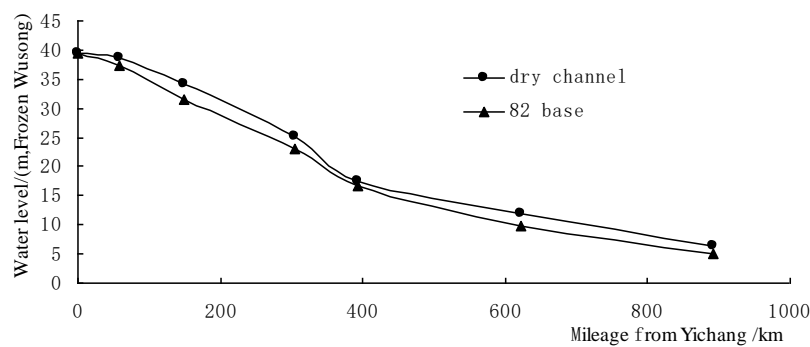


Figure 9: The low water level and the '82' sailing base level

Since the impoundment of TGR, under the influence of the sediment reduction, the riverbed in the MLYR scours generally, and the scouring quantity in dry channel accounts for more than 70 % in the flat channel (Figure 8). Figure 9 shows the contrast of the low water level and the '82' sailing base level, from which we can see the difference between above two is small, indicating that the erosion in the MLYR after TGR mainly occurs below the '82' base. With the development of erosion, the channel below '82' base scours continually, the altitude difference between the sandbar (point & central bar) and the channel is magnified, the duration of the CFRC will extend, the channel average flow will increase further, then the channel condition will be further improved.

Therefore, if the sandbar deforms rarely after impoundment of TGR, and the duration of the CFRC turns longer, the channel average flow increases, the lowest water level raises, the shoal deposition slows down but the erosion accelerates, the CFRC also tends to increase, which are all advantageous to the improvement of the channel condition, namely the change of the flow and sediment conditions is favorable for the channel.

3.3. The Impact of by Sandbar Deformation on Channel

Systematically arranging of the field terrain data in the MLYR and combining the change of navigation condition over the years, analysis shows that the effect on the channel by sandbar deformation can be divided into two kinds: the channel condition obstructs the navigation after the deformation as well as doesn't impede navigation after the deformation. Even if the same extent of the bank collapse or the low sandbar shrink, the change of the channel condition is not identical. The right margin of the Wuguizhou in the Jianli waterway collapses back about 200 m in 1996–1998, meanwhile the channel condition deteriorates sharply, only in the dry period of 1998–1999, the dredging quantity is more than

110000 m³. However it collapses back about 200m in 1994–1996, the channel condition has little change (TANG et al., 2012).

According to its definition, the CFRC means the flow when the shoal begins to scour after the flood. The smaller the CWRC, the larger the flow in unit width, the more fiercely the riverbed scours, consequently the CWRC heavily determines the shoal erosion intensity. Therefore, there exists a CWRC, when the actual CWRC is smaller than it, no matter what kind of riverbed deformation, the channel won't appear the obstructing sailing phenomenon; on the contrary, when the actual CWRC is larger than the critical value, the channel condition likely worsens and obstructs navigation.

From the viewpoint of the physical essence, the CWRC is, under the design water level, the minimum value of the WRC, when the maximum depth meets the maintenance depth within a range of channel width. Therefore, the method to determine the CWRC can be summarized as: according to the terrain data, adding up the relation between the maximum depth and the WRC under the design level within a range of channel width, from which we can find, when the actual water depth is equal to the maintenance depth, the minimum value of WRC is precisely the CWRC. Considering most shoals in the MLYR follow the discipline of “depositing in flood and scouring in dry season”, and the obstructive period focuses on the dry season, so the CWRC summarized by the above method, using the terrain data in the early days after flood (e.g. October), is relatively safe and can be used in practical engineering.

Collecting the terrain data after flood of MLRY in October of 1996 or 1998 or 2002, according to the above method, adds up the relation between the channel depth and the CWRC, the relationship of Group Five (the combination of the planning channel dimension in 2020 and the design water level in 2023) in Chenglingji – Hankou Reaches is shown in Figure 10. According to the under enveloping curve of the relationship, combining the channel maintenance depth, the various groups of CWRC in the different reaches are obtained, shown as Figure 11. As we can see from this graph, the CWRC in Shashi–Ouchikou Reaches, Ouchikou–Chenglingji Reaches, Chenglingji–Hankou Reaches, Hankou–Hukou Reaches, is respectively about 1300–1500 m, 900–1100 m, 1500–1700 m, 1800–1900 m.

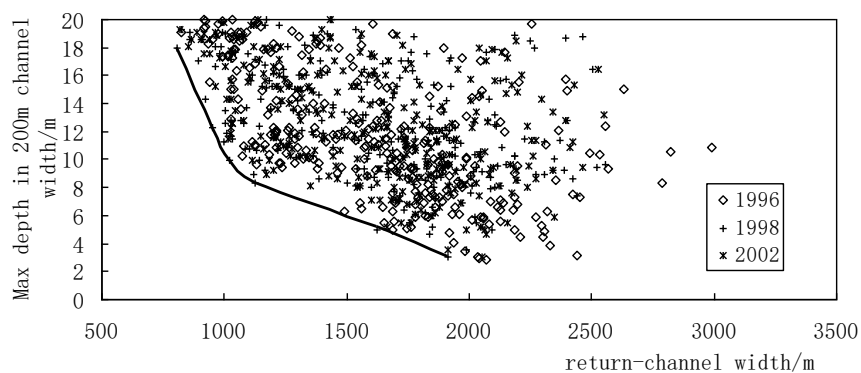


Figure 10: Relationship between CWRC and channel depth

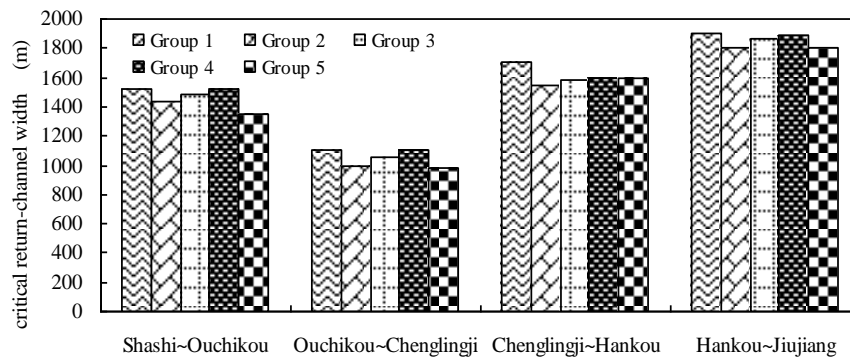


Figure 11: The critical CWRC of different combinations

As mentioned before, the right margin of the Wuguizhou in the Jianli waterway retreats back about 200 m, yet no obstructive navigation appears, the main reason lies in that the CWRC increases from 800 m to 1000 m, but is always less than the CWRC. However in 1996–1998 the right margin retreats back about 200m again, the CWRC increases to 1200m, more than the critical value, unfortunately the channel condition deteriorates and obstructs navigation. The right point bar of Nianziwan waterway deposits and accretes in 1996–1998, the CWRC constricts from 1200 m to 900 m, so the obstructive phenomenon disappears. The CWRC in the Majiazui, Jianli, Chibakou, Luxikou waterway are all larger than the critical values, thus the channel conditions obstruct navigation after sandbar cutting. Nevertheless the CWRC in the Longkou waterway is larger than the critical value, so its navigation condition is always better even though the convex sandbar cutting.

The CWRC in the Guniusha waterway before TGR is similar to the critical value, about 1900m. With the impoundment of TGR, the Guniusha bar gradually shrinks, until 2007 the CWRC increases to 2200 m, correspondingly the obstructive navigation occurs. However, although the point bars in Tiaoguan, Fanzui waterway shrink evidently too, their CWRC are still less than the critical value, consequently not yet obstructive navigation occurs. It is thus clear that, the CWRC analyzed in this paper is reasonable, which can be used to identify whether the obstructive navigation will occur or not, after the collapse, Sandbar cutting, low sandbar shrink substantially.

Based on the analysis above, after the impoundment of TGR, the change of flow and sediment process is favorable for the navigation condition, the deterioration of navigation condition mainly due to the fierce sandbar deformation, such as collapse, sandbar cutting, low sandbar shrink substantially. Owing to that the riverbed in the MLYR is subjective to the erosion of the less saturated flow in future for a long time, the low point bar and central bar will shrink further, and the nearshore riverbed scours, the slope ratio increases, the bank without the revetment will collapse further, when the CWRC caused by the sandbar deformation is larger than the critical value, the channel that originally not obstructs navigation will appear obstructive phenomenon.

Therefore, the channel regulation should guard timely the sandbar whose CWRC approaches or exceeds the critical value, avoiding of getting into the extremely passive situation of obstruction navigation. The longer the duration of CFRC, the more sufficiently the shoal scours. Thus the cascade reservoir dispatching in upstream should try to extend the duration of the CFRC (the flow below $12000 \text{ m}^3/\text{s}$ in Yichang station) in the MLYR as far as possible.

4. Conclusions

This paper analyzes the change of the flow and sediment process in the MLYR and the characteristics of sandbar deformation, combining with the field data before and after TGR, dissects their effect on channel in the MLYR, the main conclusions are as follows:

- 1) After the impoundment of TGR, the flow below 5000 m³/s basically disappears, the occurrence frequency in 5000–12000 m³/s increases substantially, the occurrence frequency above 12000 m³/s reduces a little, meanwhile the sediment concentration decreases sharply. After the TGR, both the frequency and the length of bank collapse increase significantly, the frequency of the low sandbar cutting increases and the low sandbars shows a trend of shrink.
- 2) After TGR, the change of flow and sediment process is favorable for the channel condition, concretely represented as the duration of the shoal scouring extends, the scouring intensity strengthens, the driest flow increases, the lowest water level raises, the reduction of sediment discharge causes the shoal deposition slows down, but the erosion accelerates.
- 3) After TGR, the channel condition deteriorates mainly due to the fierce sandbar deformation, such as collapse, sandbar cutting, low sandbar shrink substantially. Whether the channel obstructs navigation or not, depends on the size of the CWRC. When the CWRC is smaller than the critical value, the channel won't appear obstructive phenomenon, yet when the width is larger than the critical value, the waterway is likely to obstruct sailing.

Acknowledgment

This study was supported by the National Program on Key Research Project of China, No: 2016YFC0402306.

Thanks to Bureau of Hydrology, Changjiang Water Resources Commission, Wuhan University for providing the topographic and hydrological data.

References

- Chao Gao, Shi Chen, and Jian Yu. River islands' change and impacting factors in the lower reaches of the Yangtze River based on remote sensing. *Quaternary International*. 2013. 304; 13–21.
- Chen, Z.Y., Wang, Z.H., Finlayson, B., Chen, J. and Yin, D.W. Implications of flow control by the Three Gorges Dam on sediment and channel dynamics of the Middle Yangtze River, China. *Geology*. 2010. 38; 1043–1046.
- Harman, C., Stewardson, M., and Derose, R. Variability and uncertainty in reach bankfull hydraulic geometry. *J. Hydrol.* 2008. 351; 13–25.
- Harmar, O.P. Morphological and process dynamics of the lower Mississippi River. University of Nottingham, Ph.D Dissertation. 2004. 409.
- XIONG Zhiping et al. Fluvial processes of shoals in Upper Jingjiang Reach before and after construction of Three Gorges Project in Yangtze River. *Journal of Chongqing Jiaotong Institute*. 2000. 19 (1) 88–91.
- LI Xianzhong et al. Influences on waterway of Jingjiang River Key Reach after impoundment of Three Gorges Junction and research on countermeasures. *Port & Waterway Engineering*. 2004. (8) 55–59.

CAI Dafu et al. Variation of channel condition above and below the dam after impoundment of Three Gorges Reservoir. *Port & Waterway Engineering*. 2006. (12) 62–65.

LIU Huaihan et al. Recent waterway evolution and treatment measures in the reach between Yichang and Chenglingji. *Port & Waterway Engineering*. 2005. (12) 37–41.

HAN Qiwei et al. Influence on flood occurrence of Dongting Lake due to change of relation between Yangtze River and Dongting Lake. Paper Collection of the Second Yangtze Forum. Beijing. 2007. 18–35.

Zhijun Dai, and James T. Liu. Impacts of large dams on downstream fluvial sedimentation: An example of the Three Gorges Dam (TGD) on the Yangtze River. *Journal of Hydrology*. 2013. 480; 10–18.

TANG Jinwu, DENG Jinyun, YOU Xingying et al. Forecast method for bank collapse in Middle and Lower Yangtze River. *Journal of Sichuan University*. 2012. 44 (1) 75–81.

Lee, J.S. and Julien, P.Y. Downstream hydraulic geometry of alluvial channels. *J. Hydraul. Eng.* 2006. 132 (12) 1347–1352.

Junqiang Xia, Quanli Zong, Shanshan Deng, Quanxi Xu, and Jinyou Lu. Seasonal variations in composite riverbank stability in the Lower Jingjiang Reach, China. *Journal of Hydrology*. 2014. 519; 3664–3673.

Ming–Wan Huang, Jyh–Jong Liao, Yii–Wen Pan, and Meng–Hsiung Cheng. Rapid channelization and incision into soft bedrock induced by human activity–Implications from the Bachang River in Taiwan. *Engineering Geology*. 2014. 177; 10–24.

Qiang Zhang, Chunling Liu, Chong–yu Xu, Youpeng Xu, and Tong Jiang. Observed trends of annual maximum water level and streamflow during past 130 years in the Yangtze River basin, China. *Journal of Hydrology*. 2006. 324; 255–265.

Xu, Q.X., Yuan, J., Wu, W.J., and Xiao, Y. Fluvial processes in the Middle Yangtze River after impoundment of Three Gorges Project. *J. Sediment Res.* 2011. 2; 38–46.